NORTHWESTERN UNIVERSITY

Low Temperature Electrical Transport Behavior of
AlO_x / $KTaO_3$ Based Two Dimensional Electron Gases

A DISSERTATION

SUBMITTED TO THE GRADUATE SCHOOL
IN PARTIAL FULFILLMENT OF THE REQUIREMENTS

for the degree

DOCTOR OF PHILOSOPHY

Graduate Program in Physics

By

Patrick W Krantz

EVANSTON, ILLINOIS

September 2023

ABSTRACT

Low Temperature Electrical Transport Behavior of

AlO$_x$ / KTaO$_3$ Based Two Dimensional Electron Gases

Patrick W Krantz

Necessity is the mother of innovation. In the wake of the pandemic, with no flow of samples and limited fabrication techniques available, necessity demanded a new material platform and adaptable methods to make complex oxide samples worth measuring. The material platform was KTaO$_3$, the younger successor to the mainstay of complex oxide work, SrTiO$_3$, and the method was in-house aluminum evaporation that generated a conducting gas on the surface of the unassuming crystal squares. The result of this innovation was the conducting gas at the interface of the AlO$_x$ / KTaO$_3$ heterostructure, fabricated into Hall bars to measure conducting properties and search for novel physics. KTaO$_3$ has previously been shown to host a number of interesting properties, including large spin orbit interactions due to the conducting $5d$ orbitals on the Ta atoms, superconductivity on the (110) and (111) crystal terminated faces up to 2 K, and a readily tunable set of conducting properties with an applied back gate voltage. These properties were confirmed in two sets of conducting samples fabricated as described, and showed improvement in both carrier concentration and carrier mobility compared to similar works in the literature. The samples also showed a series of novel results, in particular the emergence of macroscopic magnetism evident in hysteretic peaks observed in magnetotransport measurements. The second set of samples were fabricated in such a way to induce superconductivity, and those samples showed peaks in carrier concentration as a function of applied gate voltage, indicated the presence of a Lifshitz transition in the nature of the conduction. This unexpected carrier dependence on gate voltage was reflected

in the superconducting properties, which showed other novelties including an upper gate limit to the superconductivity, a coexistence of the superconductivity with the macroscopic magnetism, and non-trivial relationship between carrier concentration and T_c, which is a strict departure from the literature. An analysis of the superconducting state followed, showing other peculiarities, and the work extends to measurements of the quantum nonlinear Hall effect which do not agree with theory for most of the samples investigated. In total, this work forms a broad basis for research on the novel transport properties of the AlO_3 / KTO interface, and suggests several experiments to dive deeper into unexplained results encountered along the way.

ACKNOWLEDGEMENTS

There have been many people who have contributed in one way or another to my journey up to this point. There are those who taught me invaluable lessons of physics or life, those who supported me or believed in me when I didn't fully believe in myself, and many people who have shared meaningful experiences with me throughout the years. I would like to thank all of you for your contributions to my life and to my career, I would not have been able to do it without you.

First and foremost I would like to thank my advisor, Prof. Venkat Chandrasekhar, for being a wonderful advisor and for teaching me nearly everything that I learned in graduate school. You are the reason I wanted to come to Northwestern in the first place and I would not have been let in without your advocacy. You have accounted for nearly half of my classes and nearly all of the experimental techniques I have learned here. I particularly appreciate your patience and even judgement as I learned all of this. it was your suggestion to try to make devices on KTO, and it is an enormous understatement to say that this work would not be possible without you.

I would like to thank my committee members, Prof. Vinayak Dravid and Prof. Pallab Goswami, both of which I have had the privilege to work with on this and other projects, and to learn from in my time at Northwestern. You expect great things from your students, and I hope I have lived up to those expectations. I would also like to thank a few of the other Professors in the Department, in particular Prof. Bill Halperin and Prof. Jens Koch, who were both generous with their time and support, and who were patient with my many, and sometimes outlandish questions.

To the members of University Toledo's PVIC, in particular Prof. Mike Heben, Prof. Randy Ellingson, and Dr. Adam Phillips, you taught me a lot about solar cells, physics, and vacuum systems, skills that I would be useless without. I would also like to thank Dr. Zhaoning Song, Jon DeWitt, and Rosa Zartman who mentored me for years at UT, to Ammaarah El-Amin who believed

in me when I dared to want to return to graduate school, and to Dr. Bob Clark-Phelps who taught me many things at First Solar. Similarly, I would like to thank Dr. Sam Davis, who tried valiantly to teach me all he could before graduating from our group, and Dr. Andrew Zimmerman, who was the closest thing I had to an older lab mate for a long time. I would not be the scientist I am now without your tutelage.

My time at Northwestern would have been much worse also without the support and kindness of the members of the Administration and Accounting Offices. In particular I would like to thank Bud Robinson, who was both the first person I interacted with from the Department and was my good friend for a number of years. I would also like to thank Julia Blend and Vaso Ventresca who had to deal with me directly more than probably anyone else, and who were always willing to at least entertain my creative purchase requests, or just talk about something for a few minutes on a long day.

To my many friends I have made in my time at Northwestern, like Alex, Bianca, Maddy, Jovan, John Scott, Abdul, Ingrid, Renée, Yizhou, Joey, Dylan, Anirudh, Clayton, and Max, I appreciate you, your kindness, and your friendship. To my junior lab-mates, in particular Kevin Ryan and Max Wisne, but also to the younger students Yan, Nanxi, Austin, and all the rest, thank you for joining me on this journey, we have been through a lot and I wish you the best in your remaining time here.

I would like to give special recognition to Dr. Samantha Huddleston, my partner. She has been a wonderful friend for along time, my partner in exploration, my Frisbee teammate, and my motivation for the last two years. Thank you for your support and patience while I finish this work. I love you, and look forward to the adventures that we will find now. I would also like to give special thanks to Dr. Christian Contreras, who was my friend and fellow Frisbee Fanatic for many years, who introduced me to may Frisbee teams, and by way of them to Sam. You were a

wonderful roommate, and a wonderful confidant, and a lifeline when we both sorely needed it. My youngest brother Ryan also deserves special thanks, as he took the chance to be my roommate here in the Big City, during the pandemic, and has put up with many late nights and high stresses for two years. For the three of you I am forever grateful.

I also would like to give a huge shout-out to all of my friends I have made through Frisbee, both at Northwestern and before. In particular the members of Jurassic Shark, including Gilson, Soldini, Chris, Danny, Poland, Peaches, TK, RJ, Drew Wood Attorney at Law, Austin, Watertower, and many others; from Peanuts, our perennial Champion Intramural team, with Christian, Jamie, Sam, and many more; and from Big Fun, our Chicago summer league team, with Sean, Ryan, Camen, Carly, Karli, Madds, and all the rest. Your friendship and shared joy I could not have done without.

And last but certainly not least, I would like to thank my parents David and Susan Krantz, who taught me from an early age to think for myself, and who believed that it was not *if* I would earn my doctorate, but *when*. Your love and support I could not have survived without, and I hope that I can continue to make you proud as I move on to the next phase of this journey.

LIST OF ABBREVIATIONS

ac - Alternating Current

AlO_x - Amorphous Aluminum Oxide

dc - Direct Current

DFT - Density functional theory

KTO - $KTaO_3$ Potassium Tantalate

LIA - Lock-in Amplifier

LCAO - Linear Combination of Atomic Orbitals

LSAT - $(La_{0.3}Sr_{0.7})(Al_{0.65}Ta_{0.35})O_3$

PLD - Pulsed laser deposition

s.c. - Superconducting (samples)

SOC - Spin-orbit Coupling

STO - $SrTiO_3$ Strontium Titanate

T_c - (Superconducting) Transition Temperature

2DCG - Two Dimensional Conducting Gas

2DEG - Two Dimensional Electron Gas

QNLHE - Quantum Non-Linear Hall Effect

V_g - Backgate Voltage (Alternatively V_{Bg})

TABLE OF CONTENTS

LIST OF FIGURES

LIST OF TABLES

CHAPTER 1

INTRODUCTION

Condensed matter physicists seek an understanding and control over material systems to use them as tools to further probe our world, or to harness the power in technologies that transform our daily lives. Like semiconductor research of the 1940s which lead to the digital revolution, fundamental research of the modern era seeks the next advancement in fields like high temperature superconductivity, quantum computation, or spintronics. These technologies often require materials that combine different properties, making them challenging to study but scientifically interesting as platforms to explore the interactions between disparate forces or to search for new physics.

The family of complex oxide materials represent one such confluence of properties, and they respond readily to external, experimentally tunable parameters. $SrTiO_3$ (STO) is the preeminent example of a material system hosting multiple competing electronic states including normal metallic conductivity, superconductivity, and magnetism. The two dimensional electron gas (2DEG) hosted on its interface has been exhaustively studied since its discovery in 2004. One worthy successor to STO is $KTaO_3$ (KTO), which boasts a number of improvements over STO including stronger spin orbit interactions and higher transition temperatures for superconductivity. The work presented here in this manuscript seeks to probe this new platform through electrical transport measurements performed on the 2DEG formed at the AlO_x / KTO interface, looking for signatures of novel quantum phenomenon.

The results here focus on two sets of samples fabricated by the author; the first where the 2DEG is metallic but not superconducting down to the lowest measurement temperatures, the sec-

ond which did go superconducting. Each set of samples included (001), (110), and (111) crystal terminated KTO substrates, to compare the effects of crystal orientation on the transport properties, which are substantial. Both sets of samples show signatures of magnetism at low temperatures, despite there being no magnetic constituents in the fabrication components. The magnetism even persists in the superconducting regime of the second set of samples. On this largely phenomenological bedrock we also explore more advanced experimental techniques to probe the Berry curvature of the system, which manifests itself as an anomalous component in the second harmonic response of the Hall effect at low temperatures. These findings inform future experiments which would look for further signatures of topological transport and potentially topological superconductivity.

The remainder of this thesis is organized as follows:

Chapter 2 discusses in detail the previous experimental results that informed this work. KTO cannot escape comparison to STO, and many of the works in STO find parallels in the current work on KTO. Examples of these parallels include works on heterostructure construction using similar materials, works on spin-charge conversion and other manifestations of the spin-orbit coupling (SOC), and the coexistence of superconductivity and magnetism. This chapter will also discuss recent experimental work on KTO and potential applications.

Chapter 3 establishes a theoretical foundation for many of the phenomenon observed in KTO devices. It discusses the origin of the conduction seen at the interface of complex oxide heterostructures, introduces some selected results from Ginsburg-Landau theory that describe physical characteristics of the superconductivity, delves deeper into magnetoresistance, covers the Hall effect, and finally introduces the quantum non-linear Hall effect (QNLHE). This will inform the analysis

conducted on experimental results later in the manuscript, and is not meant to be an exhaustive discussion of these topics.

Chapter 4 describes the experimental techniques used to produce our results. Special attention is paid to novel procedures developed to prepare superconducting samples, and to probe the quantum non-linear Hall effect in those samples. Additionally, a discussion of specific experimental artifacts is included, with examples and explanations so future experimentalists can avoid pitfalls common to these type of measurements.

Chapter 5 is the core of the thesis, where the experimental studies on the normal metal and superconducting KTO sample sets are presented and interpreted. This chapter is generally broken into two parts, one discussing the transport properties of the AlO_x / KTO system in the normal and superconducting state, and one focused on the quantum non-linear Hall effect and its implications for the system.

Chapter 6 summarizes the findings of the thesis, details future experiments to be conducted on these systems, and predicts the results of those experiments.

CHAPTER 2

PRIOR WORKS: KTO AND STO

$KTaO_3$ is a cubic perovskite material first appearing in the literature in a Physical Review article detailing the Proceedings of the American Physical Society[1] from the April 28th - 30th Meeting, 1949. There, B. T. Matthias of Bell Labs gave a talk about the ferroelectric Curie temperatures of a number of newly synthesized materials, including $KTaO_3$. For the next few decades, experimental interest focused on the optical and ferroelectric properties[2–4] of KTO and its solid solutions.[4–6] It took until 1965 that the transport properties of the material came of interest[7] in the wake of the discovery of bulk superconductivity[8] in Nb doped $SrTiO_3$. Superconductivity remained elusive in KTO despite attempts at doping[9] or modifying the material with oxygen vacancies.[7] Research into the material continued, still tightly bound to the fate of STO, and many of the seminal works on STO include KTO as a reference, e.g. the establishment of STO as an intrinsic quantum paraelectric also incriminates KTO.[10]

Work on the surface of KTO accelerated in 2004 when Ueno *et al.*[11] investigated the potential of the KTO surface, constructing FET devices showing n-type semiconducting behavior, once again extending work that had already been done on STO substrates.[12] The two dimensional electron gas (2DEG) was later shown to be metallic down to cryogenic temperatures,[13] but it was not until 2011 that Ueno *et al.* showed that the system could be gated into superconductivity[14] using a polyethylene oxide/ $KClO_4$ top gate. From there the field expanded to include many different heterostructure top layers including $LaAlO_3$,[15,16] EuO,[17,18] and $LaVO_3$[19] among others. The material remains a promising platform for a number of potential applications due to its high superconducting transition temperature, large spin-orbit interactions, and potential topological qualities.

2.1 Material Properties and Band Structure

KTaO$_3$ is a body centered cubic (BCC) perovskite with the Pm$\bar{3}$m space group,[20] as shown in Fig. 2.1 (a). It is a 3.64 eV indirect band gap n-type semiconductor with the smallest direct gap of 4.35 eV,[21] as shown in Fig. 2.1(a) and (b). KTO also has a large dielectric constant that increases from a few hundred at room temperature to $\sim$5000 at low temperatures.[6] At these temperatures KTO is a quantum paraelectric material, also referred to as incipient ferroelectric material, where quantum fluctuations suppress a true ferroelectric phase transition.[10] This transition can be recovered through defect engineering,[22,23] or by creating polycrystalline films, where it shows a Curie temperature[24] of 60 K.
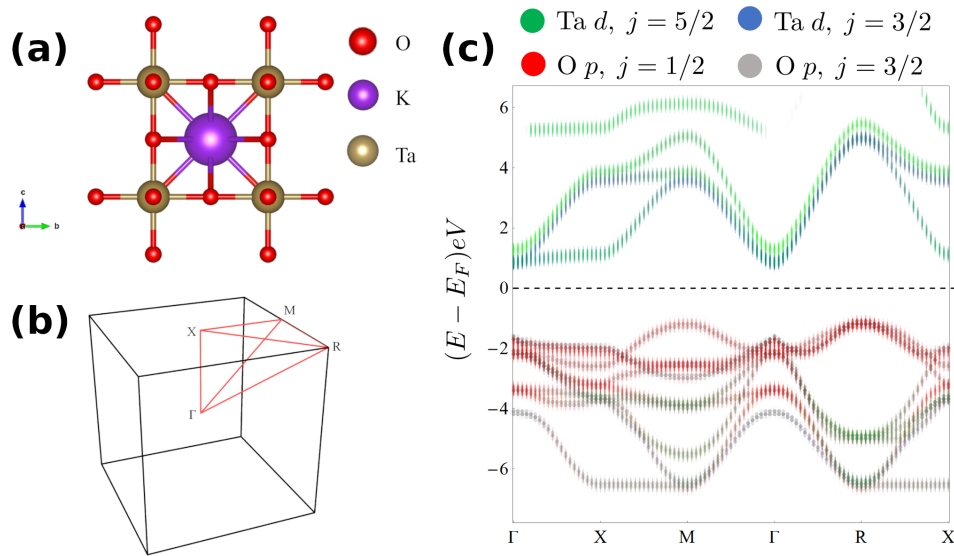
Figure 2.1: **Crystal structure and band structure of bulk KTaO$_3$** (a) Unit cell of the bulk body-centered-cubic perovskite KTaO$_3$, (b) orientation description of the first Brillouin zone, and (c) bulk density functional theory calculation color coded by band character. Figure generated by Alex Tyner, (unpublished).

All of these properties mirror findings in SrTiO$_3$, which has the same crystal structure,[20] a smaller indirect band gap[25] of $\sim$3.2 eV, and a low temperature dielectric constant[10] of $\sim$ 30,000.
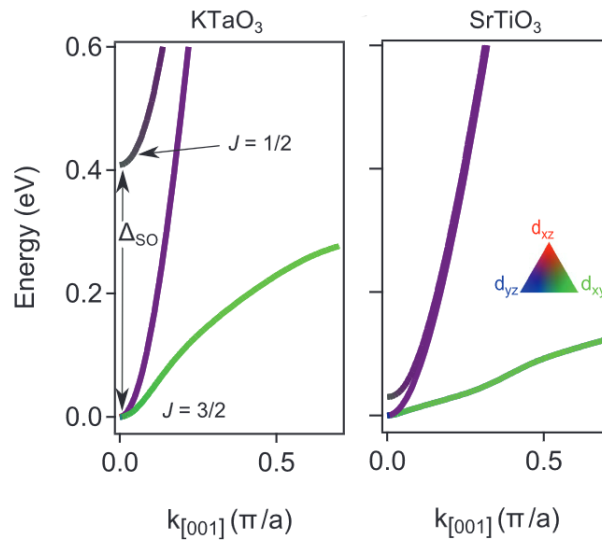
Figure 2.2: **Spin-orbit splitting at the Γ - point in bulk KTaO$_3$** A direct comparison of the band splitting between the $J = 3/2$ and $J = 1/2$ bands in KTaO$_3$ and in SrTiO$_3$, along with color coded band mixing. Figure adapted from Bruno *et al.*[32]

STO is also a quantum paraeletric material at low temperatures,[10] but unlike KTO it undergoes a cubic to tetragonal distortion[26] at $\sim$105 K. This structural transition contributes to many of the transport properties of STO at low temperatures, most notably due to the prevalence of tetragonal domains which have been shown to be polar,[27] magnetic,[28] and to host preferential conducting channels.[29,30] These domains are also responsible for some of the reproducibility problems in measurements of STO based systems, as the domains randomly order as long fingers with the primary axis along [001] crystal direction when passing through the structural transition at 105 K.[29,30] The domains can be moved with strain,[31] and can be modulated or diluted with gate voltage sweeps.[27] Without this added complication and random ordering, KTO boasts improved stability and reproducibility in its transport behavior, a characteristic that the author is quite thankful for.

The band structure of KTO has been a subject of investigation since at least the early 70s, when L.F. Mattheiss[33] and D.R. Edmondson[34] independently published calculations of the bulk

band structure using a modified linear combination of atomic orbital (LCAO) model, a method introduced by Slater and Koster[35] in 1954. The results identified Ta $5d$ and O $2p$ orbitals as the two main contributing conduction bands for electrons and holes respectively, and fit the band gap to the experimentally observed 3.6 eV value obtained from optical transitions. Fifty years later, this result holds qualitatively, though the precision of the result has improved with the advancement of computing power. Fig. 2.1 (c) shows DFT results for the bulk band structure of KTO calculate by Alex Tyner, showing color coded contributions to the conduction band agreeing with Edmonson's result that Ta $5d$ and O $2p$ orbitals dominate. These results have been corroborated by Fermi surface reconstruction through high magnetic field measurements of bulk KTO in 1987 by Uwe *et al.*,[36] and spectroscopic ellipsometry in 2006 by Jellison *et al.*[21] amongst other measurements. The Ta $5d$ bands also feature very strong spin-orbit coupling, which results in a 400 meV gap between the $J = 3/2$ and $J = 1/2$ bands at the Γ - point, as reproduced from Bruno *et al.*[32] in Fig. 2.2. The figure also shows the more modest 17 meV splitting in STO, arising from the much lighter Ti $3d$ bands. In summary, bulk KTO is a standard band insulator that can be doped in to conductivity,[7] but is otherwise only notable for its large spin-orbit splitting.

In contrast to the bulk, the surface of KTO has proven to be a significantly more interesting physical system, partially because of differences in symmetry. The three major crystal terminations of the BCC crystal group are the (001), (110), and (111) surfaces, corresponding to a cut along the face of the BCC bulk cell, along one facial diagonal, and along the major diagonal cut respectively. Each of the resulting surfaces boasts a distinct symmetry: the (001) has C_4 rotational symmetry with $a = 3.99\text{Å}$, the (110) elongates one of the sides and breaks the symmetry into two fold C_2 symmetries with $a = 3.99\text{Å}$ and $b = 5.64\text{Å}$, and the (111) has C_3 rotational symmetry with $a = 5.64\text{Å}$. A reflection of these differences can be seen in the reciprocal space surface states, as shown in Fig. 2.3. These symmetry difference coincide with a crystal direction dependent mixing
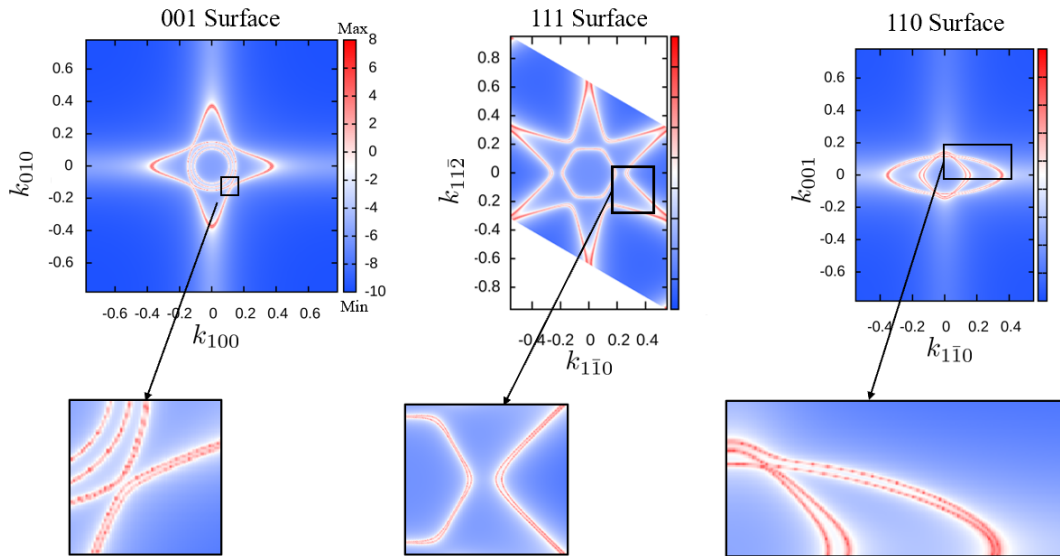
Figure 2.3: **Band structure of the surface of KTaO$_3$.** From left to right: surface states of the (001), (111), and (110) crystal terminations, with insets showing details of the spin-split Rashba bands. Figure generated by Alex Tyner, (unpublished).

of the Ta $5d$ orbitals,[37] which can lead to distinct transport behaviors for each surface.

On each of the crystal faces the strong spin-orbit coupling of the Ta $5d$ electrons form Rashba spin-split bands heavily dependent on crystal direction. This has been studied in a number of angle-resolved photo-emission spectroscopy (ARPES) measurements and subsequent band recon-structions.[32,37–39] The studies identified the contributing sub-band structure of the surface conduct-ing gases,[37,38] and highlighted the complex band mixing of the surface gas, which contrasts sharply with the structure of STO.[37] As shown in Fig. 2.4 all three of the t_{2g} orbitals (d_{xy}, d_{xz}, and d_{yz}) contribute with varying weights to the nature of the conducting bands at the surface.[37] Moreover, the mixing of the bands creates interesting spin textures at the surface due to the large spin-orbit coupling, an effect that is most prominent for the (111) surface,[32] as shown in Fig. 2.4 (a). This band mixing is directional, with the maximal mixing in the $[1\bar{1}0]$ surface crystal direction, as shown
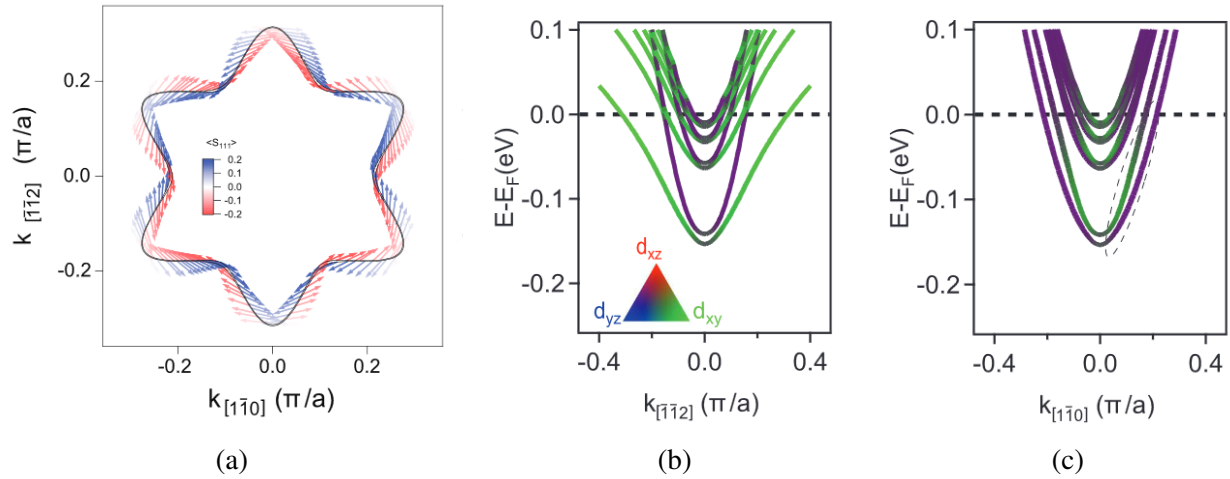
Figure 2.4: **Spin texture and band mixing on the (111) surface.** (a) Spin texture with out of plane component for the (111) KTO surface. (b) Band dispersion along the $[1\bar{1}0]$ direction, where band mixing is maximized, (c) band dispersion along the $[1\bar{1}2]$ direction where band mixing is minimized. All figures adapted from Bruno *et al.*[32]

in Fig. 2.4 (b), which results in a large out-of-plane spin texture.[32] In contrast, the orthogonal surface direction $[1\bar{1}2]$ has both the mixing and out-of-plane contribution minimized, Fig. 2.4 (c). This combined symmetry and spin-orbit effect results in anisotropic transport[18,40,41] and nearly two orders of magnitude difference in superconducting transition temperatures depending on crystal termination.[14,18] These results, and many others, are the subject of the next section.

2.2 Interfacial Two-Dimensional Conducting Gases

The first probes of interfacial conductivity in KTO sought to use electrostatic gating to induce a surface charge,[11] following the procedure that showed success in STO.[12] This simple field effect transistor was constructed on (001) KTO and serendipitously featured a 50 nm thick Al_2O_3 rf-sputtered overlayer separating the surface of the KTO from a gold paint top gate. The device showed moderate ON/OFF ratios of 10^4, with low mobility of only 0.4 (cm^2 / V s), in sharp

contrast to the behavior of the 10,000 (cm^2 / V s) shown in LaAlO$_3$ / STO shown by Ohtomo and Hwang,[42] earlier that year. Nevertheless, the result marked the start of a number of studies seeking to improve the technique of generating a two dimensional gas at the interface of complex oxides. In 2008 Ueno *et al.*[43] demonstrated superconductivity in (001) STO gated with an ionic liquid gel: a mixture of polyethylene oxide/ KClO$_4$. Such a technique takes advantage of the large electric fields induced by the electric double layer formed from ionic ordering at the surface of the ionic liquid gel when a gate voltage is applied, and would later be used to great effect in doping van der Waals thin films like MoS$_2$.[44] This approach was soon applied to KTO, when in 2011 Ueno *et al.*[14] applied the same top gate to (001) KTO substrates and showed superconductivity at 50 mK, the only (001) terminated KTO system to do so. The sample configuration and the report of the superconducting transition are presented in Fig. 2.5. These superconducting devices showed dramatic improvement in conducting properties over the earlier Al$_2$O$_3$ topped samples, with carrier concentrations of 2.3 x 10^{14} to 3.7 x 10^{14} (e / cm^2) and an improved mobility of 7,000 (cm^2 / V s). This was far from the end of attempts to engineer two dimensional conducting gases at the interface of KTO though, and further investigation highlighted the impact of crystal termination on the conducting properties.

Once again following previous works on STO, other oxide capping layers and surface treatments have been applied to KTO in hopes of generating a conducting gas with tailored properties. In an effort to probe the natural electronic structure of KTO, a (001) sample was lightly doped with Ba and then cleaved to reveal a polar conducting gas on the surface, which was probed with ARPES.[38] This work had followed previous studies on STO which showed the generation of a 2DEG by vacuum cleaving[45] or exposure to UV light.[46] Similar results have been shown with Ar$^+$ ion bombardment, which allowed for the generation of both 2D and 3D conductivity in (001) KTO as probed by Shubnikov–de Haas oscillations measured at 2 K.[47] The practice of directly probing
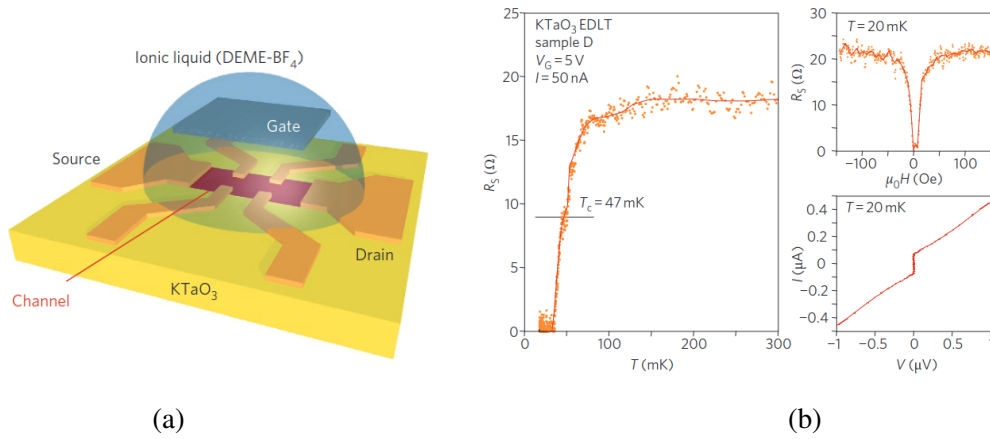
Figure 2.5: **Ionic liquid gating (001) KTO into superconductivity.** (a) Schematic of the KTO sample with ionic liquid top gate. (b) Temperature dependence of the superconducting transition, low field magnetoresistance, and I - V characteristics of the KTO sample. All figures adapted from Ueno *et al.*[14]

crystal surfaces was extended to (111) KTO samples, which were cleaved in ultrahigh vacuum to reveal a six-fold symmetric Fermi surface with the suggestion that such a surface could host a topological 2D-metal due to the odd parity of the electron wave function at a pair of $\bar{M}$ points.[39]

Other methods of generating 2DEGs involve the deposition of capping layers directly onto the KTO via pulsed laser deposition (PLD), molecular beam epitaxy (MBE), or sputtering. The resulting device generated a conducting gas at the intersection of two dissimilar layers, in a configuration called a heterostructure. The first heterostructure to be fabricated this way was made from a $LaTiO_3$ over-layer in 2015 by Zou *et al.*[48] They showed a very poor carrier mobility of 21 (cm^2 / V s) with a carrier concentration between 5 x 10^{13} and 1.5 x 10^{14} (e / cm^2). They explained their data in terms of a polar discontinuity model resulting in charge transfer at the interface, which at the time was the predominant theory for conductivity in LAO/STO, and will be discussed in detail later. Soon better systems were realized for conductivity at the KTO interface, revealing a wealth of new physics to probe.

The next most obvious choice of capping layer is LaAlO$_3$ (LAO) given its success in STO heterostructures,[42] and indeed devices were successfully fabricated[15] with an amorphous LaAlO$_3$ over-layer deposited on (001) KTO via PLD. The study reported similar transport properties to those previously discussed, with lower carrier concentrations of 2 x 10^{12} cm^{-2} and mobilities of $\sim$ 2,000 (cm^2 / V s). A later study[15] on LAO / KTO showed that the spin relaxation time could be tuned by nearly two orders of magnitude by the application of back gate voltage, an improvement over STO that reflects the larger spin-orbit interactions.[32] Ironically, amorphous LAO has also been used as a mask for ionic liquid gel doping of KTO surfaces. In 2021 Rubi *et al.*[49] used PLD to deposit amorphous LAO to define a negative Hall bar which was doped into conduction using the popular ionic liquid gel (DEME-TFSI). Their study probed the nature of the resulting 2DEG using angle dependent magnetotransport down to 80 mK, revealing sub-band structure in the 2DEG and the existence of a 3D conducting band similar to those shown through Ar$^+$ bombardment.[47]

Crystalline LAO has also been used as a capping layer for KTO. The first observation of superconductivity on (110) oriented KTO was made in an LAO heterostructure by Chen *et al.*[16] in 2021. They report a transition temperature of $\sim$ 900 mK for carrier concentrations of $\sim$7 x 10^{13} (e / cm^2), with an estimated superconducting layer thickness of $\sim$ 8 nm and coherence length of $\sim$ 30 nm. Interestingly, they note that similar samples made on (001) and (111) KTO showed amorphous LAO due to lattice mismatch, potentially accounting for the results shown earlier by other groups. Furthermore, studies looking at the critical thickness of LAO capping layers on (111) KTO show a $\sim$3 nm critical thickness below which conductivity is extinguished.[50] This is despite several computational studies suggesting the formation of a two dimensional *hole* gas formed at KO terminated surfaces without a critical thickness.[51] Indeed, all reported conducting samples of KTO have electron like character at the time of writing.

One significant difference between work on KTO and prior works on STO is the importance
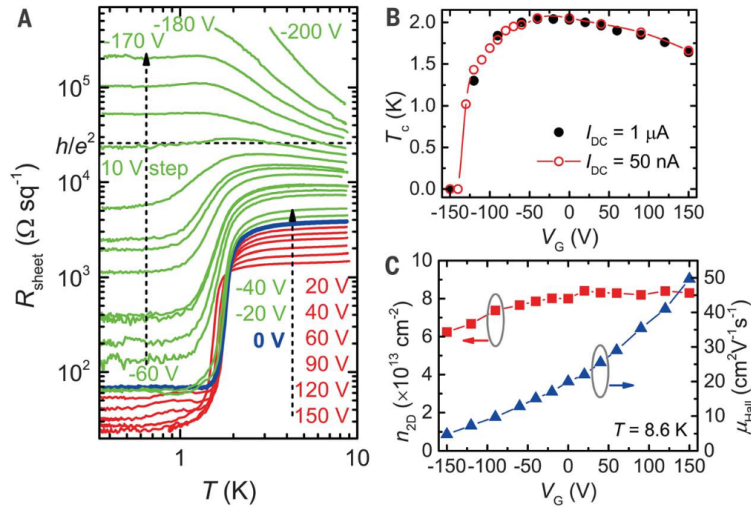
Figure 2.6: **Gate voltage control of the conducting properties in (111) KTO.** (a) Res vs Temp demonstrating the gate voltage tuning from superconductivity to insulator at low temperatures, (b) transition temperature and (c) carrier concentration and mobility as a function of back gate voltage. Figure adapted from Chen *et al.*[16]

of strain from lattice mismatch. Significant attention was paid to the effect of strain in epitaxial thin films, both as a method for tuning film properties,[52] but also as a consideration for tuning the qualities of the two dimensional gas in epitaxial heterostructures. In particular, efforts to improve the carrier mobilities[53] at the STO interface sought alternative capping layers with lower crystalline mismatch, leading to work on $(La_{0.3}Sr_{0.7})(Al_{0.65}Ta_{0.35})O_3$ (LSAT) / STO. The improvement from 3% strain in LAO / STO to 1% strain in LSAT / STO accounted for improvements in performance evident in Kondo scattering studies,[54] and detailed magnetoresistance studies.[55–57] Such efforts have been largely unexplored in KTO systems, partially due to the mixture of amorphous and epitaxial heterostructures. There may still be room for studies like this though, as reported mobilities for KTO systems remain significantly lower than those reported in STO, as discussed in this section.

One of the most important experimentally tunable parameters is back gate voltage, and the

transport properties of KTO are pliable in that regard. Chen *et al.*[16] demonstrated this for a LAO/KTO system in 2021. Their study showed that back gate voltage could be used to tune the carrier concentration, mobility, and superconducting properties of a 2DEG generated at the interface of a crystalline LAO/KTO (111) interface, results which are reproduced in Fig. 2.6. The maximum upper critical field, H_{c2}, and maximum superconducting transition temperature, T_c, reported were ∼2.2 T and ∼2 K respectively, corresponding to a backgate tuned carrier concentration of ∼8 x 10^{13} (e / cm^2). Additionally, they showed that a full superconductor-to-insulator transition could be realized with gate voltage swept from +150 V to -200 V. This study followed closely on the heels of the large comparative study of Liu *et al.*[18] who looked at the transport properties of both LAO / KTO and EuO / KTO, boasting a maximum T_c of 1.47 K in LAO / KTO for a carrier concentration of 8.9 x 10^{13} cm^{-2}. The EuO system proved to be the more fruitful than LAO for the results in that study, but it was not the first time that it had been used to create heterostructures with KTO.

The first report of a conducting gas formed at the interface of EuO and KTO was by Zhang *et al.*[17] in 2018. Their study reported a moderate mobility of 111.6 (cm^2 / V s) but identified signatures of magnetic order in hysteretic parallel field magnetoresistance up to 30 K, a result which is shown in Fig. 2.7. This hysteretic behavior they attributed to an induced magnetism in the conducting gas from the ferromagnetic ordering of the EuO film, which is an in-plane easy axis ferromagnet with a measured magnetic moment of 6.8 (μ_B / Eu), and a measured Curie temperature[17] of 71K. This is in sharp contrast with other heterostructures made on KTO which generally do not have intrinsically magnetic constituents, and interestingly, EuO is the only heterostructure fabrication process known to generate both oxygen vacancies and inter-diffusion of Eu into K sites.[18] Surprisingly, this does not seem to deter superconducting transitions in the resulting 2DEG, which show transition temperatures as high[58] as 2 K for a normal carrier concentrations of
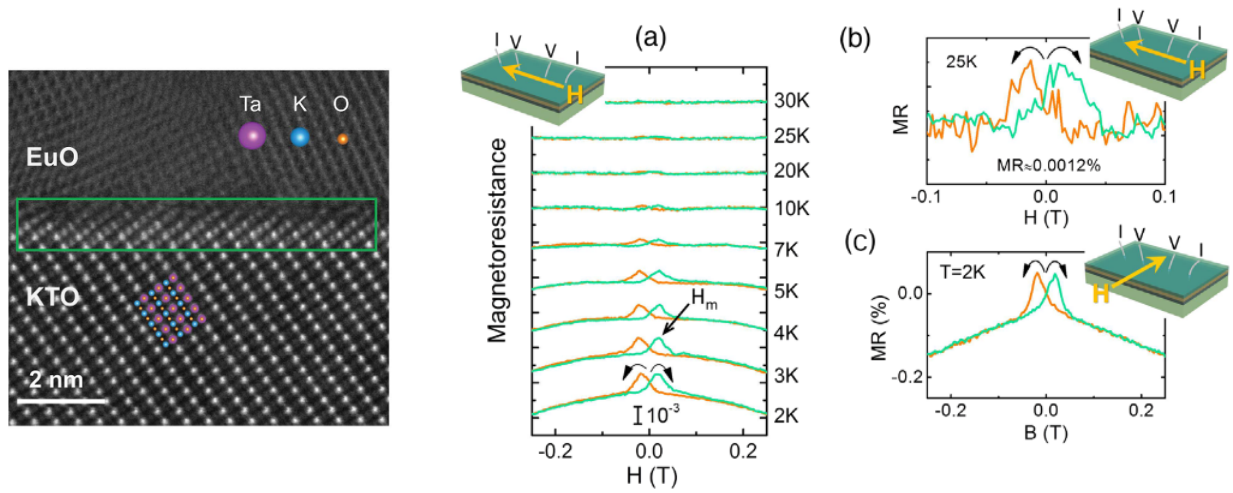
Figure 2.7: **Hysteretic parallel field magnetoresistance of EuO on KTO.** Left: Scanning transmission electron microscopy image of the interface between EuO and KTO, adapted from Liu *et al.*[18] Right: hysteretic magnetoresistance, adapted from Zhang *et al.*[17] (a) Parallel field magnetoresistance showing emerging hysteretic peaks, shifted for clarity. (b) Low field focus of the 25K data for field aligned with the current. (c) MR measured at 2 K with the in-plane fields that are perpendicular to the current.

7.4 x 10^{13} to 2.4 x 10^{14} (e / cm^2). The study[58] also reports the existence of a Griffith's Phase, a quantum phase transition of disparate superconducting puddles with divergent dynamical critical exponent, which is also a finding with precedence in STO systems.[59] Other studies have shown strong spin-orbit effects coexisting with superconductivity,[60] exotic forms of magnetoresistance,[61] and striped superconductivity[18] believed to be a result of a magnetic stripe phase.[41] It seems that the magnetism is inextricably tied to the nature of the superconductivity in EuO heterostructures, and as a result this system boasts the highest observed critical temperature[18] of 2.2 K for the (111) direction.

Another prominent option for a KTO heterostructure partner is LaVO$_3$ (LVO), which was first shown to be a candidate material for STO heterostructures by Hotta *et al.*[62] in 2007. LVO first attracted attention due to the multiple valence states for vanadium, which is stable for formal charges

between 2^+ and 5^+. The flexibility promised a large phase space to generate a conducting gas in STO,[62] but was soon adapted for its large, tunable spin orbit interactions.[63] The same reasoning led to the adaptation for KTO systems by Wadehra *et al.*[19] in 2020. Their study found many manifestations of the large spin orbit coupling, including planar Hall effect, and anisotropic magnetoresistance for gases of $\sim 10^{14}$ (e / cm^2). Further studies demonstrated photo-sensitivity and gate voltage tuning of the 2DEG,[64] and suggestions of a realized chiral anomaly have also been seen in parallel field magnetoresistance,[65] though the data an analysis were not definitive. Superconductivity was also recently demonstrated[66] in epitaxially grown films of LVO on (111) KTO, but with a modest T$_c$ of only 510 mK. The system remains an active area of research, with some advantages over the growing list of competing overlayers.

Many other materials have been used as a capping layer for heterostructures to varying success. LaCrO$_3$ and TiO$_x$ heterostructures were grown by MBE by Al-Tawhid *et al.*[67,68] to look at the interplay between weak localization, superconductivity, and potential Kondo physics. The TiO$_x$ forms a conducting gas by gettering oxygen from the surface, much in the same way as Al getters oxygen in results reported in this thesis. Other works have explored this same mechanism, in particular Mallik *et al.*[69] who showed gate tunable superconductivity up to 600 mK in (111) AlO$_x$ / KTO, complete with a minimum critical carrier concentration of 1 x 10^{13} (e / cm^2) for hosting superconductivity.[69] They also report high frequency ac measurements to probe the superfluid stiffness, and calculate a gapped superconductivity with T$_c$ of 2.2 K, well above the experimental observation. A similar technique was used by Vicente-Arche *at al.*[70] to generate thin conducting layers on KTO for spin-charge conversion studies. There are also reports of using γ - Al$_2$O$_3$ as a top layer,[71] but conductivity measurements were only conducted down to 5 K as the study focused on photo-activated conductivity and made ambitious claims about Kondo effects in the upturn of resistance at low temperatures.[71] Similar controversial claims have been made about potential

topological signatures from heterostructures using LaTiO$_3$ and EuTiO$_3$ as capping layers,[72] and theoretical predictions have identified LaGaO$_3$ / KTO and NdGaO$_3$ / KTO (001) as potentially interesting conducting platforms with no critical over-layer thickness,[73] though at the time of writing these systems have not been realized.

The realm of potentially conducting heterostructures seems to grow unrestricted, limited only by practicality of the conducting mechanism and the promise of the properties brought out by the surface engineering. The only requirements for conductivity seem to be adherence to one of the two main generating mechanisms for the 2DEG: charge transfer and oxygen vacancy generation, which will be discussed in detail later. Importantly, all heterostructure fabrication methods in the literature required a high temperature, high vacuum anneal prior to, or as a part of material deposition. The resulting gas routinely has a areal charge density of 10^{13} to 10^{14} (e / cm^2), larger than similar gases seen in STO by about an order of magnitude but with modest carrier mobility by comparison. The gas is thus an attractive platform for harnessing a number of physical phenomenon, with an eye toward practical application in devices. This is especially true of superconducting devices, due to KTO's comparatively high superconducting transition temperatures and large upper critical fields, which are the topics of the next section.

2.3   Superconductivity in KTO

As was made plain by the previous section, the correlation between conductivity and superconductivity in KTO based 2DEGs has less to do with the material completing the heterostructure and more to do with the crystal termination. Unlike STO, the highest observed transition temperatures in KTO exist in the (111) direction[18] with only one system[14] showing superconductivity in the (001). This is in sharp contrast to STO, where only a few instances of superconductivity in the (111) were observed,[74,75] due to differences in band structure between STO and KTO. What

follows here is a discussion of some of the properties of the superconductivity that resides at the surface of KTO.

Many studies have characterized the superconductivity at the surface of KTO, with a focus on the high superconducting transition temperature in the (111) direction. These systems boast transition temperatures above 1 K for several heterostructure materials in both the (110) and (111) crystal directions,[18,58,60,66,69] with the highest transitions measured for EuO capping in both directions.[18,60] The dimensionality of the superconductivity is unanimously considered to be two dimensional,[16,18,60,66,76] owing in large part to the lack of superconductivity in the bulk, but verified with fits to the shape of the T_c vs. H_{c2} curve,[60,66] or to the shape of the Berezinskii-Kosterlitz-Thouless transition in I-V measurements.[77] Estimates of the thickness of the superconducting layer[40,60] of $\sim$8 nm are thinner than seen in LAO / STO 2DEGs,[78,79] but consistent with interfacial mechanisms for generation.[77] Estimates of coherence length are larger, with values as high as $\sim$30 nm, which is much larger than the thickness,[77] indicating that the superconductivity in KTO is two dimensional.

It has been widely reported that the superconductivity in KTO is strongly gate voltage dependent, allowing for study of superconducting-to-metal,[58,66,69] superconducting-to-insulator,[16] or Griffith's phase transitions.[58] While the nature of the tuning does not appear to depend on one factor in all cases,[16] there are independent findings of lower critical carrier densities[69] with linear scaling with increasing density[66], as presented in Fig. 2.8. There are even some hints of band dependence hidden in Lifshitz transitions,[60] though it was not officially identified as such. Both a Lifshitz transition, and an upper critical carrier density are presented in the results of this thesis, and at the time of writing have no precedent.

The superconductivity in KTO has also been shown to be anisotropic, hosting a striped superconducting phase identified from magnetoresistance data in both EuO[18] which is shown in Fig. 2.9. There have also been reports of critical field anisoptropy in LaSrMnO$_3$ heterostructures built
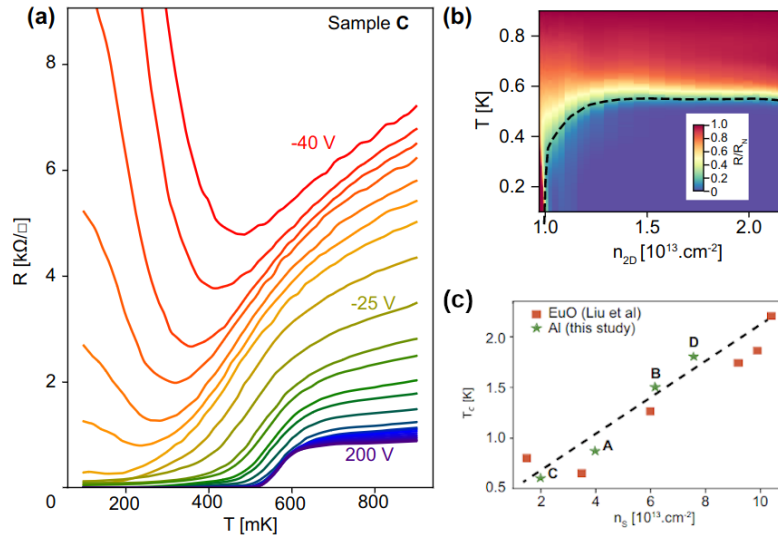
Figure 2.8: **Gate voltage tunability of the superconducting transition.** (a) Temperature dependent resistance through the superconducting transition, measured as a function of gate voltage. (b) Phase diagram of the superconducting transition as a function of carrier concentration. (c) Comparison of transition temperature and carrier concentration for AlO_x / KTO and EuO / KTOs. Figure adapted from Mallik *et al.*[69]

on (111).[40] The origin for this effect has been explained as a striped magnetic phase[41] in the case of EuO, which would result in a superconducting phase similar to a pair-density wave. Arnault *et al.*[40] sought to explain their anisotropy in terms of the band mixing at the (111) surface, where the maximal Rashba mixing has been shown[80] to enhance T_c by a factor of $\sqrt{2}$. These results once again mirror similar findings in STO, which showed anisotropic transport in the (111) samples due to more modest, but similar effects.[81,82]

The work presented in this manuscript expands on the anisotropic effects in KTO, as will be discussed in detail later. This work will also demonstrate the first coexistence of superconductivity and magnetism in KTO. This coexistence was once thought to be impossible but has abundant precedent in high temperature superconductors[83] and in LAO / STO.[84] Indeed, the success of EuO as a capping layer, and the emergence of the striped phase discussed above,[18,41] is due to symbiosis
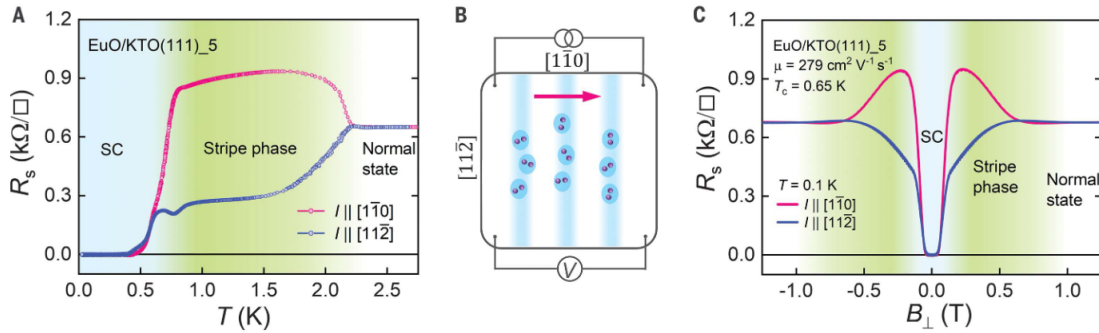
Figure 2.9: **Evidence for a striped superconducting phase in EuO / KTO.** (a) Temperature dependent resistance through the superconducting transition, measured along perpendicular crystal directions. (b) illustration of the striped phase (c) Magnetoresistance of striped phase measured at 100 mK. Figure adapted from Liu *et al.*[18]

of the two disparate states. The signatures of coexistence discussed in the results of this manuscript are markedly different than those seen in EuO / KTO, but similarly result in anisotropies in the nature of the superconductivity.

2.4   Spin Orbit Effects

One of the most attractive qualities of KTO is the strength of the spin-orbit interactions due to the Ta $5d$ electron bands and their prominence in interfacial conduction.[32] These interactions show up in magnetoresistance, and have been shown to be readily tunable via backgate voltage.[13,60,85] As a consequence, KTO has been identified as a promising platform for spintronic applications, a topic that is discussed in detail by Gupta *et al.* in their 2022 review article.[86] The same spin effects that cause the spin textures, Rashba splitting,[32] and anisotropic transport properties[18,40] discussed above can also be used for easily fabricated next-generation spintronic devices.

Many studies looked at the spin-charge effects in STO for its relatively large Rashba coefficient and high mobility gas. In 2016 both Lesne *et al.*[87] and Chauleau *et al.*[88] demonstrated efficient spin charge conversion using the inverse Edelstein effect[89] with a NiFe overlayer on LAO / STO. Spin

currents themselves were the subject of study by Jin *et al.*[90,91] in 2017 and 2021, when LAO / STO

Hall bars were used to detect nonlocal spin currents via the spin Hall effect, under the application of

an applied magnetic field parallel to the surface. Similar schemes were used previously by Reyren

et al.[92] to measure spin precession lengths in STO by way of the Hanle and inverted Hanle effects.

Each of these measurements used the native spin-charge conversion of STO to detect charge signals

resulting from spin effects at the interface. Those same effects were predicted to be larger in KTO,

given the improvement in spin orbit coupling and comparable electron mobilities.
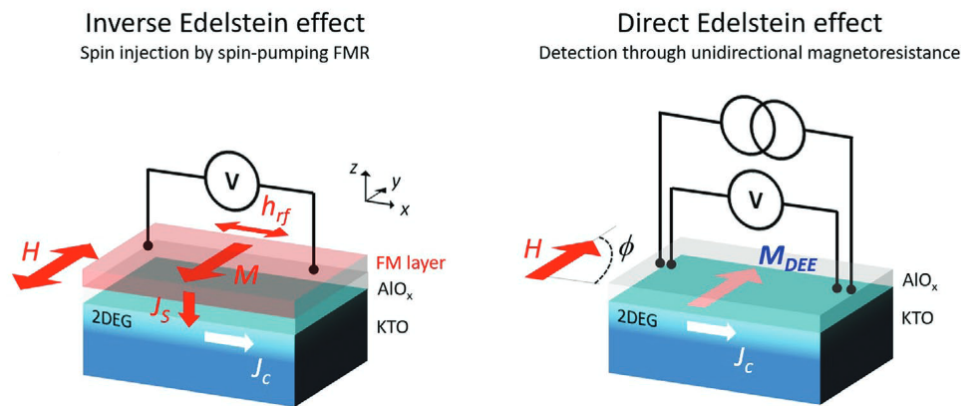
Figure 2.10: **Schematic diagrams for experiments measuring the direct and inverse Edelstein effects. Left:** Experimental design for detecting the inverse Edelstein effect. Combine a dc magnetic field H and a radio-frequency driving field h_{rf} to induce ferromagnetic resonance in the ferromagnet with magnetization M. The result is a spin current J_S injected by spin-pumping from the ferromagnet into the adjacent Rashba 2DEG. A transverse charge current J_C is generated through the IEE. **Right:** Experimental design for detecting the direct Edelstein effect. Pass a charge current into the Rashba 2DEG to produce a transverse spin gradient. When an in-plane magnetic field is applied perpendicular to the current it generates a unidirectional magnetoresistance which is detected by measuring the longitudinal resistance as a function of angle ϕ with respect to the current J_C. Figure adapted from Vicente-Arche *et al.*[70]

Indeed, preliminary experimental results in KTO have shown great promise. In 2017 Zhang *et al.*[15] demonstrated that the spin relaxation time could be modulated by nearly 70x by backgating

LAO / KTO. In 2018, another group of Zhang *et al.*[17] claimed to have evidence of a spin polarized

gas at the EuO / KTO interface, a conclusion supported by analysis of an anomalous Hall effect emerging below the Curie temperature of EuO, and coexisting with an onset of in-plane hysteretic magnetoresistance. In 2019 the same group demonstrated[93] a realization of the inverse Edelstein effect[94] using ferromagnetic resonance in EuO / KTO samples, which is a direct demonstration of spin-charge conversion.
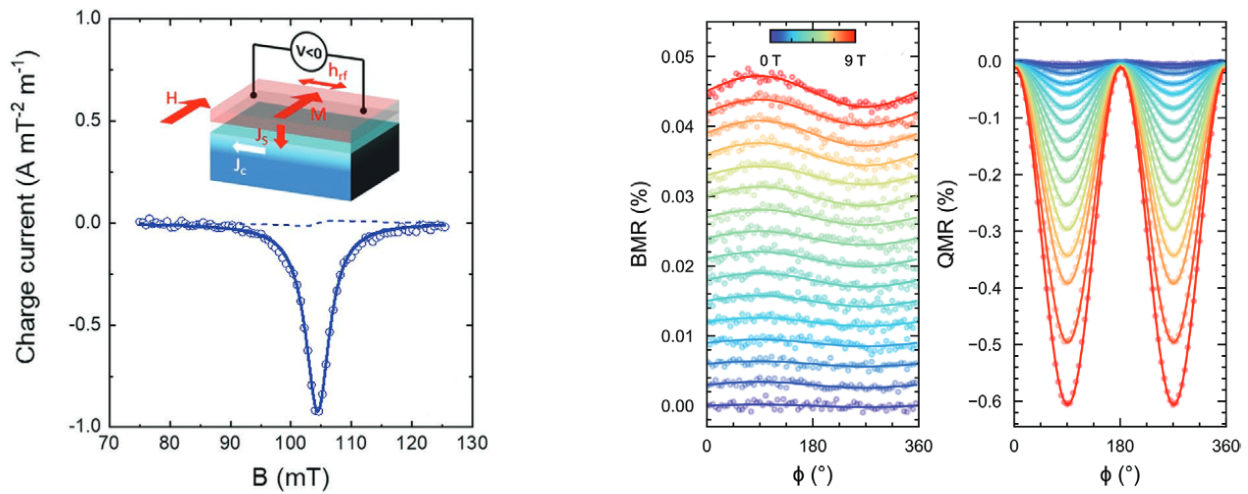
Figure 2.11: **Measured data from Edelstein effect investigations. Left:** Ferromagnetic resonance induced current as a function of an applied, in-plane dc magnetic field. **Center:** Angular dependence of bilinear magnetoresistance for various field strengths. **Right:** Angular dependence of quadratic magnetoresistance for various field strengths. Figure adapted from Vicete-Arch *et al.*[70]

These results were only the beginning though, as Vicente-Arch *et al.*[70] demonstrated in 2021 in a thorough study of spin charge conversion at the KTO interface. Their study used several different fabrication methods to make samples to explore the direct Edelstein effect and the inverse Edelstein effect, schematically described in Fig. 2.10, which allowed for a calculation of the spin-charge and charge spin conversion lengths, and by extension the magnitude of the Rashba coefficient. These measurements were extracted from fits of the magnitude of the current induced by ferromagnetic resonance, and by the ratio of the magnitudes of the bilinear and quadratic magnetoresistance, as

shown in Fig. 2.11. They found the negative Rashba coefficient to be -70 meVÅ from this method and compared it to the value extracted from fits to bilinear magnetoresistance measurements which gave a higher value of -280 meVÅ, significantly higher than that seen in STO, as expected. These values were used to calculate the spin-conversion efficiency, given in terms of conversion length as -5 to -25 nm, which was one of the highest reported values at the time. These results strongly support the potential for KTO to be employed in spintronic devices in the future, and tease the possibility of further topological behavior to be found at the interface.

2.5 Probes of Berry Curvature with Quantum Non-Linear Hall Effect

While many established transport phenomenon can be explained in terms of manifestations of Berry curvature, sometimes it takes a more complicated probe for more conventional materials to betray their hidden topological nature. Such a probe was suggested by Sodemann and Fu[95] in 2015, when they predicted the existence of a signal in the second harmonic (2ω) Hall response for materials hosting a Berry curvature dipole. The resulting anomalous Hall signal was dubbed the quantum non-linear Hall Effect (QNLHE), as the response is due solely to the orientation of the Berry curvature dipole, its coupling to an oscillating probing field (current) I_{ac}, and the scaling of the voltage of the second harmonic transverse signal: $V_T^{2\omega} \propto (I_{ac})^2$. This prediction has spawned a deluge of measurements claiming to have discovered higher order topologies because of a 2ω signal, ignoring coincident effects and the history of cumulant measurements. This section will discuss some of the important results involving Berry curvature dipole measurements, and some limitations of the technique, while leaving a detailed discussion of the theory for the next chapter.

The genesis of the era of QNLHE may have been in 2015, but the first experimental test of the prediction came in 2019 when Ma *et al.* published an observation[96] of the QNLHE in WTe_2, a result which is reproduced in Fig. 2.12. This first paper on realizing the QNLHE built heavily
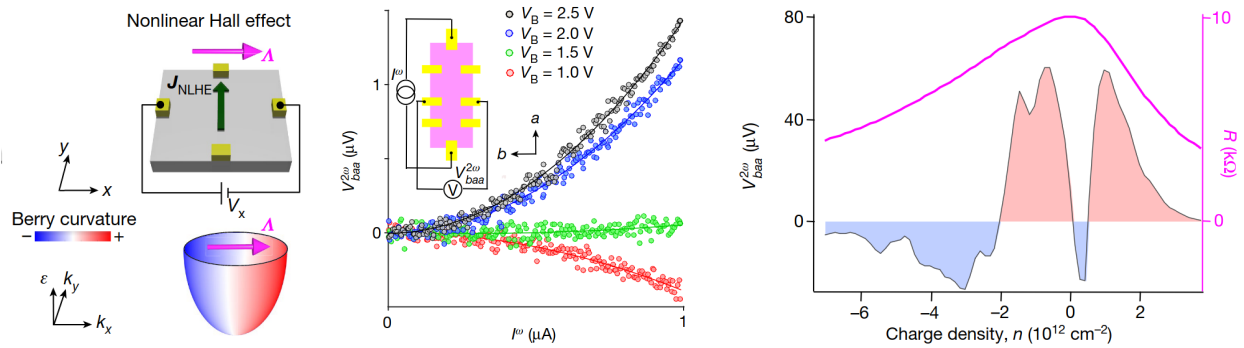
Figure 2.12: **Observation of the quantum non-linear Hall effect in WTe$_2$ Left:** Measurement schematic for inducing a Berry curvature dipole Λ which generates the quantum non-linear Hall response. **Center:** Gate voltage dependence of the $V_T^{2\omega} \propto (I_{ac})^2$ signal. **Right:** Magnitude of the $V_T^{2\omega}$ signal as a function of carrier density, compared to the longitudinal resistance (pink). Figure adapted from Ma *et al.*[96]

on earlier works[97] characterizing the Berry curvature dipole using circular polarized mid-infrared photogalvanic techniques, which used circularly polarized light to selectively excite a current response from either side of the Berry curvature dipole. Both of these studies came on the back of work describing potential experimental schemes for breaking the required symmetries in transition metal dichalcongenides to be able to see the effect. In particular, the 2018 paper by Zhang *et al.*[98] showed that the nonlinear anomalous Hall effect could be realized in monolayers of WTe$_2$ and MoTe$_2$ through the application of an out of plane electric field. This is a particularly attractive suggestion for experimentalists because of the advancement of technology around graphene in recent years,[99] where charge tuning[100] and perpendicular electric field are easily applied through graphite top and bottom contacts built into heterostructures.[101–103]

The necessity of this technique is rooted in the requirements of the theory of Sodemann and Fu: there is a maximum allowable symmetry to realize a Berry curvature dipole. In three dimensions this means that only point group with a polar axis[95] can host an uncompensated Berry dipole and show the second harmonic effect, while in two dimensions the maximal symmetry is a single

mirror line.[95] Very few materials can meet these criteria intrinsically, but additional symmetries can be broken for experimental systems, which is the case with the out of plane electric field in the experiments on WTe$_2$. This electric field breaks the inversion symmetry of the crystal, resulting in a gap opening at the Dirac point which is polarized in Berry curvature.[96] When the ac probing field is passed along the resulting Berry curvature dipole, which is perpendicular to the remaining mirror plane, the system produces a transverse current that manifests in both the zero frequency (0ω) and 2ω Hall response.

A perpendicular field is not the only way to break this additional symmetry though. Another study on WTe$_2$, Kang *et al.*[104] showed the existence of the QNLHE in few-layer samples as a function of in-plane angle with respect to the mirror plane. There the mechanism for breaking the added symmetry is discussed in terms of a current induced perpendicular magnetic field in the paper,[104] but has also been speculated to be due to symmetry breaking at the surface of the sample.[105] In either case, the effect was seen to match the expected relation to the symmetry of the crystal and was shown to be independent of potential confounding mechanisms such as ratchet scattering[95] by comparing the temperature scaling, and by extension, the scattering time dependence.[95,104]

This technique of using fields to break added symmetries has been extended to in-plane fields too. Ye *et al.*[105] showed that thicker pieces of WTe$_2$ can realize Berry curvature dipoles by breaking the extra mirror symmetries by applying a floating dc electric field along one of the two crystal symmetry axes. The resulting Berry curvature dipole is perpendicular to the applied field and to the remaining mirror line, which means the NLQHE is maximum for a field passed along the pair of Hall probes. The strength and sign of the Berry curvature dipole is tuned with the strength of the dc field up to some saturation limit, and $E_{dc} \ll E_{ac}$ to preserve the $(I_{ac})^2$ dependence. This is the scheme that was adopted to results presented in this manuscript, where a floating dc voltage is applied along Hall probes to modulate the sign and strength of the NLQHE response. A more

detailed discussion of the experimental technique can be found in Chapter 4.

Recently, the use of the QNLHE has blossomed to a number of systems that are *not* WTe_2, and any attendee at the 2023 March Meeting will tell you that the 2ω technique has graduated to the level of popular proof of topological behavior. This claim may be premature, but the number of materials that have been shown to demonstrate the effect is significant, and should include any suitably low-symmetry conductor. In this spirit, the technique has been applied to the "magic" system of twisted bilayer graphene,[106] which showed a massive second order Hall response (~ 500 μV) tunable by filling factor, that the authors attributed to skew scattering effects. $MoTe_2$, the sister compound of WTe_2, has also been shown to host a non-linear Hall effect[107] in a paper suspiciously reminiscent of Kang *et al.*[104] published three years earlier. This result should come as no surprise as the material was exposed along with WTe_2 in the same perpendicular electric field paper[98] that informed Ma *et al.*[96]

Similar mechanisms have been seen in topological semimetals such as $SrIrO_3$, whose room temperature second order Hall response could be tuned directly with applied in-plane magnetic field and was thus attributed to spin-charge conversion processes.[108] Other room temperature observations have come from Dirac semimetals such as $BaMnSb_2$ which showed[109] somewhat confusing results to temperatures up to 400 K. It remains to be seen if these temperature ranges are compatible with the explanation that the effect arises from Berry curvature. Back at cryogenic temperatures, the list of materials continues to grow, including the van der Waals ferromagnet Fe_3GeTe_2,[110] an organic conductor $(BEDT-TTF)_2I_3$,[111] and the trigonal superconductor $PbTaSe_2$.[112] Important for the results discussed here, the effect has also been shown in LAO / STO, with the claim that both spin and orbital effects contribute to the Berry curvature dipole in the system supported by a compellingly detailed volume of magnetoresistance measurements.[85]

This field is not without pitfalls though, and more work will need to be done to disentangle con-
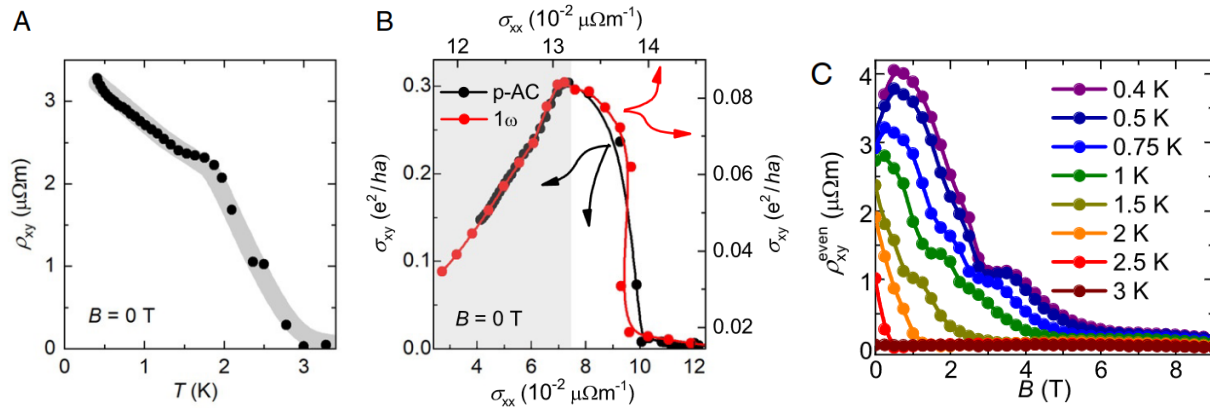
Figure 2.13: **QNLHE where is should not be, observation of spontaneous Hall effect in $Ce_3Bi_4Pd_3$.** (a) Temperature dependence of zero field spontaneous Hall effect. (b) Spontaneous DC Hall conductivity σ_{xy} vs. longitudinal conductivity σ_{xx}. Data for the DC response of the sample (black) and for the 1ω response (red), both in zero magnetic field. (c) Symmetric contribution to the transverse magnetoresistance as a function of temperature. Figure adapted from Dzaber *et al.*[113]

founding effects from bonafide signatures of Berry curvature. In this vein, Dzaber *et al.*[113] reported signals of the QNLHE not in 2ω response but in the 1ω Hall signal for a candidate Weyl-Kondo semi-metal $Ce_3Bi_4Pd_3$. Their result showed a giant spontaneous Hall effect at low temperatures, an effect which combines a zero field transverse signal that arises in the absence of magnetic order, so is distinct from the anomalous Hall effect, and a symmetric contribution to the Hall signal upon the application of a field. This result is corroborated with by 0ω and 2ω measurements showing the appropriate scaling, with the explanation that the Weyl cones quickly break the system out of the "probing field" limit of the derivation in Sodemann and Fu,[95] resulting in a 1ω signal. Other sources of anomalous signals can also arise though, as demonstrated by Schade *et al.*[114] who showed an emergent 2ω simply due to circular conducting paths in graphene, or Ho *et al.*[115] who showed that simply corrugating graphene can produce a 2ω response through strain modification of the Dirac cone.

The take-away message should be to proceed with caution. The quantum non-linear Hall effect

is certainly a potent tool to help characterize the topological transport response of materials, but it is not proof in itself. This can be seen in the the works from the late 1980s on mesoscopic physics systems of normal metals, where higher cumulant measurements[116] showed distinct non-linearities up to the 10th harmonic. Even Sodemann and Fu warned about potential added corrections to the second order response intrinsic to band structure, or from inversion asymmetric scattering.[95] These considerations will become all the more important as the technique becomes more common, and as higher order effects are predicted[117] to keep up with the ever-increasing complexity of topological material classification.

CHAPTER 3

THEORETICAL BACKGROUND AND PHYSICAL UNDERSTANDING

This chapter seeks to provide a theoretical framework for understanding the transport behaviors demonstrated in the experimental results discussed in Chapter 5. As such, particular focus will be paid to theories which have experimentally relevant predictions, or that allow experimentalists a rigorous framework for interpreting results. The goal is to inform the understanding of the 2DEG at the KTO interface and to provide a framework for a physical interpretation of the experimentally observed quantities.

The discussion starts with a review of the mechanisms that generate a conducting gas at the interface, and the consequences of those mechanisms. This will lead into the discussion of band structure, with a focus on the interfacial conductivity and coincident effects. Since the 2DEGs at the interface go superconducting, there will be a somewhat superficial discussion of the Ginsburg Landau theory of superconductivity and the resulting physical quantities that can be derived from experimental measurements. The primary tool for probing these quantities is the application of a magnetic field, so there will be a review of magnetoresistance and its components for both the longitudinal and transverse (Hall) signals. This then forms a segue to the last part of the chapter, which gives a more detailed derivation of the quantum non-linear Hall effect, a manifestation of Berry curvature dipoles interacting with an oscillating probing electric field. In all, this chapter will inform the analysis performed later in Chapter 5, the discussion of experimental results.

3.1 Conductivity at Complex Oxide Interfaces

As discussed in the previous chapter, the genesis of this field of complex oxide based 2DEGs started with the discovery of a conducting gas at the interface between resistive oxide layers by Ohtomo and Hwang[42] in 2004. Since that work a multitude of effort has been levied into understanding the exact mechanism by which a conducting gas actually forms between two bulk insulators. The resulting explanations center around two primary ideas: charge transfer via the polar catastrophe model, and crystal defects donating carriers. Both of the models enjoy support from experimental findings and each play a role in understanding the emergent physics of the resulting conducting gas.

3.1.1 Charge Transfer: The Polar Catastrophe Model

One of the first explanations for the conductivity complex oxide heterostructures is the polar catastrophe or polar reconstruction model.[42] This model is rooted in the inescapable consequences of broken translational symmetry at the surface of a crystal, coupled with the bulk charge distribution of perovskite materials. In the case of $SrTiO_3$, a crystal can be described as layered material made of SrO and TiO_2 sub-layers with a perpendicular axis aligned along the (001) direction of the full cell. The valence state of the Sr and Ti are expected to be +2 and +4 respectively, but at the interface these formal charges are modified by the transition to sub-layers of the heterostructure capping material. The details of this are discussed by many papers including by Nakagawa, Hwang, and Muller[118] in their 2006 paper on the possible interfacial constructions of LAO / STO. Fig. 3.1 demonstrates some of the potential configurations for LAO / STO, many of which run into the "polar catastrophe" problem encountered in the 2DEGs in semiconductors investigated in the 1970s.[119] This model predicts that an interface between a polar and a non-polar crystal can only
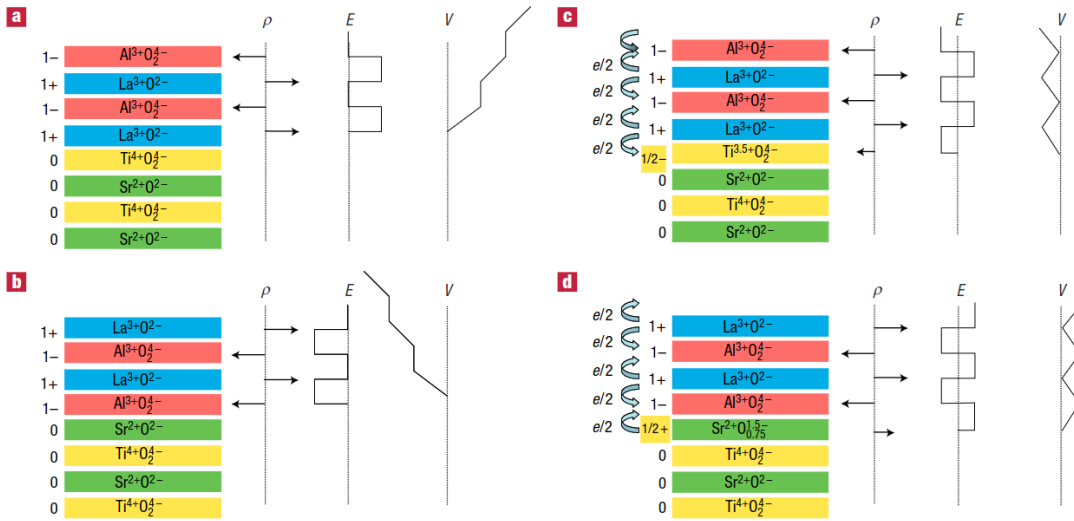
Figure 3.1: **Simplified schematic of possible interface combinations for the (001) terminated LaAlO$_3$ / SrTiO$_3$ system.** Bulk (001) SrTiO$_3$ has neutral planes of SrO and TiO$_2$, but the (001) planes in LaAlO$_3$ have alternating net charges (ρ). (a) If the interface is LaO/TiO$_2$, this produces an electric field (E) associated with an electric potential (V), that diverges with thickness. (b) If the interface is instead AlO$_2$/SrO, the potential diverges in the other direction. (c) The divergence at the LaO/TiO$_2$ interface can be avoided if half an electron is added to the last Ti layer, creating an interface dipole hosting a conducting gas. (d) The divergence for the AlO$_2$/SrO interface can also be avoided by removing half an electron from the interface. Figure adapted from Nakagawa et al.[118]

occur under certain reconstruction conditions or the charge accumulation would be too energetically costly for interface stability. The solution is the addition of a 1/2 charge to balance the two divergences[118] as shown in Fig. 3.1 (a) and (b). As a consequence, most interfaces would need to be stabilized by the growth of facets or terraces in order to support a two dimensional conducting gas.

This interpretation is supported by the observation of a critical thickness of the LAO overlayer to maintain the conducting gas. Fig. 3.2 reproduces the work of Liu et al.[120], who demonstrated both a generation of a conducting gas through layer growth and a destruction of the gas with ion milling. For crystalline layers this agrees with the prediction that 3 uc are needed to stabilize the
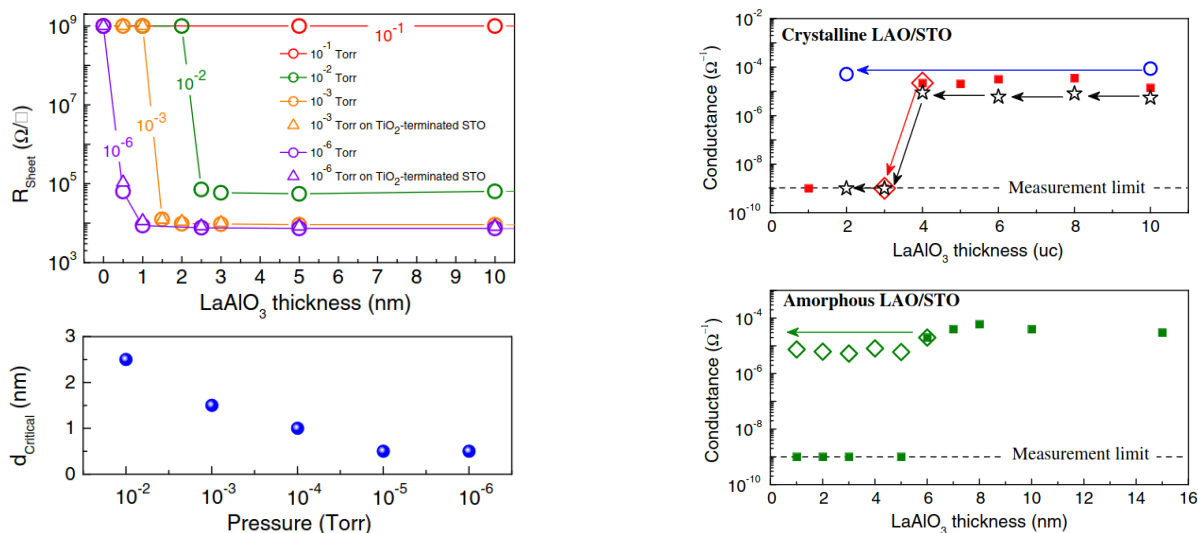
Figure 3.2: **Critical thickness of the LaAlO$_3$ capping layer. Left:** Sheet resistance of amorphous LAO/STO interfaces as a function of LAO thickness and partial pressure of oxygen during growth. **Right:** Critical thickness of crystalline and amorphous LAO overlayers as progressively thinned with argon plasma. Figures adapted from Liu *et al.*[120]

charge transfer, providing support for the polar catastrophe model.[118,120] However, for amorphous layers less than the critical thickness of 6 nm milling did not destroy the conductivity, suggested an alternative mechanism for generating the gas. It is likely that multiple mechanisms contribute to the generation of a conducting gas for any overlayer, though the leading mechanism can often be deduced from context clues.

This same principle of charge sub-layers has been applied to KTaO$_3$, but instead of neutral layers of SrO and TiO$_2$ the crystal is made up of polar layers of KO^{-1} and TaO$_2^{+1}$. This change can be used to generate interesting gases at the interface, as was the case of LaVO$_3$ / KTO studied by Wadehra *et al.*[19] Their interpretation of the charge reconstruction is reproduced in Fig. 3.3, once again accompanied by a critical overlayer thickness of 3 unit cells. As mentioned, there are alternative methods for generating conducting gases for systems that do not clearly agree with the polar catastrophe model. One of those ways is oxygen vacancy formation, which is the method
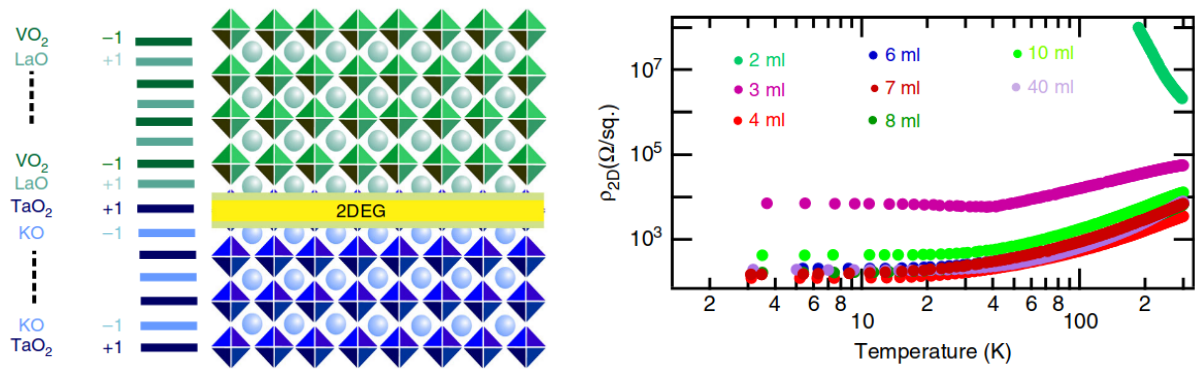
Figure 3.3: **Critical thickness of the LVO capping layer on KTO. Left:** Schematic of atomic layers and their formal charges. **Right:** Resistance vs temperature curves as a function of capping layer thickness, demonstrating the critical thickness of . Figures adapted from Wadehra *et al.*[19]

used to generate conducting samples in this work, and which is the subject of the next section.

3.1.2 *Oxygen Vacancies and Their Consequences*

The other common mechanism for inducing a conducting gas at the interface of complex oxides is the generation of carrier donor sites either from crystal defects or oxygen vacancies. The mechanism is similar to the origin of carriers in intrinsic semiconductors, and has the added benefit of being confined to the interface. Oxygen vacancies are at least partially responsible for the conductivity in all amorphous heterostructures overlayers, and are a major mechanism for EuO / KTO systems. The work in this manuscript is based on oxygen vacancy formation by aluminum gettering, and it comes with some distinct consequences.

Surface treatments that generate oxygen vacancies are numerous, including argon plasma treatments,[47] UV exposure,[46] and any thin film depositions of strongly reducing elements like Al[30,69,121] or Ti.[68] Many of these were discussed in the Chapter 2 as applied to STO and KTO, but similar treatments have been used on any number of complex oxides, which will not be covered here. The suggestion of using oxygen vacancies for conductivity in STO goes back to Tufte *et al.* 1967
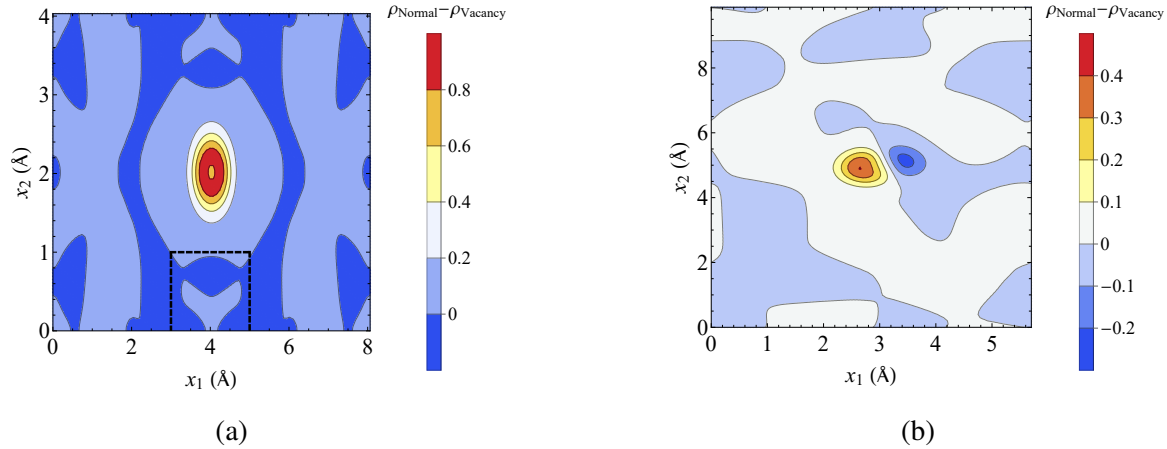
Figure 3.4: **Charge generation from oxygen vacancies.** Carrier density change from the introduction of one oxygen vacancy on the (a) (001) and (b) (111) surfaces. The result is a net charge mostly localized on the vacancy cite. Figures were generated by Alex Tyner, (unpublished).

paper[122] for conduction in the bulk, and the general mechanism for double electron donation has not changed since then. Fig. 3.4 shows the charge distribution generated on the surface of KTO from the introduction of one oxygen vacancy for the (001) and (111) surfaces. These distributions were calculated using density functional theory by Alex Tyner. Because the presented data are for the change in charge ($\rho_{normal} - \rho_{vacancy}$), a large positive charge (red) denotes a negative charge accumulation due to the vacancy. Thus, as expected, the vacancies result in an electron donation to a conducting gas, which is most closely localized on the Ta atom nearest the vacancy. Importantly, the maximum effective charge is very nearly the 0.5 electrons per unit cell after relaxing multiple configurations of possible vacancies, in agreement with the prediction for the charge singularity discussed before. As a side note, carrier densities calculated from Hall data of two dimensional gases formed on complex oxides are usually closer to 0.25 electrons per unit cell, potentially due to compensation from multiple bands, localization of additional carriers, or competing charge generation mechanisms.[118]

Once the gas is generated on the surface, the resulting surface band structure respects the sym-
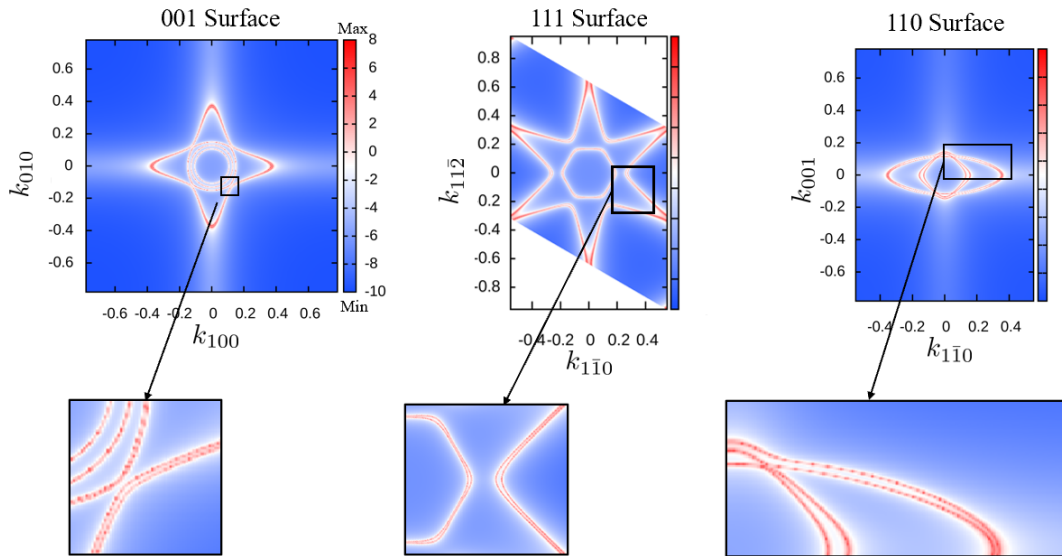
Figure 3.5: **Surface states revealed by DFT calculations.** Surface states for the (001) (left), (111) (center), and (110) (right) crystal terminations reflecting the symmetries of the surface. Insets show spin split bands at the point of largest splitting. Figures were generated by Alex Tyner, (unpublished).

metry of the crystal cut. This can be seen directly in Fig. 3.5, in DFT calculations performed by Alex Tyner. The density is shown for arbitrary units, for a slab with surface oxygen vacancies hosting a conducting gas, which reveals the symmetry-respecting patterns consistent with previous ARPES results.[32,37–39] The splitting strength due to the surface Rashba spin-orbit interactions is shown in the inset for the highest splitting parts of each surface. This splitting can be seen more clearly in the spin polarization texture shown in Fig. 3.6. The spin-split bands account for significant in plane spin-texture for the (001) and (110) surfaces, with an additional out of plane contribution for the (111) surface due to band mixing. These textures have an impact on the conducting properties of the surface, especially if they couple to additional magnetic components in the sample. It is important to reiterate that the direction with the largest spin orbit splitting on the (111) surface is the [$1\bar{1}0$] direction, which will be important later. The (110) surface also shares

the $[1\bar{1}0]$ direction, but the maximal splitting there is at the pinch point halfway between the $[1\bar{1}0]$ direction and the $[001]$ direction. This is the same for the (001) surface, where maximal splitting is between the $[001]$ and $[010]$ directions.
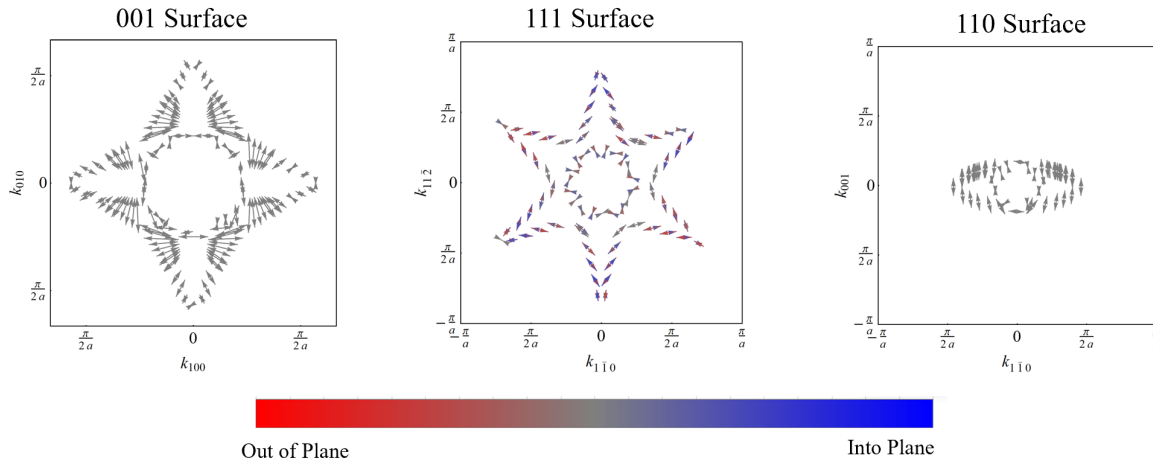
Figure 3.6: **Spin textures revealed by DFT calculations.** Surface state spin polarization for the (001) (left), (111) (center), and (110) (right) crystal terminations. The (001) and (110) surface are polarized in plane but the (111) has an appreciable component out of plane due to the band mixing. Figures were generated by Alex Tyner, (unpublished).

The same oxygen vacancies that generate the conductivity at the interface can also generate magnetic moments. This is due to local moments on the transition metal ion, and is a phenomenon that was described at least as far back as 2012, when Pavlenko *et al.*[123] calculated the local moments due to band reconstruction induced by oxygen vacancies at the $SrTiO_3$ interface. These local moments have also been shown to order, resulting in hysteretic signatures of long range magnetic order in LAO / STO, as demonstrated by Brinkman *et al.* in their 2007 paper.[124] Subsequent works measured magnetic localization along tetragonal domain walls[31] and demonstrated the co-existance of magnetic order with superconductivity.[84] The same effect can occur in $KTaO_3$, and long range magnetic order was observed in transport data for the first time in work presented in this manuscript. The suggestion of local magnetisation due to oxygen vacancies in KTO is not

new, however. In 2022 Al-Tawhid *et al.*[125] reported the observation of increased paramagnetism and an Anomalous Hall effect signal in reduced KTO samples, results that suggest the presence of local magnetic moments but not long range order.
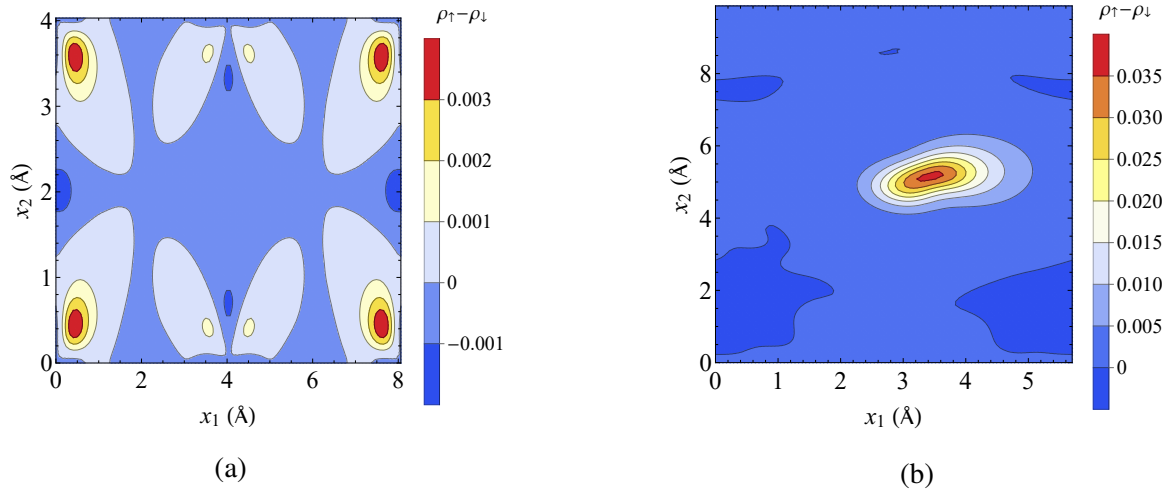
Figure 3.7: **Spin polarization resulting from oxygen vacancies.** Net spin polarization generated from one oxygen vacancy on the (a) (001) and (b) (111) surfaces. Figures were generated by Alex Tyner, (unpublished).

Confirming this result, density functional theory calculations performed by Alex Tyner show local spin polarization generated by the oxygen vacancy slabs used to calculate charge generation in Fig. 3.4. These polarization maps are shown in Fig. 3.7, and as before show net spin polarization resulting from the oxygen vacancy on the surface. The effect is strongest on the (111) surface due to the mixing of the Ta $5d$ orbitals, resulting in a calculated 6.67 μ_B per two Ta atoms, compared to only 0.56 μ_B per two Ta atoms in the (001), per Alex Tyner's calculations. The result is a substantial local moment, which can order with other moments at low temperatures to generate hysteresis and other effects in transport data, as will be shown.

3.2 Brief Theory of Superconductivity

Superconductivity remains an area of intense focus in condensed matter physics for theoretical and practical purposes. The complex oxides became a player in this field following the demonstration of superconductivity[126] in the 2DEG formed in (001) LAO / STO. $KTaO_3$ based systems represent an improvement over STO due to much higher superconducting transition temperatures with values as high as 2.2 K.[18] Combining these high transition temperatures with strong and tunable spin-orbit interactions makes KTO a promising potential platform for realizing more exotic forms of superconductivity, especially when combined with coincident magnetism. To begin to understand such a complicated system one should start with a foundational understanding of superconductivity. Here we will review some basics of superconducting theory and their implications for describing the superconducting observations in complex oxides. Most of this section is adapted from Tinkham's *Introduction to Superconductivity*[127] or notes from Professor Chandrasekhar's series of Condensed Matter classes[128], unless otherwise stated.

3.2.1 Selected Results from Ginsburg Landau Theory

Ginsburg-Landau (GL) theory[129] appeared in 1950 as a macroscopic description of the superconducting state in terms of a quantum mechanical pseudo wave function Ψ. This pseudo wave function describes the superconducting state, defining the density of the superconducting electrons by the expectation value of Ψ as $n_s = |\Psi|^2$. This macroscopic theory starts with a treatment of the thermodynamic properties of the superconductor in terms of changes to the free energy, and yields observable characteristics of the superconducting state, like the penetration depth, λ_{eff}.

$$\lambda_{eff}^2 = \frac{m^* c^2}{4\pi |\Psi|^2 e^{*2}} = \frac{m^* c^2}{4\pi n_s e^{*2}} \tag{3.1}$$

which we can estimate by taking measurements of the normal state carrier concentration. Here, m^* and e^* are the effective mass and charge of the supercurrent carriers, and λ_{eff} is the effective superconducting penetration depth. It should be noted that all of these formula use CGS unit conventions, and it is necessary to multiply the term on the right of Eq. 3.1 by ϵ_0, the vacuum permittivity. Here, λ_{eff} estimates how far an external magnetic field penetrates into the bulk of the superconductor before being completely screened. A related parameter is the superconducting coherence length given by

$$\xi(T) = \frac{hc}{4\sqrt{2}e\pi H_c(T)\lambda_{eff}(T)} = \frac{\Phi_0}{2\sqrt{2}\pi H_c(T)\lambda_{eff}(T)} \tag{3.2}$$

where $\Phi_0 = hc/2e$ is the flux quantum and H_c is the thermodynamic critical field. Combining λ_{eff} and ξ gives the Ginsburg-Landau parameter κ as

$$\kappa = \frac{\lambda_{eff}(T)}{\xi(T)} = \frac{2\sqrt{2}\pi H_c(T)\lambda_{eff}^2(T)}{\Phi_0} \tag{3.3}$$

which is the parameter that describes the difference between Type I ($\kappa < 1/\sqrt{2}$) and Type II ($\kappa > 1/\sqrt{2}$) superconductors. All of the superconductivity on the 2DEG of KTO are in the Type II regime, where the application of external fields create vortex lattices of quantized flux, Φ_0. This leads to the description of the upper superconducting critical field H_{c2}, which is the highest perpendicular applied field at which superconductivity can nucleate inside a superconducting sample in a decreasing external field. This field is related to the coherence length of the superconductor as

$$H_{c2} = \frac{\Phi_0}{2\pi\xi^2(T)} \tag{3.4}$$

which is equivalently the largest field that can be screened by a given coherence length $\xi(T)$ in units of the flux quantum. This relationship can be recast in terms of the thermodynamic critical

field H_c or in terms of κ as

$$H_{c2} = \frac{4\pi\lambda_{eff}^2 H_c^2}{\Phi_0} = \sqrt{2}\kappa H_c \tag{3.5}$$

A similar expression can be derived for the critical field applied parallel to the plane of a two dimensional conducting gas:

$$H_{c\parallel} = 2\sqrt{6}\frac{H_c\lambda_{eff}}{d} \tag{3.6}$$

This allows for an estimation of the thickness of the superconducting gas, d, when combined with measured values of the perpendicular upper critical field:

$$d = \sqrt{\frac{6\Phi_0}{\pi}}\frac{\sqrt{H_{c2}}}{H_{c\parallel}} \tag{3.7}$$

This completes the brief discussion of the time-independent consequences of GL theory. There are more theoretically definable parameters such as the lower critical field H_{c1}, but many of these parameters are not easily detectable in transport measurements, so they will be ignored here. The takeaway is that from a set of experimentally observable parameters, n_e, H_{c2}, and $H_{c\parallel}$, many characteristic parameters of the superconductivity can be extracted. Furthermore, the nature of these parameters can be tested as a function of other experimental parameters like back gate voltage V_g to draw inferences about the superconductivity in a system.

These are all static descriptions of superconductors, to describe further properties like the shape of the superconducting transition requires time-dependent Ginsburg-Landau theory (TDGL), in particular the contributions to conduction due to superconducting fluctuations in the normal state. Starting from the linearized TDGL (Equation 8.46 in Tinkham[127]) for $T > T_c$ and no electromagnetic potentials:

$$\frac{\partial \Psi}{\partial t} = \frac{1}{\tau_0}(1 - \xi^2 \nabla^2)\Psi \tag{3.8}$$

where the relaxation time for static modes with momentum $k = 0$ is given by

$$\tau_0 = \frac{\pi \hbar}{8 k_B (T - T_c)} \tag{3.9}$$

and higher energy, moving modes with momentum $k > 0$ decay faster, based on the relationship

$$\frac{1}{\tau_k} = \frac{(1 - k^2 \xi^2)}{\tau_0} \tag{3.10}$$

These equations describe the existence of superconducting fluctuations *above* T_C that decay over the relaxation time τ_k. These fluctuations have significant impacts on the material properties of superconductors near the transition, and have been expanded to explain changes in conductivity of thin films by Aslamasov and Larkin[130] (AL theory) and by Maki[131] and Thompson[132] (MT Fluctuations). The AL modification of the normal state conductivity describes the drop in resistance near (and above) T_c as

$$\sigma^{AL}(q = 0) = \frac{e^2}{16 \hbar d}\left(\frac{T_c}{T - T_c}\right) \tag{3.11}$$

where d is the thickness of the film and is constrained as $d \ll \xi$ for the form to be valid. There is a discrepancy between the original expression obtained by Aslamasov and Larkin[130] in their original, brief paper, and those presented in Tinkham,[127] so the author is deferring to the original AL form. Equation 3.11 has side-effect of diverging when $T = T_c$, but infinite conductivity is a characteristic of the superconducting state anyway, so the result is sound. There is a restriction of

the validity of this form, as discussed by Aslamasov and Larkin, which gives the constraint $\frac{T-T_c}{T_c} >$ $2\tau_0$, and τ_0 is small, 0.467×10^{-3}. If $T_c = 2$, this restricts the AL form to be at least 1 mK above T_c as a lower bound, while the upper bound of the form can be defined by $(T - T_c)/T_c \ll 1$, which would restrict the effect to only temperatures very near, but strictly above the superconducting transition temperature.

An additional correction to the AL form was pointed out by Maki[131] and later refined by Thompson[132] gives a similar correction but instead of an increase in conduction from superconducting pairs, it describes the increase in normal electron conduction from scattering off superconducting fluctuations:

$$\sigma^{MT}(H = 0) = \frac{e^2}{\pi\hbar} \left(\frac{k_B T \tau_{GL}}{1 - (\tau_{GL}/\tau_i)} ln \left(\frac{\tau_i}{\tau_{GL}} \right) \right) \tag{3.12}$$

where τ_{GL} is the GL relaxation time described in Eq. 3.10 above, τ_i is the inelastic scattering time. This form does not have the same strict temperature range of validity as the AL term, and can be used to fit changes in conductivity due to superconducting fluctuations (relatively) far above the transition temperature. The overall conductivity is generally approximated by assuming parallel conducting channels and collapsing the two terms, now in terms of resistance:

$$R_s^{-1} = R_n^{-1} + (R_c^{-1}) \left(\frac{T_c}{T - T_c} \right) \tag{3.13}$$

where R_n is the resistance of the normal conductor, R_c is the change in resistance from the superconducting fluctuations usually given by the AL term above as $16\hbar d/e^2$, but can be left free to vary to allow for better fits.

The AL and MT terms account for drops in resistance above the superconducting transition, but there is just as much structure to account for fluctuation induced residual resistance below the

transition. This is the realm of the Kosterlitz-Thouless transition and I invite the curious reader to look at Manan Mehta's thesis[133] for a more thorough investigation of this in LAO/STO systems. Instead, this work will just introduce the Halperin-Nelson formula[134] which describes residual resistance as a function of temperature below the superconducting transition due to vortex formation, as opposed to the normal $V \propto I^3$ scaling at the edge of the superconducting transition predicted by Kosterlitz and Thouless[135]. The form of the Halperin-Nelson Formula chosen here is

$$R(T) = R_n \left[1 + \frac{4}{A^2} \sinh^2 \left(b\sqrt{\frac{T_{BKT}}{T - T_{BKT}}} \right) \right]^{-1} \tag{3.14}$$

In this case A and b are material parameters which are somewhat constrained by physical arguments, and T_{BKT} is the critical temperature of the Kosterlitz-Thouless transition defined as $T_{BKT} = \frac{\kappa}{2k_B}$. κ in this expression is not the GL κ, but instead a parameter of the system that can be defined as a relevant energy scale. Equation 3.14 expression is only valid at temperatures above T_{BKT}, which is at the foot of the superconducting transition, and can accurately describe both the contributions from vortex fluctuations in the superconducting state and the superconducting fluctuations described by the AL term. Both of these sources model the change in conduction due to the emergence of excitation pairs, either flux vortices in the superconducting state due to external fields or superfluid flow, or bound superconducting pairs in the normal state. In this way the two forms can be viewed as a uniform effect, or as Halperin and Nelson put it, for superconducting thin films "the distinction between the normal and superconducting states is blurred, and it seems likely that no true phase transition occurs."

One useful consequence of this formula is the ability to calculate T_{BKT} without doing V-I measurements, though comparing the results of the two measurements would also allow an estimation of the parameters A and b which are related to the energy of the vortex core in the superconducting state and the phase stiffness of the superfluid. The extracted value of T_{BKT} can also be compared

to the critical temperature T_c to characterize the 2-dimensional-ness of the conducting gas, via the relation[136] $T_{BKT}/T_c = (1 + 0.173 R_N/R_c)^{-1}$ where $R_c = \hbar/e^2$.

This completes our discussion of the Ginsbug-Landau theories, both time independent and time-dependent. All of these theories allow for quantitative statements about the nature of the conducting gas and the superconductivity that it hosts. An emphasis was placed on experimentally measurable parameters, in particular those detectable with transport measurements, which is a theme that will be extended to the next section.

3.3 Magnetoresistance

One of the oldest and most established transport techniques for probing the nature of conductivity in materials is magnetoconductance. Most of the electronic structure of a material can be reconstructed directly from magnetoconductance measurements, and many exotic quantum mechanical signatures show up as deviations from expected dependencies on applied electric and magnetic fields.

This section will review the origins of some common contributions magnetoconductance (or inversely, magnetoresistance) and their experimental realizations. Particular attention will be paid to some of the components of longitudinal magnetoresistance and the difficulty of disentangling the sources without some some corroboration from other sources. This contrasts to the effects seen in transverse magnetoresistance, principally the Hall effect, which is easier to separate into constituents simply due to symmetry arguments. Particular attention will be paid to the interplay between magnetoresistance in normal metals and the convolution that occurs for superconducting samples.

3.3.1   Classical Magnetoresistance

Semi-classical descriptions of electron transport in materials invariably start with the Boltzmann transport equation, which should be familiar to every student in condensed matter, and describes steady state transport in the presence of external driving fields. In its most fundamental form the Boltzmann equation states[137]

$$\frac{\partial f}{\partial t}\bigg|_{diffusion} + \frac{\partial f}{\partial t}\bigg|_{fields} + \frac{\partial f}{\partial t}\bigg|_{scattering} = 0 \qquad (3.15)$$

where here f is the Fermi distribution, the first term is the change in the distribution due to diffusion processes, the second due to external fields, and the third due to scattering processes. Substituting for each of the terms in Eq. 3.15 grants more concrete forms. Diffusion can be described as a melting of a volume in phase space, giving $\frac{\partial f}{\partial t}|_{diffusion} = -\frac{\partial f}{\partial \vec{r}} \cdot v_k$. The effect of external fields can be written as $\frac{\partial f}{\partial t}|_{fields} = \left(\frac{e\vec{E}}{\hbar} + \frac{e}{\hbar c}\vec{v} \times \vec{H}\right) \cdot \boldsymbol{\nabla}_k f_k$, and the relaxation time approximation gives $\frac{\partial f}{\partial t}|_{scattering} = -g_k/\tau$ where $g_k = f_k - f_k^0$ is the small deviation from the equilibrium Fermi function, and τ is the scattering time. Taken together these give the updated Boltzmann equation as

$$-\frac{\partial f}{\partial \vec{r}} \cdot v_k + \left(\frac{e\vec{E}}{\hbar} + \frac{e}{\hbar c}\vec{v} \times \vec{H}\right) \cdot \boldsymbol{\nabla}_k f_k = \frac{g_k}{\tau} \qquad (3.16)$$

From Eq. 3.16 a number of improvements can be made to describe electronic behavior for certain limits of external fields and simple electron correlations. In the case of partially open orbits in the presence of an external magnetic field, $\vec{H}$, electrons will assume a cyclotron orbit along a "tube" of Fermi surface, resulting in changes in conductivity between directions perpendicular to the applied magnetic field. By defining an cyclotron orbital frequency $\omega_c = \frac{d\phi}{dt}$ one can write down that the orbital angle $\phi = \omega_c \frac{\hbar c}{eH} \int^k \frac{dk}{v_\perp}$ where H is the applied field and $v_\perp$ is the velocity

perpendicular to the applied field. This can then be applied to the Kubo Formula for linear response given by

$$\overleftrightarrow{\sigma} = \frac{1}{4\pi^3} \frac{e^2 \tau}{\hbar} \int_{FS} \frac{\vec{v_k}\vec{v_k}}{|v_k|} dS_f \tag{3.17}$$

in this case a single matrix element of $\overleftrightarrow{\sigma}$ can be defined by breaking $\vec{v_k}$ into the orbital component described by ϕ and the part traveling along the tube, $k_\parallel$. Substituting in the definition of the cyclotron effective mass $m_H^* = \frac{eH}{\omega_c c}$ and breaking up $\vec{v_k}$ culminates in the dreaded Shockley Tube Integration Formula, given by

$$\sigma_{\alpha\beta} = \frac{1}{4\pi^3} \frac{e^2}{\hbar^2} \int \frac{m_H^*}{\omega_c} \left[\int_0^{2\pi} \int_0^\infty v_\alpha(\phi, k_\parallel) v_\beta(\phi - \phi', k_\parallel) e^{-\phi'/(\omega_c \tau)} d\phi' d\phi \right] dk_\parallel \tag{3.18}$$

Here the only parameters that explicitly depends on the external field are ω_c and ϕ'. In the limit of low H fields $\omega_c \tau$ is small, so the angular change in ϕ' is small, we can expand $v_\beta(\phi - \phi', k_\parallel)$ in powers of ϕ' giving $v_\beta(\phi - \phi') \propto v_\beta(\phi) - \phi' \left(\frac{\partial v_\beta}{\partial \phi} \right)$ which gives an extra power of H in the integral. Separating out the field independent integrals as $A_{\alpha\beta}$ and evaluating Eq. 3.18 for three dimensions gives the conductivity tensor in response to small magnetic $H || \hat{z}$ as

$$\overleftrightarrow{\sigma}(H) = \frac{1}{H^2} \begin{bmatrix} A_{xx} & -A_{yx}H & -A_{zx}H \\ A_{zx}H & A_{yy} & -A_{zy}H \\ A_{zx}H & A_{zy}H & A_{zz}H^2 \end{bmatrix} \tag{3.19}$$

Given that $\overleftrightarrow{\rho}(H) = \overleftrightarrow{\sigma}(H)^{-1}$ we can write down the longitudinal resistance ρ_{xx} in response to small magnetic field as

$$\rho_{xx}(H) = \frac{A_{yy}A_{zz} + A_{zy}^2}{A_{xx}A_{yy}A_{zz} + A_{xx}A_{zy}^2 + A_{yy}A_{zx}^2} H^2 \qquad (3.20)$$

which shows the classical H^2 dependence of longitudinal magnetoresistance. This result only holds for partially open orbitals or inhomogeneous carrier character. In the case of a perfect, spherical Fermi surface there is no low field magnetoresistance and the in high field limit the magnetoresistance saturates. In the completely open orbit case this longitudinal magnetoresistance can continue to grow indefinitely, as the added resistance grows with the path length of a single orbit. All of the experiments in this work were conducted for relatively low values of applied magnetic field, so the focus here will reflect that.

Another major contribution to low field longitudinal magnetoresistance is weak localization or antilocalization. In this mechanism, otherwise reversible paths around a defect can pick up a quantum mechanical phase that results in either constructive or destructive interference. Constructive interference from these scattering paths increases the likelihood of back-scattering off the defect, creating an increase in low-field resistance known as weak localization. Destructive interference does the opposite, effectively decoupling the defect from the scattering and resulting in a drop in low field resistance known as weak anti-localization. The zero field form of the contribution due to weak localization in a two dimensional system is given by[138]

$$R_{loc} = -\frac{R_0^2 e^2}{2\pi^2 \hbar} p \ln \frac{T}{T_0} \qquad (3.21)$$

in which p is a factor that describes the scaling of the phase coherence length and $T_0 = \hbar/k_B\tau$. Weak anti-localization has the opposite sign, resulting in a decrease in resistance below T_0. The phase picked up between the two scattering paths is identical in the absence of magnetic field or local magnetic moment, so scattering off non-magnetic particles normally results in weak local-
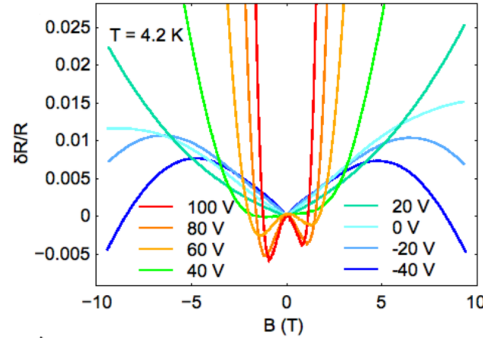
Figure 3.8: **Tuning of weak localization to weak anti-localization in an LSAT / STO system via varying backgate.** Weak localization results in an increase of low field resistance at positive gate bias, while weak antilocalization results in a dip in low field resistance for negative gate bias. Image adapted from Bal *et al.*[56]

ization and the increase in low field magnetoresistance. In the presence of spin orbit coupling, the phase winding around a defect takes on an extra character which can tune to strength of the weak localization or cause the constructive interference to switch to destructive interference, resulting in weak antilocalization. This shift from weak localization to weak anti-localization can be tuned by changing experimental parameters like temperature or backgate. An example of this tuning can be seen in Fig 3.8 for a system of $(La_{0.3}Sr_{0.7})(Al_{0.65}Ta_{0.35})O_3$ (LSAT) / $SrTiO_3$ measured by Varada Bal. For a more detailed discussion of weak localization and the efforts to fit it in complex oxides, please refer to Varada's Thesis.[139]

The magnetic dependence of weak localization in two dimensional systems was worked out by Hikami *et al*[140] and takes the form

$$R_{loc}(B) = -\frac{R_0^2 e^2}{2\pi^2 \hbar} \left[-\frac{3}{2}\Psi\left(\frac{1}{2} + \frac{B_2}{B}\right) + \frac{1}{2}\Psi\left(\frac{1}{2} + \frac{B_1}{B}\right) + \ln\frac{B_0}{B} \right] \qquad (3.22)$$

where Ψ is the digamma function, B_0 is the field associated with elastic scattering time, B_1 is defined as $B_1 = B_\phi + 2B_s$, B_2 is similarly defined by $B_2 = B_\phi + (4/3)B_{so} + (2/3)B_s$, where

B_s is the field associated with magnetic scattering, B_{so} is the characteristic field of the spin orbit coupling, and B_ϕ is the field required to destroy coherence. Close to zero applied field B this disaster of an equation simplifies to

$$R_{loc} = -\frac{3}{2}f(B, B_2) + \frac{1}{2}f(B, B_1) \tag{3.23}$$

where the function f is defined by

$$f(B, B_\alpha) = \frac{R_0^2 e^2}{2\pi^2 \hbar}\left[\Psi\left(\frac{1}{2} + \frac{B_\alpha}{B}\right) - \ln\frac{B_\alpha}{B}\right] \tag{3.24}$$

where in turn B_α is the magnetic field for the relevant contributing length scale. The result is a magnetic field and temperature dependent change in low field resistance that depends directly on the temperature scaling of the coherence times of the physical mechanism considered. Fitting all of the contributing factors requires experimental handles that decouple them, and can be estimated by effective lengths defined by the fields listed above.

The trouble with weak-localization beyond the difficulty in fitting is that the experimental signatures are nearly identical to other contributions to low temperature resistance. In particular, it can be prohibitively difficult to disentangle resistance changes due to superconducting fluctuations mentioned earlier from those due to weak antilocalization. These experimental signatures are even further confounded by electron-electron interactions. Corrections to resistance due to exchange interactions can be written as[141]:

$$R_{EEI} = \frac{-m^*}{4\pi^2 \hbar n \tau}\left(2 - \frac{3F}{2}\right) \times \left[1 - (\omega_c \tau)^2\right]\ln\left(\frac{k_B T \tau}{\hbar}\right) \tag{3.25}$$

This term once again scales with $\omega_c \tau$, which means for high mobility systems this effect is large even at low fields and is therefore difficult to distinguish from weak localization and superconduct-

ing fluctuations. F in this case is a function of the Coulomb potential, with magnitude close to unity. The difficulty in distinguishing electron-electron effects from other sources of resistance makes it hard to categorize them analytically, even for simple systems. The value of identifying it lies in the explanation for secondary effects, like increases in Hall signal or variations in coherence length independent of the cleanliness of the lattice. These effects require careful experimental planning and are nearly impossible to distinguish after the fact.

There are other contributions to high field magnetoresistance that are easier to identify and can be used to infer the nature of carriers in a conductor. One prominent contribution is the change in resistance due to the quantization of Landau levels at low temperatures. This quantization can be seen in oscillations in the longitudinal resistance, known as Shubnikov-de Haas oscillations. The magnitude of these oscillation in a two dimensional system is given by Ando *et al.*[142]

$$\Delta R_{xx} = 4R_0 \frac{\chi_T}{\sinh \chi_T} e^{-\frac{\pi}{\omega_c \tau_q}} \tag{3.26}$$

where R_0 is here defined as the zero field resistance, $\chi_T = 2\pi^2 k_B T / \hbar \omega_c$, the cyclotron frequency $\omega_c = e\boldsymbol{B}/m^*$ as before, and τ_q is the scattering time or, alternatively, the quantum lifetime. If we rewrite this in terms of $\boldsymbol{B}$ to demonstrate the scaling we can define $\chi_T^* = 2\pi^2 m^* k_B T / e\hbar$ and rewrite Equation (3.26) as

$$\Delta R_{xx} = 4R_0 \frac{\chi_T^*/\boldsymbol{B}}{\sinh(\chi_T^*/\boldsymbol{B})} e^{-\frac{\pi m^*}{e\boldsymbol{B}\tau_q}} \tag{3.27}$$

which reveals the scaling with $\boldsymbol{B}$. At very high field the contributions saturate, at intermediate fields the oscillations occur with periodicity depending on $1/\boldsymbol{B}$. Taking into account broadening of the quantized Landau Levels with temperature and the effects of carrier density we have a version of the Lifshitz-Kosevich Formula[143]

$$\Delta R_{xx} = 4R_0 \frac{\frac{\chi_T^*}{B}}{\sinh\left(\frac{\chi_T^*}{B}\right)} e^{-\frac{\xi^* T_D}{BT}} \sin\left[2\pi\left(\frac{F}{B} - \frac{1}{2}\right) + \phi\right] \tag{3.28}$$

where $T_D = k_B \hbar / 2\pi\tau_D$, is the Dingle temperature defined by τ_D the Dingle scattering time which captures the effect of scattering on the Landau levels[139]. The second factor defines the effects of carrier density by way of the shape of the Fermi surface and is characterized by $F = 2\pi\hbar n/N_s e$ where n is the carrier density and N_s is the spin degeneracy.

Other magnetic effects include disruptions of conductivity due to ferromagnetic domain switching, which have a basis in the anisotropic magnetoresistance effect. This effect shows that[144]

$$R_\phi = R_\perp + (R_\parallel - R_\perp)\cos^2\phi \tag{3.29}$$

where ϕ defines the angle between the current and the magnetization, $R_\perp$ is the resistance when the magnetic field is perpendicular to the current while $R \parallel$ is the resistance when the magnetic field and the current are in the same direction. In practice the resistance is minimized for applied field perpendicular to the current, and varying the angle between the two results in an oscillatory magnetoresistance.

This same effect can be seen in ferromagnetic samples where applied field causes switching of magnetic domains or local magnetization. In the high field limits, where the internal magnetization is a aligned with an externally applied field, the conductivity through the sample follows the same behavior as previously described, with a resistive minimum when the magnetization is perpendicular to current flow. In the low field limit, when the externally applied field opposes but does not overcome the internal magnetic moment, the magnetization in the sample can wander or switch, resulting in a signature peak in resistance. Of course the inverse can also happen, when switching causes a break in alignment of the magnetic moment, resulting in a dip in resistance. The second
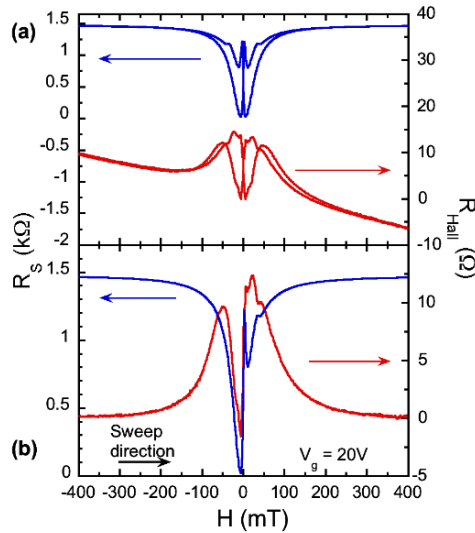
Figure 3.9: **Observation of Ferromagnetic switching in a 2DEG of an LAO/STO heterostructure.** Panel (a) shows a full magnetic field sweep showing symmetry and the peak of magnetic switching, with a single direction displayed in (b). Images taken from Dikin *et al*[145].

defining characteristic is a hysteresis as a function of applied field due to the switching of the internal magnetization. This effect can be seen in Figure 3.9 in a two dimension electron gas (2DEG) of an STO based system, and is similar to results in KTO discussed later in this manuscript.

3.3.2 Sources of Transverse Resistance

The first contribution to transverse resistance is generated by the Hall effect, the buildup of charge carriers on edges of longitudinal current resulting in a finite voltage. Classically this contribution can be calculated from the Lorentz force given by $F = e(\boldsymbol{E} + \boldsymbol{v} \times \boldsymbol{B})$. For a current flowing in the $\hat{x}$-direction and an applied magnetic field in the $\hat{z}$-direction, the buildup of carriers results in a finite transverse field $E_y = V_h/w$ where w is the width of the sample. Assuming steady state and substituting in the definition of current $I_x = ntwev$, where n is the carrier density, and t is the thickness of the sample, we have the first expression of Hall voltage:

$$V_H = \frac{I_x \boldsymbol{B}}{nte}. \tag{3.30}$$

Dividing by the longitudinal current I_x gives us the contribution to transverse resistance from classical Hall effect as

$$R_{Hall} = \frac{\boldsymbol{B}}{nte} = -R_H \frac{\boldsymbol{B}}{t} \tag{3.31}$$

and also defines the Hall coefficient $R_H = -1/n|e|$, which is particularly useful because the sign of the Hall coefficient for a single carrier type gives information on the charge of the dominate carrier. A negative Hall coefficient corresponds to negative charge carriers, positive to positive. In the case of multiple bands of carriers the Hall coefficient gives the net charge, i.e. for two bands, one electron and one hole we have $R_H = -1/(n_e - n_p)|e|$ where n_e is the number of electrons and n_p the number of holes contributing to the conduction.

This same effect can be seen in samples that have effective magnetic fields inside the material, say from magnetic impurities like those discussed in the magnetic scattering section, strong spin orbit coupling in the conducting bands which give an effective moment to the carriers, or simply a net magnetic moment due to ferromagnetism or ferrimagnetism. In these cases the derivation can be completed in much the same way as in Equations 3.30 and 3.31 but with an effective field instead of $\boldsymbol{B}$. In semiconductors a Hall signature can arise due to a difference of mobility between electron-like and hole-like carriers which gives a Hall Coefficient with form

$$R_H = \frac{p\mu_h^2 - n\mu_e^2}{e(p\mu_h + n\mu_e)^2} \tag{3.32}$$

where p is the concentration of hole-like carriers, n is the concentration of electron-like carriers, μ_h and μ_e are the mobilities of the holes and electrons respectively. Two band transport has

been reported in (111) LAO / STO systems,[81] with high-density, low-mobility electron-like band coexisting with a low-density, high-mobility hole band. Even in the case of multiple bands of the same charge character, bands with large variations in effective mass or carrier mobility can modify the Hall coefficient resulting in "non-linear" Hall signals, as is the case at the surface of KTO.[32]

It is useful to be able to fit measured data directly to a two band form, for which we need the magnetic field dependence. For two carriers with density n_1 and n_2 the form of the transverse magnetoresistance is given by Luo *et al.*[146] as

$$\rho_{xy} = \frac{H}{q} \frac{(n_1 u_1^2 + n_2 u_2^2) + (n_1 + n_2) u_1^2 u_2^2 H^2}{(n_1 u_1 + n_2 u_2)^2 + (n_1 + n_2)^2 u_1^2 u_2^2 H^2} \tag{3.33}$$

where μ_1 and μ_2 are the corresponding carrier mobilities, q is the charge of the carriers, and H the applied perpendicular magnetic field. It is not necessary for the carriers to be of different type, bending of the Hall signal can occur from different mobilities of similar carrier type as is the case in KTO.[32]. There is an equivalent form for fitting the longitudinal magnetoresistance of two bands, but it is a small effect, especially in the measurements conducted here.

Other factors that contribute to a transverse resistance can be concisely summed up as flaws in sample fabrication. These include misalignment in lithography, misalignment with respect to crystal direction, or inhomogeneities in local conductivity due to impurity gradients or preferential conduction. These effects are discussed in detail in the context of anomalous transverse signal by Wu *et al.*[147], and some of them will be discussed here.

Geometric offset can result in an anomalous transverse signal in Hall bar configurations by picking up some component of the longitudinal resistance as discussed in the experimental section. Misalignment with conducting axes can be slightly more difficult to detect. Following the Suppose there is a difference in resistance along principle axes in a sample so that there are distinct terms in the resistivity matrix of

$$\rho = \begin{bmatrix} \rho_{xx} & \rho_{xy} \\ -\rho_{xy} & \rho_{yy} \end{bmatrix} \tag{3.34}$$

with ρ_{xx} and ρ_{yy} as the resistances in major crystal directions, and ρ_{xy} and $-\rho_{xy}$ some transverse resistance arising from another source. A misalignment by an angle θ with respect to the principle axes of the crystal results in a rotation applied to Eq. 3.34 giving

$$\rho = \begin{bmatrix} \rho_x \cos^2 \theta + \rho_y \sin^2 \theta & (\rho_y - \rho_x) \sin \theta \cos \theta \\ (\rho_y - \rho_x) \sin \theta \cos \theta & \rho_y \cos^2 \theta + \rho_x \sin^2 \theta \end{bmatrix} \tag{3.35}$$

where the subscripts have been shortened for clarity. Any anisotropy in crystalline conduction can result in a transverse signal upon rotation with the magnitude $(\rho_y - \rho_x) \sin \theta \cos \theta$, even in the absence of other sources of transverse signal. This contribution has no direct dependence on temperature or applied field, unless there are other built in anisotropies in the sample. These sources often also result in their own transverse signals, such as crystalline distortions causing anisotropic conducting channels or nematic current phases, making systematic separation of sources quite difficult. Other experimental handles are necessary to separate this effect from other coexisting sources such as gate voltage changes or finely controlled angle dependent measurements[147].

3.4 Quantum Nonlinear Hall Effect

In 2015 Sodemann and Fu[95] published a paper predicting the emergence of a Quantum Nonlinear Hall Effect: the response of particular materials to an ac-drive with frequency ω would result in a Hall response at 0ω (dc) and 2ω from purely quantum mechanical origin. The prediction was different from other Hall response from Berry curvature because it would arise in materials with no net Berry flux, which is required for any observable charge Hall signal.[148] Experimental real-

izations of this effect were discussed in detail in Chapter 2, so here will be a derivation following Chapter 1 of Brenevig's 'Topological Insulators and Topological Superconductors'.[149]

3.4.1 From Time Evolution to the Berry Connection

Here we will build the theoretical foundation for the non-linear Hall effect, starting with a general time-varying Hamiltonian, $\mathcal{H}(\vec{R})$, depending on time-varying parameters $\vec{R}(t) = (R_1(t), R_2(t), ...)$. From this Hamiltonian we can write down the time independent Schrödinger equation acting on some state is given by:

$$\mathcal{H}(\vec{R})\left|n(\vec{R})\right\rangle = E_n(\vec{R})\left|n(\vec{R})\right\rangle \tag{3.36}$$

We can start in a pure state, $\left|n(\vec{R}(0))\right\rangle$, and slowly let the state evolve $\vec{R}(t)$ along some path in the parameter space given by $\mathcal{C}$. In this case, the state accumulates a phase, $\Theta(t)$, and the resulting wavefunction, $|\Psi(t)\rangle$, takes the form

$$|\Psi(t)\rangle = e^{-i\Theta t}\left|n\big(\vec{R}(t)\big)\right\rangle \tag{3.37}$$

The time evolution of this state $|\Psi(t)\rangle$ is then given by applying the time-varying Hamiltonian

$$\mathcal{H}\big(\vec{R}(t)\big)|\Psi(t)\rangle = i\hbar\frac{\partial}{\partial t}|\Psi(t)\rangle \tag{3.38}$$

or, expanding in explicit eigenvalues of energy

$$E_n\big(\vec{R}(t)\big)\left|n\big(\vec{R}(t)\big)\right\rangle = \hbar\big(\frac{\partial}{\partial t}\Theta(t)\big)\left|n\big(\vec{R}(t)\big)\right\rangle + i\hbar\frac{\partial}{\partial t}\left|n\big(\vec{R}(t)\big)\right\rangle \tag{3.39}$$

Reducing Eq. 3.39 with the scalar product of $\left\langle n\big(\vec{R}(t)\big)\right|$ and re-arraigned we have

$$E_n\big(\vec{R}(t)\big) - i\hbar \Big\langle \boldsymbol{n}\big(\vec{R}(t)\big)\Big| \frac{\partial}{\partial t} \Big|\boldsymbol{n}\big(\vec{R}(t)\big)\Big\rangle = \hbar\big(\frac{\partial}{\partial t}\Theta(t)\big) \tag{3.40}$$

which can then be integrated with respect to some intermediate time giving

$$\Theta(t) = \frac{1}{\hbar} \int_0^t E_n\big(\vec{R}(t')\big) dt' - i \int_0^t \Big\langle \boldsymbol{n}\big(\vec{R}(t')\big)\Big| \frac{\partial}{\partial t'} \Big|\boldsymbol{n}\big(\vec{R}(t')\big)\Big\rangle dt' \tag{3.41}$$

The first term in the Eq. 3.41 is the dynamical phase, relating the evolution of the energy in response to time varying parameters. The second term is the geometric phase, or Berry phase, normally denoted by γ_n for some state n. This relation can be generalized for cyclic, adiabatic processes along some path $\mathcal{C}$ as

$$\gamma_n[\mathcal{C}] = i \oint_{\mathcal{C}} \langle \boldsymbol{n}, t| \, \boldsymbol{\nabla}_{\vec{R}} \, |\boldsymbol{n}, t\rangle \, d\vec{R} \tag{3.42}$$

The Berry phase can be re-written as an integral over a vector potential with explicit dependence on some parameter t'. This is the Berry Connection, $\mathcal{A}_n$ given by

$$\mathcal{A}_n\big(\vec{R}(t')\big) = \Big\langle \boldsymbol{n}\big(\vec{R}(t')\big)\Big| \frac{\partial}{\partial t'} \Big|\boldsymbol{n}\big(\vec{R}(t')\big)\Big\rangle \tag{3.43}$$

which means we can re-write Eq. 3.42 as

$$\gamma_n[\mathcal{C}] = i \oint_{\mathcal{C}} d\vec{R} \cdot \mathcal{A}_n\big(\vec{R}(t')\big) dt' \tag{3.44}$$

It should be noted that this Berry Connection is intrinsically imaginary, resulting in a real Berry Phase and an extra phase accumulation of the time varying state Ψ, (not including the dynamical phase for simplicity)

$$|\Psi(t)\rangle = e^{-i\gamma_n} \left| \boldsymbol{n}\big(\vec{R}(t)\big) \right\rangle \tag{3.45}$$

This derivation of the Berry Connection is complete but for want of a gauge invariance. In pursuit of a gauge invariant variation, let us inject a complete set of states $\Sigma_m |m\rangle \langle m| = 1$ into our generalized definition used in Eq. 3.42 to get

$$\epsilon_{ijk} \left\langle \boldsymbol{\nabla}_i \boldsymbol{n}(\vec{R}) \right| \boldsymbol{\nabla}_k \left| \boldsymbol{n}(\vec{R}) \right\rangle = \epsilon_{ijk} \left\langle \boldsymbol{\nabla}_i \boldsymbol{n}(\vec{R}) \middle| n \right\rangle \left\langle n \middle| \boldsymbol{\nabla}_k \middle| \boldsymbol{n}(\vec{R}) \right\rangle$$
$$+ \sum_{m \neq n} \epsilon_{ijk} \left\langle \boldsymbol{\nabla}_i \boldsymbol{n}(\vec{R}) \middle| m \right\rangle \left\langle m \middle| \boldsymbol{\nabla}_k \middle| \boldsymbol{n}(\vec{R}) \right\rangle \tag{3.46}$$

The first term above is composed of two imaginary components, which means the product is real, and we are only interested in the imaginary part of the expression, as discussed previously. Thus,

$$\gamma_n = - \operatorname{Im}\left\{ \int dS_i \sum_{m \neq n} \epsilon_{ijk} \left\langle \boldsymbol{\nabla}_i \boldsymbol{n}(\vec{R}) \middle| m \right\rangle \left\langle m \middle| \boldsymbol{\nabla}_k \middle| \boldsymbol{n}(\vec{R}) \right\rangle \right\} \tag{3.47}$$

which can be extended still by evaluating each of the inner products explicitly in energy

$$E_n \left\langle m | \boldsymbol{\nabla} n \right\rangle = \left\langle m | \boldsymbol{\nabla}(\mathcal{H} n) \right\rangle = \left\langle m | (\boldsymbol{\nabla}\mathcal{H}) | n \right\rangle + E_m \left\langle m | \boldsymbol{\nabla} n \right\rangle \tag{3.48}$$

with a similar expression for the inverse of n and m. Algebra then reveals an expression similar to Fermi's Golden Rule

$$\left\langle m | \boldsymbol{\nabla} n \right\rangle = \frac{\left\langle m | (\boldsymbol{\nabla}\mathcal{H}) | n \right\rangle}{E_n - E_m} \tag{3.49}$$

Substituting this back into the expression for the Berry Connection given in Eq. 3.47 gives a complete picture of a gauge invariant construction:

$$\gamma_n = \int \int_{\mathcal{C}} d\vec{S} \, \text{Im} \left\{ \sum_{m \neq n} \frac{\langle n | (\boldsymbol{\nabla} \mathcal{H}) | m \rangle \, \langle m | (\boldsymbol{\nabla} \mathcal{H}) | n \rangle}{(E_n - E_m)^2} \right\} \tag{3.50}$$

Not only does this expression preserve gauge invariance, it also provides some insight into the nature of the Berry Connection. Namely, the phase you pick up is dependent on the states that you count. If bands are partially filled, or if k is shifted, for example, the result is a non-zero phase accumulation, which can have measurable consequences. Another quantity that can be interpreted as the source of many physical observable in Hall effect is Berry curvature. Following again the derivation presented in Xiao *et al.*[150] we can start with the Berry Connection and define a gauge-field tensor Ω

$$\Omega_{\mu\nu}^n = \frac{\partial}{\partial R^\mu} \mathcal{A}_\nu^n(\vec{R}) - \frac{\partial}{\partial R_\nu} \mathcal{A}_\mu^n(\vec{R}) \tag{3.51}$$

If we follow the derivation from the previous section, and apply Stoke's theorem we can re-write the Berry phase as

$$\gamma_n = \frac{1}{2} \int_S dR^\mu \wedge dR^\nu \Omega_{\mu\nu}^n(\vec{R}) \tag{3.52}$$

for an arbitrary surface S enclosed by the path $\mathcal{C}$. Here, $\wedge$ denotes an exterior product, the bivector created from the parallelogram defined by the two participating vectors. For a three dimensional vector space, this can be recast in vector form:

$$\vec{\Omega}_n = \boldsymbol{\nabla}_R \times \mathcal{A}(\vec{R}) \tag{3.53}$$

then the Berry phase is just the surface integral of the Berry curvature given by

$$\gamma_n = \frac{1}{2} \int_S dS \cdot \vec{\Omega}_n(\vec{R}) \tag{3.54}$$

You can convert the Berry curvature's tensor form $\Omega^n_{\mu\nu}$ to the vector form $\vec{\Omega}_n$ by the the relation $\Omega^n_{\mu\nu} = \epsilon_{\mu\nu\xi} \vec{\Omega}_n$ where $\epsilon_{\mu\nu\xi}$ is the Levi-Civitá anti-symmetry tensor.

3.4.2   Anomalous Velocity of an Electron

The gauge invariance of the Berry curvature makes it a target for measuring actual effects on the transport properties of physical systems. If we consider a system with a small probing field $\vec{E}$, we can introduce the Peierls substitution $\hat{p} = \hat{p} + eA(t)$ and write down a general Hamiltonian

$$\mathcal{H}(t) = \frac{\left(\hat{p} + eA(t)\right)^2}{2m} + V(\vec{r}) \tag{3.55}$$

Transforming this into $\vec{q}$ - space we can write

$$\mathcal{H}(\vec{q},t) = \mathcal{H}\left(\vec{q} + \frac{e}{\hbar}\vec{A}(t)\right) \tag{3.56}$$

which suggests the substitution to the gauge-invariant crystal momentum $\vec{k} = \vec{q} + \frac{e}{\hbar}A(t)$. Since $A(t)$ preserves translational symmetry, $\vec{q}$ is a good quantum number and $\frac{\partial}{\partial t}\vec{q} = 0$. This can be extended to write the simple equation of motion $\frac{\partial}{\partial t}\vec{k} = \frac{e}{\hbar}\frac{\partial A(t)}{\partial t} = -\frac{e}{\hbar}\vec{E}$. This can then be used to define the velocity of the nth state as

$$\vec{v}_n(\vec{k}) = \frac{1}{\hbar}\frac{\partial \epsilon_n(\vec{k})}{\partial \vec{k}} - \frac{e}{\hbar}\vec{E} \times \vec{\Omega}_n(\vec{k}) \tag{3.57}$$

The added Berry curvature causes an added component in the velocity of the carrier, that is per-

pendicular to the probing electric field $\vec{E}$ and the direction of the Berry curvature of the nth band, $\vec{\Omega}_n(\vec{k})$. Thus, for appropriate orientation of the Berry curvature, the added contribution shows up in the transverse voltage during a transport measurement. This is the case in the anomalous Hall effect, when the Berry curvature generated by the magnetic moments creates a Hall signature in the absence of an external field.

3.5 Berry Curvature in Bloch Electrons

To realize some of the consequences of Berry curvature, consider two examples of Hall effects arising from this anomalous electron velocity. The first is the quantum Hall effect, first demonstrated in 1980 by von Klitzing, Dorda, and Pepper[151] and later explained by Laughlin in 1981[152]. In the presence of a strong magnetic field the Hall conductivity was found to be quantized in units of e^2/h, the quantum of conduction. This behavior was explained by Laughlin in terms of gauge invariance between Landau levels, but now is understood in terms of Berry curvature. Following the work of Xiao *et al.*,[150] we can start with the description of the anomalous velocity of the electron given in Eq. 3.57 and apply this to a band insulator. In this case the first term is zero and the Hall conductivity can be recast as an integral over the first Brillouin zone:

$$\sigma_{xy} = \frac{e^2}{\hbar} \int_{BZ} \frac{d^2k}{(2\pi)^2} \Omega_{k_x k_y} \tag{3.58}$$

Here the integral of the Berry curvature defines the Chern number, and is quantized in units of 2π over a closed loop. The high magnetic field conditions of the quantum Hall effect enforce a vortex in the Brillouin zone, resulting in nonzero Chern numbers. Thus Eq. 3.58 reduces to

$$\sigma_{xy} = n \frac{e^2}{h} \tag{3.59}$$

where here n is the Chern number, and the quantum Hall effect is simply a reflection of the Chern number of the system. This leads into the second example of physical manifestation of Berry curvature, which is the anomalous Hall effect. This is the observation of a Hall signal in magnetic materials in the absence of an externally applied magnetic field. The Hall signal acquires a hysteretic loop when the external magnetic field is swept, reflecting the change of orientation of the magnetic moment of the material. Because it is a bulk phenomenon, this can be considered the continuous version of the quantum Hall effect, and the Hall conductivity can be written as

$$\sigma_{xy} = \frac{e^2}{\hbar} \int_{BZ} \frac{d\boldsymbol{k}}{(2\pi)^d} f(\epsilon_{\boldsymbol{k}}) \Sigma_{k_x k_y} \tag{3.60}$$

where $f(\epsilon_{\boldsymbol{k}})$ is the Fermi-Dirac function for some energy $\epsilon_{\boldsymbol{k}}$. This signal does not need complete bands to be quantized to generate a nonzero Hall signal, it only needs uncompensated bands with appreciable local Berry curvature. An example of this that is directly applicable to KTO the case of spin-orbit split bands. Still following Xiao *et al.*[150] we can write down a generic spin-orbit Hamiltonian

$$H = \frac{\hbar^2 k^2}{2m} + \lambda(\boldsymbol{k} \times \boldsymbol{\sigma}) \cdot \boldsymbol{e}_z - \Delta\sigma_z \tag{3.61}$$

where 2Δ is the splitting due to spin-orbit coupling, and λ is the spin-orbit coupling strength. The resulting Berry curvature can be calculated by taking the partial derivative over the components of $\boldsymbol{k}$ to give

$$\Omega_{\pm} = \mp \frac{\lambda^2 \Delta}{2(\lambda^2 k^2 + \Delta^2)^{3/2}} \tag{3.62}$$

which describes the Berry curvature of the upper (+) and lower (-) spin split bands. The contributions have opposite sign, and are concentrated near the edge of the gap. Thus, filling a single

band but not its complement can result in a nonzero Hall conductivity related to those seen in the anomalous Hall effect. Partial filling is not the only way to measure physical consequences of the Berry Curvature, as will be discussed in the next section.

3.5.1 Application to the Quantum Nonlinear Hall Effect

This then leads to the promised quantum nonlinear Hall effect. Following the derivations of Sodemann and Fu[95], we can describe the current in a direction a and momentum k

$$j_a = -e \int_k f(k) \, v_a \tag{3.63}$$

where here f is the Fermi function and v_a is the physical velocity of the current along a. In a space of dimension d the integral can be expanded explicitly as

$$\int_k = \int \frac{d^d k}{(2\pi)^d} \tag{3.64}$$

Equation 3.63 can expanded by substituting in $v_a = \partial_a E(k) + \epsilon_{abc}\Omega_b \frac{\partial}{\partial t}(k_c)$ where $\partial_a = \frac{\partial}{\partial k_a}$, $E(k)$ is the energy dispersion and Ω_b is once again the Berry Curvature. If we make use of Eq. 3.53 we can write down the Berry curvature along a direction as

$$\Omega_a = \epsilon_{abc}\frac{\partial}{\partial k_b}A_c \tag{3.65}$$

All of this recasting is designed to set up the case for the non-linear Hall effect. Consider a system under excitation from a small oscillating electric field in the c direction, $\vec{E}_c(t) = \text{Re}\{\mathcal{E}_c e^{i\omega t}\}$. From our previous discussion before Eq. 3.57 we recall $\frac{\partial}{\partial t}\vec{k} = -\frac{e}{\hbar}\vec{E}_c(t)$, but we want a higher order form to describe the response of electrons. To achieve this, we start with the relaxation time approximation of the Boltzmann equation, which assumes $\frac{\partial f(\vec{k})}{\partial k_b}|_{scatter} = \frac{f_0(\vec{k})-f(\vec{k})}{\tau(\vec{k})}$, and setting

$\hbar = 1$ we have

$$-e\tau\vec{E}_a\frac{\partial}{\partial k_a}f + \tau\frac{\partial}{\partial t}f = f_0 - f \tag{3.66}$$

for some unperturbed Fermi function f_0 and scattering length τ. Next we expand f up to second order in increasing powers of $\vec{E}_c$ as $f = \mathrm{Re}\{f_0 + f_1 + f_2\}$. In this case, f_0 has no field dependence, f_1 has

$$f_1 = f_1^\omega e^{i\omega t} \qquad f_1^\omega = \frac{e\tau\mathcal{E}_a\partial_a f_0}{1 + i\omega t} \tag{3.67}$$

which is first order in $\vec{E}_c$ as described above, while f_2 has two components given by

$$f_2 = f_2^0 + f_2^{2\omega}e^{2i\omega t} \qquad f_2^0 = \frac{(e\tau)^2\mathcal{E}_a^*\mathcal{E}_b\partial_{ab}f_0}{2(1 + i\omega t)} \qquad f_2^{2\omega} = \frac{(e\tau)^2\mathcal{E}_a\mathcal{E}_b\partial_{ab}f_0}{2(1 + i\omega t)(1 + 2i\omega\tau)} \tag{3.68}$$

Collecting all of these terms back into Eq. 3.63 and including the expansion of the velocity gives

$$j_a = -e\int_k \mathrm{Re}\left\{\left(f_0 + f_1^\omega e^{i\omega t} + f_2^0 + f_2^{2\omega}e^{2i\omega t}\right)\left(\partial_a E(k) + \epsilon_{abc}\Omega_b\frac{\partial}{\partial t}(k_c)\right)\right\} \tag{3.69}$$

In total the expansion gives 8 terms, half of which we can discard because the term is odd in k and will integrate to zero over the full Fermi Surface. Collecting the remaining terms we have

$$j_a = \frac{e^2}{2}\int_k \epsilon_{abc}\Omega_b\mathcal{E}_c^* f_1^\omega + \frac{e^2}{2}\int_k \epsilon_{abc}\Omega_b\mathcal{E}_c f_1^\omega - e\int_k f_2^0\partial_a E(k) - e\int_k f_2^{2\omega}\partial_a E(k) \tag{3.70}$$

which can be re-written as the dc and 2ω components of the current

$$j_a^0 = \frac{e^2}{2} \int_k \epsilon_{abc} \Omega_b \mathcal{E}_c^* f_1^\omega - e \int_k f_2^0 \partial_a E(k)$$

$$j_a^{2\omega} = \frac{e^2}{2} \int_k \epsilon_{abc} \Omega_b \mathcal{E}_c f_1^\omega - e \int_k f_2^{2\omega} \partial_a E(k) \tag{3.71}$$

The second terms in each of these expressions are not quantum mechanical, but vanish in the relaxation approximation because $\partial_a E(k)$ is odd under the assumption of time reversal symmetry. The only terms that are left are the contributions from the Berry curvature, and show up as the dc and 2nd harmonic contributions resulting from an ac drive at ω. Expanding these two terms explicitly with the forms given in Eq. 3.67 we have

$$j_a^0 = \epsilon_{abc} \frac{e^3 \tau}{2(1 + i\omega t)} \int_k (\mathcal{E}_c^* \mathcal{E}_b)(\partial_c f_0) \Omega_b$$

$$j_a^{2\omega} = \epsilon_{abc} \frac{e^3 \tau}{2(1 + i\omega t)} \int_k (\mathcal{E}_c \mathcal{E}_b)(\partial_c f_0) \Omega_b \tag{3.72}$$

Since the two contributions for current in Eq. 3.72 only differ now by a complex conjugate, we will only write the $j_a^{2\omega}$ equation from now on, for simplicity and concision. Now if we move the partial derivative and recognise that the applied field is independent of k we can re-write Eq. 3.72 as

$$j_a^{2\omega} = \epsilon_{abc} \frac{e^3 \tau \mathcal{E}_b \mathcal{E}_c}{2(1 + i\omega t)} \int_k f_0 (\partial_c \Omega_b) \tag{3.73}$$

The remaining integral in Eq. 3.73 is the definition of the Berry curvature dipole:

$$D_{ab} = \int_k f_0(\partial_a \Omega_b) \tag{3.74}$$

In three dimensions the contributions to the Berry dipole form a tensor, though the effect can only be nonzero if the crystal has a polar axis.[95] In this case Eq. 3.73 can be written as

$$j_a^{2\omega} = \frac{e^3\tau}{2(1+i\omega t)} \mathcal{E} \times (\vec{d} \times \mathcal{E}) \tag{3.75}$$

where $\vec{d}$ is the vector contribution along the polar axis resulting from the antisymmetric part of the Berry curvature dipole contributions perpendicular to that axis, given by $\vec{d} = \vec{d}_a \epsilon_{abc} D_{bc}/2$. In two dimensions the only non-zero part of the Berry curvature dipole is out of plane, meaning the forms in Eq. 3.75 can be simplified to the forms

$$j_a^{2\omega} = \frac{e^3\tau}{2(1+i\omega t)} \hat{z} \times \mathcal{E}(\vec{D} \cdot \mathcal{E}) \tag{3.76}$$

This 2D Berry dipole term is only non-zero if the crystal has at most a single mirror plane perpendicular to the plane of the crystal. This forces the dipole term D_a to be orthogonal to the mirror line, and means that if the driving field is parallel to D_a all of the transverse current, along the mirror plane, is a result of the Berry curvature contribution.

The symmetry requirements of the quantum nonlinear Hall effect are strict in two dimensions. Even for the most heavily studied material in this field, WTe$_2$, the observation of the effect requires breaking an additional symmetry with some part of the experimental setup. Ma *et al.*[96] used the stacking asymmetry of bilayer WTe$_2$ to reduce the symmetry of the two dimensional conduction and realize the Berry curvature dipole. Out of plane symmetry was also broken in the work of Kang et al.[104] by the surface, and their discussion focused on the scaling of the observed effect with scattering time as proof for the origin of the effect. In plane field was used to break the crystal

symmetry by Ye *et al.*[105] and the magnitude of the quantum nonlinear Hall response was shown to be modulated by the direction and strength of the driving field. This was the method adapted for use in the work on KTO in this manuscript, where a transverse field was applied to tune the second harmonic response of the 2DEG.
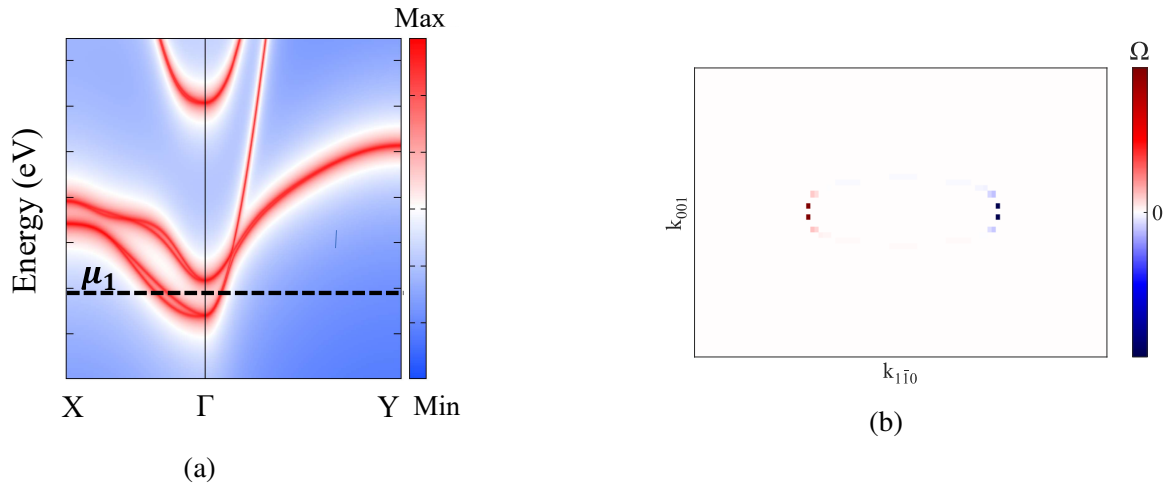
Figure 3.10: **Calculated Berry curvature for the (110) surface.** (a) Density of states along the (110) surface from the Γ point to the the X and Y symmetry points of the Brillouin zone. (b) Low energy cut along μ_1 in (a) showing a Berry Curvature dipole along the [1$\bar{1}$0]. Figures were generated by Alex Tyner, (unpublished).

Each of the crystal interfaces measured in this work have more than the prescribed maximum symmetries. As a result, the Berry curvature on the surface is minimal, only existing due to the 3D inversion symmetry breaking of the interface, or from reconstructions of the crystal lattice. This minimal signal can be seen in Fig. 3.10, which shows DFT calculations along a filling fraction cut on the (110) surface. Fig. 3.10 (a) shows the band structure on the (110) surface with the lowest bands at the Γ-point hosting the spin splitting along the [1$\bar{1}$0] direction. The resulting Berry curvature can be seen in Fig. 3.10 (b), revealing a vanishingly small dipole moment along the [1$\bar{1}$0] direction. Additional tuning through in plane field would be required to realize any effect when only considering contributions from the native Berry curvature.
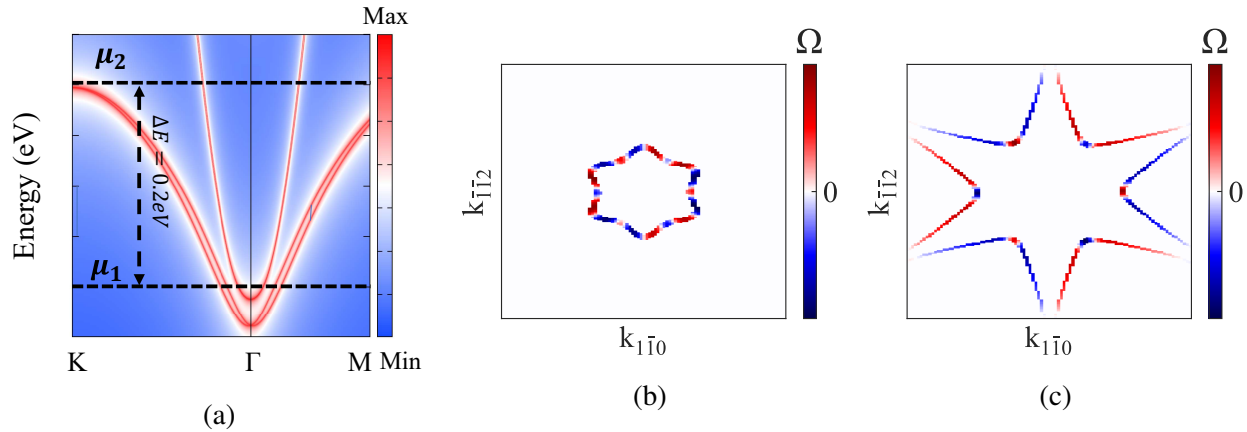
Figure 3.11: **Calculated Berry curvature for the (111) surface.** (a) Density of states along the (111) surface from the Γ-point to the the K and M symmetry points of the Brillouin zone. (b) Low energy cut denoted by μ_1 in (a), showing 3-fold rotationally symmetric Berry curvatures. (c) High energy cut along μ_2 showing weaker Berry curvature. Figures were generated by Alex Tyner, (unpublished).

A similar calculation for the (111) surface can be seen in Fig. 3.11. There is a noticeable increase in the strength of the Berry curvature, shown in Fig. 3.11 (b) and (c) for two cuts μ_1 and μ_2 in the band structure of Fig. 3.11 (a). Two things are evident from these calculations: the strength of the Berry curvature is still primarily in the lowest, spin-split bands at the Γ-point, and the resulting cuts do *not* host a Berry curvature dipole. Despite the interesting spin texture, in the limit of a probing field the directional integration over the whole Brillouin zone that would reveal a Berry curvature dipole is zero, by symmetry. This just means that the un-shifted measurement of the QNLHE should be zero for low currents, and only show shape or dependence for shifted Fermi surfaces or additional broken symmetries. This will represent topics of the coming chapters, where the experimental details and results of the QNLHE measurements will be discussed.

CHAPTER 4

SAMPLE FABRICATION AND EXPERIMENTAL SETUP

This section outlines the experimental considerations specific to fabricating and measuring AlO_x / $KTaO_3$ samples. The technique for fabricating samples dates back to a 2012 paper by Delahaye and Grenet[153] who used oxygen deficient aluminum oxide to fabricate metallic surfaces on STO. The use of elemental aluminum as an overlayer started in 2016 in a paper by Rödel *et al.*[121] who demonstrated the generation of a conducting gas with a 1.25 nm thick layer of Al on several oxide substrates. The technique was first suggested to me by Sam Davis in 2017, and became a staple of fabrication during COVID lockdown times. Additionally, these samples require some special consideration due to eccentricities in the measurements, which will be covered in some detail.

4.1   Sample Preparation

Single crystal substrates of KTO were purchased from MSE Supplies[a] as Single Side Polished (SSP) 5mm x 5mm x 0.5mm squares individually sealed in plastic. Batches of each (001), (110), and (111) crystal terminated substrates were purchased for simultaneous processing, with the intention of comparing the effects of crystal termination on the transport properties as discussed in previous chapters. The substrates from MSE were *not* marked with the normal chamfered corners to denote surface crystal terminations, so additional characterization was necessary to distinguish between the $[1\bar{1}2]$ and $[1\bar{1}0]$ on the (111) substrates.

To determine crystal orientation for measured devices, each of the six substrates used in this

---

[a]KTO substrates available through msesupplies.com

study were subjected to Laue backscatter diffraction at the Jerome B. Cohen X-Ray Diffraction Facility in Cook Hall on Northwestern's campus. Laue diffraction is a very old diffraction technique that is explained in detail in Sam Davis's thesis,[154] and can be used to distinguish crystal orientation and surface crystal directions. This test was critical, not only to distinguish surface directions for the (110) and (111) samples but because it revealed discrepancies in the assumed crystal orientations. It was found that the the non-superconducting (111) sample was in fact a (110) terminated sample, with the measurement conducted along the $[1\bar{1}0]$ direction, and that the (110) superconducting sample was oriented 45 degrees to the edges of the crystal instead of square the the edges as expected. This revelation dramatically changed the analysis of the samples, so a full list of orientation of the samples has been added in an Appendix A.

4.1.1 Cleaning and Surface Preparation

The substrates were inspected and then rinsed off in de-ionized water, acetone and isopropanol before being processed further. The only difference in the processing of normal samples and superconducting samples was an additional annealing step for the superconducting samples that removes excess potassium oxide, generating a clean, terraced TaO_2 terminated surface, as can be seen in Fig. 4.1. This step is critical for the samples to host superconductivity and results in an increase in carrier concentration and maximum carrier mobility by nearly an order of magnitude as measured by Hall effect. The anneal also reduces the effect of inhomogenities generated during the fabrication of the samples, which is critical for the fidelity of the measured results.

The superconducting anneal step is two parts: a high temperature bake in normal atmosphere, and an elevated temperature soak in DI water. Adapted from the work of Tomar *et al.*,[155] this process starts with a 2 hour anneal in a tube furnace at 650 C, in 25 sccm flow of atmosphere. The substrates were arranged in a sandwich configuration with a pair of substrates facing each other,
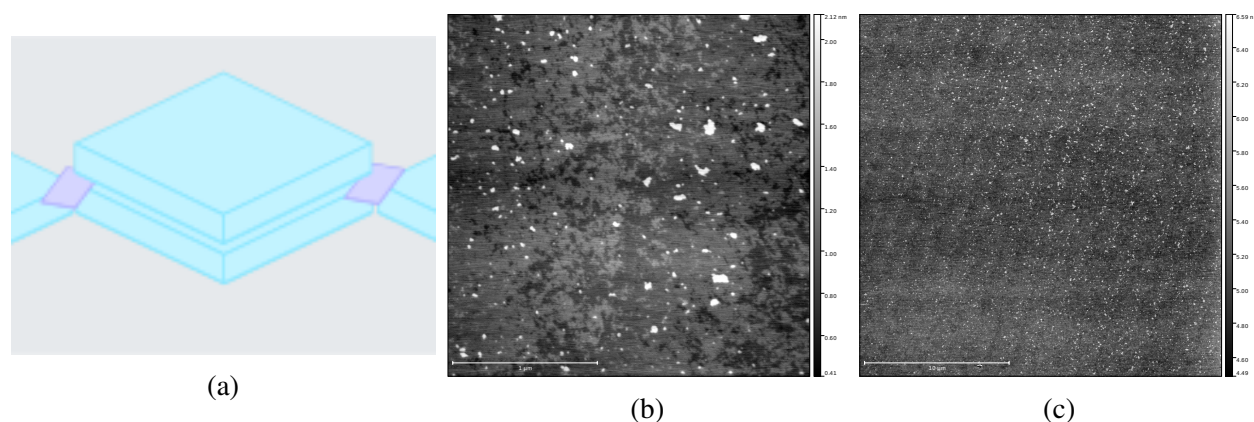
Figure 4.1: **Preparation of the KTaO$_3$ surface.** (a) Schematic of the annealing setup showing two KTO substrates (blue), polished side facing in, separated by two slivers of cover glass at the corners (purple). (b) Contact AFM scan showing the as-received surface over a small range and (c) over a larger area showing steps. Size bars are 1 and 10 μm.

polished side in, separated by small pieces of 130 μm thick cover glass. The glass is arranged on the

corners of the substrates, supported by additional substrates on the sides, as shown schematically in

Fig. 4.1 (a). The reason for this configuration is to create a small gap that keeps excess potassium

from leaching out of the samples due to its high vapor pressure, which normally would cause

pitting and a breakdown of the sample behavior.[155] This etch process proved quite successful and

is an improvement on previous etch processes employing HF based buffered oxide etch,[156] both in

terms of toxicity and in positive impact on carrier properties. The original authors use thin sapphire

spacer instead of cover glass, and this may be an improvement for future processing. Although the

anneal temperature is below the melting temperature of glass, it is near the softening temperature

of $\sim$ 735C,[b] so the slides sometimes stick to the substrates. Because of this, it is recommended to

only prop on corners of the samples, away from the region of the surface that will host the device.

The 650C bake was followed by a two hour soak in 65C DI water. This removes remaining KO

nodules and helps to reconstruct the surface into atomic terraces reminiscent of those seen on STO.

[b]Schott D263M Glass Coverslips Technical Data (Ted Pella)

The importance of this annealing can be seen in Fig. 4.1 (b) and (c), where globular KO nodules are clearly visible over the entire samples surface. This second anneal step was followed by rising in isopropanol, and an immediate lithography preparation to preserve the state of the surface, as described below. An improvement to this process may be to skip the lithography step entirely and coat the entire surface in AlO_x immediately after annealing. This not only improves the state of the interface by preserving the clean atomic TaO_2 atomic termination, but allows for easier extension to electron beam lithography processes. The AlO_x layer can be readily removed through a chemical etch with Tetramethylammonium hydroxide, the active ingredient of MF-319 photolithography developer. This allows for negative patterning of the devices, and may dramatically improve the fabrication process moving forward.

4.2   Photolithography and Thermal Evaporation

All samples were cleaned with a standard ultrasonication process prior to the application of photoresist: three min of ultrasonication in acetone, 3 min of ultrasonication in DI water, and finally 3min of ultrasonication in isopropanol. Samples were then dried with nitrogen and baked briefly on the hotplate set to 125 C for ~60 sec to remove any residual solvents or adsorbed contaminants. Visual inspection should show a flat, mildly reflective surface on a clear but slightly opaque bulk.

Sample were then coated in LOR-5A photoresist,[c] which was beaded and spun on at 3k rpm for 60 sec, then baked at 125 C for 3 min on top of a hot plate with a Petri dish covering it. Before baking, any excess bubbles or edge beads were cut off of the corners of the samples with a razor blade to ensure the success of future exposures. Care was also taken to clean the back of the samples of any excess resist to ensure a flat and consistent contact with the hot plate. Samples

---

[c]LOR-5A data sheet via Kayakuam.com

were then coated with S-1813 photoresist,[d] which is beaded and spun on at 4k rpm for 60 seconds and baked at 165 C for 3 min on the hot plate, also covered with glass. The same cleaning and edge preparation procedure was employed as with the LOR underlayer.

Coated samples were then exposed using the MBJ4 Mask Aligner [e] in the NUFAB cleanroom, which allowed for precise alignment with the primary surface crystal directions by way of the crystal edges. The mask used was a Cr_2O_3 mask designed by the author[f] and the pattern used was a standard positive polarity Hall bar pattern with a 600 μm long and 50 μm wide channel. 8.5 seconds of exposure at 20 μW/cm^2 intensity gave a standard dose of $\sim$170 μJ/cm^2 which was tuned to be slightly above the recommended 150 μJ/cm^2 of the S-1815 resist due to the near-UV transparency of KTO.[157] The samples were then developed with fresh MF-319 photoresist developer[g] and visually inspected to ensure cleanliness and completion of the lithography process.

Figure 4.2: **True color optical microcraph of the completed Hall bar with normal lighting.** The 2DEG appears light due to the clear crystal background, but will appear dark to the naked eye.

The resulting patterns featured four rotationally symmetric Hall bars in two set of perpendicular pairs that were aligned to $< 0.1°$ to the edge of the KTO substrates. The Hall bars themselves have two sets of Hall probes along the 50 μm wide channel, separated by 600 μm, giving a total four terminal aspect ratio of 12 squares. Each probe is defined by a 2 μm wide constriction at the

---

[d]Microposit S1813 data sheet via Kayakuam.com

[e]Suss MBJ4 Mask Aligner instrument page (NUFAB)

[f]Mask_2021_v3.dxf design

[g]Microposit MF-319 data sheet via Kayakuam.com

junction with the channel, and all leads are terminated with a 200 μm wide square contact for wirebonding. Estimated probe misalignment is $< 0.1\%$ from optical imaging, and is corroborated by geometric contribution estimations from resistance tests, which are discussed later. An optical micrograph of a completed samples can be seen in Fig. 4.2.

4.2.1 Aluminum Evaporation

Once the samples were patterned with photolithography, they were mounted in our Joetek ebeam evaporator for metallization. The samples were adhered to the rotating sample block using double-sided-adhesive conducting copper tape, and the chamber was pumped down below 1×10^{-6} Torr overnight. The samples were then cleaned for 45 s by a 100 mTorr of oxygen plasma powered by a home-built power supply discussed in detail in Zhigang Jiang's thesis,[158] p. 72. The chamber was allowed to pump back down below 1×10^{-6} Torr before deposition of aluminum. The aluminum crucible was pre-evaporated for 20 nm of deposition both to clean the aluminum source of any surface contaminants and to allow for a layer of aluminum to coat the chamber, which will act as an oxygen getter to improve the quality of the film. The actual deposition starts with a 1.5 nm thick layer of aluminum deposited on the samples at ~ 1.5 Å s^{-1} evaporation rate. This aluminum getters oxygen from the surface of the samples, forming a 2DEG hosted by the oxygen vacancies induced in the KTO.[69,153] The aluminum was allowed to sit on the samples, in high vacuum, for 10 min to allow for this gettering process to progress. The samples were then coated with a second layer of aluminum, also 1.5 nm thick, before being flushed with 100 mTorr of oxygen. This layer dwelled in the oxygen for 10 min, completely converting the film to amorphous aluminum oxide. A final layer of 2 nm of aluminum was applied and oxidized, primarily to protect the surface and aid in visibility of the sample. A summary of the deposition procedure can be found in Table 4.1.

Table 4.1: **Deposition recipe for depositing AlO$_x$ films on KTO.** Step 3 can be repeated as many times as is necessary to protect the sample, or can be skipped entirely.

Layer Number	Material	Thickness (nm)	Dwell (min)	P(O$_2$) (mTorr)
1	Al	1.5	10	0
2	Al	1.5	10	100
3	Al	2	10	100

Liftoff was performed, removing the remaining photoresist with Remover PG[h] by soaking at 50 C for 5 min before a finishing soak in isopropanol. This isopropanol was removed with pressurized nitrogen, which takes some time because the Remover PG leaves an iridescent film that can be mitigated by repeated isopropanol rinses and pressurized nitrogen cycles.

As mentioned above, the amorphous aluminum oxide can be removed with MF-319. This fact was discovered accidentally by the author when attempting to fabricated tunnel junction heterostructures on STO, which created perfect negative impressions of the pattern on the already-defined Hall bars. The active ingredient in MF-319 is Tetramethylammonium hydroxide at 2.2% concentration and can etch ALD deposited Al$_2$O$_3$ at $\sim$ (1 nm / min),[159] with faster rates for sputtered Al$_2$O$_3$ layers (4.3 nm / min with equivalent developer AZ 300 MiF),[160] and even faster for amorphous Al$_2$O$_3$ (anecdotal). It can also etch Si and SiO$_2$ and other metal oxides, but these should not be a problem for complex oxide samples. Work will need to be done to quantify how the definition of the AlO$_x$ impacts the conducting gas underneath, but this technique should scale with any available level of lithography because it is a highly selective chemical etch and the AlO$_x$ layers are very thin.

---

[h]Remover PG data sheet via Kayakuam.com

4.3   Mounting the Sample and Room Temperature Checks

Successfully fabricated samples were mounted on home built PCB sample headers designed by Kevin Ryan. These 32 pin headers plug into all of the measurement instruments in our lab interchangeably, and feature gold plated copper pads for wirebonding to the sample and a central conducting area for sample mounting and back gate application. These sample headers were explicitly designed to be non-magnetic, in contrast to the previous generation of headers. Each set of three samples, one of each of the nominally (001), (110), and (111) crystal terminations, were adhered to the central conducting pad with silver paste Ted Pella #16062,[i] to allow for good mechanical and electrical contact. Each of the leads, and the connections to the back gate, were twice-wirebonded using aluminum wire (1% silicon) using our Hybond 572A ultrasonic wedge bonder.[j] The wirebonding process for complex oxides is very forgiving, as there is no resistive layer to punch through as is the case with thin layers of SiOx on conducting silicon. The crystal takes aluminum bonds well, allowing contact directly to the 2DEG in the pre-defined contact pads. Care must be taken for gold capped Hall bar pads, as this challenges the adhesion of the wirebonds.

Wirebonded samples were then tested for conductivity and isolation using our Room Temperature Breakout Box, built by the author. All measured samples were tested for continuity with two point resistance between each set of 6 connected leads, with resistances in the $10 \text{ k}\Omega - 100 \text{ k}\Omega$ range but not higher.[k] Each Hall bar was also tested for isolation to each of the other Hall bars, to the back gate, and to any unused pins or ground. These tests would be repeated when installed on the cryogenic probe, but this allowed for easy qualification of the sample and allowed for fast repair and quick turnaround, in the rare case that a wirebond was broken or a lead was lost. The samples were then mounted on the cryogenic probe.

---

[i]Ted Pella Conducing Silver Paint #16062 data sheet
[j]Hybond 572A wirebonder data page
[k]See PK Physical Notebook 1 pages 147, 182, and 194

4.4 Cryogenic Probes

The primary cryogenic probe used in these measurements was the Oxford Instruments Kelvinox MX100 dilution refrigerator.[l] This is a wet dilution refrigerator capable of 100 μW cooling power at 100 mK, outfit with 32 bundled superconducting wires for transport measurements. The MX100's resident dewar is equipped with a two axis superconducting magnet described below, and has been retrofit with a Cryomech HeRL15[m] helium reliquifier unit. The MX100 can reach base temperatures below 20 mK due in large part to grounding and electrical noise optimization performed by Max Wisne, and improvements made to the pumping system and to the ^{3}He mixture.

The temperature of the MX100 was controlled by virtual instruments (VIs), programmed in LabVIEW by the author, that interfaced with the existing LabVIEW VIs provided by Oxford to run the cryostat. In particular, static temperatures were controlled with the MC_PID_2022.vi program, which is a modified version of an existing two step error loop from a former student. This new version TempRamp2020.vi

The other system used to measure the samples discussed in this manuscript was the Janis (now Lake Shore Cryogenics) ^{3}He insert, though the applications were limited as the system is still on the process of recommissioning at the time of writing. The Janis is a closed ^{3}He pumping system with a base temperature of ∼250 mK and a verified base temperature below 300 mK. Its revival was made possible through several rewiring cycles by the author and Max Wisne, culminating in a thermometry overhaul and rebuild of the bottom of the probe for improved thermal anchoring and decreased heat load.

Both probes have had the sample header completely replaced with a PCB socket designed by Kevin Ryan. These headers were intended to make all of the probes in the lab interchangeable

---

[l]MX100 brochure via nanoscience.oxinst.com
[m]HeRL15 data page from cryomech.com

with a unified sample mount, and to correct for the discovery of ferromagnetic components of the previous sample headers. Special non-magnetic sockets, part identifier Cambion 945-8177-01-03-00, were purchased from Bisco Industries Inc.[n] and were paired with non-magnetic 1 mm brass rods purchased from K&S Precision Metals[o] which were etched down to ~ 0.9 mm with a combination of $FeCl_3$ and HCl. To protect the PCB and solder joints, the underside of the headers are first coated liberally with MMA or PMMA because it is readily available, easy to remove, and resists acids. The headers are then placed in a Petri dish filled with $FeCl_3$, so that the meniscus just touches the bottom of the header, and allowed to sit for 15 min. The same process is repeated with HCl, then the headers are rinsed in water, cleaned with acetone, and finally IPA. The brass pins were then polished with a wire brush, or Dremel, until shiny. The diameter of the pins was measured to match the 0.9 mm target, to ensure that the header could mount to the sockets.

4.5 Measurement Techniques

4.5.1 Magnetotransport

Cryogenic magnetotransport measurement was the main technique used to probe the conducting properties of the two dimensional conducting gases (2DCGs) at the interface of these devices. All measurements reported here used current bias transport measurements where a dc or low frequency current is generated from a home built analogue current source enclosed in a μ-metal box and operated on battery power. The extravagance of the μ-metal box and battery set-up is designed to reduce electrical noise, in particular by shielding the primary measurement circuits from ambient magnetic radiation. The current sources are built around a AD549 OP Amp[p] with common mode input impedance (output impedance of the current source circuit) of 10^{15} Ω. A low frequency

---

[n]Cambion socket information page from biscoind.com
[o]Brass rods from ksmetals.com
[p]AD549 data sheet via analog.com

ac current is generated using the oscillator output from a lock-in amplifier or signal generator to drive the current source. All measurements are phased with respect to this oscillating current by measuring the voltage across the sense resistor built into the current sources. These oscillating currents generate voltages in the sample in either a four-terminal or a related configurations which are measured using home-built analog differential amplifiers.

The first stage of voltage signal processing for all measurements were enclosed in a μ-metal box as mentioned above. In nearly all cases the first stage consisted of a differential amplification between 1x and 500x gain. The two primary circuits employed here center on the INA110 Instrumentation Amp[q] and AD624 Instrumentation Amp,[r] low-noise, differential-input instrumentation amplifiers with 10^{12} Ω and 10^9 Ω input impedance respectively. The most important quality of these amplifiers are the very low noise figures, with refer-to-input voltage noise of 10 $\mathrm{nV}/\sqrt{\mathrm{Hz}}$ and 4 $\mathrm{nV}/\sqrt{\mathrm{Hz}}$ respectively. This enables precise measurement of very small signals, which can be further improved through the use of lock-in amplification techniques.

Lock-in amplifiers greatly improve the signal-to-noise ratio of small oscillating signals by measuring the signals at the frequency of an oscillating drive. Lock-ins used in these measurements include the Princeton Applied Research (PAR) 124A,[s] the Stanford Research Systems (SR) 124,[t] and the Edgerton, Germeshausen, and Grier (EG&G) 7260.[u] Both the PAR 124A and the SR 124 are single channel analog lock-in amplifiers, but the EG&G 7260 has the ability to record in-phase and out-of-phase signals simultaneously, so many of the out-of-phase measurements discussed in the manuscript were recorded on the EG&G, unless otherwise stated. Signals from the PAR 124As and SR 124 were then monitored with HP 34401A multimeters[v] (now Keysight 34401a) connected

---

[q]INA110 data sheet via ti.com

[r]AD624 data sheet via Analog.com

[s]PAR 124A manual via manualzz.com

[t]SR 124 manual via thinksrs.com

[u]EG&G 7260 manual via atecorp.com

[v]HP 34401A manual via engineering.purdue.edu

via GPIB to the measurement computer, and recorded on measurement software written by Professor Chandrasekhar. The EG&G were connected directly via GPIB to the measurement computer, simplifying some of the measurement racks considerably.

Most of the results discussed in this manuscript are differential resistance measurements taken as a function of externally controlled experimental parameters, most commonly magnetic field H and back gate voltage V_g. Magnetic fields were applied either perpendicular to the surface of the sample, denoted from now on as $H_\perp$, or parallel to the surface of the sample, denoted by $H_\parallel$. Both the MX100 dilution refrigerator and the Janis ^{3}He probes employed 3 T perpendicular field solenoids and 1 T split Helmholtz coils, whose field strength was recorded by monitoring the voltage drop across a 1-2 mΩ sense resistor. The magnets on the MX100 were powered by a Kepco BOP 20-50MG digital power supply,[w] while those on the Janis's blue Dewar were powered by a Kepco BOP 20-20 bipolar power supply.[x] Back gate voltage was applied to the samples with a Keithley (now Tektronix) 2400 SourceMeter[y] equipped with a low pass filter, and normally monitored externally with an HP 34401A multimeter as previously described.

4.5.2 Drift Corrections in Longitudinal Magnetoresistance

It is well known that complex oxide samples drift over time whenever changes are made to significant experimental parameters such as back gate voltage. This drift is persistent over the course of hours to days, so is accounted by subtracting off a time dependent logarithmic form as described by Biscaras *et al.*[161] This procedure was conducted automatically by finding the change in resistance of the zero field values of longitudinal magnetoresistance and fitting to the Biscaras form, $R(t) = R_0 + A \log(t + C)$. Here t is time, and is recorded as an experimental parameter

---

[w]Kepco BOP 20-50MG manual via kepcopower.com
[x]Kepco BOP 20-20 manual via kepcopower.com
[y]Keithley 2400 SourceMeter manual via tek.com

during measurement. For hysteretic magnetoresistance traces or those with few passes or large drift this procedure was conducted by hand. An example of the correction can be seen in Fig. 4.3, the the as-measured data (a), and the corrected data with the fit parameters $R_0 = 1040$, $A = 250$, and $C = 10000$. In this case R_0 is not the residual resistance but the shift necessary to recover the appropriate resistance at the start of the run, which is important for calculating percent magnetoresistance. The results shown in Fig. 4.3 (b) are then interpolated along 751 evenly spaced values of magnetic field, and averaged together into one representative trace, as seen in Fig. 4.3 (c). A zoomed in view of the center, showing the preservation of the hysteresis can be seen in Figure 4.4. Drift was also seen in the transverse magnetoresistance, but only for the lowest gate voltages, which were often excluded due to overwhelming noise obscuring the signal.
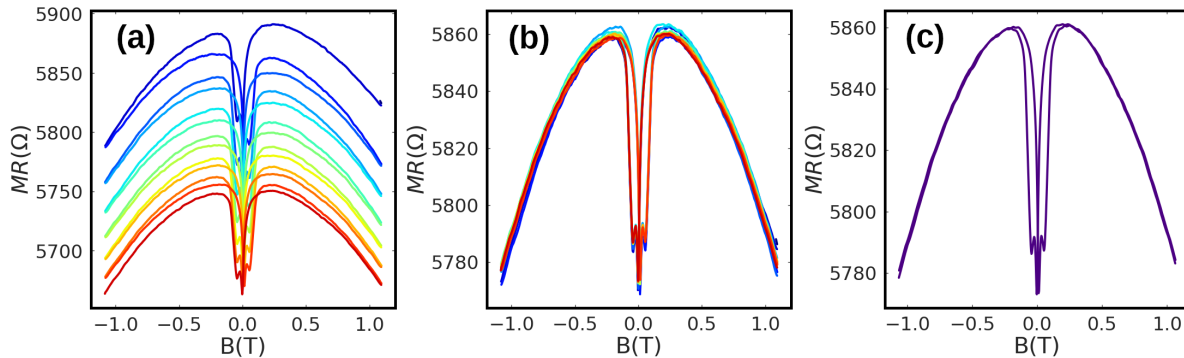
Figure 4.3: **Demonstration of drift correction procedure for a longitudinal magnetoresistance trace taken at $\sim$ 30mK and V_g = 200V.** (a) shows raw data demonstrating a time dependent drift of magnetoresistance after a change in gate voltage. (b) drift corrected data showing good agreement after multiple traces. (c) shows the resulting trace after the repeated sweeps were interpolated and averaged together. (Results reproduced from the Supplemental Materials of Krantz *et al.*, arxiv.org/abs/2209.10534)

4.5.3 *Second Harmonic Measurements*

One of the more novel measurement configurations discussed in this manuscript is a measurement of the second harmonic of the differential resistance transverse to the ac current exci-
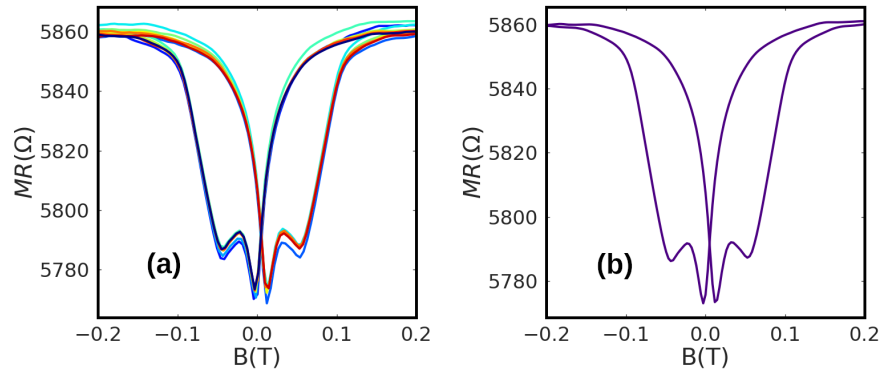
Figure 4.4: **Demonstration of low external magnetic field drift correction procedure.** (a) shows drift corrected data showing good agreement after multiple traces, while (b) shows the resulting smoothed data, demonstrating the fidelity of the procedure. (Results reproduced from the Supplemental Materials of Krantz *et al.*, arxiv.org/abs/2209.10534)

tation. Second harmonic measurements date back to the 1980s, but this particular measurement is designed to measure the quantum non-linear Hall effect arising from Berry curvature dipoles coupling to the ac excitation of the measurement. A detailed discussion of the origin of this effect is given in Chapter 3, but here will be details of the experimental actualization of the measurement.

Second harmonic measurements, also refereed to as 2ω measurements, employ a lock-in technique at the second harmonic of the primary drive current. To accomplish this, a drive source of either the primary lock-in or a signal generator is used to generate the first harmonic, and all first harmonic measurements are phased to the current as previously described. The signal for this first harmonic is fed into the external reference input of a second lock-in, which is set to measure the second harmonic, either External $2f$ on the SR124, External $f/2$ on the PAR 124A, or 2nd harmonic in the Reference Channel menu of the EG&G. These lock-ins are then phased to the current response of the second harmonic drive frequency, accomplished by taking the oscillator output of the second lock-in and feeding it into the current source, then phasing as normal.

The primary drive is returned to the first harmonic, and the lock-ins are then adjusted to monitor the -90° out-of-phase contribution of the second harmonic. This negative is important for recov-

(a)   (b)
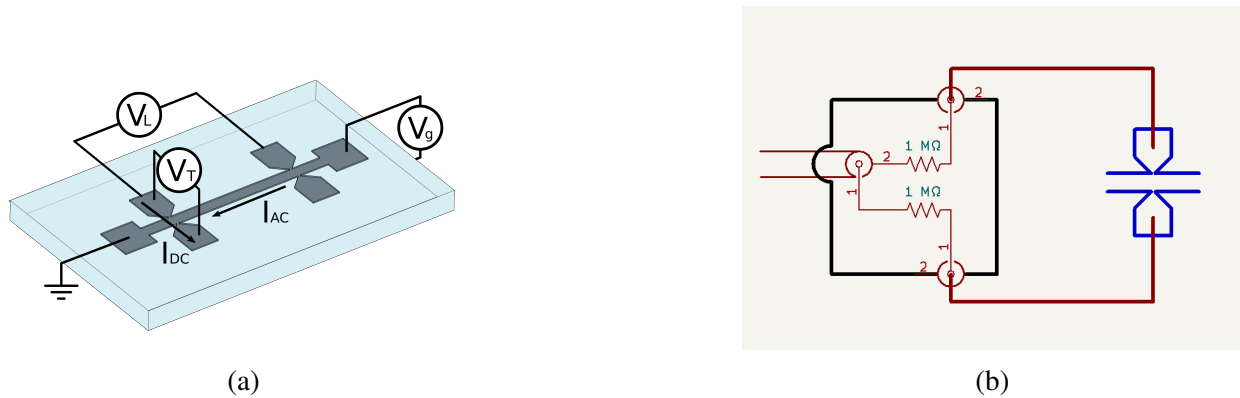
Figure 4.5: **Experimental configuration for measuring the quantum non-local Hall effect.** (a) Schematic of the normal 2ω measurement with the dc field shown as I_{dc}. Here V_T can measure both the 1ω and 2ω signals depending on the configuration of the lock-in amplifiers. (b) Circuit diagram for implementing the floating dc drive along the V_T leads, sourced (left coax) from a floating voltage of an Agilent output.

ering the correct sign of the measurement, and corresponds to the case of a sine drive, dictated by the nature of the oscillator circuits in the lock-ins themselves. An easy check is to match changes in the slope of the first harmonic to the shape of the second harmonic response, as part of the second harmonic records the derivative of the first harmonic signal. A schematic of this experimental setup can be seen in Fig. 4.5 (a), with $I_{dc} = 0$.

The previous description completes the passive monitoring of the second harmonic of the transverse response to an ac drive, but an additional layer was also added. The Berry curvature dipole response can be modified by applying a transverse dc field (current), as discussed Chapter 3. A dc field is generated by creating a floating voltage across the same two probes used to measure the second harmonic transverse response. The floating voltage is provided by the dc offset output of an Agilent synthesizer, with the central conductor of the coaxial line and ground shield of the coaxial line split across two 1 MΩ source resistors before connecting to the measurement lines of the transverse probes. This generates a floating dc voltage (current) with the only ground reference in the center of the sample Hall bar, but with no net current flow along the Hall bar. This is shown

schematically in Fig. 4.5 (a) for some non-zero I_{dc}, and the circuit configuration for the floating dc field can be seen in Fig. 4.5 (b).

4.5.4   Phasing for a Second Harmonic Measurement

The -90° shift for the second harmonic that was mentioned in a previous paragraph is not a steadfast rule. The oscillator outputs and the measurement inputs of the lock-in amplifiers are internally referenced, and need to be checked on an external oscilloscope to identify the nature of the oscillation and timing of the internal circuitry. If the output is a sine wave, which means the trigger is matched on the zero of the oscillation, then the second harmonic is a cosine, measured as the negative 'out-of-phase' to the drive. If the output is a cosine wave, so the trigger is at the peak of the oscillation, then the second harmonic is 'in-phase' with the drive. This is a somewhat confusing consequence of phase shifts and what it means to be in-phase for harmonic frequencies. To help elucidate this difference a brief discussion is presented below.

We want to understand the appropriate phase for the second harmonic, and this requires an understanding of ac lock-in techniques. To start, the familiar expression of Ohms Law, $V = IR$ can be broken into two parts for the dc and ac responses.

$$V(I_{DC} + I_{AC}) = (I_{DC} + I_{AC})R = I_{DC}R_0 + I_{AC}R_{AC} \tag{4.1}$$

Here I_{DC} and I_{AC} are the dc and ac parts of the current which can be explicitly controlled in the experimental setup, R_0 is the dc resistance, and R_{AC} is the impedance or ac differential resistance. This distinction seems trivial but it relates to the practical operation of lock-in amplifiers which normally measure the differential resistance given simply by $R(V, I) = \frac{\partial V}{\partial I}$. Substituting this back into Eq. 4.1 gives

$$V(I_{DC} + I_{AC}) = I_{DC}R_0 + I_{AC}R_{AC}$$

$$= V_{DC} + I_{AC}\left(\frac{\partial V}{\partial I}\right) \tag{4.2}$$

This describes the zeroth harmonic and first harmonic response of a sample under current excitation. Normally the first term is dropped because lock-ins are ac-coupled and do not see the dc voltage, but the term can have consequences for very resistive samples, an effect that is discussed later in this Chapter. If Eq. 4.2 is expanded as a Taylor series for higher powers of $\frac{\partial V}{\partial I}$ the expression becomes

$$V(I_{DC} + I_{AC}) = V_{DC} + I_{AC}\frac{\partial V}{\partial I} + \frac{I_{AC}^2}{2}\frac{\partial^2 V}{(\partial I)^2} + \mathcal{O}\left(\frac{\partial^3 V}{(\partial I)^3}\right) \tag{4.3}$$

Moving forward the dc components will be dropped for clarity. Additionally, I_{AC} can be rewritten in terms of a magnitude and an explicitly oscillating part as $I_{AC} = |I_{AC}|\sin(\omega t + \phi)$ with a characteristic frequency ω and arbitrary phase ϕ. Importantly, the oscillating part of I_{AC} is chosen to be $\sin$ instead of $\cos$ here. Substituting this into Eq. 4.3 gives

$$V(I_{AC}) = |I_{AC}|\left(\frac{\partial V}{\partial I}\right)\sin(\omega t + \phi) + \frac{|I_{AC}|^2}{2}\left(\frac{\partial^2 V}{(\partial I)^2}\right)\sin^2(\omega t + \phi) + \mathcal{O}\left(\frac{\partial^3 V}{(\partial I)^3}\right) \tag{4.4}$$

The second term in Eq. 4.4 can be reduced from $\sin^2$ by remembering a set of identities for double angles and sum of angles in trigonometry:

$$\cos(2\alpha) = 1 - 2\sin^2(\alpha)$$

$$\cos(2\alpha) = 2\cos^2(\alpha) - 1 \tag{4.5}$$

substituting the first cosine identity for $\sin^2$, we can recover an expression for the second harmonic measurement on the lock-in amplifier.

$$
\begin{aligned}
\frac{|I_{AC}|^2}{2}\left(\frac{\partial^2 V}{(\partial I)^2}\right)\sin^2(\omega t + \phi) &= \frac{|I_{AC}|^2}{4}\left(\frac{\partial^2 V}{(\partial I)^2}\right)\left(1 - \cos(2\omega t + 2\phi)\right) \\
&= \frac{|I_{AC}|^2}{4}\left(\frac{\partial^2 V}{(\partial I)^2}\right) - \frac{|I_{AC}|^2}{4}\left(\frac{\partial^2 V}{(\partial I)^2}\right)\cos(2\omega t + 2\phi)
\end{aligned} \tag{4.6}
$$

which has a dc component $A = \frac{|I_{AC}|^2}{4}\left(\frac{\partial^2 V}{(\partial I)^2}\right)$ and two time varying components depending on the original offset phase ϕ. If the expression is reduced by taking $\phi \to 0$ the second harmonic response is produced:

$$V^{2\omega}\big(|I_{AC}|\sin(\omega t)\big) = \frac{|I_{AC}|^2}{2}\left(\frac{\partial^2 V}{(\partial I)^2}\right)\sin^2(\omega t) = -\frac{|I_{AC}|^2}{4}\left(\frac{\partial^2 V}{(\partial I)^2}\right)\cos(2\omega t) \tag{4.7}$$

In this case the value measured by the lock-in amplifier on second harmonic mode is the $\left(\frac{\partial^2 V}{(\partial I)^2}\right)\cos(2\omega t)$ term, the second derivative of the voltage at 2ω. The phase shift mentioned earlier is seen from the change from $\sin$ in the first harmonic to $-\cos$ for the second harmonic. If the starting term is a $\cos$ instead of a $\sin$ as was noted above Eq. 4.4 giving $I_{AC} = |I_{AC}|\cos(\omega t + \phi)$, then Eq. 4.4 becomes

$$V(I_{AC}) = |I_{AC}| \left(\frac{\partial V}{\partial I}\right) \cos(\omega t + \phi) + \frac{|I_{AC}|^2}{2} \left(\frac{\partial^2 V}{(\partial I)^2}\right) \cos^2(\omega t + \phi) + \mathcal{O}\left(\frac{\partial^3 V}{(\partial I)^3}\right) \quad (4.8)$$

This change seems to be innocuous but some difficulty arises from the second harmonic term when the procedure from Equation 4.6 is repeated

$$\frac{|I_{AC}|^2}{2} \cos^2(\omega t + \phi) \frac{\partial^2 V}{(\partial I)^2} = \frac{|I_{AC}|^2}{4} \left(\cos(2\omega t + 2\phi) + 1\right) \frac{\partial^2 V}{(\partial I)^2}$$
$$= -\frac{|I_{AC}|^2}{4} \frac{\partial^2 V}{(\partial I)^2} + \frac{|I_{AC}|^2}{4} \frac{\partial^2 V}{(\partial I)^2} \cos(2\omega t + 2\phi)$$

which is an identical expression up to the inclusion of an overall negative. Once again taking the limit as $\phi \to 0$ we are left with the reduced expression

$$V^{2\omega}\left(|I_{AC}| \cos(\omega t)\right) = \frac{|I_{AC}|^2}{2} \left(\frac{\partial^2 V}{(\partial I)^2}\right) \cos^2(\omega t) = \frac{|I_{AC}|^2}{4} \left(\frac{\partial^2 V}{(\partial I)^2}\right) \cos(2\omega t) \quad (4.9)$$

which also has a $\cos$ term in the second harmonic. This is a distinctly different result from Eq. 4.7 because it has lost the -90° shift, and is instead directly "in-phase" from the first harmonic drive to the second. The location of the appropriate second harmonic signal depends entirely on the nature driving signal. To summarize:

$$\sin(\omega t) \to \sin^2(\omega t) \to -\cos(2\omega t)$$

$$\cos(\omega t) \to \cos^2(\omega t) \to \cos(2\omega t)$$

This distinction does not take into account frequency dependent phase shifts from other parts of the circuit, and in practice the ϕ mentioned above changes between the first and second harmonic. To account for this it may be wise to check the incidence of the first and second harmonic signals from the sample on an oscilloscope to ensure that the relative phasing is correct. This should be obvious from the last form of Eq. 4.6. Any finite ϕ would result not only in an offset but a second oscillating component that would modify the nature of the 2ω signal. Reducing the sources of error in this way is necessary for realizing publishable results, but it is not the only pitfall to be cognisant of when measuring complex oxides.

4.5.5 *Measurement Limitations and Experimental Artifacts*

When looking for small signals and potentially new physics in transport measurements of complicated samples it is important to know the limits of the measurement setup. Such limitations can manifest in strange ways that seem to mimic interesting behaviors, so understanding them is critical to supporting the truth of a finding. Here I will summarize some of the limitations of the measurement setup that I found, the signatures of those limits as seen in data, and several red herring signals generated from sample imperfections.

Frequency Limits and Considerations

Each of the instruments listed in the Measurement Techniques section above comes with a characteristic bandwidth of operation most commonly described by the gain-bandwidth product. This determines the operational frequency range of the instruments, but even within this frequency range there are additional considerations that must be made to things like harmonics, beating effects, and signal phase shift. These effects are covered in detail in other sources, such as Jonghwa Eom's thesis,[162] and will not be belabored here.

What is important to include here are specific limits of the measurement probes employed in the lab. Each have their own limits imposed by the native complex impedance of the lines. For example, the MX100 is equipped with sets of twisted bundles of superconducting lines which have some unavoidable capacitance and inductance, even when in the superconducting state. This creates an effective low-pass filter well below the frequency cut-offs of the measurement instruments or the inline radio frequency filters installed in the breakout box at the top of the fridge. The response of the lines changes between different pairs but a representative trace was taken as a function of frequency using an Agilent 33220A Arbitrary Waveform Generator[z] and can be found in Fig. 4.6 (a). The effective cutoff frequency for the lines can be estimated to be 70 kHz, above which frequency the signal experiences a large phase shift and attenuates sharply in amplitude. Measurements that need frequencies above this cutoff will need to be conducted with coaxial lines or some other clever workaround.

This is not the only manifestation of the limits of the complex impedance of the fridge though. Even at lower frequencies but large measurement loads strange artifacts can arise. Fig. 4.6 (b) shows two traces made on KTO samples as a function of magnetic field. Back gate voltage was continuously changed (green curve) between the two measurements resulting in a large resistance

---

[z]Agilent (Now Keysight) 33220A data sheet via keysight.com
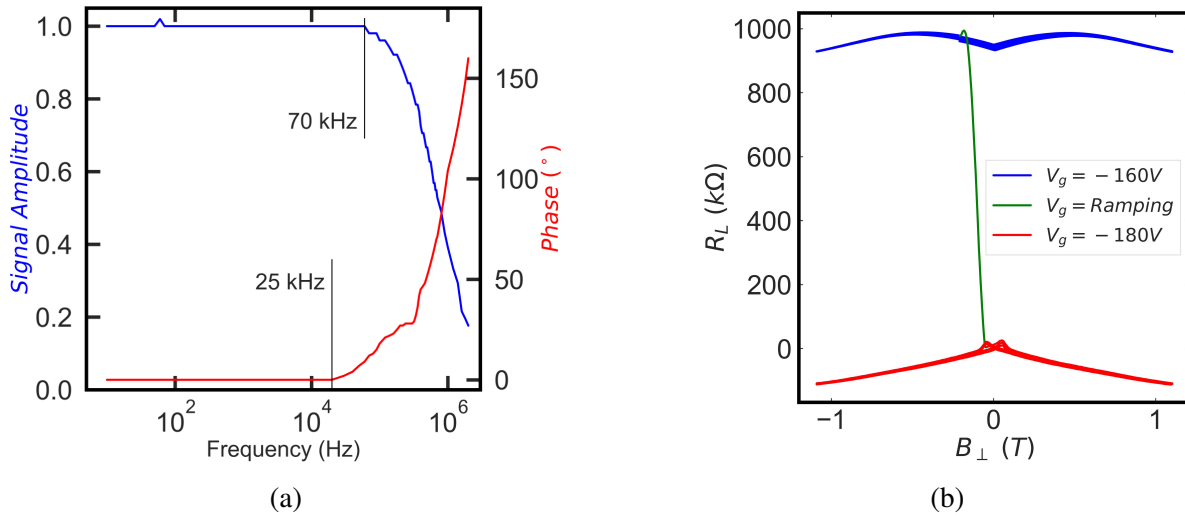
Figure 4.6: **Complex response of the experimental setup.** (a) Measurement of the frequency response of the MX100 cryogenic probe, showing normalized transmission signal amplitude and phase shift. (b) Voltage inversion at ~ 1 MΩ for the transition from V_g = -160 V to V_g = -180 V. The blue curve is "right side up", the green curve is the gate voltage sweep between setpoints, and the red curve is "upside down" from exceeding the limit of the measurement.

and large capacitive response of the sample. As a result, some threshold was crossed which inverted the signal of the second trace (red curve) when compared to the right-side-up trace (blue curve). This behavior arises well below the level of input impedance of the instrumentation amplifier, which in this case is an INA 110 with impedance of 10^{12} Ω. Most samples do not exhibit this level of resistance or capacitance, but there were similar signatures seen by other lab members before (see the thesis of Varada Bal[139] pg 116), so it is something to keep in mind.

Amplifier and Current Source Voltage Limits

In addition to the gain bandwidth limits of amplifiers discussed above, there are other limits that can be approached when measuring resistive samples. If the limit of the differential inputs of the instrumentation amplifiers is reached the resulting signal can saturate, which is well known, but it does not always result in a saturated high signal in the measurement. Fig. 4.7 shows two

different manifestation of a saturated signal. The first, seen in Fig. 4.7 (a), is a voltage signal from an INA 110 amplifier measuring differential resistance of a KTO Hall bar as a function of dc current, and shows a sharp drop above a certain value of the dc current despite associated drops in differential resistance. This is due to a saturation of the dc differential voltage seen at the input of the amplifier, and results in a purely dc output. This output is not seen by the ac-coupled input of the lock-in amplifier but does entirely mask the ac response, causing the signal measured by the lock-in amplifier to drop to zero, usually with some rebound bump. This is accompanied by a spike in the out of phase part of the lock-in signal or a jump in the second harmonic, all of which are indications that the amplifier has saturated.

(a)   (b)
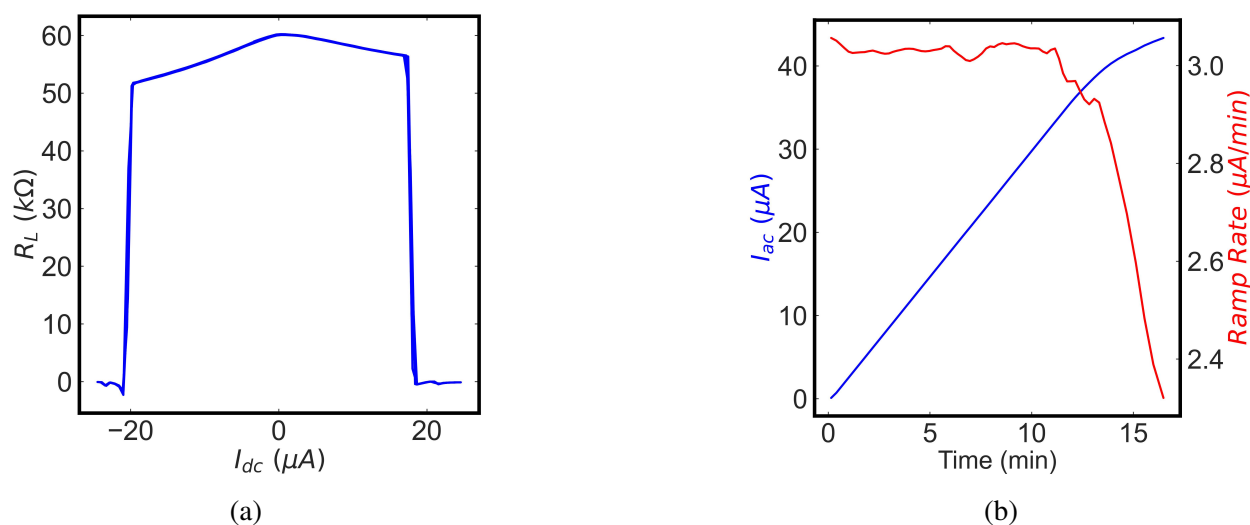
Figure 4.7: **Saturation effects in large drive currents.** (a) Saturated dc voltage while measuring a dV/dI trace, resulting in a sharp drop off of measured resistance. (b) A drop in the ramp rate of an increasing alternating current drive due to voltage limits on the current source output, for measured signal and numerical derivative.

The second example, shown in Fig. 4.7 (b), is a drop in the response to an ac current of increasing amplitude. In this case the drop in signal is not due to the instrumentation amplifier, but instead the voltage limit of the current source output, known as the voltage compliance. Despite
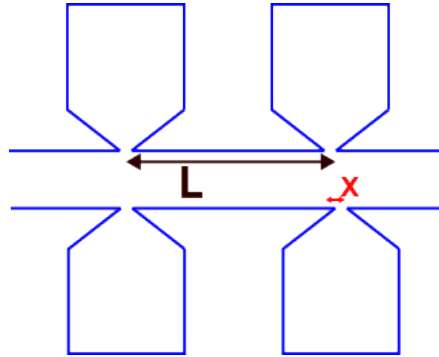
Figure 4.8: **Transport signatures from probe misalignment in the Hall bar configuration.** Schematic of a misaligned Hall bar.

having an output impedance of 10^{15}, the current sources are only able to enforce 12 V of sourcing voltage, and when the load from the sample nears this limit the response dips, then starts to drop, likely due to the truncation of the outputted sine wave. Once again this occurs only for very resistive samples, but is something to keep in mind when measuring systems like complex oxides which can have very large resistances and non-trivial contact resistances.

Hall Probe Misalignment and Stranger Things

It is commonly known that sample imperfections can lead to transport measurement artifacts. The most common of these are imperfections of Hall probe alignment, which can cause some fraction of the longitudinal resistance to be picked up by the Hall probes. This can be characterized by a geometric factor given by $R_T = R_H + \frac{x}{L} R_L$, where R_T is the measured transverse resistance, R_H is the normal Hall response, x is the length of Hall probe misalignment along L, which is the length of of the Hall bar between voltage probes. R_L is the longitudinal resistance of the Hall bar measured between a pair of voltage probes, as shown in Fig. 4.8. This should should be easily identifiable by comparing the shapes of the longitudinal and transverse responses as a function of some external parameter that causes large variation of the longitudinal response,

Table 4.2: **Geometric contributions to the transverse response estimated for AlO$_x$ / STO samples.** Data given for two Hall bars at room temperature and liquid nitrogen temperature, reporting longitudinal resistance R_L, and transverse resistance R_T and the estimated geometric contribution. (Adapted from the Supplementary Materials of Krantz and Chandrasekhar.[30])

Sample	Temp (K)	R_L (Ω)	R_T (Ω)	$\frac{R_T}{R_L}$ (%)
[111]	300	77600	48.0	0.06
	78	22700	15.3	0.07
[001]	300	59400	-74.8	0.13
	78	10300	-13.8	0.13

such as gate voltage or temperature. One good estimation of this effect is to take four terminal resistance measurements at room temperature and again at liquid nitrogen temperatures, allowing for an estimation of the geometric contribution to the transverse signal. An example of this is given in Table 4.2 for samples of AlO$_x$ / STO fabricated with the same photolithography process as the KTO samples discussed in this manuscript.

The geometric response should manifest as the combination of resistive components of the longitudinal and transverse responses. Both of these should be purely the in-phase contributions to those lock-in signals. There are other ways of generating an errant signal though, such as poor phasing of the lock-in amplifiers or large shifts in the complex impedance of the sample due to the breakdown of the 2DEG or some loss of contact. In this case the out-of-phase component of the signal can bleed into the in-phase measurement due to phase shifts, causing a spurious signal. This can be probed by a careful measurement of the lock-in phase at critical points of the measurement, by simultaneously measuring the out-of-phase contribution on a dual channel lock-in like the EG&G, or by monitoring the frequency dependence of the signal. The out-of-phase contributions to the signal caused by capacitance or inductance of the measurement configuration scale with frequency, while the resistive components do not, providing an avenue for additional verification of a signals validity. This is clearly demonstrated in Fig. 4.9, which shows the in-

phase (a) and out-of-phase (b) contributions of a longitudinal resistance of an AlO_x / KTO sample as a function of gate voltage for three different frequencies. Fig. 4.9 (c) shows the collapsed signals when the out-of-phase data from (b) was divided by the drive frequency, a clear indication of capacitive or inductive response.
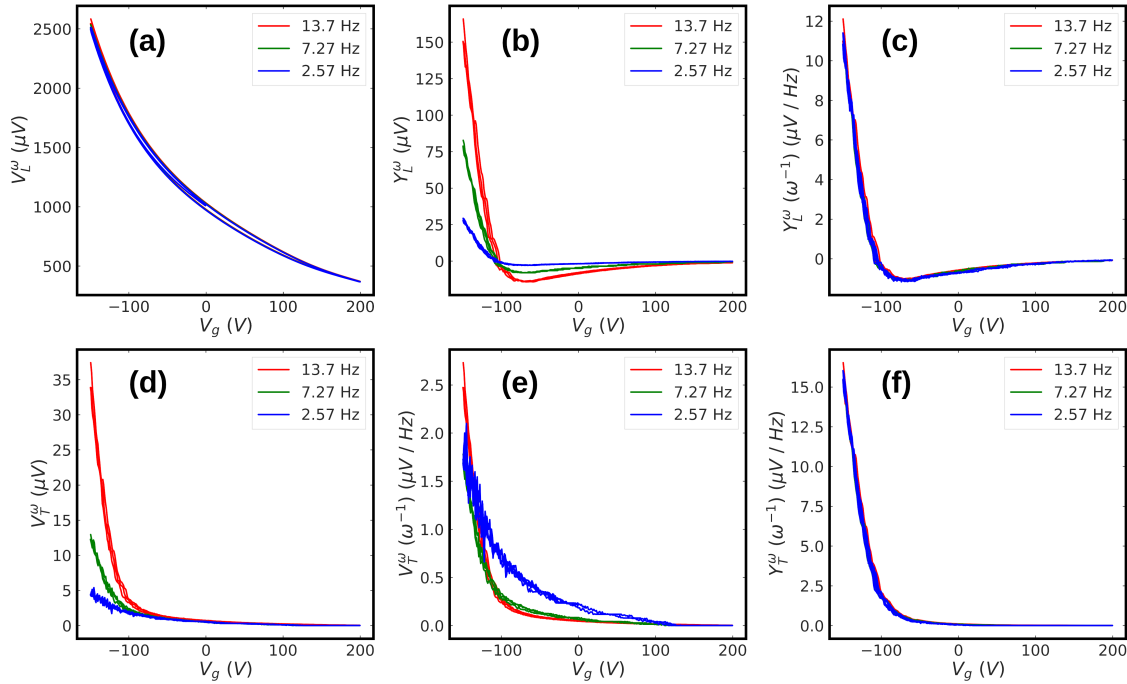
Figure 4.9: **Frequency dependence of the measured 1ω signals as a function of gate voltage.** (a) In-phase and (b) out-of-phase contributions of the longitudinal resistance, and the the same out-of-phase signal scaled with frequency (c). (d) In-phase contribution to the transverse resistance and (e) in-phase contribution with the frequency scaling. (f) Out-of-phase of the transverse resistance with the frequency scaling. All measurements were taken at 4 K.

The mechanism for this effect is not established at this point, though the prevailing understanding is that an imbalance of the complex impedance of the measurement leads creates an out-of-phase signal in the transverse measurement. This effect can be seen in Fig. 4.9 (d), which shows the in phase contributions to the transverse resistance measured simultaneously to the longitudinal resistance shown in (a). The low V_g part of the signal clearly scales with frequency as demon-

strated in Fig. 4.9 (e), while the out of phase can similarly be seen to collapse as a function of drive frequency in Fig. 4.9 (f). While there may be a compelling physical reason for this spurious signal, the possibility of a mixing of in-phase and out-of-phase to generate a spontaneous transverse signal is certainly not a signature of Berry curvature generated response as we first thought, and serves as a warning for future experiments.

CHAPTER 5

EXPERIMENTAL RESULTS AND INTERPRETATION

Now it is time for my actual results! These measurements were taken over the course of a year on the MX100 dilution refrigerator. The first set of normal metal samples were measured continuously from April 16th, 2022 until July 25th 2022 using only 79 L of helium, and will henceforth be referred to as the normal samples. The second set was measured from December 15th, 2022 until April 3rd, 2023, using 108 L of helium, and will henceforth be referred to as the superconducting (s.c.) samples. The pair of measurement runs accounted for a combined 728 data files measuring everything from magnetoresistance to non-local differential resistance to multiple harmonic response under ac current drive. Because of the breadth of the measurements, many of which were entirely exploratory, not everything will be discussed in this manuscript. Instead, the author would suggest future students look at the original data especially the peculiar results of non-local differential resistance discussed in Krantz and Chandrasekhar.[163]

This Chapter will discuss the nature of the two dimensional electron gas in these AlO_x / KTO samples, investigated through resistance measurements at low temperatures. The discussion will be generally divided into three parts: measurements on the normal states of the conducting gas, measurements on the superconducting state of the gas and its transition to the normal state, and second harmonic measurements to probe the quantum nonlinear Hall effect. As discussed previously, the primary tools for this characterization are electrical transport measurements taken as a function of temperature, back gate voltage, and applied magnetic field. Details of the experimental setup are included in Chapter 4, and the foundation of the analysis was covered in Chapter 3.

The results demonstrate the successful fabrication of metallic and superconducting two di-

mension gases at the KTO interface, with carrier concentrations and mobilities comparable or better than those referenced in the literature. There are a number of novel observations, including the observation of a Lifshitz transition tuned by back gate voltage, an upper gate voltage limit for superconductivity, the observation of magnetic order at the KTO surface and its coexistence with superconductivity, and an appreciable second harmonic response in a material that nominally should not show a quantum nonlinear Hall effect. A discussion of these results in contrast to the established literature is included, as are suggestions for future studies to build on this work.

5.1   The Normal State

The normal state of the conducting gas was accessible for both sets of samples and was probed with complete sets of magnetoresistance traces at several temperatures. Additionally, the temperature dependence of the resistance was recorded over a limited range based on the thermometry of the MX100 dilution refrigerator. To supplement this, room temperature two terminal measurements were taken as described in the experimental details of Chapter 4. From these measurements an estimation of the two-dimensional resistivity could be calculated using the geometric composition. The results are summarized in Table 5.1 below for the normal samples and in Table 5.2 for the s.c. samples.

Table 5.1: **Estimation of sheet resistance of the normal samples from two terminal measurements at room temperature.** Samples are labeled by crystal termination and Hall bar direction, and estimates of the sheet resistance of the Hall bar are compared to an average lead resistance.

Sample	Orientation	Sheet Res. ($\Omega/sq.$)	Lead Res. ($k\Omega$)
(001)	[001]	16130 ($\pm$ 420)	166.4
(110)	[001]	7660 ($\pm$ 210)	45.3
(110) (1)	[1$\bar{1}$0]	7780 ($\pm$ 270)	37.8
(110) (2)	[001]	8880 ($\pm$ 220)	47.3

The two sets of samples were initially thought to have one of each of the three primary crystal

termination, (001), (110), and (111), based on the manufacturer's information. They were ordered in sets, processed in sets, and treated based on the assumption that the crystal information provided at purchase was correct. It was not. Laue spectroscopy showed that the presumed (111) sample in the normal set was actually another (110) sample, and showed that the (110) sample in the superconducting set was actually aligned 45° to the edges of the sample, contrary to convention. These changes are reflected in the labeling in Tables A.1 and A.2, and are discussed in detail in Appendix A.

Table 5.2: **Estimation of sheet resistance from two terminal measurements at room temperature for the superconducting samples.** As before, samples are labeled by crystal termination and Hall bar direction, and estimates of the sheet resistance of the Hall bar are compared to an average lead resistance.

Sample	Orientation	Sheet Res. ($\Omega/sq.$)	Lead Res. ($k\Omega$)
(001)	[001]	3930 ($\pm$ 110)	25.3
(110)	[001]	4800 ($\pm$ 140)	26.1
(111) (1)	[$1\bar{1}0$]	7100 ($\pm$ 270)	47.2
(111) (2)	[$1\bar{1}2$]	6300 ($\pm$ 160)	33.0

The samples were cooled down directly to helium temperatures so no corroborating data point at nitrogen could be taken. Additionally, despite measuring the drop in resistance as a function of time as the MX100 cooled down, there is no thermometry for the sample stage above 6.5 K, so only low temperature $R(T)$ could be taken directly. From what data were available, both samples showed metallic-like temperature dependences, with lower resistance at lower temperatures. This trend is expected for the metallic gas in these samples and agrees with previous works.[18,67,139,154] Additionally, these samples showed a resistance minimum around 8 - 10 K that is common for these types of systems. Other works have interpreted this dip as a Kondo minimum,[71] but no definitive statement can be made about these samples due to the multitude of potential sources for such an effect, such as weak localization, electron - electron interactions..

(a) Normal Set (5 K)   (b) Superconducting Set (4 K)

Figure 5.1: **Back gate voltage annealing curves for longitudinal sheet resistance, measured at elevated temperature.** (a) Sheet resistance of normal samples measured as a function of back gate voltage from V_g = 30 V to 150 V. Data taken at 5 K. (b) Sheet resistance of the superconducting samples measured as a function of back gate voltage from V_g = -200 V to 200 V. Data taken at 4 K.

Both samples were initially cooled down to mK temperatures with the back gate grounded to qualify the measurement space and perform exploratory tests. After the initial cooldown both sets of samples were warmed up to higher temperatures for a back gate voltage anneal. The anneal trained the samples for measurement stability by repeatedly sweeping the back gate back and forth along the full operating range of V_g. These annealing curves can be seen in Fig. 5.1 (a) for the longitudinal resistance of the normal samples measured at 5 K and in Fig. 5.1 (b) for the s.c. samples measured at 4 K. These data were taken with no applied magnetic field. The shape of the annealing curves are typical of complex oxide samples, showing increased resistance with decreasing gate voltage. This is also an early indication of metallic, electron-like conducting behavior, as the positive backgate induces a negative potential in the Hall bar, increasing electron-like carrier density. There is also a clockwise sweep hysteresis arising from the same source as the magnetoresistance drift detailed in Chapter 4. It should be noted that the downturn in resistance for the (001) sample in Fig. 5.1 is not a superconducting transition, but is instead a breakdown of the

conductivity in the sample, resulting in a loss of voltage signal. This is identical to the downturn seen by Varada Bal in LSAT / STO samples[139] for similarly low values of V_g.

(a) Normal Samples (2.25 K)
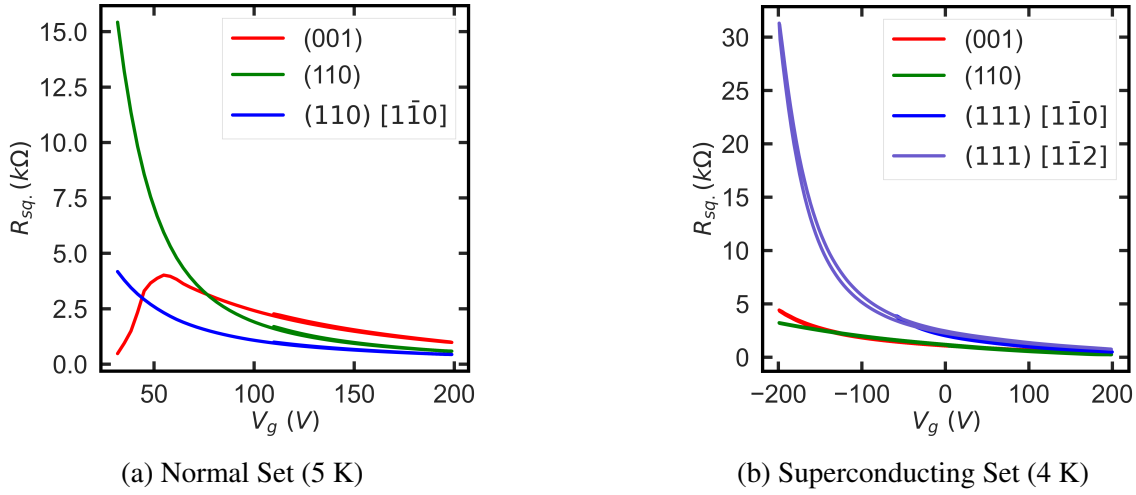
(b) Superconducting Samples (4 K)
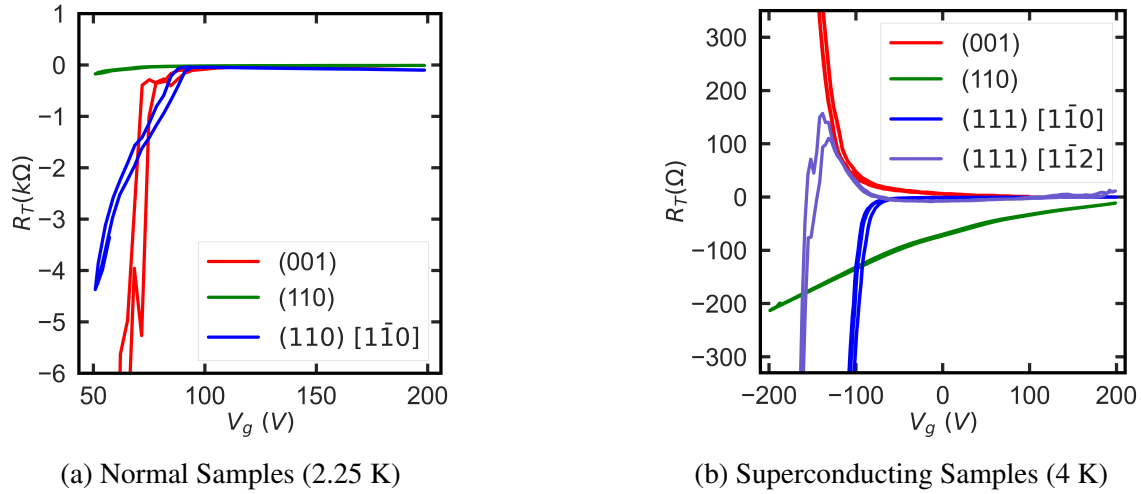
Figure 5.2: **Back gate voltage annealing curves for transverse resistance, measured at elevated temperature.** (a) Transverse resistance of normal samples measured as a function of back gate voltage from V_g = -50 V to 200 V, in zero applied magnetic field. Data taken at 2.25 K. (b) Transverse resistance of normal samples measured as a function of back gate voltage from V_g = -200 V to 200 V, in zero applied magnetic field. Data taken at 4 K. The sharp change in resistance at low values of V_g coincides with an increase in the out-of-phase of the longitudinal resistance.

From the longitudinal annealing curves it seems that the samples were behaving as expected, but the first unexpected result came when monitoring the transverse resistance during the same annealing process. Fig. 5.2 presents this result, showing a marked increase in the transverse signal at low values of gate voltage. Normally, in the absence of time reversal symmetry breaking processes like magnetic fields, there should be no transverse signal, or it should be very small. As discussed in Chapter 4 and in our previous works on a similar system,[30] there are sources of transverse voltage in the absence of external fields which could lead to a nonzero transverse signal. However, the signals presented in Fig. 5.2 did not seem to follow the expected behavior of these sources; they do not track with the longitudinal annealing curves, they are well above any

superconducting transitions or macroscopic magnetism, and they are crystal direction dependent. At first, we interpreted this as a sign of a spontaneous Hall effect related to the quantum nonlinear Hall effect,[164] but further testing proved that the effect instead arose from the out-of-phase component of the longitudinal resistance, generated by large sample capacitance and large, imbalanced lead resistance. A detailed discussion of this effect and its influence on the 2ω measurements of the quantum nonlinear Hall effect are being written up for publication.
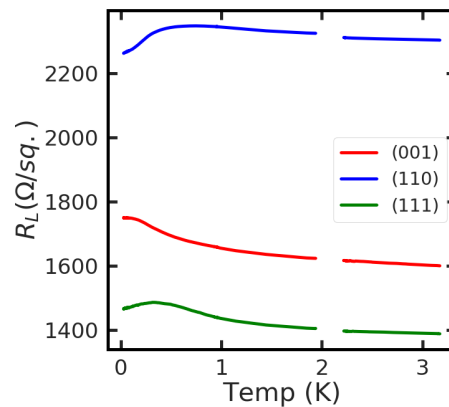
Figure 5.3: **Temperature dependent resistance of normal samples, 6 K to 25 mK.** Temperature dependence of the three normal samples taken in two data sets during cooldown to mK temperatures. $V_g = 0$ V.

After annealing, the samples were cooled down to millikelvin temperatures, yielding longitudinal $R_L(T)$ traces of the normal metal samples shown in Fig. 5.3. The conducting properties of metallic complex oxide samples are unlikely to change significantly with temperature below roughly 4 K.[15] There are exceptions to this, as is the case for metal-to-insulator transition tuned by backgate,[16] but the expectation is that un-gated samples do not change resistance by more than a few percent at low temperatures. This is the case in these samples, and as a result the carrier concentration and mobility do not change significantly in the measurement range.

To summarize the initial normal state measurements, the samples showed expected conducting behavior, with the exception of the transverse traces which could be explained as an artifact of the

measurement design. The behavior of the gas as a function of gate voltage and temperature was consistent with expectation for these types of samples. Further qualification of the conducting gas required the application of a magnetic field to measure longitudinal magnetoresistance and Hall effect. These results are the subject of the next section.

5.1.1 *Magnetoresistance in the Normal State*

A full characterization of the longitudinal magnetoresistance (MR) for both sets of samples was taken for the range of gate voltages. The data showed features expected of complex oxide samples, and several figures are included in Appendix B. Instead of the longitudinal MR, this section will focus on the results from the transverse magnetoresistance, and the novel results shown for the carrier characteristics in the normal state. These novelties include improved carrier concentration and mobilities compared to literature, the observation of several Lifshitz transitions evident in carrier concentration kinks, and the observation of macroscopic magnetic order in the samples. Each of these effects can be derived from Hall effect measurements, the transverse voltage generated from a driving current in perpendicular magnetic field.

These Hall traces allowed for an estimation of the carrier concentration and carrier mobility as discussed in Chapter 3. The traces for the normal sample set are shown in Appendix B, but traces for the s.c. samples can be seen in Fig. 5.4. The zero field offsets values for the traces have been removed, and each trace uniformly shifted for clarity. For large positive values of V_g this is a minimal shift, as shown by the annealing curves in Fig. 5.2. Indeed, for large positive values of V_g the Hall is well behaved, reflecting the expected dependence for a single band, electron-like conductor. In contrast, for low values of V_g there is a pronounced curvature of the Hall traces, arising from symmetric components in the Hall. This is especially prominent for the (001) sample and the (111) sample, $[1\bar{1}0]$ direction, shown in Fig. 5.4 (a) and (b), respectively.

(a) (001) Sample (4 K)

(b) (110) Sample (4 K)

(c) (111) Sample, [1$\bar{1}$0] dir. (4 K)

(d) (111) Sample, [1$\bar{1}$2] dir. (4 K)
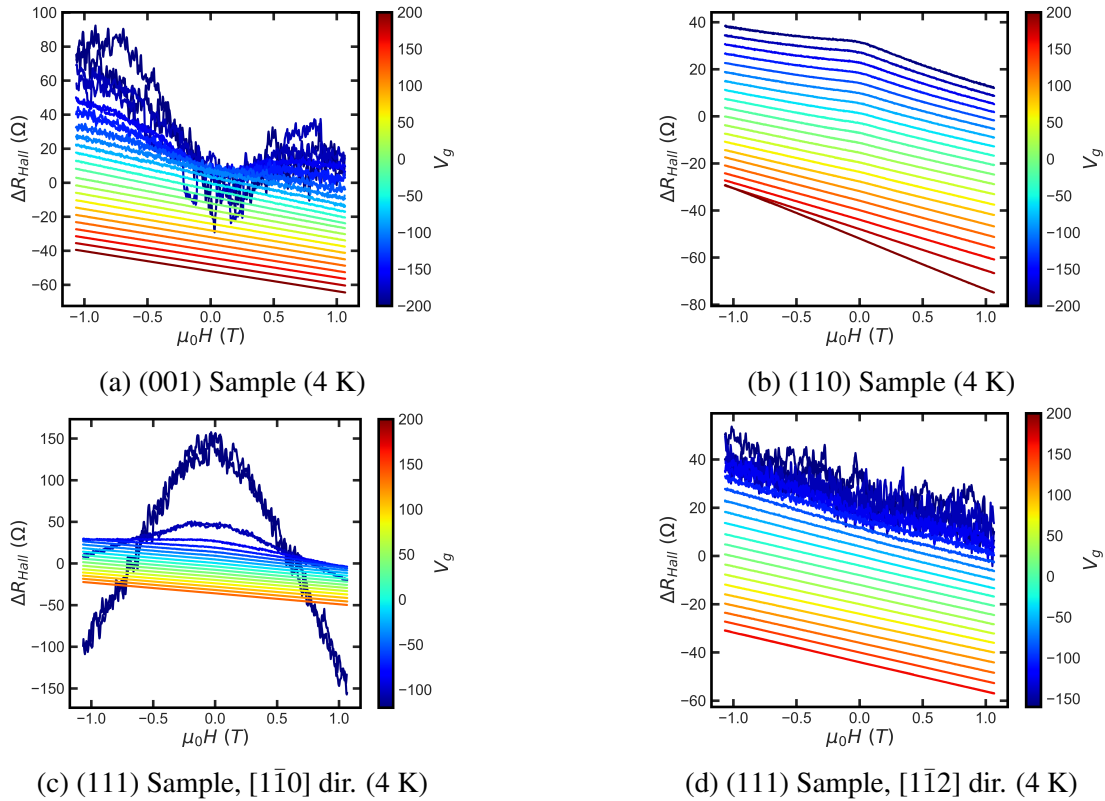
Figure 5.4: **Gate voltage dependence of transverse magnetoresistance for superconducting samples at 4 K.** (a) - (d) Transverse magnetoresistance traces of the (001), (110), (111) [1$\bar{1}$0], and (111) [1$\bar{1}$2] samples respectively. The curves have been incrementally shifted for clarity. Unconventional contributions to the Hall signal are apparent for lower values of V_g.

If these curves are decomposed into their symmetric (even in field) and antisymmetric (odd in field) contributions the gate voltage dependences become more apparent. This can be accomplished with simple algebra, $R_T^{even} = \frac{1}{2}(R_{Hall}(-H) + R_{Hall}(H))$ and $R_T^{odd} = \frac{1}{2}(R_{Hall}(H) - R_{Hall}(-H))$, and is shown for the (110) sc sample in Fig. 5.5. Fig. 5.5 (a) reproduces the combined curves, now without the incremental shifts shown in Fig. 5.4 (b), which are broken into the antisymmetric contribution shown in Fig. 5.5 (b), and the symmetric contribution in Fig. 5.5 (c). The antisymmetric component is just the classical Hall effect, and reflects the carrier concentration as described in Eq. 3.31, but the symmetric contribution is something different, which will be addressed later.

(a) Combined transverse signal

(b) Antisymmetric part (Hall Effect)

(c) Symmetric part
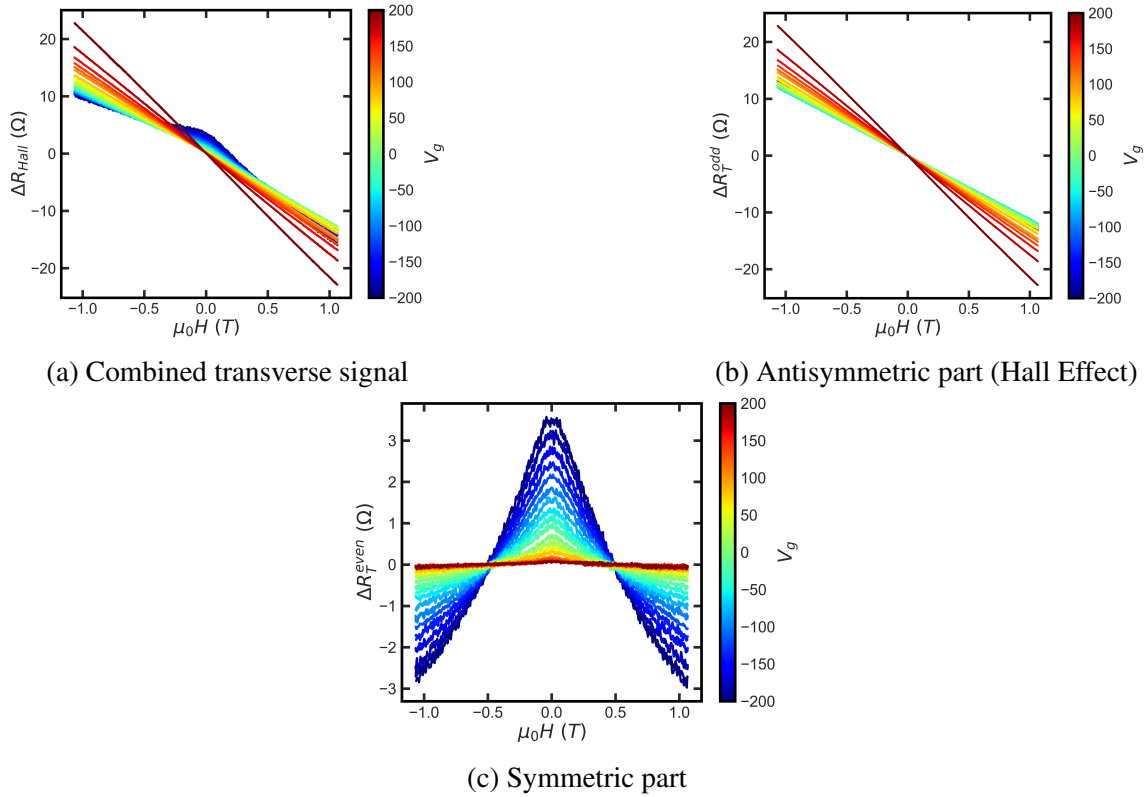
Figure 5.5: **Example of symmetric and antisymmetric decomposition for the superconducting (110) sample.** (a) Shifted but not yet decomposed Hall data showing modulation of the Hall slope with gate voltage. (b) Antisymmetric contribution to the transverse resistance, the classical Hall effect, from which carrier concentration is calculated. (c) Remaining symmetric contribution to the transverse resistance.

The antisymmetric contributions for all of the samples show negative slope with applied field, indicating that the conducting gas is electron-like. Additionally, there are no indications on the field range of multi-carrier transport which had been reported previously in the more complicated Hall traces in STO samples.[81] Instead, the antisymmetric contributions were largely well behaved and suggested a single conducting band. Higher field tests may shed light on a more complicated conducting character, in particular if there is compensated transport or dramatically different carrier mobilities, as has been predicted.[32] In lieu of this, both sets of samples were fit to a single band

form described in Eq. 3.30. The results of this fitting are collected in Fig. 5.6.

(a) Normal Set (5 K)

(b) Superconducting Set (4 K)

Figure 5.6: **Gate voltage dependence of carrier concentration at elevated temperatures.** (a) Carrier concentration for each of the normal samples, showing monotonic increase of carriers with increasing back gate voltage V_g. Data were taken at 5 K. (b) Carrier concentration for each of the superconducting samples showing significantly higher carrier concentrations and more structure as a function of V_g. Peaks in carrier concentration indicate Lifshitz transitions tuned by V_g. Data taken at 4 K.

The normal samples shown in Fig. 5.6 (a) are well behaved. Each of the three samples increase carrier concentration with increasing V_g, as is expected for these samples and for metallic 2DEGs. The concentrations are comparable to those seen in literature for similar samples, with a range of 4×10^{13} (e$^-$ cm^{-2}) to 9×10^{13} (e$^-$ cm^{-2}). The highest concentration was seen in the (001) sample, with similar carrier concentrations seen in both of the (110) samples. For these analyses the (110) sample, [001] direction will just be referred to as the (110) sample while the (110) sample, [1$\bar{1}$0] direction will be referred to by its direction.

There are surprises in the data for the superconducting set. Signatures of at least one, possibly two Lifshitz transitions[165] for each of the s.c. samples shown in Fig. 5.6 (b). Lifshitz transitions are changes in the topology of the Fermi surface with some external parameter like pressure or applied gate voltage. These transitions show up as kinks in the carrier concentration, and correspond to

a changes in conduction band character that can be tuned with V_g. Here the peaks in the carrier concentration are found at V_g = -120 V for the (110) sample, and at V_g = 100 V and V_g = 120 V for the [1$\bar{1}$0] and [1$\bar{1}$2] directions of the (111) sample, respectively. Other features can be seen at V_g = 0 V in the [1$\bar{1}$2] directions of the (111) sample, and at V_g = -160 V and V_g = 180 V in the (001) sample but these are not as clear. The transitions for the (110) and (111) Hall bars are undeniable, corresponding to maximum carrier concentrations for both samples. This is the first time such a transition has been observed in a KTO system, though previous works have demonstrated Lifshitz transitions in STO systems.[139] Comparing the kinks in the carrier concentration to measurements of higher field MR could provide insight into the particular nature of the conducting bands, as was done by Varada Bal[139] on (111) LSAT / STO. The transition in the sc samples also means that the carrier concentration does not increase linearly with applied gate voltage as was the case for other works on KTO,[18,66] and will have consequences for the nature of the superconductivity observed in these samples.
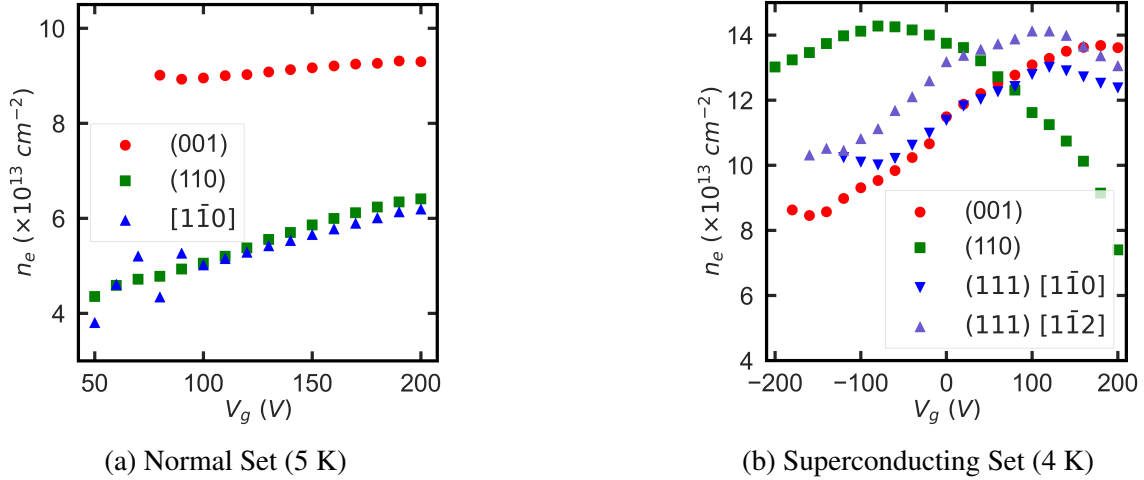

(a) Normal Set (5 K)

(b) Superconducting Set (4 K)
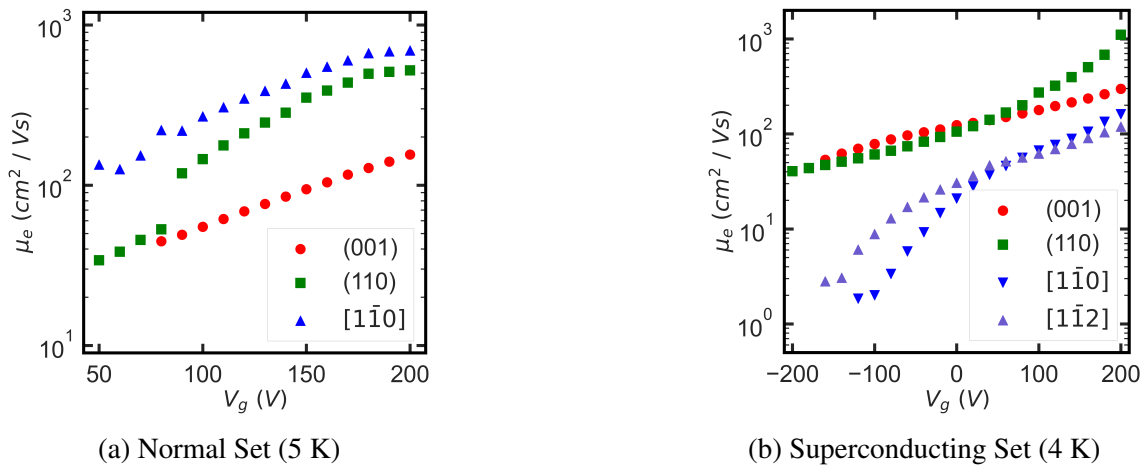
Figure 5.7: **Gate voltage dependence of carrier mobility at elevated temperatures.** (a) Carrier mobility for each of the normal samples showing monotonic increase with gate voltage V_g, to a maximum of $\sim$ 700 (cm^2/ V s). Mobilities are plotted on a log scale to show clearer dependence. (b) Carrier mobility for each of the superconducting samples showing monotonic increases from a few (cm^2/ V s) to over 1000 (cm^2/ V s) for the (110) sample.

Carrier mobility was also calculated for the samples from the carrier concentrations and the annealing curves presented in Fig. 5.7. By definition $\sigma_{xx} = ne\mu_e$ and for two dimensional systems $\sigma_{xx} = R_{sq.}^{-1}$, so $\mu_e = 1/(R_{sq}ne)$. The result of this conversion can be seen in Fig. 5.7, and shows monotonic increases in mobility with increasing V_g with the highest mobility seen in the (110) sample, [110] direction. In the normal samples the carrier mobilities are comparable those seen in literature,[16,18,48] or slightly better. This could simply be due to lack of strain at the interface because the AlO_x is amorphous. The superconducting samples show mobilities that are higher than those reported in the literature,[16,18,48] with maximum mobility of 1108 cm^2 V$^{-1}s^{-1}$ on the (110) sample. While this represents a significant improvement for KTO samples, it does not compete with some of the high mobilities reported in STO systems.[42] Interestingly, the measured mobility does not appear to vary significantly through the Lifshitz transitions observed in carrier concentration.

(a) Normal Set (5 K) (b) Superconducting Set (4 K)
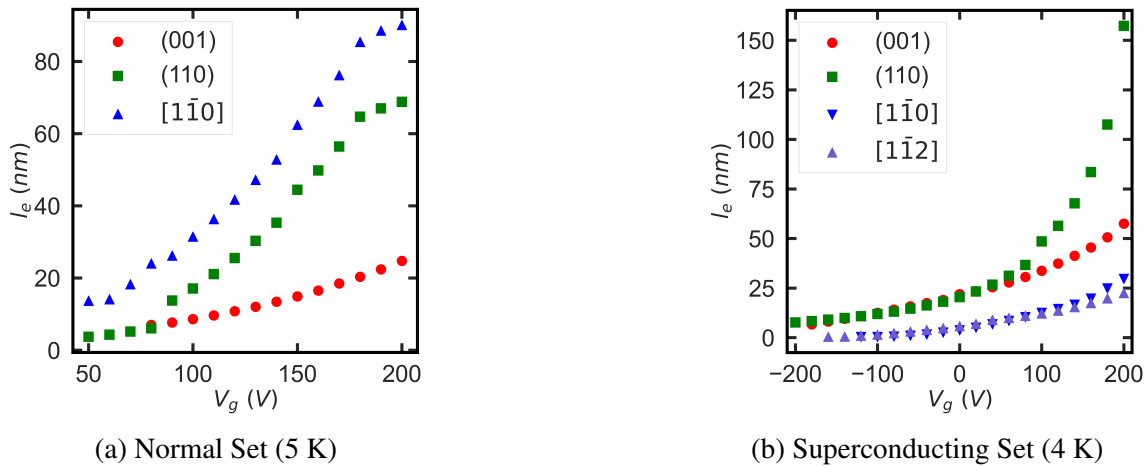
Figure 5.8: **Gate voltage dependence of electron mean free path.** (a) Mean free path, l_e, for each of the normal samples showing monotonic increase with gate voltage V_g. (b) Mean free path for each of the superconducting samples showing similar monotonic increases, with the (110) sample boasting the largest l_e.

These simple analyses can be extended to other observable carrier properties. If we make the simplifying assumption that the Fermi surface for KTO is well behaved and not strongly interact-

ing, then the carrier density can give an estimate of the Fermi energy for two dimensions from the relation $E_F = \frac{\hbar^2}{m_0} \left(\frac{\pi N}{A}\right)$ for $n = N/A$, our normal carrier concentration, and m_0, the rest mass of the carrier. This can then be related to the Fermi velocity by $v_F = \sqrt{\frac{2E_F}{m_0}}$ and the Fermi wavevector as $k_F = \frac{v_F m_0}{\hbar}$. For these samples, which have carrier concentrations of 3.9×10^{13} to 9.3×10^{13} (e^- cm^{-2}) for the normal set and 7.4×10^{13} to 14.1×10^{13} (e^- cm^{-2}) for the s.c. set, we get Fermi wavevectors of 160 to 240 Å^{-1} and 230 to 300 Å^{-1}, respectively. The values of k_F can then be used to estimate the electron mean free path l_e from the relation $l_e = \frac{\hbar k_F}{ne^2 \rho}$, where $n = N/A$ as before, and the resistivity ρ is simply $R_{sq.}$ in two dimensions. The results of this calculation are shown in Fig. 5.8 revealing long mean free paths for high values of V_g. This result reflects the nature of the electron mobilities shown in Fig. 5.7, as expected. The values of k_F can also be used to estimate the effective dimension of the normal conducting layer as via $L = \frac{2\pi}{k_F}$ which gives $L =$ 0.2 to 0.4 nm. These effective lengths are much less than the thickness $d = 8$ nm from literature[16], which indicates that in the normal state the gas is not strictly two dimensional. The takeaway is that the conducting interface is clean and relatively free of scattering for high values of V_g. Tuning V_g down to negative gate voltages causes a large increase in resistance that is primarily driven by scattering effects, as reflected in the values of μ_e and l_e.

What remains to be discussed is the strange symmetric contribution to the Hall traces. Following the procedure outlined in the discussion of Fig. 5.5, the symmetric decomposition for the normal state samples are presented in Fig. 5.9. What appears is a gate tunable symmetric dependence for each of the three samples, though with modest contributions for the (001) and (110), [1$\bar{1}$0] dir. samples of only a few ohms at the maximum, for the smallest values of V_g. This is significantly less than the magnitude of the normal Hall (odd) contribution, and could potentially be explained by an errant contribution to the transverse resistance discussed at the end of Chapter 4. However, the [1$\bar{1}$0] direction of the (110) sample has a symmetric component of similar

(a) (001) Sample (5 K)

(b) (110) Sample, [001] dir. (5 K)

(c) (110) Sample, [1$\bar{1}$0] dir. (5 K)
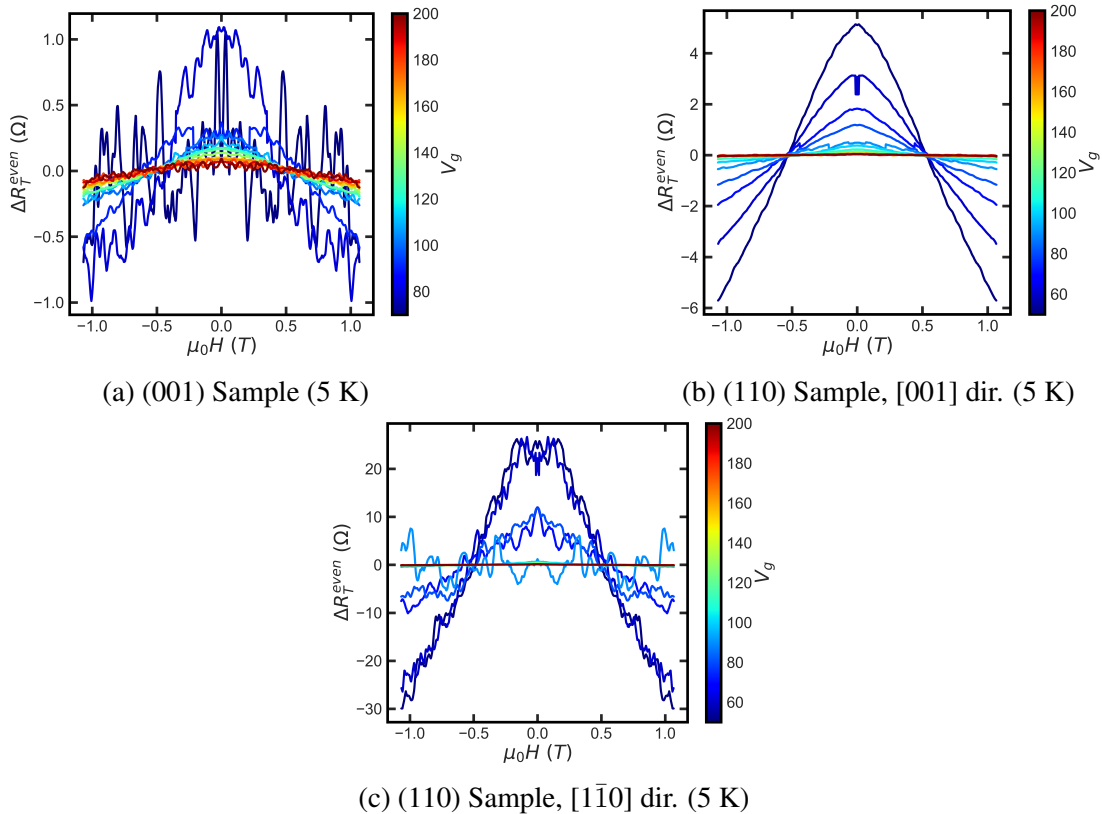
Figure 5.9: **Symmetric contribution of R_T for normal samples at 5 K.** (a) - (c) Symmetric contributions to transverse magnetoresistance for the (001), (110), and (110) [1$\bar{1}$0] samples respectively. The curves have been shifted for clarity. Gate voltage only has a small effect on the magnitude of the signal, with the maximum effect seen at the lowest values of V_g.

magnitude to the normal Hall, and it changes inflection with changes in gate voltage. This was initially interpreted as a spontaneous Hall effect,[164] but we know understand is a consequence of the large, imbalanced complex impedance of the sample leads. It arises from the same source as the transverse annealing curve downturn shown in Fig. 5.2 for low values of V_g.

A similar result can be see in the traces for the s.c. samples which are shown in Fig. 5.10. These data show very large symmetric contributions, particularly in the (001) sample and the (111) sample, [1$\bar{1}$0] direction shown in Fig. 5.10 (a) and (c) respectively, where the magnitude of the effect is much larger than the normal Hall contribution for the same samples. The (110) sample,

(a) (001) Sample (4 K)

(b) (110) Sample (4 K)

(c) (111) Sample, [1$\bar{1}$0] dir. (4 K)

(d) (111) Sample, [1$\bar{1}$2] dir. (4 K)
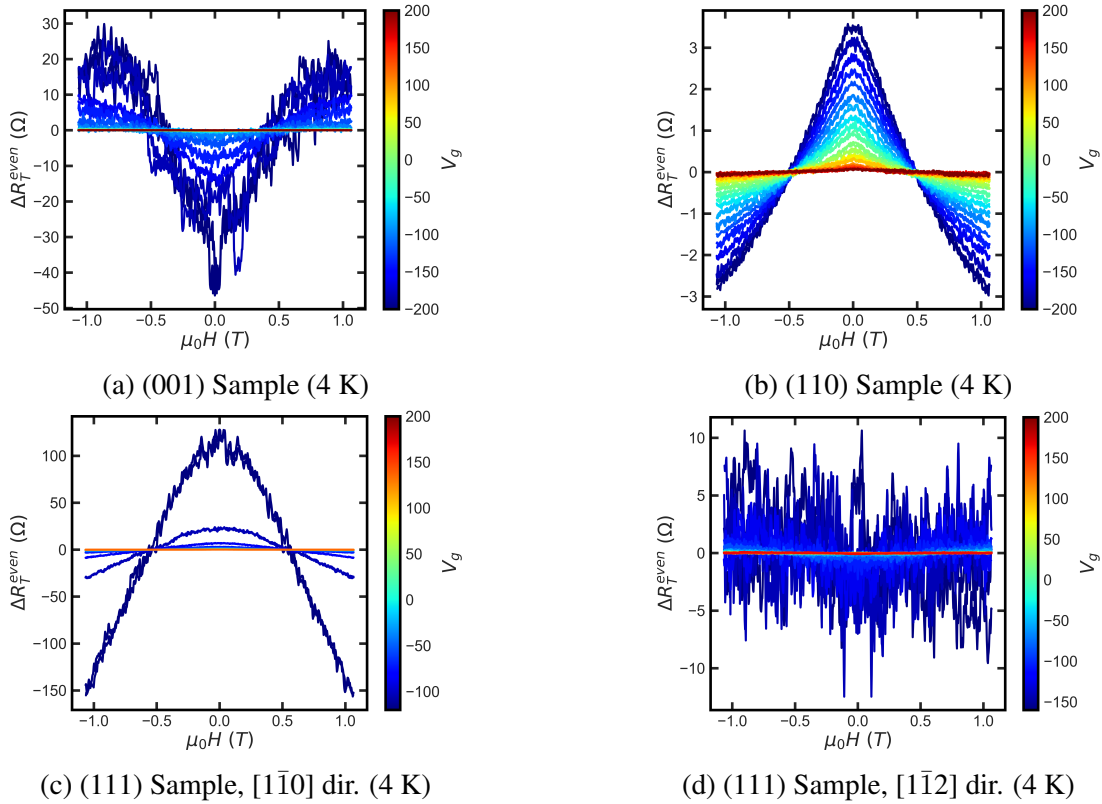
Figure 5.10: **Symmetric contribution of R_T for superconducting samples at 4 K.** (a) - (d) Symmetric component of the transverse magnetoresistance traces of the (001) sample, the (110) sample, the (111) sample [1$\bar{1}$0] direction, and the (111) sample [1$\bar{1}$2] direction, respectively. The curves have been shifted for clarity. The magnitude of the symmetric contribution increases sharply for the lowest values of V_g.

which was featured in Fig. 5.5, shows a well tuned but small symmetric contribution, while the (111) sample, [1$\bar{1}$2] direction in Fig. 5.10 (d) has almost no symmetric signal above noise levels. Interestingly, the sign of the symmetric contributions changes between samples. While most samples show a "positive" peak in shifted Hall response, the (001) shows a negative peak with hints of saturation or downturn. While these data can still be explained as the consequence of differences in the lead resistance as before, it may be useful to conduct higher field tests on these samples to allow for a more quantitative dis-entangling of the longitudinal and transverse signals. Particular

attention should be paid to the out-of-phase signal of the longitudinal, and if the effect can be saturated at high fields

In summary, the carrier density and mobilities for the 2DEGs on all samples are comparable to similar samples reported in the literature. Some of the densities and mobilities are better than those reported in literature, especially for the s.c. samples, indicating that the interface is clean. Furthermore, calculations of carrier mobility and mean free path indicate that scattering is the primary contribution to the resistance increase at low gate voltages. There are some strange results, like the insensitivity of the (001) to gate voltage tuning, and the emergence of the symmetric Hall contributions. Both of these oddities may be addressed by improved fabrication techniques, as suggested in Chapter 4, and all measurements should be extended to higher fields, should the opportunity allow. It would also be interesting to perform corroborating transport techniques on these samples, like high field tests to look for Shubnikov-de Haas oscillations which can yield independent estimations of carrier density and mobility. Even just extending magnetoresistance traces to higher fields would allow for fits to look for multi-carrier transport that could potentially shed light on the strange gate voltage dependence of the superconducting state, which will be discussed later.

5.1.2   *Magnetism*

The next major finding in the KTO samples was the observation of macroscopic magnetic order at lower temperatures. This magnetism was seen in hysteretic peaks in the longitudinal magnetoresistance (MR) at mK temperatures, and in an anomalous Hall-like signal in zero field. As discussed in Chapter 3, density functional theory results suggest that the oxygen vacancies that host the conducting gas generate local magnetic moments which can order at low temperatures. This magnetic order was also seen in the s.c. samples, even up to 4 K, but the discussion here will

start with the findings of the normal samples.

(a) (001) Sample (30 mK)

(b) (110) Sample, [001] dir. (30 mK)

(c) (110) Sample, [1$\bar{1}$0] dir. (30 mK)

Figure 5.11: **Gate voltage dependence of longitudinal magnetoresistance for the normal samples at 30 mK.** (a) - (c) Magnetoresistance traces of the (001), (110), and (110) [1$\bar{1}$0] samples respectively. The curves have been incrementally shifted for clarity. Gate voltage only has a small effect on the shape of the low field dip, and minimal tuning of the spin orbit interactions shown the slope of the curves in high field.

Fig. 5.11 shows the hysteresis in longitudinal MR measured at $\approx$ 30 mK. All three samples show unique versions of hysteretic dips at low fields, superimposed on the large low field valley. The magnitude of the MR is dominated by this low field dip, and as a result is quite large in these samples, with the (110) [001] dir. sample reaching nearly 20 % MR for the lowest values of V_g. The MR of the (001) sample was significantly reduced compared to the (110) sample, [001] dir.,

with only 3 % MR at the lowest gate values, thought the hysteretic peaks are prominently displayed on this background. The (110), [1$\bar{1}$0] sample also has lower MR compared to the (110) [001] dir., and features both enhanced noise at the lowest values of V_g, and multiple features in the hysteretic dips.

(a) (001) Sample (30 mK)

(b) (110) Sample, [001] dir. (30 mK)

(c) (110) Sample, [1$\bar{1}$0] dir. (30 mK)
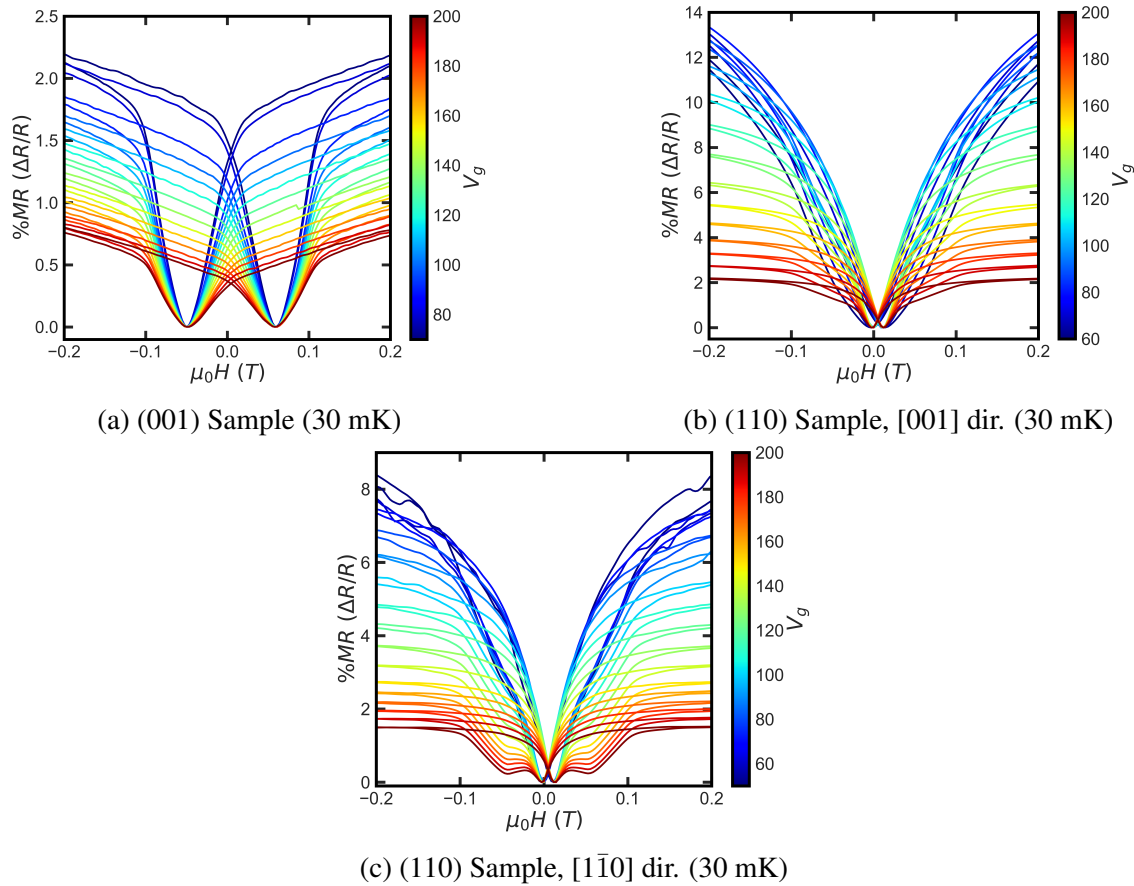
Figure 5.12: **Gate voltage dependence of longitudinal magnetoresistance of the normal samples for small applied magnetic field.** (a) - (c) Magnetoresistance traces of the (001), (110), and (110) [1$\bar{1}$0] samples respectively. The curves have been incrementally shifted for clarity. Gate voltage only has a small effect on the shape of the low field dip, and minimal tuning of the spin orbit interactions shown the slope of the curves in high field.

These features are more obvious in Fig. 5.12, which shows the small field values for each of the data sets presented in Fig. 5.11. Here, the tuning of the hysteresis with gate voltage is apparent,

with broadening in the (001) as V_g is increased contrasting the emergence of prominent features with increasing gate voltage in the [1$\bar{1}$0]. These results strongly suggest a complicated magnetic texture, or at least an effective distribution of sizes of magnetic patches that result in the features seen in the [1$\bar{1}$0]. This is not surprising, as the film is expected to be disordered, which would naturally result in variations in magnetic regions tied to the density of oxygen vacancies.

(a) (001) Sample (30 mK)

(b) (110) Sample, [001] dir. (30 mK)

(c) (110) Sample, [1$\bar{1}$0] dir. (30 mK)
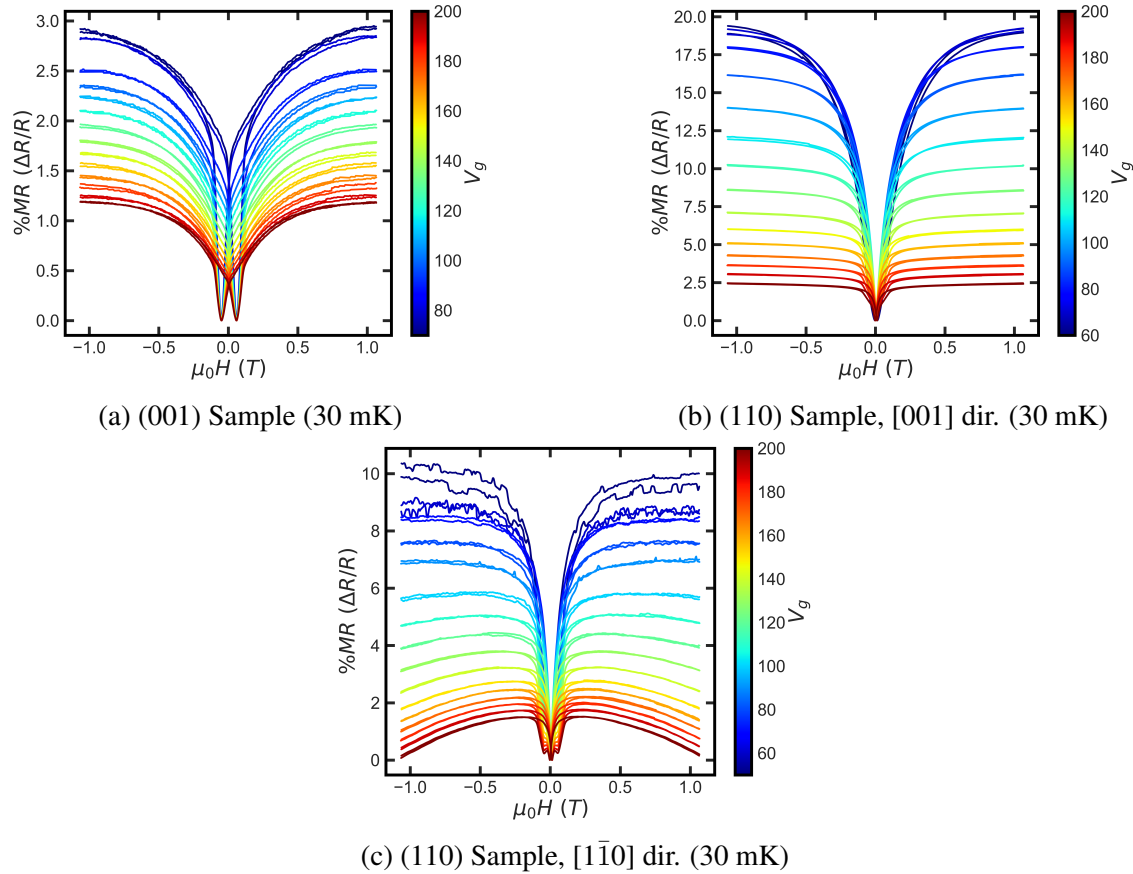
(d) 200 V trace from [1$\bar{1}$0] dir.
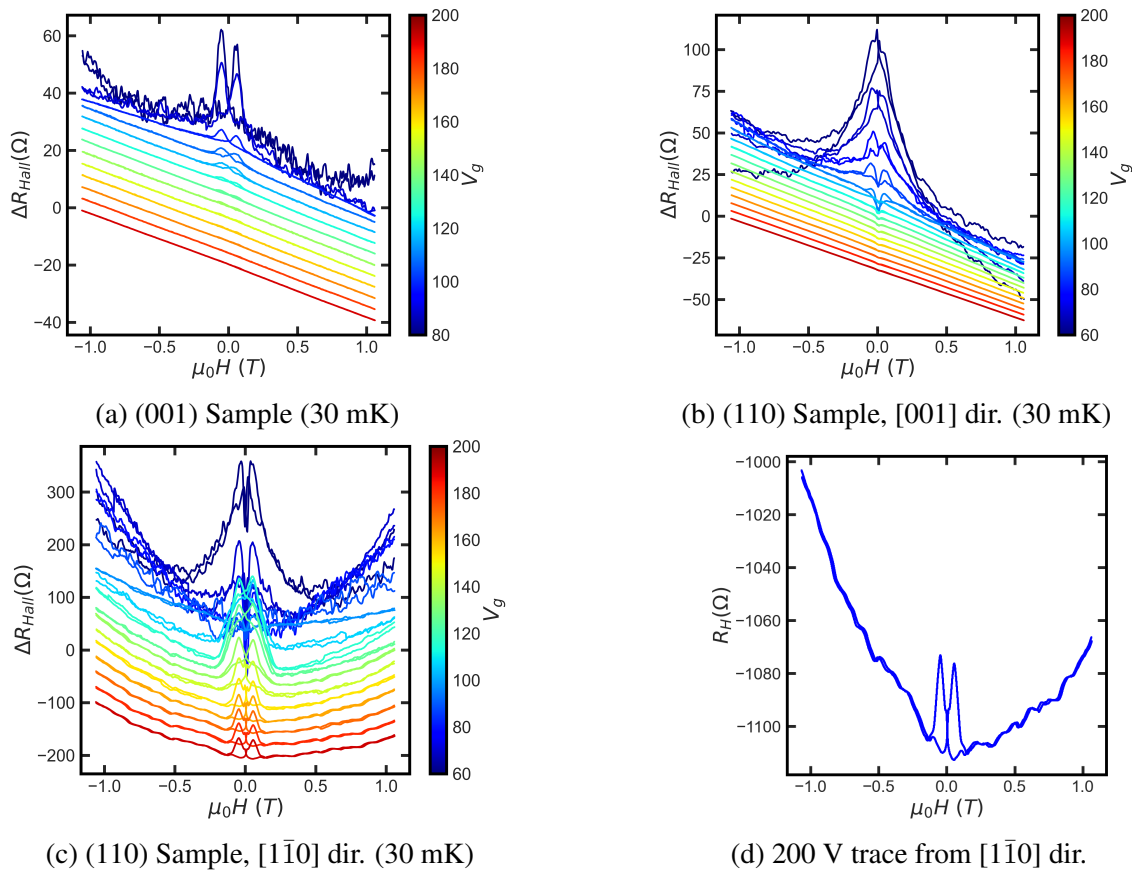
Figure 5.13: **Gate voltage dependence of transverse magnetoresistance for the normal samples at 30 mK.** (a) - (c) Magnetoresistance traces of the (001), (110), and (110) [1$\bar{1}$0] samples respectively. (d) Isolated trace of the V_g = 200 V data showing background structure. Data show prominent hysteresis that is strongest at low values of V_g.

Looking now at the transverse MR shown in Fig. 5.13, the tuning of the hysteresis becomes more apparent. The magnitude of the hysteretic peaks is increased dramatically for the (001) and

(110) samples with decreasing values of V_g. It is important to note that these data are uniformly shifted from their zero field values, but their zero field offset is negative for all reported data. Thus, the peaks shown in these figures are actually *dips* in the magnitude of the resistance, similar to those seen in the longitudinal MR traces. At the highest values of V_g the Hall looks normal, with slopes that agree well with those measured at higher temperatures indicating again that the carrier concentration does not change substantially below 4 K.[15]

The $[1\bar{1}0]$ is more complicated, showing the same tuning of the low field hysteretic peaks but superimposed on a textured background. The gate voltage dependence of the low field hysteretic peaks is not trivial, and at no value of V_g does the Hall resemble the simple line expected from a normal conductor. The background structure is shown more clearly in Fig. 5.13 (d), which is a single trace of the $V_g = 200$ V for the $[1\bar{1}0]$. The background oscillations are somewhat of a mystery. They are too low in field to be Shubnikov – de Haas oscillations based on previous works on STO,[166] and the Hall bar is too long to be detecting spin precessions due to the Hanle effect.[92] The oscillations may reflect the spin texture of the $[1\bar{1}0]$ direction somehow, but the origin is unknown at this time.

The temperature dependence of this strange $[1\bar{1}0]$ sample is shown in Fig. 5.14 (a). The background texture is suppressed above ≈ 800 mK but the hysteretic peaks persist up to ≈ 1.7 K in the transverse MR. As a point of comparison, Fig. 5.15 shows that the hysteresis is present in the longitudinal MR of the (111) s.c. samples at least up to 4 K. The signatures in the transverse MR of the normal samples is only up to half of that temperature. This discrepancy may be due to the difference in density of magnetic moments, which should be tied to the density of oxygen vacancies and by extension the carrier concentration, and the relative strength of the local moments on the different crystal surfaces. The superconducting samples had nearly twice the carrier concentration of their normal metal counterparts, and the expected magnitude of the magnetic moment generated

(a) (110) Sample [1$\bar{1}$0] dir.
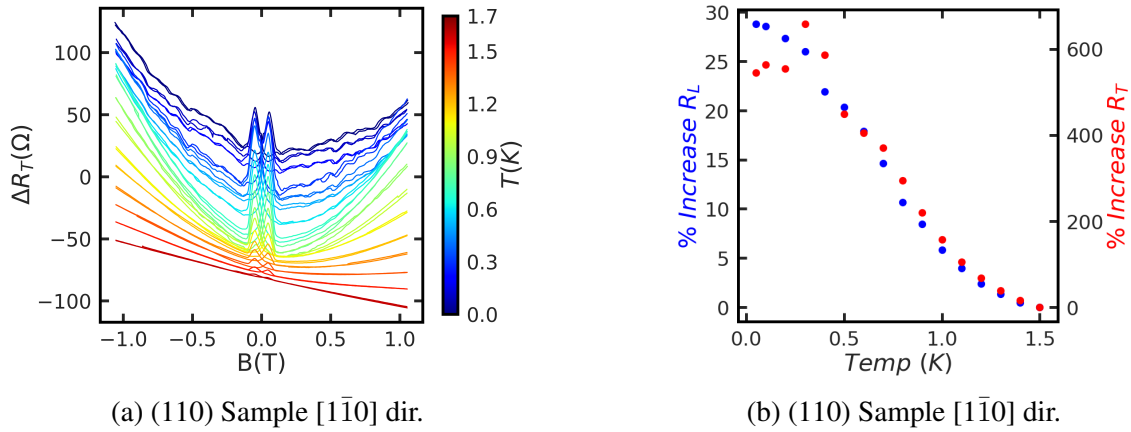
(b) (110) Sample [1$\bar{1}$0] dir.

Figure 5.14: **Temperature dependence of hysteretic peaks.** (a) Temperature dependence of the transverse magnetoresistance for the (110) sample, [1$\bar{1}$0] direction. The curves have been shifted for clarity, and reflect the return to normal Hall effect above 1.7 K. (b) Magnitude of the zero field offset of the transverse magnetoresistance compared to the increase in resistance in longitudinal zero field value.

by an oxygen vacancy is largest for the (111) surface. It could also be due to changes in the exchange interactions on the (111) surface, though it is difficult to tell from the experimental data.

The shape of the transverse signal and prominence of the hysteretic peaks are not the only indications of magnetic order. The shift that was removed from each of the curves shown in Fig. 5.14 (a) also scales with temperature. This zero field offset of the transverse is shown in Fig. 5.14 (b), and matches well with the additional change in resistance seen in the longitudinal zero field values. The scaling of the offset agrees qualitatively with a skew scattering process, one of the extrinsic sources of the anomalous Hall effect. There are problems with this explanation though, namely that the offset does not switch sign with field sweep direction as one would expect for an anomalous Hall signal, and the magnitude of the effect is too large for normal skew scattering processes.[148] The correlation remains intriguing, but the offset is likely not skew scattering.

From DFT calculations we can estimate the magnitude of the local moments generated from oxgyen vacancy formation as 0.56 Bohr magnetons for the (001) surface and 6.67 Bohr magnetons

for the (111). Calculated magnetic moment is not available for the (110) surface, but we can estimate that the magnitude for the (110) to be somewhere closer to the (001) due to band similarities, so we will use 2.0 Bohr magnetons for the purpose of comparison. Combining this local magnetic moment strength with the highest observed temperature of hysteresis can give an estimation of the magnetic exchange interaction via $k_b T_{Curie} \simeq E_{EX} = -\Sigma_{ij} J_{ex}(S_i \cdot S_j)$. Here T_{Curie} is the Curie temperature, E_{EX} is the exchange energy, J_{ex} is the so-called exchange integral and S_i are reduced moments.

(a) (110) Sample [1$\bar{1}$0] dir.   (b) (110) Sample [1$\bar{1}$0] dir.
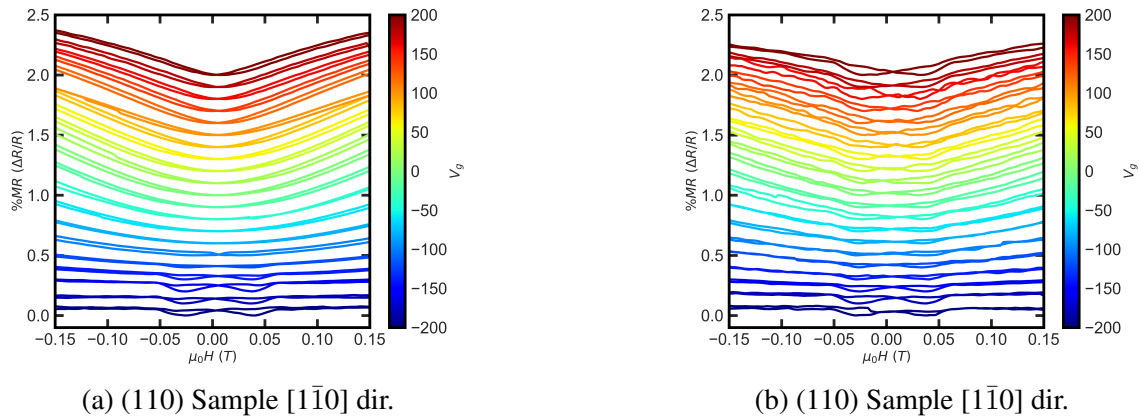
Figure 5.15: **Small field hysteresis in the longitudinal magnetoresistance of the (111) s.c. samples at 4 K.** (a) Longitudinal magnetoresistance of the (111) sample, [1$\bar{1}$0] direction showing hysteretic dips at low field. Traces have been uniformly shifted for clarity. (b) Longitudinal magnetoresistance of the (111) sample, [1$\bar{1}$2] direction showing hysteresis over the full gate voltage range.

In these samples, the Curie temperature can be estimated from the maximum temperature of observed hysteresis, though this is a rough estimation. To do this we look to the data taken at the same time as those presented in Fig. 5.14 for the (001) sample showed that the hysteresis was suppressed in the transverse by 1 K, and the data from the longitudinal of the (111) superconducting samples showed hysteresis up to 4 K. If we take those temperatures to be an estimation of the T_{Curie}, this gives a total exchange energy of 1.38×10^{-23} J, 2.48×10^{-23} J, and 5.66×10^{-23} J for the

(001), (110), and (111) samples, respectively. Reducing this by the relative magnitudes of the moments gives values of 4.4×10^{-23} T^2/J, 6.4×10^{-24} T^2/J, and 1.3×10^{-24} T^2/J, which shows no consistent trend. This could be due to other influences on the exchange energy, such as moment density or screening effects. Unfortunately, there was not enough experimental data to determine if the magnetism was itinerant or not, as only Curie temperature per crystal termination and relative density were obtained between the two data sets.

(a) (001) Normal Sample (30 mK)

(b) (001) Normal Sample, 30 mK, V_g = 80V
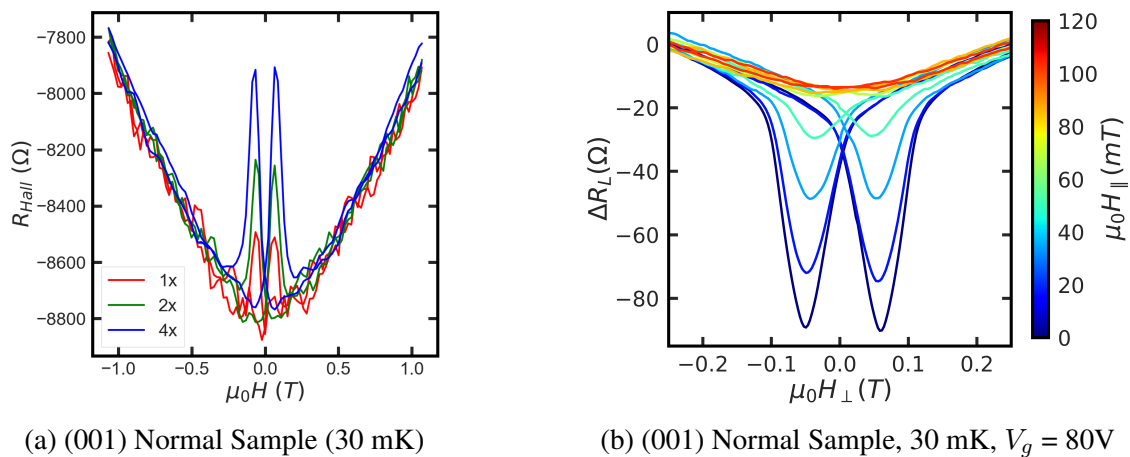
Figure 5.16: **Magnetic field sweep rate dependence of hysteretic peaks, and parallel field suppression.** (a) Magnetic field sweep rate dependence of the peaks in the transverse magnetoresistance on the (111), [1$\bar{1}$0] direction, showing increased peak height with increased sweep rate. (b) Peak suppression in longitudinal magnetoresistance with applied parallel magnetic field, $\mu_0 H_{\parallel}$. Figure (b) were adapted from Krantz *et al.*[164]

A more detailed investigation of the field dependence of the hysteretic peaks is shown in Fig. 5.16. Varying the sweep rate of the magnetic field, as shown in Fig. 5.16 (a), reveals an increase in the peak height and total size with increasing sweep rate, reminiscent of the results reported in superconducting samples in Manan Mehta's thesis.[133] The peaks are definitely of magnetic origin though, and can be suppressed with the application of a parallel magnetic field, as shown in Fig. 5.16 (b) for the (001) sample longitudinal MR traces. They also have a very weak dependence on gate voltage, showing small increases in coercive field with increasing V_g, roughly correlating to

carrier mobility.

Further investigation of parallel field MR reveals complicated behavior, as shown in Fig. 5.17 for transverse traces. There is a small planar Hall effect for all three samples, though it is difficult to know if this is simply a result of misalignment with respect to the parallel field, or some intrinsic effect. Planar Hall effects have been reported in EuO / KTO systems before,[19] though the magnetism in those systems is primarily in the EuO layer, which is an in plane ferromagnetic below 70 K. Superimposed on this planar Hall background are hysteretic peaks, at different field values and with different structure than those seen in perpendicular MR. This result suggests that some part of the magnetic moment is in plane, agreeing with the calculated spin texture of the surface bands of KTO.[32] As before, the $[1\bar{1}0]$ sample shows additional structure, potentially reflecting the anomalous Hall-like offset and background oscillations seen in the traces shown in Fig. 5.13.
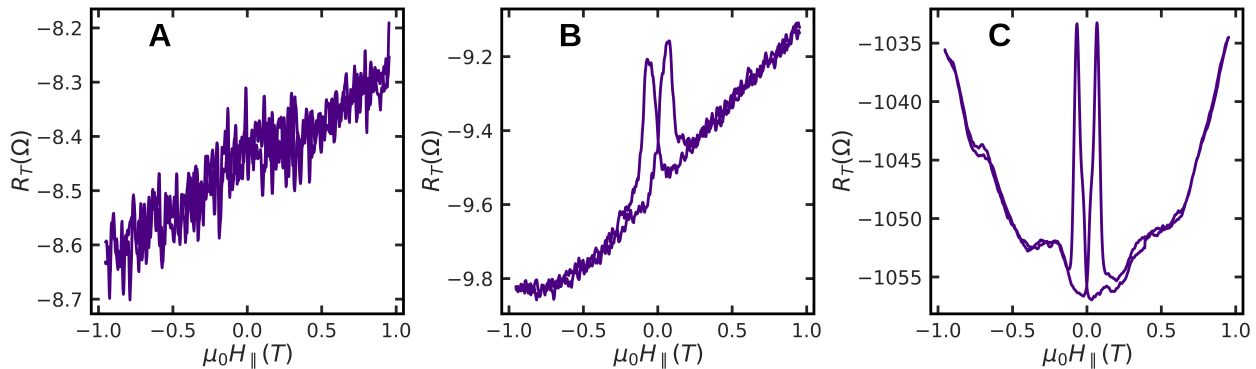
Figure 5.17: **Transverse magnetoresistance under parallel magnetic field at 30 mK.** (a) - (c) Transverse magnetoresistance traces for the (001), (110) and (110) $[1\bar{1}0]$ samples respectively. The (001) and (110) samples show a small planar Hall effect with central hysteretic peaks for the (110), while the (110) $[1\bar{1}0]$ sample shows stronger behavior and background oscillations. Figure was adapted from Krantz *et al.*[164]

In summary, the local magnetic moments associated with oxygen vacancies order at low temperatures to form a macroscopic magnetism, causing hysteretic peaks at low fields that show up in both the longitudinal and transverse MR for all samples. The hysteresis caused by this magnetism

can be tuned with gate voltage, changing the shape and the magnitude of the low field peaks. It is likely that the same magnetic order also generates the anomalous Hall-like offset in the [1$\bar{1}$0] sample. The hysteretic peaks themselves persist in the transverse up to 1.7 K and in the longitudinal of the s.c. samples up to 4 K, though there is additional structure at lower temperatures. In particular, the [1$\bar{1}$0] sample shows significant background texture that is currently unexplained. This texture is suppressed around 800 mK, but seems independent of gate voltage tuning. Finally, parallel field measurements show a weak planar Hall effect for all samples, with hysteretic peaks at low fields, indicating some in-plane magnetic texture as expected from previous theoretical results.[32] The next section will discuss the effect of this magnetism as it is shown to coexist with superconductivity for some of the crystal terminations of the s.c. sample set.

5.2 Superconductivity

So far the discussion of experimental results has focused on the qualities of the normal state, but both the (110) and (111) terminated samples of the sc set did show superconducting transitions below $\approx$ 2 K, as their naming convention suggests. The (001) surface did not go superconducting down to the lowest measurement temperatures, in contrast to the (110) and (111) samples, but in agreement with historical results.[14] All three samples did show signs of magnetism, as revealed by a survey of gate voltage dependent MR similar to those discussed in the previous sections. Through the extraction of upper critical field, H_{c2}, and critical temperature, T_c, we can qualify the nature of the superconductivity in these samples using the Ginsburg-Landau results discussed in Chapter 3. This analysis was then extended to include the Halperin-Nelson fit given in Eq. 3.14, characterizing the shape of the transition and its relevant parameters of Berezinskii–Kosterlitz–Thouless transition temperature, T_{BKT}, and thermodynamic critical field, H_c. This analysis showed limited results, likely constrained by disorder and the confounding effect of magnetic order.

5.2.1 Critical Temperature and Upper Critical Field

For this section on the focus will be on the two superconducting (s.c.) samples, the (110) and the $[1\bar{1}0]$ direction of the (111) (which will be referred to as the (111) samples for simplicity). The longitudinal MR data of the previous section will be augmented with parallel field MR and temperature dependence to qualify the superconducting state in terms of the Ginsburg-Landau theory. To start, the critical temperatures, T_c, of the two samples were extracted from temperature sweeps shown in Fig. 5.18 (a) and (c) for the (110) and (111) respectively.

The value of T_c were taken to be the point of greatest slope in the transition, which has previously been shown[18] to be a good estimate of T_c. The dependencies of T_c with respect to normal state carrier concentration is presented in Fig. 5.18 (b) and (d) for the (110) and (111) respectively, and show a increase of T_c with decreasing V_g for both samples. In contrast to works in the literature,[18,69] the T_c does not scale linearly with carrier concentration, n_e, at all over the measured range. This is another indication that the suppression of the superconducting state in the (111) is not due to carrier concentration, as there is no dip in T_c right up to the point that it is no longer superconducting. It is possible that the system hosts multicarrier transport, in which case the T_c may reflect a sub-population of the carrier concentration measured here, and this would be revealed in higher field tests of longitudinal and transverse magnetoresistance.

With the critical temperature in hand we can move to extract the upper critical field, H_{c2}. Fig. 5.19 (a) and (c) show the full field traces of MR shown previously in Fig. 5.23 (a) and Fig. 5.24 (a) for the low field (110) and (111) samples, respectively. H_{c2} was calculated by fitting a line to the section of the superconducting transition with the largest rate of rise, similar to the point that defined T_c above, and finding its intercept with a line defined by the normal state MR at the largest fields measured. The results of this calculation, plotted as a function of gate voltage, V_g, can be seen in Fig. 5.19 (b) and (d), and show a mostly linear increase in critical field with decreasing

(a) (110) Sample

(b) (110) Sample

(c) (111) Sample
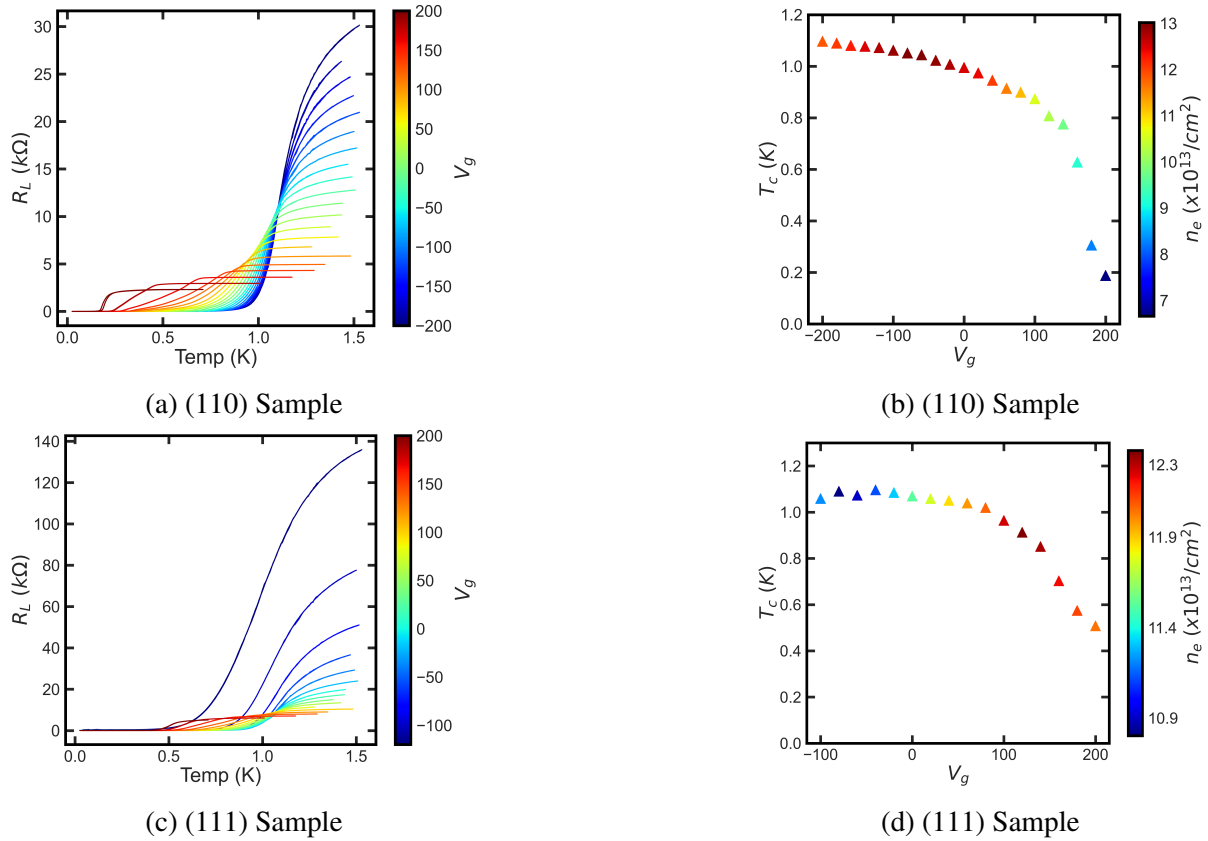
(d) (111) Sample

Figure 5.18: **Gate voltage dependence of R(T) traces for the (110) and (111) superconducting samples measured up to 1.5 K.** (a) R(T) traces for the (110) superconducting sample showing modulation of critical temperature, T_c. (b) Extracted T_c for the (110) plotted as a function of V_g, color coded by carrier concentration. (c) R(T) traces for the (111) superconducting sample, $[1\bar{1}0]$ direction, also showing modulation of critical temperature, T_c. (d) Extracted T_c for the $[1\bar{1}0]$ plotted as a function of V_g, color coded by carrier concentration.

gate voltage for both samples in the region they are still superconducting.

If the results for the two samples are combined, plotting H_{c2} against T_c, as shown in Fig. 5.20, they collapse onto a single curve. This is unexpected, as there is no intrinsic reason that the curves from different samples would correlate at all. The result does show is a clear gate voltage dependence for the edge of the psuedo-phase diagram, mapping the upper end of the superconductivity for these KTO samples. Although the two curves do not produce the same effects at the same gate

(a) (110) Sample (30 mK)

(b) (110) Sample (30 mK)

(c) (111) Sample (30 mK)

(d) (111) Sample (30 mK)
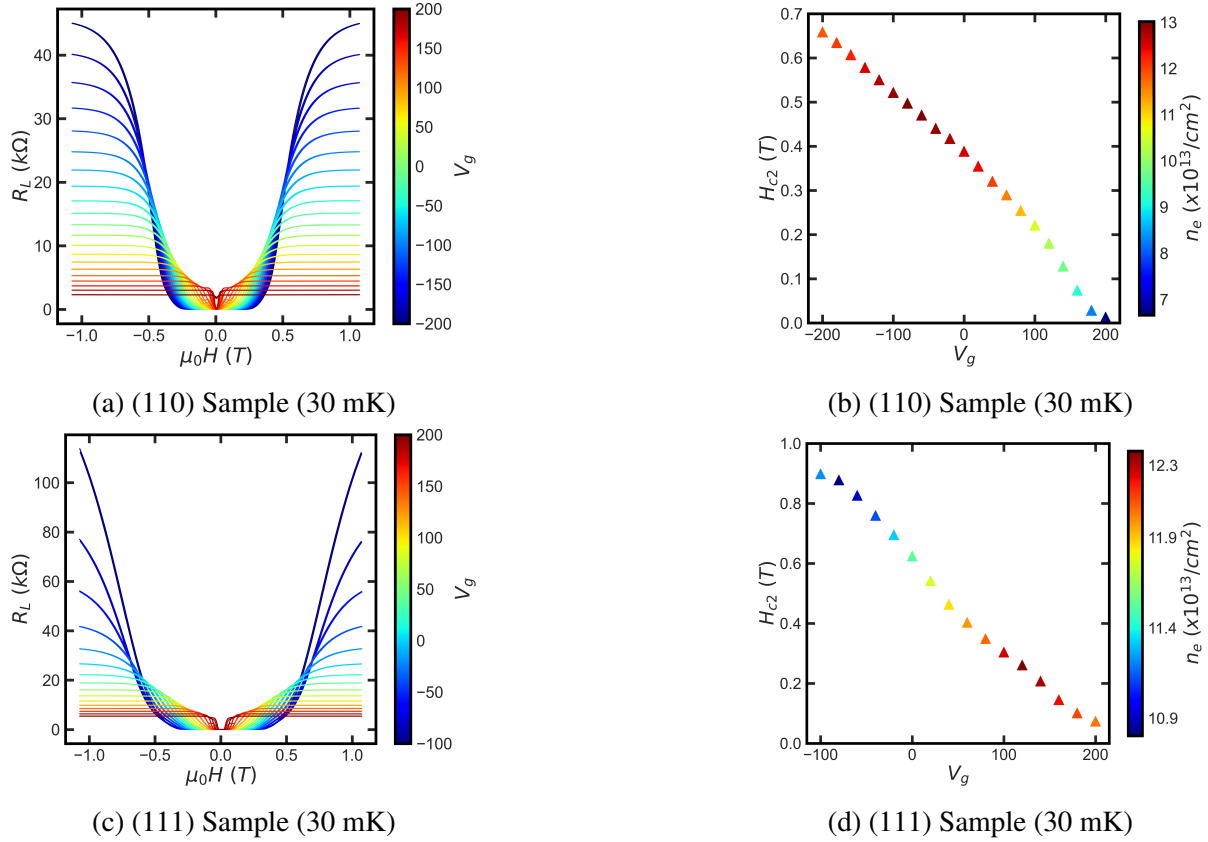
Figure 5.19: **Gate voltage dependence of perpendicular magnetoresistance for the (110) and (111) superconducting samples measured at 30 mK.** (a) Magnetoresistance traces for the (110) superconducting sample showing modulation of upper critical field, H_{c2}. (b) Extracted H_{c2} for the (110) plotted as a function of V_g, color coded by carrier concentration. (c) Magnetoresistance traces for the (111) superconducting sample, $[1\bar{1}0]$ direction, also showing modulation of critical temperature, H_{c2}. (d) Extracted H_{c2} for the $[1\bar{1}0]$ plotted as a function of V_g, color coded by carrier concentration.

voltage, they do fall on the same curve.

This could simply be a reflection of the scaling of the two terms, as $H_{c2} \approx 1/\xi^2$ and $T_c \approx 1/\xi$. The coherence length, ξ, is very similar for the two samples, as will be shown in the next section, so the coincidence is not unreasonable. It could also be a consequence of the shared transport direction; both the (110) and (111) samples have components along the $[1\bar{1}0]$ direction, through
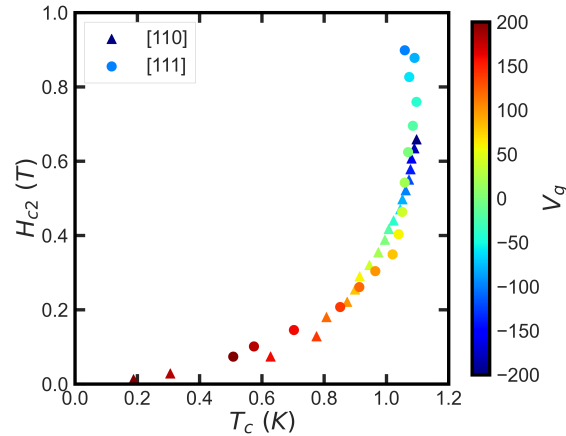
Figure 5.20: **Combined critical temperature and upper critical field for both superconducting samples.** Upper critical field, H_{c2}, plotted as a function of critical temperature, T_c, for each corresponding gate voltage. The two samples show remarkably similar dependencies.

the (110) is 45° to it due to strange crystal axis misalignment. It could be that this is a preferred transport direction for these samples, though this hypothesis would need to be tested against more samples before such a claim is made.

5.2.2 Analytical Characterization of the Superconducting State

Building on the characterization of the previous section, we can apply the Ginsburg-Landau relations detailed in Chapter 3, to calculate the penetration depth, λ_{eff}, and the coherence length, ξ. Taking the ratio of the two gives κ, the Ginsburg-Landau parameter, which describes system as either Type-I for $\lambda_{eff} < \frac{1}{\sqrt{2}}$ or Type-II for $\lambda_{eff} > \frac{1}{\sqrt{2}}$. The results of these calculations can be seen in Fig. 5.21.

In STO samples the superfluid density has been shown to be tied to the density of a high mobility carrier population, despite it making up a small percentage of the total carrier concentration as measured by Hall effect.[167] In KTO, the bulk conductivity is suppressed but the same multiband transport is expected,[32,69] and previous works have shown that the superfluid ratio is only a few

(a) Penetration Depth   (b) Coherence Length   (c) GL parameter
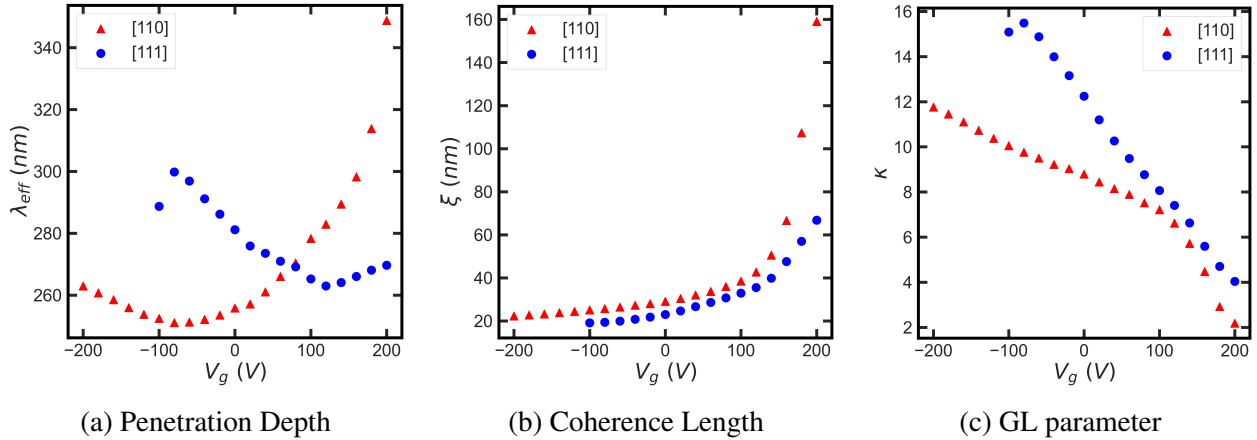
Figure 5.21: **Superconducting parameters from Ginsburg-Landau Theory.** (a) Ginsburg-Landau penetration depth, λ_{eff}, reported in units of nm. (b) Ginsburg-Landau coherence , ξ, also reported in units of nm, showing sharp increases at high gate voltages. (c) Ginsburg-Landau parameter, κ, showing the films are very much Type-II.

percent of the total two dimensional carrier concentration.[69] Using a participation ratio of 2.5% and an effective mass of $m^* \simeq 0.5m_0$ from Mallik *et al.*[69] we can estimate the penetration depth, λ_{eff}, for the superfluid in these samples via Eq. 3.1. The result in Fig. 5.21 (a) shows a penetration depth from 250 to 350 nm for both samples, with the highest calculated value for the (110) sample at the largest gate voltage. Similarly, from the extracted H_{c2} measurements we can calculate the coherence length, ξ, shown in Fig. 5.21 (b). These calculations show lengths around 20 nm for most gate voltages, which agree with literature,[16] and a growing length up to 160 nm for the (110) sample at highest gate values, again. Combining the two parameters gives the Ginsburg-Landau parameter, shown in Fig. 5.21 (c), which is very Type - II and sports a kink in the behavior of the (110) at V_g = 100 V.

Unfortunately the in-plane (parallel) magnetic field was not large enough for most values of V_g to measure the critical parallel field, $H_{c\parallel}$, so they will be neglected here. This limits the completion of the planned analysis, and there is no longer a method for extracting the thickness of the

superconducting gas given by Eq. 3.7. There is one exception to this, as the V_g = 200 V trace of the (110) sample had a parallel critical field of $\approx$ 0.28 T, giving an estimate of the thickness at 25 nm. This is well above the reference values in literature,[69] and it is more likely that the sample is slightly misaligned to the field, or that the magnetism in the samples is suppressing the superconductivity enough that the effective field is much larger and more perpendicular to the plane than applied in-plane field. For the rest of the data we can put an upper bound on the thickness of 20 - 100 nm, which is an order of magnitude larger than the literature value[69] of 8 nm used in previous calculations for the normal state. Due to the nature of this system, this analysis is limited in physical implication, though there are still some interesting observations in the parallel field that will be discussed later.

(a) Extracted T_{BKT}

(b)
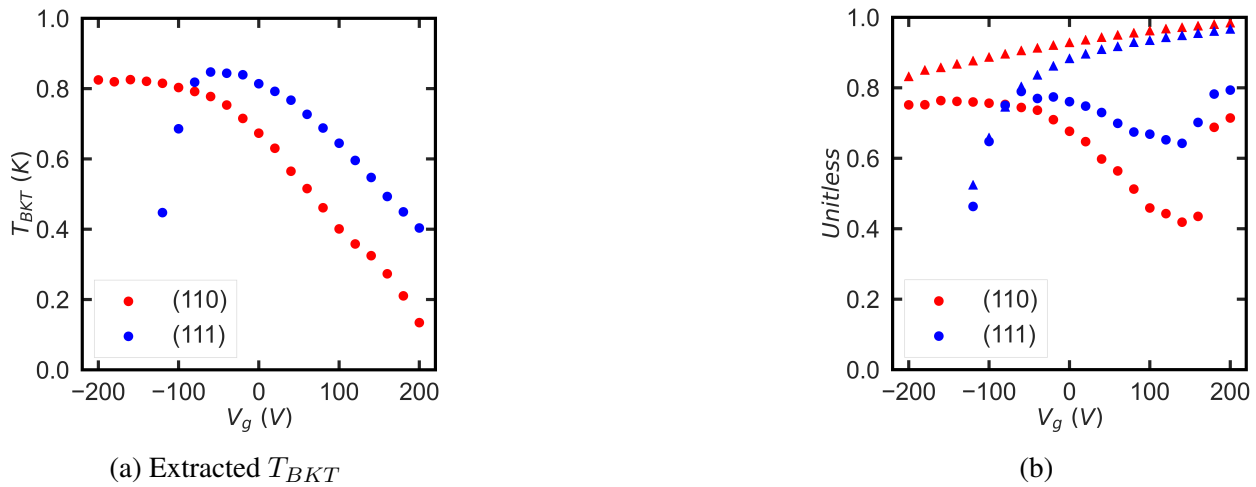
Figure 5.22: **Results from Halperin-Nelson form.** (a) Berezinskii-Kosterlitz-Thouless temperature extracted from $R(T)$ fits to the Halperin-Nelson formula. (b) Comparison of the reduced critical temperature, T_{BKT} / T_C, shown in • symbols, and the resistance form for two dimensional superconductivity, $(1 + 0.173 R_N / R_c)^{-1}$, shown in ▲ symbols, for the (110) (red) and (111) (blue) samples.

Fig. 5.22 (a) show the result of an attempt at the Halperin-Nelson fit, giving values of the Berezinskii-Kosterlitz-Thouless temperature, T_{BKT}, as a function of gate voltage for the two su-

perconducting samples. Values of T_{BKT} can be extracted from R(T) curves through the form[126] $\left(\frac{\partial(lnR)}{\partial T}\right)^{(-2/3)} = A(T - T_{BKT})$, for some material parameter A, though the extrapolation did not produce consistent results. The downturn in the (111) at low gate voltages is associated with the destruction of the superconducting phase with disorder as discussed before. Fig. 5.22 (b) show the comparison of the ratio of the Berezinskii-Kosterlitz-Thouless temperature and the critical temperature extracted above, with a form predicted to hold for two dimensional superconductors, $T_{BKT}/T_C = (1 + 0.173R_N/R_c)^{-1}$. The deviation of the two sides of the equation would superficially suggest that the superconductivity is not two dimensional, as the values do not agree well at all. However, it is more likely that the disorder and intrinsic magnetism in the system are responsible for difficulty in fitting the Halperin-Nelson formula which impacts the estimation of T_{BKT} and R_N. Indeed, it may be that the disorder broadens the transition enough that the Halperin-Nelson formula no longer accurately describes the transition, in contrast to results in other KTO systems.[66] This also limits the extent of further analysis, as the parameters A and b in the Halperin-Nelson formula can be related to the vortex energy and phase stiffness of the superfluid, which cannot be estimated from the presented data.

To summarize, there was difficulty in fitting some analytical expressions to the data, likely due to disorder and magnetic effects modifying the nature of the transition. Despite this difficulty, some compelling results were shown which may warrant further investigation. The extracted critical temperature and upper critical fields were shown to fall on the same curve for both samples and were definitively not linear in carrier concentration, in contrast to results in the literature.[18,69] Ginsburg-Landau penetration depth and coherence length were estimated, the latter agreeing well with previous reports,[69] though an estimation of the superfluid thickness seemed to disagree with the same previous works, likely due to the magnetism in the system. Fits to the Halperin-Nelson formula were also inconsistent, possibly due to inhomogeneities in the samples broadening the

transition. A detailed investigation of these analytic results would require the fabrication of more homogeneous samples, or some accounting for the inhomogeneities and magnetism in the system. It would also be interesting to measure the T_c vs H phase boundary, as the slope of the trace gives a more accurate estimation of the coherence length, ξ, and may show interesting results.

5.2.3   Coexistence of Superconductivity and Magnetism

The first crystal termination to discuss is the (110), which boasted the highest carrier concentrations and mobilities in the normal state. The sample went superconducting upon cooling with an applied back gate of 100 V, allowing for a MR study of the superconducting state, shown in Fig. 5.23. At the highest gate voltages the sample is actually not fully superconducting and instead shows a finite resistance, representing an upper limit to the superconducting gate dependence which has not been reported for KTO samples. The rest of the longitudinal MR shows both a strengthening of the superconducting state with decreasing gate voltage, and the emergence of hysteretic peaks in the superconducting state. These peaks can be seen clearly in the low field traces shown in Fig. 5.23 (b). This coexistence of superconductivity and magnetism is not unprecedented in the complex oxides,[84] but is a novel observation in KTO. The peaks themselves appear due to vortex motion instigated by hysteretic magnetic switching under applied field, and the height of the high field curves reflects the increase in normal state resistance with decreasing gate voltage.

The transverse MR of the (110) shows several features mirroring those seen in the longitudinal traces. In the superconducting gap the transverse MR is zero for most gate voltages, with the exception of the emergence of hysteretic peaks from the same magnetism generating peaks in the longitudinal MR. In the transition edge there are multiple features that could be from different vortex dynamics, though it is hard to say. For some values of V_g there is additional structure *inside* the superconducting valley, at the foot of the transition. This structure is a finite resistance in the

(a) (110) Sample (30 mK)

(b) (110) Sample (30 mK)

(c) (110) Sample (30 mK)
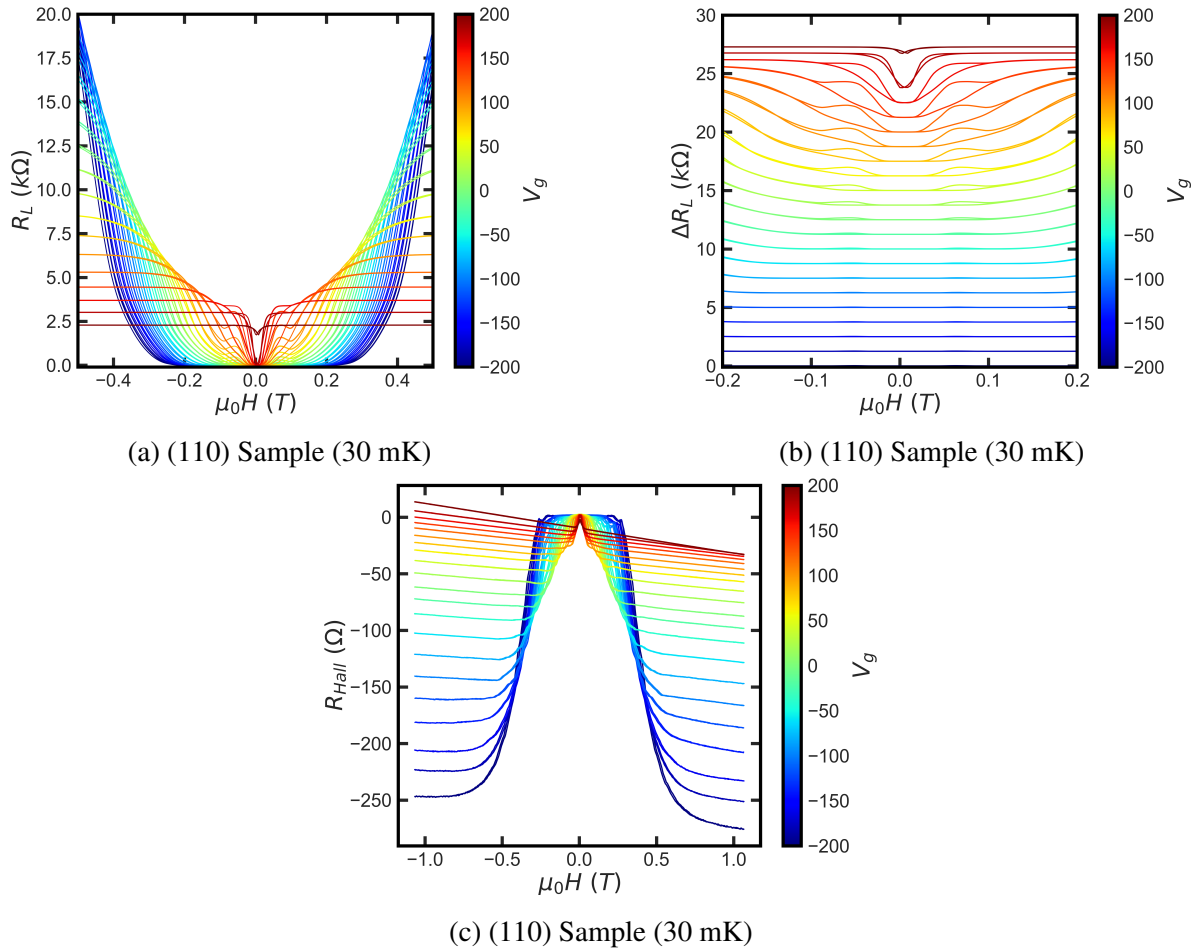
Figure 5.23: **Magnetoresistance traces of the (110) superconducting sample measured at 30 mK.** (a) Longitudinal magnetorestistance showing gate tuning of the superconducting state, and magnetism represented in hysteretic peaks in the superconducting state. (b) Small field component of the longitudinal magnetoresistance uniformly shifted to highlight the hysteretic peaks. (c) Transverse magnetoresistance as a function of back gate voltage, shifted for clarity, showing a symmetric component in the superconducting state superimposed on a normal metal background.

Hall signal that is opposite in sign to the normal state resistance. This effect is replicated in the temperature dependence, and will be discussed at length later.

A similar set of measurements can be seen for the $[1\bar{1}0]$ direction of the (111) sample shown in Fig. 5.24. Similar to the (110) sample, the longitudinal MR shows both a strengthening of the

(a) (111) Sample, [1$\bar{1}$0] dir. (30 mK)

(b) (111) Sample, [1$\bar{1}$0] dir. (30 mK)

(c) (111) Sample, [1$\bar{1}$0] dir. (30 mK)

Figure 5.24: **Magnetoresistance traces of the (111) superconducting sample, [1$\bar{1}$0] direction, measured at 30 mK.** (a) Longitudinal magnetorestistance showing gate tuning of the superconducting state, and magnetism represented in hysteretic peaks in the superconducting state. (b) Small field component of the longitudinal magnetoresistance uniformly shifted to highlight the hysteretic peaks. (c) Transverse magnetoresistance as a function of back gate voltage, uniformly shifted for clarity, showing a symmetric component in the superconducting state superimposed on a normal metal background.

superconducting state with decreasing gate voltage, and the emergence of hysteretic peaks in the

superconducting state. As was the case with the (110), the shape of the high field curves reflects the

increase in normal state resistance with decreasing gate voltage V_g. For V_g = -120 V the samples

actually loses its superconductivity, as can be seen in the lifting of the lowest curve in Fig. 5.24

(a). The carrier concentration at this point is $\approx 5.6 \times 10^{13}$ e$^-$ cm^{-2}, well above the threshold for hosting superconductivity seen in other works.[69] This suggests that the superconducting state in the (111) is not protected by the areal carrier concentration as shown previously,[66] but is instead suppressed through potentially magnetic scattering at low value of V_g. Scattering in this way would also account for the finite residual resistance seen inside the superconducting gap of the (111) sample that increases with field before the suppression of superconductivity.

Interestingly, this suppression of the superconducting state appears to occur at higher V_g for the transverse. In the superconducting valley the transverse is zero for most gate voltages, again with the exception of the hysteretic peaks due to vortex motion induced by magnetic switching in the superconducting state. The breakdown of the zero resistance state appears to occur at $V_g = 60$V, a result which will be important for the discussion later. Unlike the (110), there are large, symmetric dips on either side of the superconducting transition, around 300 to 500 mT, corresponding to vortex motion, and for some values of V_g, there are again features in the superconducting valley of the Hall with opposite sign to the vortex motion peaks. The results are remarkably similar to those shown in the (110), which is a fact which will be explored later.

For both samples the transverse has more features than was initially unexpected, but there is precedent for many of them. Ma *et al.*[58] showed that the Hall in the superconducting state of KTO had both this symmetric component due to the shorting of the superconducting leads, and the normal state Hall effect above the transition. They even showed the emergence of peaks on either side of the transition but offered no comment on the origin. What is unexpected is the suppression of superconductivity in the Hall at higher gate voltage values than in the longitudinal, an observation which changes the interpretation of the superconducting nature in the (111).

For the [1$\bar{1}$2] direction of the (111) sample, superconductivity did not present itself in the longitudinal direction. Fig. 5.25 (a) shows the rather strange traces of the longitudinal MR for the [1$\bar{1}$2].

(a) (11) Sample, [1$\bar{1}$2] dir. (30 mK)   (b) (111) Sample, [1$\bar{1}$2] dir. (30 mK)
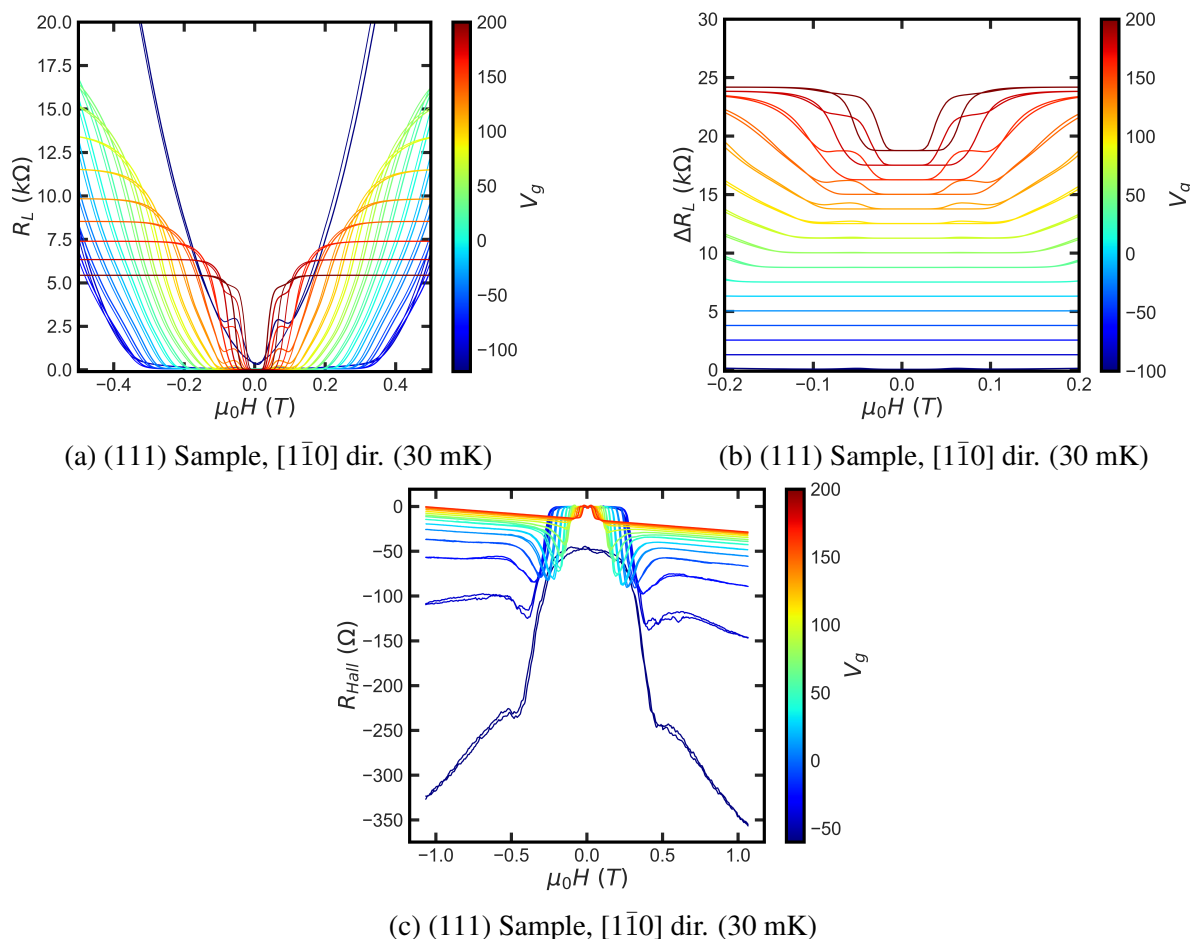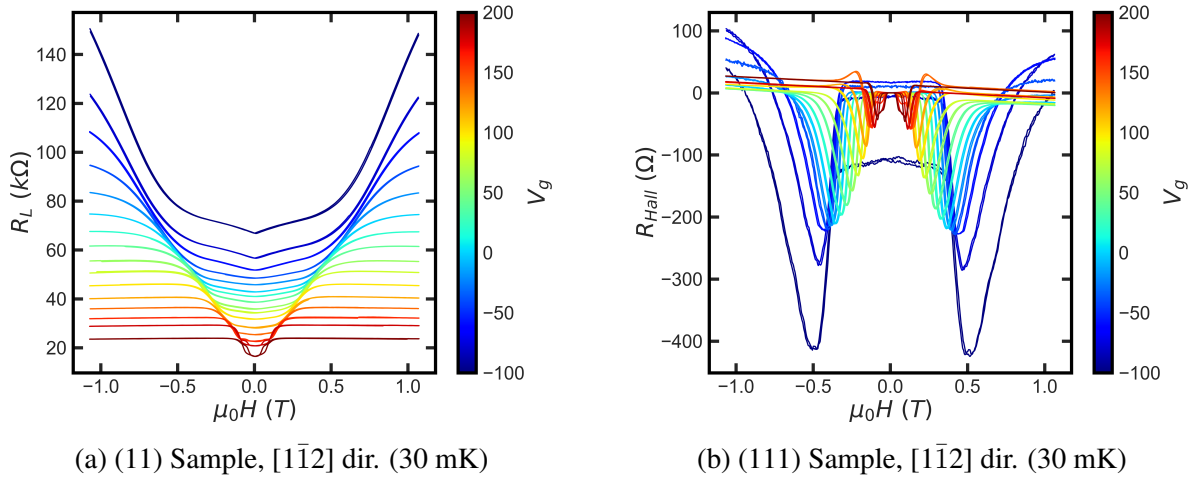
Figure 5.25: **Magnetoresistance traces of the (111) superconducting sample, [1$\bar{1}$2] direction, measured at 30 mK.** (a) Longitudinal magnetoresistance showing gate tuning of the low field dip, and emergent hysteresis, but no zero resistance state. (b) Transverse magnetoresistance as a function of back gate voltage, uniformly shifted for clarity, showing a zero resistance symmetric component superimposed on a normal metal background.

The sharp drops in the resistance suggest a superconducting transition mirroring the one seen in the [1$\bar{1}$0], but one that is stopped before realizing the zero resistance state. Once again, the shape of the high field curves reflects the increase in normal state resistance with decreasing gate voltage V_g, and there are hysteretic features in the low field traces from macroscopic magnetic order. This supports the finding that the superconducting state has more than a simple dependence on carrier concentration as previously reported,[18,69] because the differences between the conducting properties of the two (111) directions were minimal at higher temperatures. In fact, the [1$\bar{1}$2] direction has a higher carrier concentration at 4 K, but does not show a fully formed superconducting state.

Also unexpected is the transverse MR of the [1$\bar{1}$2] direction, shown in Fig. 5.25 (b). It appears to match the behavior of the two previous samples, indicating a superconducting transition by the zero resistance state at low fields. Still present are the hysteretic peak, the background normal state resistance, and the large, symmetric dips from vortex motion, as seen for the [1$\bar{1}$0] direction.

All indications from the transverse magnetoresistance suggest that the Hall bar is superconducting, for a similar range as seen in the [1$\bar{1}$0] direction, but has a large residual resistance in the superconducting state.

Taken together, the results of the two orthogonal (111) Hall bars suggest striped superconductivity, with a preferred direction along the [1$\bar{1}$0]. This accounts for the similar range gate voltages showing superconductivity in the longitudinal [1$\bar{1}$0] and the transverse of the [1$\bar{1}$2], because both are in the [1$\bar{1}$0] surface crystal direction. The central dips in the longitudinal MR in the [1$\bar{1}$2] direction could also be explained, as it could be that the longitudinal measurement is made up of many superconducting strips connected by tunnel processes, resulting in large residual resistances inside a failed valley. Similarly, the early suppression of the superconducting state in the transverse of the [1$\bar{1}$0] sample could be from stripes forming across the Hall bar or at the constriction points of the voltage contacts.

There is precedent for this in other works, as discussed before in Chapter 2. Liu *et al.*[18] showed striped superconductivity in (111) EuO / KTO which resulted in direction dependent hysteresis in MR. It was later explained that this striped superconductivity was likely due to a striped magnetism,[41] resulting from an interaction between the complex spin texture of the (111) KTO surface and the in-plane ferromagnetism of the EuO capping layer. If the coupling of those two effects is sufficiently strong, it is plausible that it could break the superconductivity into stripes that are coupled only through tunneling processes. Additional techniques would be needed to test this hypothesis. Probing techniques that can access spatially resolved states, such as microwave impedance microscopy, magnetic force microscopy, or squid magnetometry would be able to confirm the existence of this striped state, and should be conducted if possible. Confirmation of the striped state would be scientifically interesting, as it would suggest that the striped state is intrinsic to the (111) surface of KTO, potentially due to the strong spin-orbit character and spin texture of the surface.

5.2.4   Hall Effect in the Superconducting State

What was neglected in the discussion of the last section was an analysis of the Hall effect in the superconducting state. One would normally expect that a superconductor would have zero Hall signal in the superconducting state, and this is largely true. The two voltage contacts that define the transverse voltage measurement are shorted by the superconductor, just as the longitudinal is, and there is no voltage difference between them. This is not the full picture though, and in the presence of current flow a finite resistance can be measured. The simplest source of this transverse voltage is superconducting vortex flow, where vortices experience a force perpendicular to super-current flow.[168] For longitudinal flow, this moves the core to the edge of the material, effectively transporting a charge along with the motion of the vortex.[133,169] Any time there is vortex flow, like in the event of lattice melting near T_c or at sufficiently large magnetic field near H_{c1}, there is a transverse voltage that should be the same sign as the normal state resistance.

This is particularly evident in the symmetric component of the transverse magnetoresistance for the the (111) sample, [110] direction, which is shown in Fig. 5.26 (b). The large dips on either side of the superconducting transition for some values of V_g are caused by superconducting vortex flow as superconducting state is destroyed with increasing field. These dips have the same sign as the normal state resistance seen at high field, as expected, and after they subside the Hall resistance returns to that of a normal electron-like metal, for most gate voltages. Inside the gap the Hall signal is not well behaved though, as it is not uniformly zero as one would expect for the Hall in the superconducting state. Not only are there the same signatures of hysteretic peaks from the magnetic order that appeared in the longitudinal magnetoresistance shown in Fig. 5.23 and Fig. 5.24, but there is residual resistance that is tuned by back gate voltage. This can be seen in detail in the small field data presented in Fig. 5.27. For very few gate voltage values does the Hall signal actually reach the zero resistance state expected for normal superconductors. Instead, for some

(a) (110) Sample (30 mK)   (b) (111) Sample, [1$\bar{1}$0] dir. (30 mK)

Figure 5.26: **Symmetric component of transverse magnetoresistance in the superconducting state.** (a) Symmetric component of transverse magnetoresistance of (110) sample as a function of back gate voltage, V_g. Traces have been uniformly shifted for clarity. (b) Transverse magnetoresistance of the (111) sample, [1$\bar{1}$0] direction, as a function of V_g. Traces have also been uniformly shifted for clarity. All data were taken at 30 mK.

values of V_g the sign of the residual resistance is opposite that of the normal state at the foot of the transition, which is not what one would expect if this were from a mechanism of vortex formation as in the case of the BKT transition. There must be another explanation, and the transverse signals measured through the superconducting transition will help to elucidate it.

Fig. 5.28 (a) and (b) shows the transverse resistance, R_T(T), as a function of temperature and gate voltage for the (110) sample and the (111) sample, [1$\bar{1}$0] direction, respectively. All data were taken in the absence of externally applied magnetic field. Both longitudinally superconducting samples start with transverse resistances of zero below T_c, and transition to a finite R_T well above T_c. There are several notable features of the data which are worth discussing. The first is that for each value of V_g the normal state transverse resistance reached above T_c is not zero. We would normally expect a Hall measurement in zero field to be zero, but the annealing curves shown in Fig. 5.2 demonstrate that this is not the case in these samples. Instead there is a finite transverse

(a) (110) Sample (30 mK)
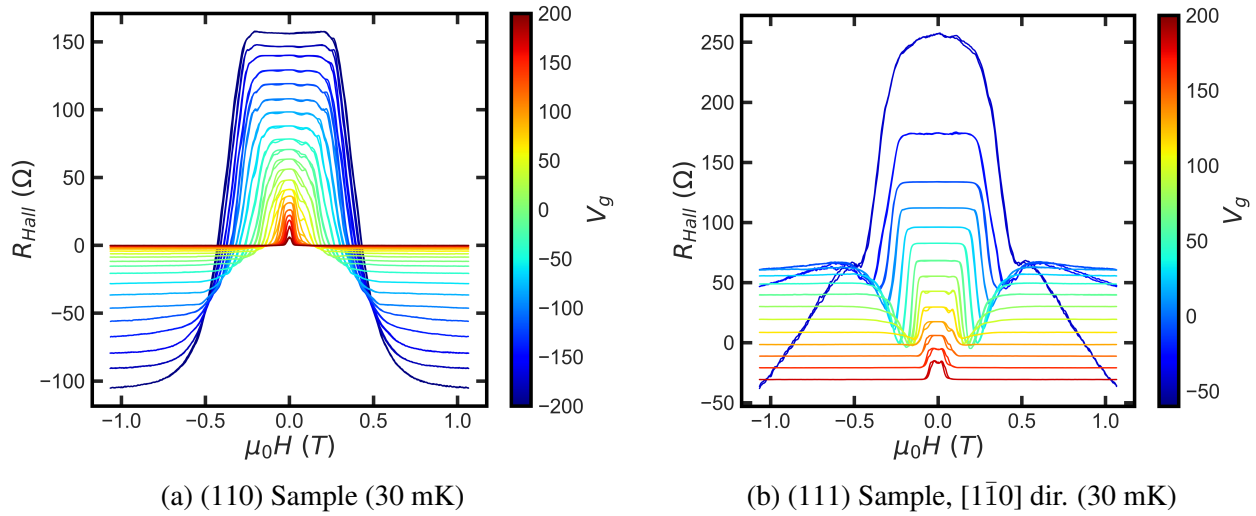
(b) (111) Sample, [1$\bar{1}$0] dir. (30 mK)
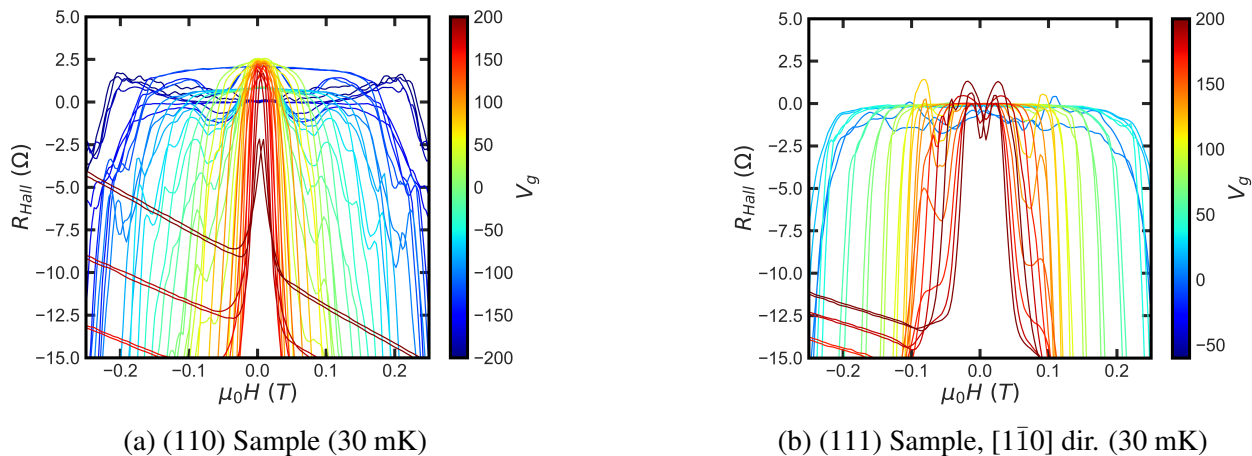
Figure 5.27: **Symmetric component of transverse magnetoresistance in the superconducting state.** (a) Symmetric component of transverse magnetoresistance of (110) sample as a function of back gate voltage, V_g. Traces have been uniformly shifted for clarity. (b) Transverse magnetoresistance of the (111) sample, [1$\bar{1}$0] direction, as a function of V_g. All data were taken at 30 mK.

(a) (110) Sample
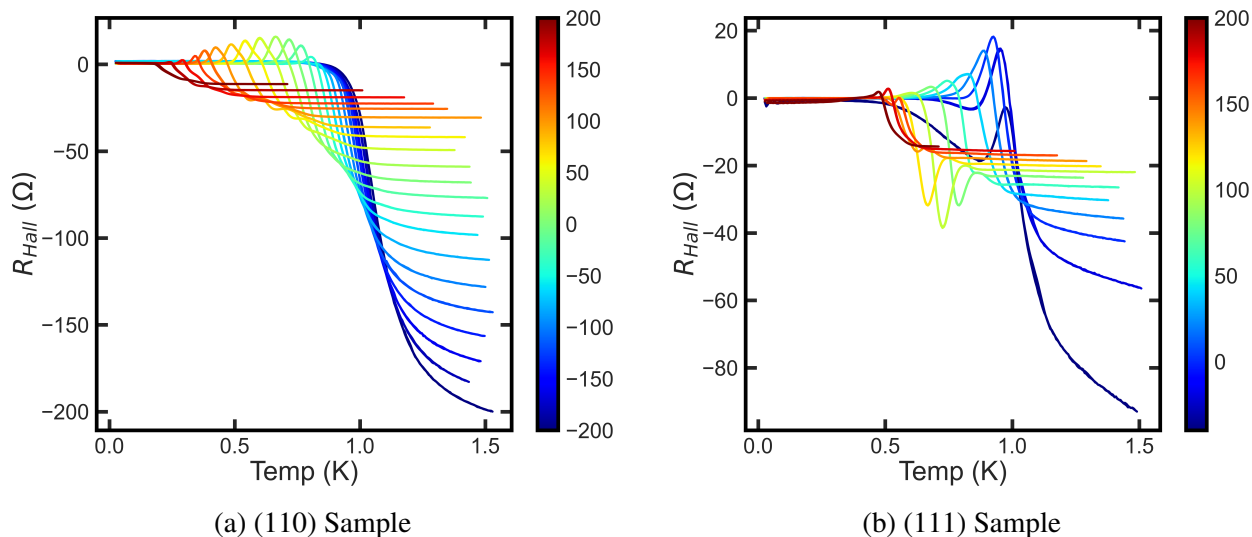
(b) (111) Sample

Figure 5.28: **Transverse $R_T(T)$ through the superconducting transition.** (a) Transverse resistance of the superconducting state of the (110) sample as a function of back gate voltage, V_g. (b) Transverse resistance of the (111) sample, [1$\bar{1}$0] direction, as a function of V_g. All data was taken in zero applied magnetic field.

signal, which shows up as the normal state R_T in these traces. Similar offsets were removed from the other Hall measurements for clarity, which is why they were referred to as shifted traces.

The second notable feature is a dip in R_T at and above the superconducting transition coming from vortex motion as discussed earlier for the transverse magnetoresistance. The important thing about these peaks is that they extend above T_c. This is an interesting indication of the persistence of superconducting fluctuations or remnant superconducting regions, similar to those anticipated by Aslamazov-Larkin type theories.[130–132,134]

The third notable feature is the emergence of a peak in the signal below T_c with opposite sign to the normal state resistance. This is a feature reminiscent of the Hall anomaly seen in high temperature superconductors, which was the subject of significant debate in the early 1990s.[127] The effect was suggested to arise from several different physical sources, including vortex pinning,[170] quasiparticle backflow,[171] and even anisotropic superconducting behavior in layered superconductors.[172] Recently, Zhao *et al.*[173] showed the effect for thin layers of exfoliated $Bi_{2.1}Sr_{1.9}CaCu_{2.0}O_{8+\delta}$ for various applied fields, and concluded that the effect arose from vortex dynamics based on analysis from a 1995 paper by Feigel'man *et al.*.[174] Both above and below T_c the formalism describing vortex-like dynamics fits the data, supporting the idea that effect stems from a topological contribution to the Hall conductivity due vortex-normal core interactions. Other results, for disordered superconductors with high transition temperatures like NbN showed[175] that the effect is more broad than to apply to only certain classes of high-T_c superconductors, and it could be that the superconducting gas in these samples is another case of systems that can show negative flux flow. This can be verified by monitoring the transverse signal while taking the T_c vs H traces suggested at the end of the last section, and should also yield interesting results. It should not be hysteretic, but it should change sign and magnitude with applied field and changing gate voltage.

5.2.5   *Parallel field Results*

While parallel field magnetoresistance was unable to provide critical fields for calculating thickness a the previous section, the tests did show interesting and unexpected results. Fig. 5.29 shows a series of traces of parallel field magnetoresistance for different gate voltages in the superconducting state for the (a) (110) and (b) (111) samples. The field is not strong enough to fully suppress the superconductivity below $V_g = 200V$, but it does reveal large hysteretic peaks and asymmetries in the direction of applied field. For the (111) sample the longitudinal magnetoresistance is strongly asymmetric and seems to have background oscillations similar to those seen in the transverse of the normal state samples. At no gate voltages does the parallel field break the superconductivity in the (111) sample, so the wandering river structure may just be due to vortex motion, or could be something more exotic. The transverse magnetoresistance is even stranger.

Fig. 5.29 (c) and (d) shows a series of traces of parallel field transverse magnetoresistance for the (110) and (111) samples, respectively. Both samples seem to reflect the nature of the longitudinal traces shown in Fig. 5.29 (a) and (b), including the nature of the hysteretic peaks and the wandering river shape of the (111). Many of the features seen in the longitudinal traces are reflected in the transverse traces, and both are reminiscent of the background oscillations seen in the transverse of the normal state (110) Hall trace at mK temperatures. At the time of writing this does not have an explanation. It could simply be vortex dynamics in the superconducting state, it could be a spin precession effect, such as Hanle precession, or something else entirely unexpected. At this point it will be mentioned as a curiosity, and a potential area of investigation for a future student should they choose to pursue it.

In the normal state, the magnetoresistance traces show strong antisymmetric dips with hysteretic loops that are heavily tuned with gate voltage. Fig. 5.30 shows the longitudinal (a) and transverse (b) magnetoresistance of the (001) superconducting sample measured at 30 mK. The data

(a) (110) Sample (30 mK)

(b) (111) Sample, [1$\bar{1}$0] dir. (30 mK)

(c) (110) Sample (30 mK)

(d) (111) Sample, [1$\bar{1}$0] dir. (30 mK)
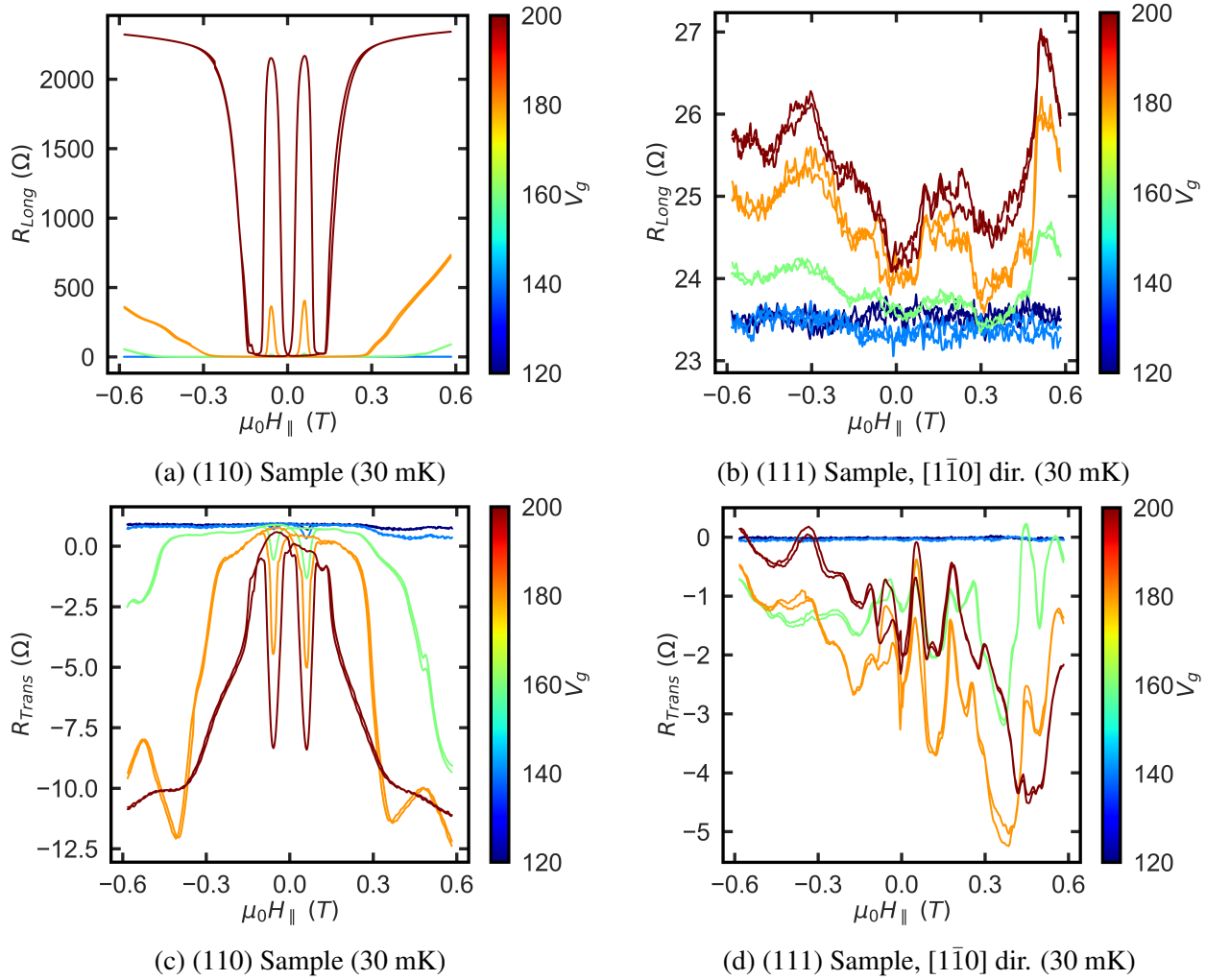
Figure 5.29: **Parallel field magnetoresistance in the superconducting states.** (a) Longitudinal magnetoresistance of the (110) in parallel applied magnetic field, $\mu_0 H_\parallel$, for a range of gate voltages. Data was taken at 30 mK. (b) Longitudinal parallel field magnetoresistance in the superconducting state of the (111). (c) Transverse resistance in parallel applied magnetic field, $\mu_0 H_\parallel$, for the (110) sample. (d) Transverse parallel field magnetoresistance for the (111) sample. All data taken at 30 mK.

have a strong antisymmetric dip that looks like the curve you would expect for a spin-valve.[176,177]

In particular, there is a antisymmetric component that shows up in both longitudinal and transverse that is tuned with gate voltage just like the results shown by Agarwal *et al.*[176] This is not a spin

(a) Long. (001) s.c. sample (30 mK)

(b) Trans. (001) s.c. sample (30 mK)
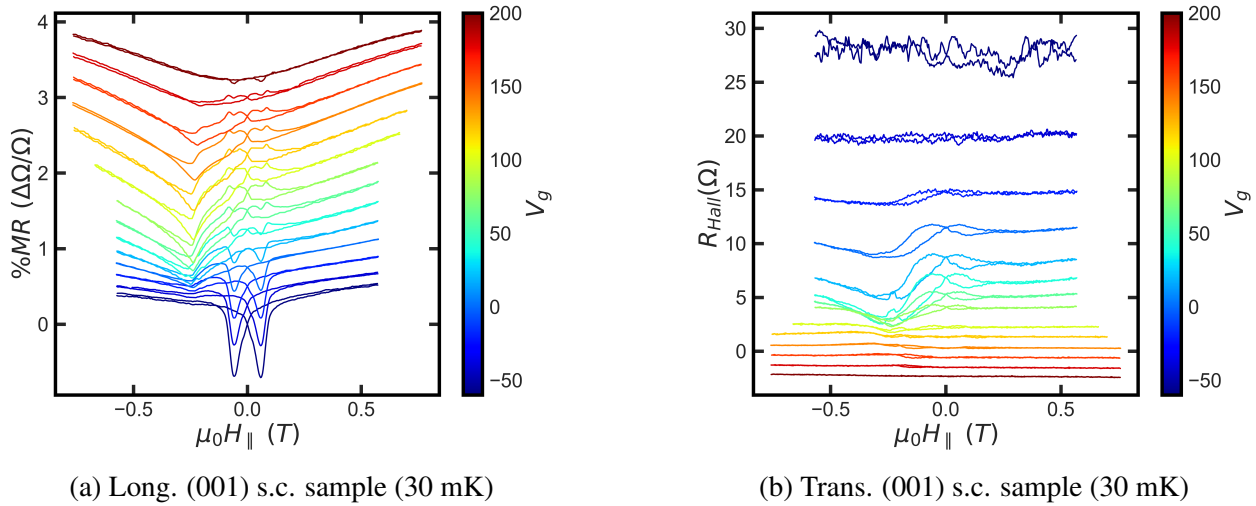
Figure 5.30: **Parallel field magnetoresistance of the (001).** (a) Longitudinal magnetoresistance for parallel field, $\mu_0 H_\parallel$, for a range of gate voltages. All data was taken at 30 mK and incrementally shifted for clarity. (b) Transverse parallel field magnetoresistance for the same data range.

valve system though, and there is no reason for the traces for the (001) to show this behavior, it should be the most symmetric of any sample. One possibility is that the magnetism is related to the atomic steps on the surface due to the crystal miscut, shown in Fig. 4.1. If this is the case, there is an added anistropic component to the transport that is not accounted for in the analysis conducted here, but could explain the parallel field results and anisotropic conduction.

A similar anistropy is seen in measurements of critical current, shown in Fig. 5.31 for (a) the trace of the (110) sample with zero applied field, revealing hysteresis in the transition current due to heating effects and many features in the edge of the transition indicating significant inhomogeneity in the sample. Fig. 5.31 (b) shows the traces for the same sample but under a persisted parallel field of ± 200 mT. For both fields the critical current was reduced, and there is some asymmetry in the up-sweep critical current, in particular in the +200 mT data, but this change was inconsistent over multiple sweeps and there was no definitive evidence of a superconducting diode-like effect.

In contrast for the (110), the data for the (111) show something unexpected. Fig. 5.32 (a)
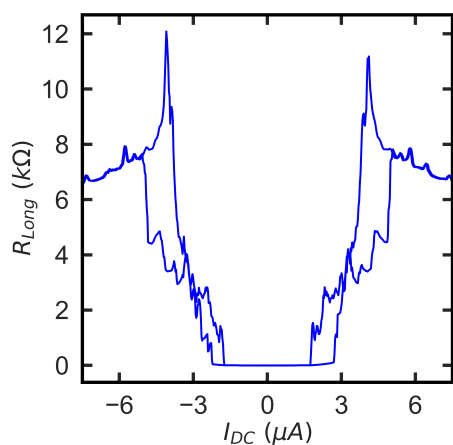
(a) (110) Sample (30 mK)
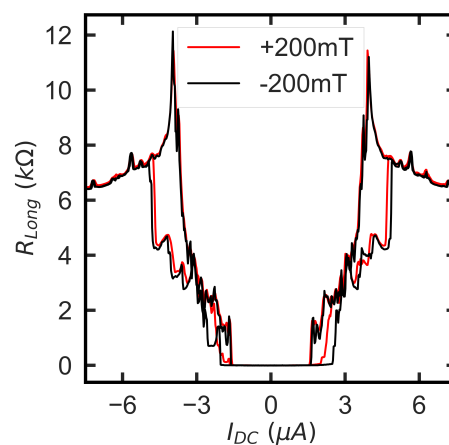
(b) (110) Sample (30 mK)

Figure 5.31: **Critical current measurements in parallel field for (110) sample.** (a) Critical current measurement showing resistance as a function of dc current. Data was taken at 30 mK. (b) Critical current measurement under applied parallel field, for +200 mT (red) and -200 mT (black).
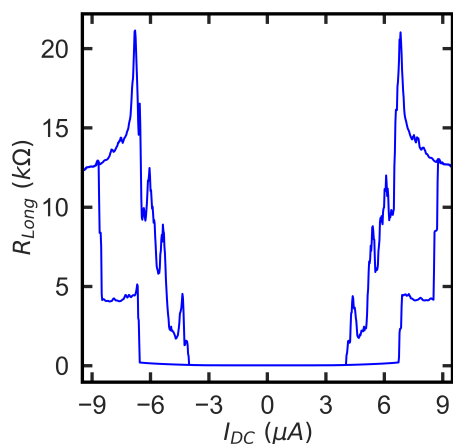
(a) (111) Sample, [1$\bar{1}$0] dir. (30 mK)
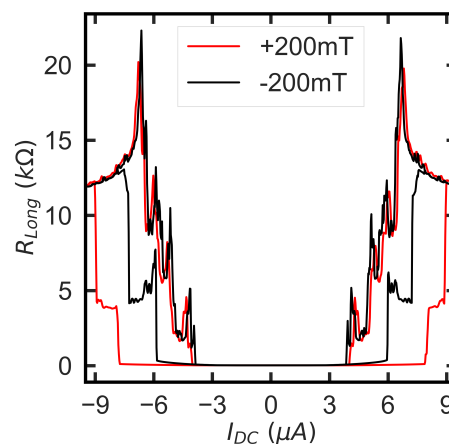
(b) (111) Sample, [1$\bar{1}$0] dir. (30 mK)

Figure 5.32: **Critical current measurements in parallel field for (111) sample.** (a) Critical current measurement showing resistance as a function of dc current. Data was taken at 30 mK. (b) Critical current measurement under applied parallel field, for +200 mT (red) and -200 mT (black).

shows critical current measurements in the absence of applied field, once again indicating hysteresis direction and showing numerous features indicating disorder in the sample. The critical current is larger than in the (110) samples but otherwise the curves are well behaved. Fig. 5.32

(b) holds the surprising result, showing an increase in critical current under applied parallel field in one direction, and the expected suppression in the other.

At its face value this asymmetry in field dependence is surprising, especially in the absence of critical current anisotropy. It could be that the magnetic moments in the sample have some component that is in plane that somehow couples with the applied parallel field. This would result in a lower effective field, and could explain the increase in critical current seen in the measurements presented in Fig. 5.31. Such a signature did not appear in other measurements though, at least not on the (111) samples, so there is no definitive answer pending further testing. Once again it may be good to look at low temperature scanning probe techniques to try and qualify the nature of the magnetism in the samples, as this would shed light on the strange parallel field results. Until then it will remain an oddity, an unexplained piece of the transport data that awaits further investigation.

5.3   Measuring the Quantum Nonlinear Hall Effect

As discussed in Chapter 4, the quantum nonlinear Hall effect (QNLHE) has recently emerged as a powerful tool for directly measuring the Berry curvature dipole. The dipole exists only in materials with sufficiently low symmetry, and anything more than a single mirror line in a two dimensional conductor should suppress the effect.[95] Because of this, several methods[96,104,105] for breaking additional symmetries have been employed with success in materials with large Berry curvature, like WTe_2. Here, we apply the same scheme as Ye *et al.*,[105] modifying the measurement through the application of an in-plane electric field along the transverse direction. Each of the three crystal terminations show second harmonic signals that respond to this transverse field, applied as in the schematic representation shown in Fig. 4.5, though the results are not fully explained by theory, and often contradict the predictions of Sodemann and Fu.[95]

To start the investigation of the QNLHE, we first checked the responses of the longitudinal
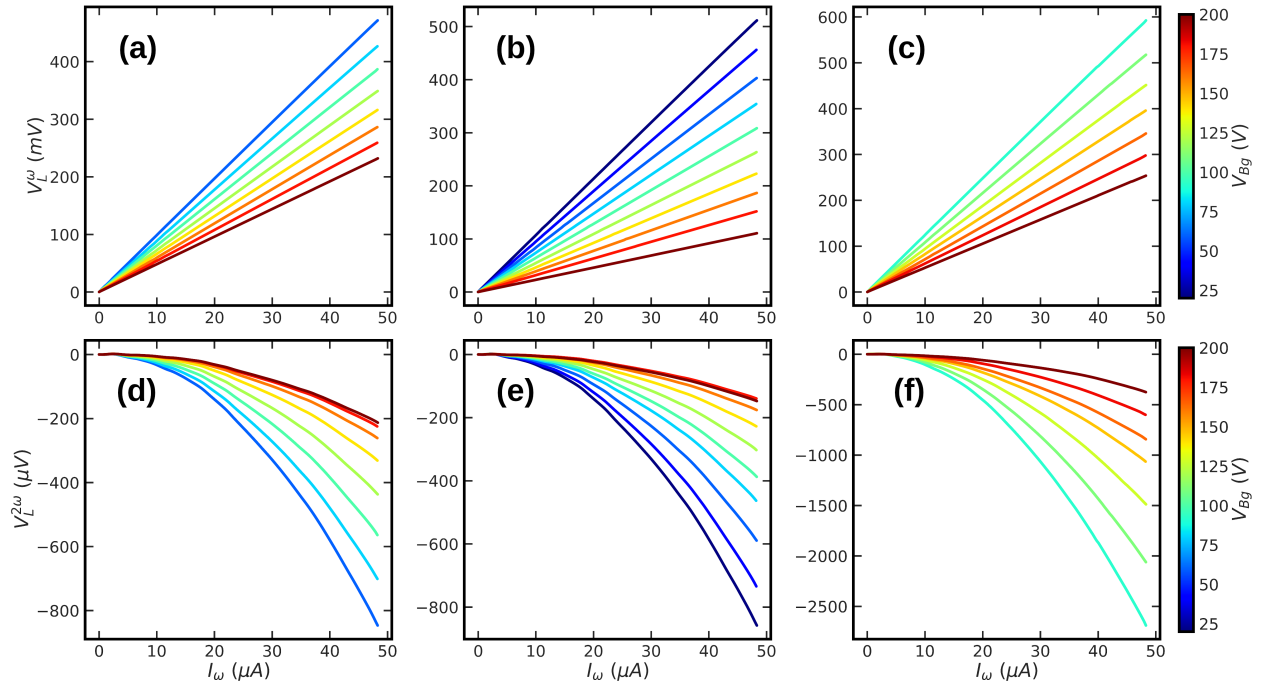
Figure 5.33: **Longitudinal 1ω and 2ω voltage signals in response to ac drive, I_ω, as a function of V_{Bg}.** Longitudinal 1ω voltages for the (a) (001), (b) (110), and (c) (111) samples. All data taken at 4 K and I$_{DC}$ = 1 μA. The corresponding longitudinal 2ω signals for the (d) (001), (e) (110), and (f) (111) samples.

resistance to an alternating current drive, I$_\omega$. Fig. 5.33 (a - c) show the results of this test, the first harmonic voltage response, $V_L^{1\omega}$, to the ac driving current for the (001), (110), and (111) samples. All data were taken at 4 K, well above the superconducting transition, and with a fixed transverse dc current of I$_{DC}$ = 1 μA as the back gate voltage was varied. Here, the (111) sample is the [1$\bar{1}$0] direction, but will be referred to as just the (111) for simplicity. The range of the reported values was restricted simply by the magnitude of the response. The samples are very resistive, especially at lower values of V_{Bg}, so a 50 μA drive produces substantial voltages across the sample. This limited the longitudinal data in particular, but had the bonus effect of avoiding many of the poor sample behaviors caused by large out-of-phase components seen at negative gate voltage in Fig. 5.1 and Fig. 5.2.

The slope of the first harmonic response is predominantly linear, which is to be expected for a well thermalized conductor, and the differential resistance values agree reasonably well with those observed in annealing curves like those shown in Fig. 5.1. There are some discrepancies on the exact resistance from annealing tests and those extracted from the differential resistance, but this is unsurprising given the long term drift in the resistance of the samples upon repeated sweeps to low gate voltages, and the nonlinear response of the samples to a longitudinal dc current drive.
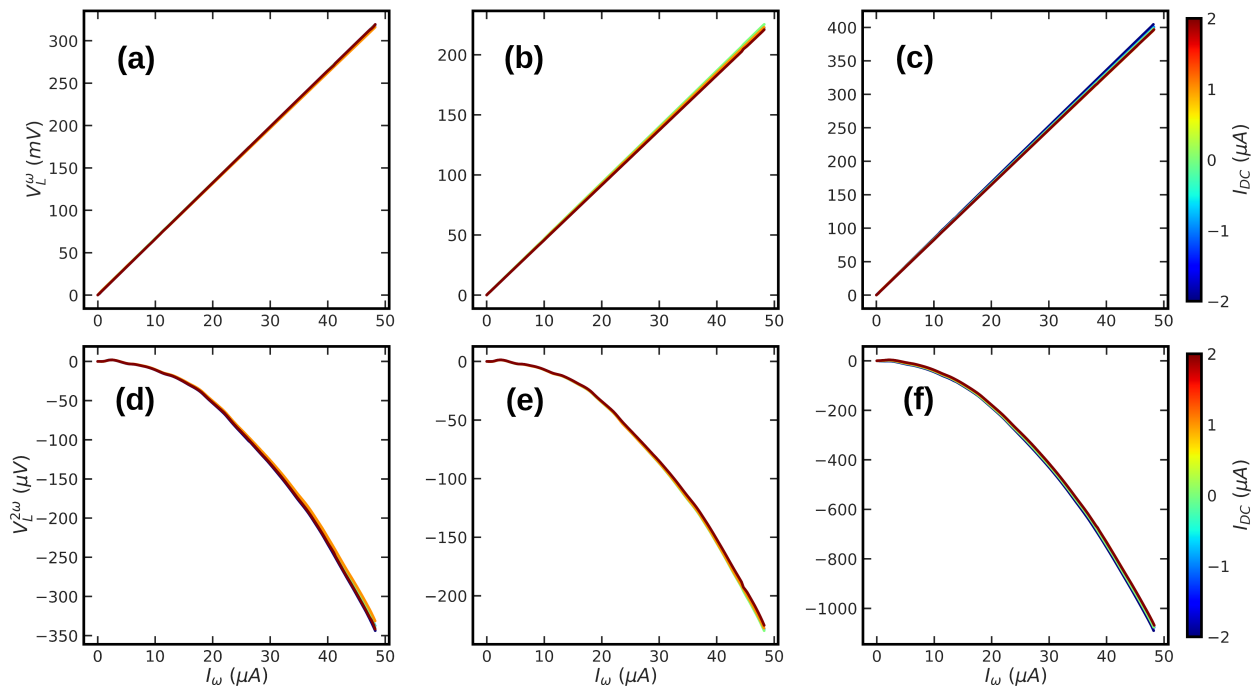
Figure 5.34: **Longitudinal 1ω and 2ω voltage signals in response to a $\mathbf{I}_\omega$ drive, as a function of $\mathbf{I}_{DC}$.** Longitudinal 1ω voltages for the (a) (001), (b) (110), and (c) (111) samples. All data taken at 4 K and V_{Bg} = 140 V. The corresponding longitudinal 2ω signals for the (d) (001), (e) (110), and (f) (111) samples.

The second harmonic voltage response, $V_L^{2\omega}$, is shown in Fig. 5.33 (d - f), and is substantially smaller in magnitude. This is to be expected, as the second harmonic should simply be the derivative of the first harmonic response with respect to drive current. The magnitude of the signal should also scale with the resistance of the first harmonic, creating the fan of larger responses for lower

gate voltages. These effects are expected, but there are obvious deviations from this behavior. The variation with I_{DC} is shown in Fig. 5.34, and produces little change in the $V_L^{1\omega}$ for any of the three samples shown in (a - c). This is good, as we don't expect that a transverse field should impact the longitudinal resistance substantially. The second harmonic response, $V_L^{2\omega}$, shown in (d - f) is similarly unaffected by the transverse I_{DC} drive, in agreement with theory and previous works.[104,105] One unexpected result is the emergence of oscillations at low current drives in the second harmonic response which do not agree with features in the first harmonic. These data, shown in Fig. 5.35, are averaged over several sweeps, both increasing and decreasing the magnitude of I_ω, so it is unlikely that these are experimental artifacts such as ringing effects.
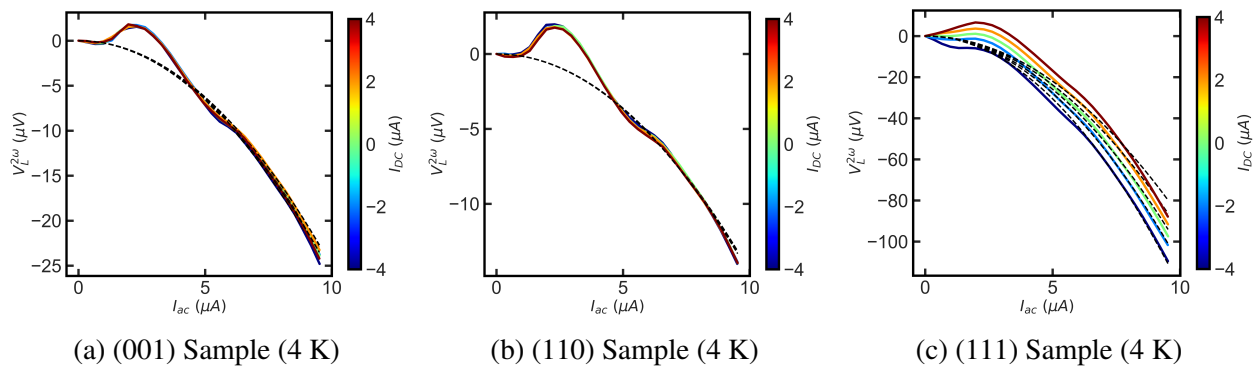
Figure 5.35: **Small I_ω drive for the 2ω voltage signals at fixed V_{Bg}.** Low ac drive data for the (001), (110), and (111) samples in (a - c), respectively. The data were taken at $V_g = 80$ V, and show the similar oscillations for each crystal direction.

Now that the longitudinal has been checked, we can turn our attention to the transverse response. Fig. 5.36 shows the first harmonic response $V_T^{1\omega}$ (a - c) and second harmonic response $V_T^{2\omega}$ (d - f) transverse responses for the (001), (110), and (111) samples, respectively. The $V_T^{1\omega}$ show the same scaling with transverse resistance as was discussed for the longitudinal data, but are not all curves are positive in slope. The sign of the signals change between samples, reflecting the sign of the resistance between Hall probes, but lacking any systematic dependence on experimental

considerations. Care was taken to account for possible sources of transverse signal such as probe misalignment, as were discussed in detail in Chapter 4, so they are unlikely to be responsible for the observed signal.
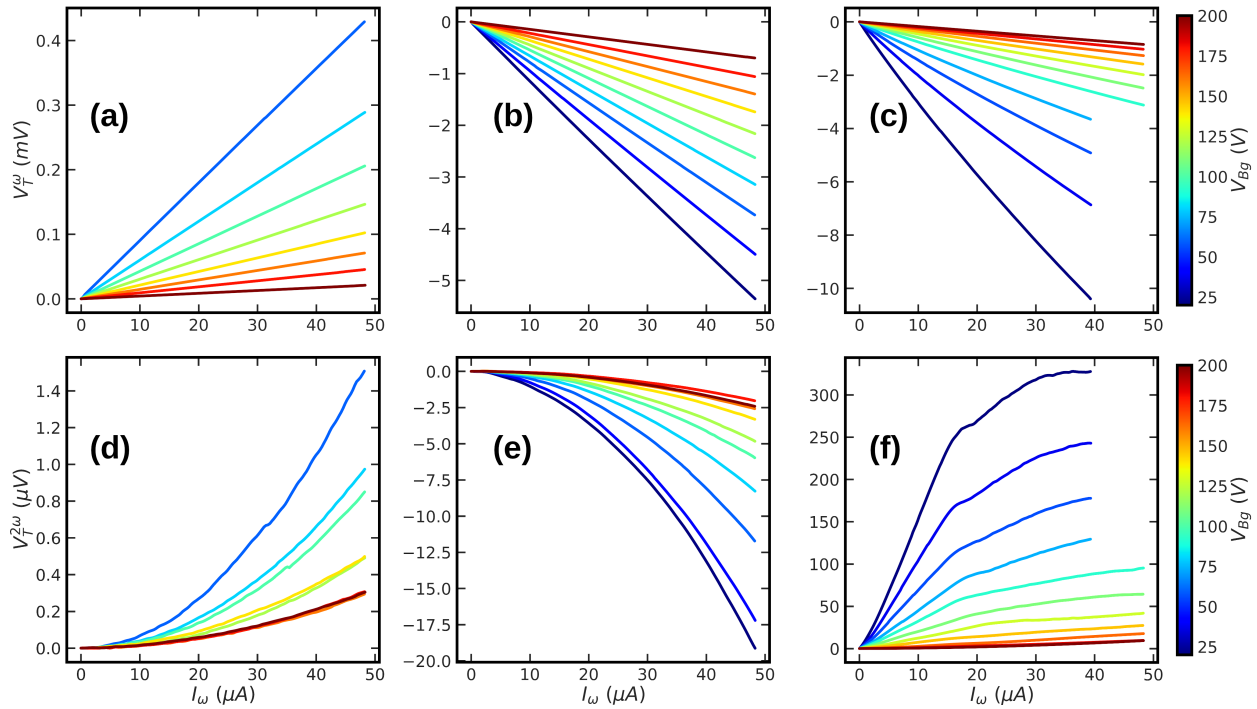
Figure 5.36: **Transverse 1ω and 2ω voltage signals in response to a I$_\omega$ drive, as a function of I$_{DC}$.** Transverse 1ω voltages for the (a) (001), (b) (110), and (c) (111) samples. All data taken at 4 K and V_{Bg} = 140 V. The corresponding transverse 2ω signals for the (d) (001), (e) (110), and (f) (111) samples.

Another deviation is the shape of the $V_T^{1\omega}$, which should be linear and is not, especially in the (111) which shows added curvature at low values of I$_\omega$. This change of slope does not seem to be reflected in the second harmonic signals, which mostly show the expected I$_\omega^2$ dependence predicted for the QNLHE. The response is smallest in the (001) and larger in the (110). Unexpectedly, the magnitude of the response is far larger in the (111), and does not follow the expected I$_\omega^2$ dependence at all. All of the data shown in Fig. 5.36 are taken for I$_{DC}$ = 1 μA, as with the longitudinal data,

and each of the $V_T^{2\omega}$ show a sizable response that is modified with V_{Bg} as expected. What is not expected is the sign of the response, which once again seems to change with no clear dependence on external parameters or the sign of the $V_T^{1\omega}$.

There is also no explanation for the added features in the (111) sample, in particular the peak that appears at different values of I_ω for different gate voltages, and punctuates a clear deviation from the expected I_ω^2 dependence predicted for the QNLHE. This deviation can be seen clearly in Fig. 5.37, which shows the data for fixed $V_{Bg} = 140$ V and the full range of I_{DC}. The $V_T^{1\omega}$ shows a weak dependence on I_{DC}, potentially reflecting a change in resistance along the current path, but is otherwise unaffected by the transverse current. The $V_T^{2\omega}$ is modified strongly by I_{DC}, as expected, and even changes sign for the (001) sample.

The $V_T^{2\omega}$ dependence of the (001) sample, shown in Fig. 5.37 (d), behaves exactly how we would expect this measurement to work. The (001) surface has C_4 symmetry, as discussed in Chapter 3, and applying the in-plane field breaks this symmetry, leaving the single mirror line and a clean I_ω^2 dependence as predicted by Sodemann and Fu. Even the deviation from zero for the I_{DC} = 0 trace could be explained by the crystal miscut or some small deviations in lithography. This is a good indication of the validity of this measurement and the magnitude reflects the small Berry curvature dipole potential due to minimal spin-orbit coupling on the (001) surface.

The other two signals are not as well behaved. The (110) sample shown in Fig. 5.37 (e) does appear to be modulated by I_{DC}, and does have a nice I_ω^2 dependence. The fact that it does not go through zero for I_{DC} = 0 μA could be due to the existence of a large Berry curvature dipole native to the surface, which was shown in Fig. 3.10. The combination of 2-fold C_2 symmetry and anisotropic spin-orbit interactions combine to create a Berry curvature dipole along the $[1\bar{1}0]$ direction, which would give a transverse response like this. Additional symmetry breaking from the driving current is expected to modulate the response, and it does, but not monotonically. Indeed,
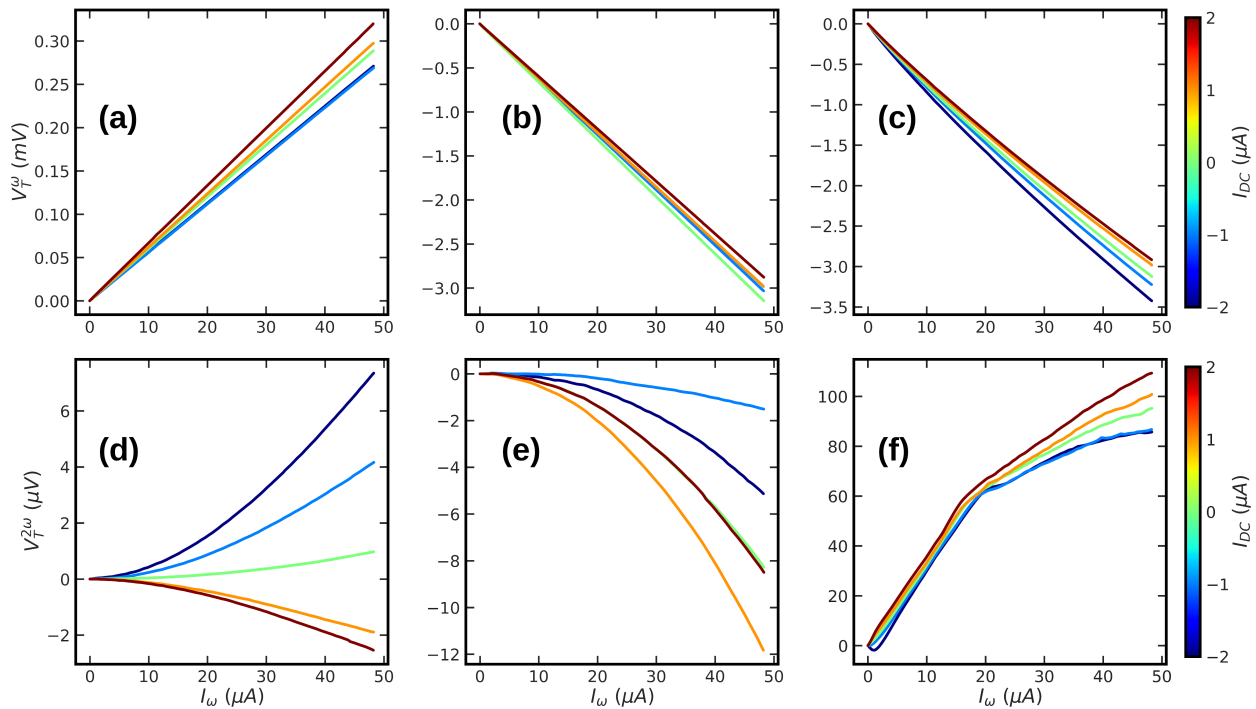
Figure 5.37: **Transverse 1ω and 2ω voltage signals in response to a I_ω drive, as a function of I_{DC}.** Transverse 1ω voltages for the (a) (001), (b) (110), and (c) (111) samples. All data taken at 4 K and V_{Bg} = 140 V. The corresponding transverse 2ω signals for the (d) (001), (e) (110), and (f) (111) samples.

the I_{DC} response of the (110) sample is not monotonic in I_{DC}, a fact reflected in the ordering of the curves in Fig. 5.37 (e). It is not clear why this happens, and it is a deviation from the theory, despite the surface having the best chance of natively hosting the QNLHE response.

The (111), shown in Fig. 5.37 (f) does not agree with theory at all. For low I_ω it may have the expected I_ω^2 dependence, but that it is quickly collapsed into a large linear response up to I_ω = 20 μA. At this point there is a cusp and a further fanning that is sub I_ω in scaling. This, coupled with the magnitude of the response, mark strong deviations from the expectations of the QNLHE, and suggest that another mechanism is responsible for the sizable and feature rich signal seen in the traces. This is all in a sample that, by symmetry considerations, should not have a QNLHE signal

at all. The C_6 (C_3 effectively) symmetry shown in Fig. 3.11 should not host a Berry curvature dipole in any direction, though it may do so under applied I_{DC}. None of the traces for the (111) cross zero except at very low values of I_ω, a strong deviation from prediction.

Both the (110) and (111) seem to deviate from the theoretical predictions of the QNLHE, in both the shape of the response and the ordering of the dependence on I_{DC}. One possible reason for this is simply a matter of competing phenomenon. The (111) sample was shown to have magnetic ordering in the magnetoresistance traces taken at 4 K, the same temperature as these QNLHE measurements. In the presence of time reversal symmetry breaking processes, the signal of the QNLHE has other contributions from other sources, which could potentially explain the data.

Additionally, the theory of Sodemann and Fu assumes the limit of a probing field, here supplied by I_ω, which is too small to disrupt the Fermi surface or modify the Berry curvature. The effective fields use in this study were more than an order of magnitude higher than those used in comparable studies in thin films,[104,105] due largely to the scale and resistance of the samples. It could be that the interactions of this large field with the Berry curvature result in other, larger effects seen in the $V_T^{2\omega}$. There is precedent for this in the work of Dzaber et $al.$[113] who showed the emergence of the QNLHE in both the $V_T^{2\omega}$ and $V_T^{1\omega}$ signals of a dilute Kondo semimetal, $Ce_3Bi_4Pd_3$. The explanation proposed in that work was that the measurement quickly left the probing field limit, resulting in a large response in both harmonics. This could certainly be the case for different materials, in particular when there is an emergent magnetic order, or dilute magnetic moments as is the case in these KTO samples.

At the time of writing there is no good theory that fully describes the results shown on KTO. This could be due to compounding effects of the other physical phenomena like magnetism in the samples, or it could be due to the limitations of the assumptions of the theory of Sodemann and Fu. To correct for this, measurements should be reproduced above the temperatures where compound-

ing effects take hold, and smaller samples should be made to allow for a more delicate probing of the effect. Additionally, it may be useful to track the scattering scaling as was done for WTe$_2$ by Kang *et al.*[104] Either way, the takeaway is the same as discussed previously in Chapter 2, that simply measuring a QNLHE signal is insufficient so claim a Berry curvature dipole effect. Even the first paper[96] on the observation of the QNLHE used corroborating measurements to support the claim of Berry curvature dipole reconstruction. Such caution should be taken in any measurement that deviates strongly from established results.

Despite the deviation, it does appear that a QNLHE signal can be realized in KTO samples given the correct experimental design. The (001) sample behaved quite well, obeying the symmetry constraints and showing signals comparable to those seen in literature.[96,105] A careful analysis of the deviation from experiment have yielded interesting points of inquiry that would benefit greatly from more theoretical support. In particular, the large signals in the (111) may need more testing to disentangle secondary effects, but may provide a fruitful platform for further study. The (110) surface also holds promise, in particular due to its native Berry curvature dipole, which can be addressed in other ways to test the interaction between its magnetism and or superconductivity. If it could be established that the features in the (111) did in fact come from magnetic moments, it may be that the QNLHE is a secondary, purely electronic, probe for emergent magnetic order in samples such as these. This would be easy enough to test on the (110), which should have a magnetic ordering transition below 4 K. In any case, there are many potential experiments to perform using the QNLHE as a probe, and careful control may yield the original idea of reconstructing the Berry curvature from experimental observation.

CHAPTER 6

THESIS CONCLUSION AND FUTURE DIRECTIONS

6.1   Summary of Thesis Work

To summarize the works presented in this thesis, we first reflect on the nature of the project. This was a largely exploratory work, testing a novel fabrication technique and adjusting expectations as new results were measured. Because of this a large amount of data was not included in this work, but may be useful as a basis for future studies. There were many novelties introduced in the work of the manuscript, representing improvements to material properties shown in literature, or showing novel phenomena for the KTO system. An effort to understand and explain these results followed, with limitations due to experimental constraints or simply time. Despite this, the system proved to be a fruitful test bed, and should be the subject of further study.

The work started with a discussion of the fabrication steps necessary to create conducting gases at the KTO interface. We used a modification of a little-used technique of aluminum deposition to generate a conducting gas on the surface hosted by oxygen vacancies. The process was improved between generations of samples, and suggestions for further improvement are included in Chapter 4. With the improvements, the two dimensional gases were shown to be electron-like conductors through annealing curves and Hall measurements in the normal state. The testing revealed that the devices hosted carrier concentrations higher than those seen in literature for similar devices, with concentrations as high as 1.4×10^{14} (e$^-$ / cm^2) for the (110) and (111) superconducting samples. Carrier mobilities were also improvements over literature results, with over 1100 cm^2 V^{-1} s^{-1} at the highest gate voltages in the (110) superconducting sample. All of the carrier behavior was

shown to be readily tuned with gate voltage, and revealed several Lifshitz transitions in the samples shown by peaks in carrier concentrations as a function of applied V_g. These results are novel for KTO systems, and should be published.

Further investigation of the normal state magnetoresistance revealed the emergence of magnetism, shown in hysteretic features in the 30 mK longitudinal and transverse traces of the normal sample set. This magnetism was shown to be suppressed with parallel field, tuned with gate voltage, and was only present below 1.7 K in the normal samples. In the superconducting samples the (111) direction showed hysteresis up to 4 K in longitudinal magnetoresistance traces, once again representing a novel result. This magnetism was further shown to coexist with the superconductivity hosted on the (110) and (111) superconducting samples, shown as peaks in the zero resistance state arising from vortex motion in response to the magnetic switching.

A characterization of the superconducting state followed, showing not only the coexistence with magnetism mentioned above, but a novel dependence on gate voltage. The (110) sample could be gated out of superconductivity with increasing V_g, and the (111) sample showed a suppression of the superconducting state with increasing V_g, a sharp departure from the literature expectation of a linear modulation of both the carrier concentration and the superconducting T_c with increasing V_g. This upper limit to the superconductivity is novel, as is the observation of suppressed superconductivity in the (111) and the relation to the possible observation of a striped phase resulting in directional superconductivity in the (111) sample, [$1\bar{1}0$] direction. Analytic analysis of the superconducting state revealed strange dependences for both T_c as mentioned, but also H_{c2}, and a comparison of the relation between these two values as a function of gate voltage revealed a surprising agreement between the two surfaces. Further analysis estimated the penetration depth, coherence length, and GL κ for the samples, in agreement with references in literature. The films are very much Type-II, as expected, and the value of κ was shown to vary by nearly an order of

magnitude with V_g, with κ lowest for the highest gate voltage values.

An extension of the analysis to the Halperin-Nelson forms proved difficult. Fits to the edges of the superconducting transition were not good, but did allow for an estimation of T_{BKT} and a comparison of the two-dimensionalness of the superconductivity, which was also poor. A combination of the intrinsic magnetism and the disorder in the samples combined to broaden the transitions and make the assumptions of the Halperin-Nelson form questionable. This inhomogeneity was also on display in critical current and parallel field measurements. Parallel field magnetoresistance showed strange, spin-valve like behavior in the normal state and wandering river like asymmetric traces in the superconducting state. Critical current measurements revealed much inhomogeneity, and showed an enhancement of I_c under parallel field for the (111) superconducting state, but only in one direction. These results are also novel, but lack sufficient experimental evidence to make conclusive statements about the nature of the underlying physics.

Finally, an investigation of the quantum nonlinear Hall effect showed promising results that also do not agree with established theory. The measurement scheme adopted from Ye *et al.* proved effective, yielding good results for the (001) and (110), but the (111) deviated strongly from expectation. Additionally, there were several features of the measurements that could not be accounted for in normal theory, and may be a result of competing physical phenomena in the samples, including magnetism. Further investigation is necessary to reach the goal of the measurements, which sought to reconstruct the Berry curvature dipole as a function of gate voltage, but some of the results are in the process of being written up for publication.

In total, there were many novel results, and the work largely will serve as a foundation for future studies. Many of the results do stand alone, and will be published after the time of writing. Additionally, based on the analysis completed there are several suggestions for future works presented in the next section.

6.2 Future Work

Because the nature of this work was largely exploratory, measurements focused on characterizing the AlO_x / KTO system as thoroughly as reasonably possible. As a result was only able to expand testing for certain results like for the quantum nonlinear Hall effect. Part of this limit was time, part of it was sample design, and part was limited by the novelty of the preliminary results obtained and the limit of our understanding of them at the time. As a result, there are many ideas of experiments to try on these samples should future students take an interest, and some of the more serious designs are detailed here.

6.2.1 Critical Temperature vs Field

The first suggested experiment is relatively simple to perform, and has many potentially interesting results based on measurements already performed. Using a PID technique to bias the sample at a midpoint of the transition, trace out the temperature dependence of the critical field, H_c. This technique is discussed in detail in Manan Mehta's thesis,[133] and is the same used in Kevin Ryan's recent paper.[178] It uses a bridge to track changes in resistance in the superconducting transition, using it as the error signal to run a PID that keeps the sample in the transition as the magnetic field is swept. The result is a trace of the phase boundary of the superconducting state in the T_c vs H phase space, a more complete way of characterizing the information contained in $R(T)$ and magnetoresistance traces taken here.

The measurement would look for a number of things, most fundamentally the shape of the superconducting phase boundary which should be linear in perpendicular field for normal superconductors in the absence of more exotic forms of order. I expect that there will be hysteresis in the shape of the curve similar to what was shown in STO systems[84], and this would be further proof

of magnetic order coexisting with the superconductivity. Measuring this as a function of back gate voltage would create an information dense map of the relative strength of the magnetisation for different superfluid densities, potentially illuminating the nature of the superconducting and magnetic contributions to the conduction. This procedure can be completed for parallel field as well, and the derivative of the curves would give information about the effective coherence length and superfluid thickness for the perpendicular and parallel field traces respectively.[178] Additional measurements at various points on the transition curve could be completed should compelling results show for the first test, since transition shape changes dramatically with gate voltage.

Simultaneously, a measurement of the transverse signal should be taken while performing the same tests detailed above. This would be looking for the magnitude and sign of the Hall signal as a function of field and back gate voltage. I strongly suspect that the resulting signal will be non-trivial and show strong variation with gate voltage and bias point in the transition. More work would need to be done to understand the nature of this effect, but there is a large body of work to pull from as discussed in Chapter 5. It may be that the signal is related to the magnetism in the conducting layer, in which case the Hall would be most pronounced at low fields and should also show hysteresis. In either case, KTO should be an ideal system to study the Hall sign change problem which has only briefly been explored outside of high T_c superconductors.

The challenge of this technique will be capturing all of the compounding effects in these samples. Unlike with many other superconductors, the resistance of the samples changes dramatically with back gate and applied field, which means biasing at a fixed percentage of the transition will be difficult or impossible. On the other hand, the large resistance range and wealth of potential effects lends itself well to the technique, and the newly revived Janus probe would be ideal for measuring the temperature ranges of the transition observed in this work.

6.2.2 Mesoscopic Samples

One of the advantages of using amorphous aluminum oxide as a top layer for the conducting heterostructure is that it can be readily adapted to much smaller devices than traditional etching techniques for STO heterostructures. This unlocks a number of interesting experimental possibilities, made possible by a combination of conducting discharge layer that I adapted for the use on STO systems, and the chemical etching process for AlO_x using MF-319. These technical tools will allow for mesoscopic devices with feature sizes of 1 μm or less, wedding this complex oxide platform to the other techniques of the Mesoscopic Physics Lab. The breadth of experimental design would widen significantly, and a few suggestions for starting experiments are listed below.

The most obvious improvement would be a simple extensions of the Hall bar geometry to sub-micron size scales. This dimensional reduction would allow for an investigation of potential physics like Spin Hall Effect, quantum Hall effect, or non-reciprocal transport. Similar works were completed on STO based systems but the application to mesoscopic KTO samples is very limited. It would also allow for a more detailed investigation of crystalline anisotropy, particularly in the superconducting state on the (111) terminated samples. These measurements be made possible by the scale of the sample and by improved homogeneity, as suggested in the experiment section of Chapter 4. In particular, improvements to fabrication techniques may allow for further improvement in the carrier concentration on the (001), which *may* allow for gating into the superconducting state, an observation that has not been replicated since the first discovery using ionic liquid gel.[14]

The same mesoscopic fabrication techniques could easily be adapted to other experimental configurations. The Little-Parks effect could be investigated, probing changes in resistance due to flux quanta trapped in a superconducting ring kept at the foot of the transition. This would probe the pairing of the superconductivity hosted at the interface, and may be surprisingly non-trivial due to the compounding effects of the intrinsic magnetism. Similar interference experiments could

make use of asymmetric Little-Parks rings, or asymmetric SQUIDs, both of which would probe the superconducting pairing in comparison to a second superconducting arm. Even simple planar tunnel junctions would be interesting, making use of the thin AlO_x overlayer to make a normal metal, superconducting, or magnetic tunnel contact onto the Hall bar to probe density of states, superconducting gap, or spin polarization of the 2DEG. The possibilities are numerous, and are limited only by priority and a few remaining technical hurdles.

6.2.3 Thin Film Heterostructures

A potential future project would look at the interactions between the AlO_x / KTO conducting gas and van der Waals thin films with various properties. Once again taking advantage of the thickness of the AlO_x overlayer, thin films with interesting magnetic or electronic order can be stamped on top of existing conducting structures or built into them. The flexibility of fabrication combines well with the ease of optical identification of thin films on KTO substrates, opening a whole realm of possible experiments. In particular, it would be interesting to see the interplay with other gate-dependent superconducting materials like MoS_2, both for use in mesoscopic devices suggested above and for planar heterostructures. Even if the KTO is only used as a platform for heterostructure construction, the consistency of the surface, the strong spin orbit effect, and the ease of fabrication would make it a compelling playground for more advanced device fabrication.

There are already many examples of experiments conducted on STO substrates to use as a starting point, and much of the technical barrier for device fabrication has been lifted with advancements in our groups fabrication processes. Combining these improvements with the technical fabrication advances for KTO described here and the availability of the new Tescan SEM should allow for creative control over sample design, should future students be interested.

REFERENCES

1. Darrow, Karl K. Minutes of the Meeting at Washington, April 28 – 30, 1949. *Physical Review* **76,** 160–193 (July 1949).

2. Matthias, B. T. New Ferroelectric Crystals. *Physical Review* **75,** 1771–1771 (June 1949).

3. Perry, C. H., Fertel, J. H. & McNelly, T. F. Temperature Dependence of the Raman Spectrum of $SrTiO_3$ and $KTaO_3$. *The Journal of Chemical Physics* **47,** 1619–1625 (Sept. 1967).

4. Frova, A. & Boddy, P. J. Optical Field Effects and Band Structure of Some Perovskite – Type Ferroelectrics. *Physical Review* **153,** 606–616 (Jan. 1967).

5. Perry, C. H. & Tornberg, N. E. *The Raman Spectra of $PbTiO_3$ and Solid Solutions of $NaTaO_3$ – $KTaO_3$ and $KTaO_3$ – $KNbO_3$* in *Light Scattering Spectra of Solids* (ed Wright, G. B.) (Springer Berlin Heidelberg, Berlin, Heidelberg, 1969), 467–476. ISBN: 978-3-642-87357-7.

6. Davis, T. G. Dielectric Properties and Soft Modes in the Ferroelectric Mixed Crystals $K_{(1-x)}$ $Na_x TaO_3$. *Physical Review B* **5,** 2530–2537 (Apr. 1972).

7. Wemple, S. H. Some Transport Properties of Oxygen-Deficient Single-Crystal Potassium Tantalate ($KTaO_3$). *Physical Review* **137,** A1575–A1582 (Mar. 1965).

8. Schooley, J. F., Hosler, W. R. & Cohen, M. L. Superconductivity in Semiconducting $SrTiO_3$. *Physical Review Letters* **12,** 474–475 (Apr. 1964).

9. Thompson, J. R., Boatner, L. A. & Thomson, J. O. Very low-temperature search for superconductivity in semiconducting $KTaO_3$. *Journal of Low Temperature Physics* **47,** 467–475 (June 1982).

10. Müller, K. A. & Burkard, H. $SrTiO_3$: An intrinsic quantum paraelectric below 4K. *Physical Review B* **19,** 3593–3602 (Apr. 1979).

11. Ueno, K. *et al.* Field-effect transistor based on $KTaO_3$ perovskite. *Applied Physics Letters* **84,** 3726–3728 (May 2004).

12. Ueno, K. *et al.* Field-effect transistor on $SrTiO_3$ with sputtered Al_2O_3 gate insulator. *Applied Physics Letters* **83,** 1755–1757 (Sept. 2003).

13. Nakamura, H. & Kimura, T. Electric field tuning of spin-orbit coupling in $KTaO_3$ field-effect transistors. *Physical Review B* **80,** 121308 (Sept. 2009).

14. Ueno, K. *et al.* Discovery of superconductivity in $KTaO_3$ by electrostatic carrier doping. *Nature Nanotechnology* **6,** 408–412 (July 2011).

15. Zhang, H. *et al.* Highly Mobile Two-Dimensional Electron Gases with a Strong Gating Effect at the Amorphous $LaAlO_3$ /$KTaO_3$ Interface. *ACS Applied Materials & Interfaces* **9,** 36456–36461 (Oct. 2017).

16. Chen, Z. *et al.* Electric field control of superconductivity at the $LaAlO_3$ /$KTaO_3$ (111) interface. *Science* **372,** 721–724 (May 2021).

17. Zhang, H. *et al.* High-Mobility Spin-Polarized Two-Dimensional Electron Gases at EuO / $KTaO_3$ Interfaces. *Physical Review Letters* **121,** 116803 (Sept. 2018).

18. Liu, C. *et al.* Two-dimensional superconductivity and anisotropic transport at $KTaO_3$ (111) interfaces. *Science* **371,** 716–721 (Feb. 2021).

19. Wadehra, N. *et al.* Planar Hall effect and anisotropic magnetoresistance in polar-polar interface of $LaVO_3$-$KTaO_3$ with strong spin-orbit coupling. *Nature Communications* **11,** 874 (Dec. 2020).

20. Jain, A. *et al.* Commentary: The Materials Project: A materials genome approach to accelerating materials innovation. *APL Materials* **1,** 011002 (2013).

21. Jellison, G. E., Paulauskas, I., Boatner, L. A. & Singh, D. J. Optical functions of $KTaO_3$ as determined by spectroscopic ellipsometry and comparison with band structure calculations. *Physical Review B* **74,** 155130 (Oct. 2006).

22. Aktas, O., Crossley, S., Carpenter, M. A. & Salje, E. K. H. Polar correlations and defect-induced ferroelectricity in cryogenic $KTaO_3$. *Physical Review B* **90,** 165309 (Oct. 2014).

23. Prater, R. L., Chase, L. L. & Boatner, L. A. Raman scattering studies of the impurity-induced ferroelectric phase transition in $KTaO_3$: Nb. *Physical Review B* **23,** 221–231 (Jan. 1981).

24. Skoromets, V. *et al.* Ferroelectric phase transition in polycrystalline $KTaO_3$ thin film revealed by terahertz spectroscopy. *Applied Physics Letters* **99,** 052908 (Aug. 2011).

25. Cardona, M. Optical Properties and Band Structure of $SrTiO_3$ and $BaTiO_3$. *Physical Review* **140,** A651–A655 (Oct. 1965).

26. Unoki, H. & Sakudo, T. Electron Spin Resonance of Fe^{3+} in $SrTiO_3$ with Special Reference to the 110°K Phase Transition. *Journal of the Physical Society of Japan* **23,** 546–552 (1967).

27. Ma, H. J. H. *et al.* Local Electrical Imaging of Tetragonal Domains and Field-Induced Ferroelectric Twin Walls in Conducting $SrTiO_3$. *Physical Review Letters* **116,** 257601 (June 2016).

28. Frenkel, Y., Xie, Y., Hwang, H. Y. & Kalisky, B. Magnetism and Conductivity Along Structural Domain Walls of $SrTiO_3$. *Journal of Superconductivity and Novel Magnetism* **33,** 195–197 (Jan. 2020).

29. Kalisky, B. *et al.* Locally enhanced conductivity due to the tetragonal domain structure in $LaAlO_3$/$SrTiO_3$ heterointerfaces. *Nature Materials* **12,** 1091–1095 (Dec. 2013).

30. Krantz, P. W. & Chandrasekhar, V. Observation of Zero-Field Transverse Resistance in AlO_x / $SrTiO_3$ Interface Devices. *Physical Review Letters* **127,** 036801 (July 2021).

31. Christensen, D. V. *et al.* Strain-tunable magnetism at oxide domain walls. *Nature Physics* **15,** 269–274 (Mar. 2019).

32. Bruno, F. Y. *et al.* Band Structure and Spin–Orbital Texture of the (111)-$KTaO_3$ 2D Electron Gas. *Advanced Electronic Materials* **5,** 1800860 (May 2019).

33. Mattheiss, L. F. Energy Bands for $KNiF_3$, $SrTiO_3$, $KMoO_3$, and $KTaO_3$. *Phys. Rev. B* **6,** 4718–4740 (12 Dec. 1972).

34. Edmondson, D. Electronic band structure of $KTaO_3$. *Solid State Communications* **12,** 981–984 (1973).

35. Slater, J. C. & Koster, G. F. Simplified LCAO Method for the Periodic Potential Problem. *Phys. Rev.* **94,** 1498–1524 (6 June 1954).

36. Uwe, H., Okubo, N., Yoshizaki, R. & Sakudo, T. Magnetic Breakdown Effect in $KTaO_3$. *Japanese Journal of Applied Physics* **26,** 639–640 (1987).

37. Santander-Syro, A. F. *et al.* Orbital symmetry reconstruction and strong mass renormalization in the two-dimensional electron gas at the surface of KTaO$_3$. *Physical Review B* **86,** 121107 (Sept. 2012).

38. King, P. D. C. *et al.* Subband Structure of a Two-Dimensional Electron Gas Formed at the Polar Surface of the Strong Spin-Orbit Perovskite KTaO$_3$. *Physical Review Letters* **108,** 117602 (Mar. 2012).

39. Bareille, C. *et al.* Two-dimensional electron gas with six-fold symmetry at the (111) surface of KTaO$_3$. *Scientific Reports* **4,** 3586 (May 2015).

40. Arnault, E. G. *et al.* Anisotropic superconductivity at KTaO$_3$ (111) interfaces. *Science Advances* **9,** eadf1414 (Feb. 2023).

41. Villar Arribi, P., Paramekanti, A. & Norman, M. R. Striped electron fluid on (111) KTaO$_3$. *Physical Review B* **103,** 035115 (Jan. 2021).

42. Ohtomo, A. & Hwang, H. Y. A high-mobility electron gas at the LaAlO$_3$/SrTiO$_3$ heterointerface. *Nature* **427,** 423–426 (Jan. 2004).

43. Ueno, K. *et al.* Electric-field-induced superconductivity in an insulator. *Nature Materials* **7,** 855–858 (Nov. 2008).

44. Saito, Y. *et al.* Superconductivity protected by spin–valley locking in ion-gated MoS$_2$. *Nature Physics* **12,** 144–149 (Feb. 2016).

45. Santander-Syro, A. F. *et al.* Two-dimensional electron gas with universal subbands at the surface of SrTiO$_3$. *Nature* **469,** 189–193 (Jan. 2011).

46. Meevasana, W. *et al.* Creation and control of a two-dimensional electron liquid at the bare SrTiO3 surface. *Nature Materials* **10,** 114–118 (Feb. 2011).

47. Harashima, S. *et al.* Coexistence of two-dimensional and three-dimensional Shubnikov–de Haas oscillations in Ar$^+$ -irradiated KTaO$_3$. *Physical Review B* **88,** 085102 (Aug. 2013).

48. Zou, K. *et al.* LaTiO$_3$ /KTaO$_3$ interfaces: A new two-dimensional electron gas system. *APL Materials* **3,** 036104 (Mar. 2015).

49. Rubi, K. *et al.* Electronic subbands in the a - LaAlO$_3$ / KTaO$_3$ interface revealed by quantum oscillations in high magnetic fields. *Physical Review Research* **3,** 033234 (Sept. 2021).

50. Sun, Y. *et al.* Critical Thickness in Superconducting $LaAlO_3$ / $KTaO_3$ (111) Heterostructures. *Physical Review Letters* **127,** 086804 (Aug. 2021).

51. Wang, Y. *et al.* Creating a two-dimensional hole gas in a polar/polar $LaAlO_3$ /$KTaO_3$ perovskite heterostructure. *Journal of Materials Chemistry C* **8,** 14230–14237 (2020).

52. Deng, X. *et al.* Strain engineering of epitaxial oxide heterostructures beyond substrate limitations. *Matter* **4,** 1323–1334 (2021).

53. Huang, Z. *et al.* The Effect of Polar Fluctuation and Lattice Mismatch on Carrier Mobility at Oxide Interfaces. *Nano Letters* **16.** PMID: 26959195, 2307–2313 (2016).

54. Han, K. *et al.* Controlling Kondo-like scattering at the $SrTiO_3$ -based interfaces. *Scientific Reports* **6** (May 2016).

55. Han, K. *et al.* Electrical properties and subband occupancy at the $(La, Sr)(Al, Ta)O_3/SrTiO_3$ interface. *Phys. Rev. Mater.* **1,** 011601 (1 June 2017).

56. Bal, V. V. *et al.* Strong spin-orbit coupling and magnetism in (111) $(La_0.3Sr_0.7)(Al_0.65Ta_0.35)O_3$ / $SrTiO_3$. *Physical Review B* **98,** 085416 (Aug. 2018).

57. Bal, V. V. *et al.* Low-temperature magnetoresistance of (111) $(La_{0.3}Sr_{0.7})(Al_{0.65}Ta_{0.35})O_3/SrTiO_3$. *Phys. Rev. B* **99,** 035408 (3 Jan. 2019).

58. Ma, Y. *et al.* Superconductor-Metal Quantum Transition at the EuO/$KTaO_3$ Interface*. *Chinese Physics Letters* **37,** 117401 (Nov. 2020).

59. Shen, S. *et al.* Observation of quantum Griffiths singularity and ferromagnetism at the superconducting $LaAlO_3/SrTiO_3(110)$ interface. *Phys. Rev. B* **94,** 144517 (14 Oct. 2016).

60. Hua, X. *et al.* Tunable two-dimensional superconductivity and spin-orbit coupling at the EuO/$KTaO_3$ (110) interface. *npj Quantum Materials* **7,** 97 (Sept. 2022).

61. Kumar, N. *et al.* Observation of Shubnikov–de Haas Oscillations, Planar Hall Effect, and Anisotropic Magnetoresistance at the Conducting Interface of EuO–$KTaO_3$. *Advanced Quantum Technologies* **4,** 2000081 (Jan. 2021).

62. Hotta, Y., Susaki, T. & Hwang, H. Y. Polar Discontinuity Doping of the $LaVO_3/SrTiO_3$ Interface. *Phys. Rev. Lett.* **99,** 236805 (23 Dec. 2007).

63. Liang, H. *et al.* Nonmonotonically tunable Rashba spin-orbit coupling by multiple-band filling control in $SrTiO_3$-based interfacial d-electron gases. *Phys. Rev. B* **92,** 075309 (7 Aug. 2015).

64. Goyal, S., Wadehra, N. & Chakraverty, S. Tuning the Electrical State of 2DEG at $LaVO_3$-$KTaO_3$ Interface: Effect of Light and Electrostatic Gate. *Advanced Materials Interfaces* **7,** 2000646 (Aug. 2020).

65. Silotia, H. *et al.* Possible Signatures of Chiral Anomaly in the Magnetoresistance of a Quasi-2-Dimensional Electron Gas at the Interface of $LaVO_3$ and $KTaO_3$. *Advanced Electronic Materials,* 2200195 (June 2022).

66. Liu, Y. *et al.* Superconductivity in epitaxially grown $LaVO_3$ /$KTaO_3$ (111) heterostructures. *Chinese Physics B* **32,** 037305 (Mar. 2023).

67. Al-Tawhid, A. H., Kumah, D. P. & Ahadi, K. Two-dimensional electron systems and interfacial coupling in $LaCrO_3$ /$KTaO_3$ heterostructures. *Applied Physics Letters* **118,** 192905 (May 2021).

68. Al-Tawhid, A. H. *et al.* Superconductivity and Weak Anti-localization at $KTaO_3$ (111) Interfaces. *Journal of Electronic Materials* (Aug. 2022).

69. Mallik, S. *et al.* Superfluid stiffness of a $KTaO_3$-based two-dimensional electron gas. *Nature Communications* **13,** 4625 (Aug. 2022).

70. Vicente-Arche, L. M. *et al.* Spin–Charge Interconversion in $KTaO_3$ 2D Electron Gases. *Advanced Materials* **33,** 2102102 (Oct. 2021).

71. Qi, S. *et al.* Large Optical Tunability of 5d 2D Electron Gas at the Spinel/Perovskite γ-Al_2 O_3 /$KTaO_3$ Heterointerface. *Advanced Materials Interfaces* **9,** 2200103 (July 2022).

72. Zou, Y. *et al.* Transport behaviors of topological band conduction in $KTaO_3$'s two-dimensional electron gases. *npj Quantum Materials* **7,** 122 (Dec. 2022).

73. Wang, F.-N. *et al.* Prediction of high-mobility two-dimensional electron gas at $KTaO_3$ -based heterointerfaces. *Chinese Physics B* **28,** 047101 (Apr. 2019).

74. Monteiro, A. M. R. V. L. *et al.* Two-dimensional superconductivity at the (111)$LaAlO_3/SrTiO_3$ interface. *Phys. Rev. B* **96,** 020504 (2 July 2017).

75. Davis, S. *et al.* Magnetoresistance in the superconducting state at the (111) LaAlO$_3$ / SrTiO$_3$ interface. *Physical Review B* **96,** 134502 (Oct. 2017).

76. Ren, T. *et al.* Two-dimensional superconductivity at the surfaces of KTaO$_3$ gated with ionic liquid. *Science Advances* **8,** eabn4273 (June 2022).

77. Chen, Z. *et al.* Two-Dimensional Superconductivity at the LaAlO$_3$ / KTaO$_3$ (110) Heterointerface. *Physical Review Letters* **126,** 026802 (Jan. 2021).

78. Reyren, N. *et al.* Anisotropy of the superconducting transport properties of the LaAlO$_3$/SrTiO$_3$ interface. *Applied Physics Letters* **94.** 112506 (Mar. 2009).

79. Han, Y.-L. *et al.* Two-dimensional superconductivity at (110) LaAlO$_3$/SrTiO$_3$ interfaces. *Applied Physics Letters* **105.** 192603 (Nov. 2014).

80. Gor'kov, L. P. & Rashba, E. I. Superconducting 2D System with Lifted Spin Degeneracy: Mixed Singlet-Triplet State. *Phys. Rev. Lett.* **87,** 037004 (3 July 2001).

81. Davis, S. *et al.* Anisotropic multicarrier transport at the (111) LaAlO$_3$/SrTiO$_3$ interface. *Phys. Rev. B* **95,** 035127 (3 Jan. 2017).

82. Davis, S. *et al.* Anisotropic superconductivity and frozen electronic states at the (111) LaAlO$_3$/SrTiO$_3$ interface. *Phys. Rev. B* **98,** 024504 (2 July 2018).

83. Felner, I., Asaf, U., Levi, Y. & Millo, O. Coexistence of magnetism and superconductivity in R$_{1.4}$Ce$_{0.6}$RuSr$_2$Cu$_2$O$_{10-\delta}$s (R=Eu and Gd). *Phys. Rev. B* **55,** R3374–R3377 (6 Feb. 1997).

84. Dikin, D. A. *et al.* Coexistence of Superconductivity and Ferromagnetism in Two Dimensions. *Phys. Rev. Lett.* **107,** 056802 (5 July 2011).

85. Lesne, E. *et al.* Designing spin and orbital sources of Berry curvature at oxide interfaces. *Nature Materials* (Mar. 2023).

86. Gupta, A. *et al.* KTaO$_3$ —The New Kid on the Spintronics Block. *Advanced Materials* **34,** 2106481 (Mar. 2022).

87. Lesne, E. *et al.* Highly efficient and tunable spin-to-charge conversion through Rashba coupling at oxide interfaces. *Nature Materials* **15,** 1261–1266 (Dec. 2016).

88. Chauleau, J.-Y. *et al.* Efficient spin-to-charge conversion in the 2D electron liquid at the LAO/STO interface. *EPL (Europhysics Letters)* **116,** 17006 (Oct. 2016).

89. Sánchez, J. C. R. *et al.* Spin-to-charge conversion using Rashba coupling at the interface between non-magnetic materials. *Nature Communications* **4,** 2944 (Dec. 2013).

90. Jin, M.-J. *et al.* Nonlocal Spin Diffusion Driven by Giant Spin Hall Effect at Oxide Heterointerfaces. *Nano Letters* **17,** 36–43 (Jan. 2017).

91. Jin, M.-J. *et al.* Pure Spin Currents Driven by Colossal Spin–Orbit Coupling on Two-Dimensional Surface Conducting $SrTiO_3$. *Nano Letters* **21,** 6511–6517 (Aug. 2021).

92. Reyren, N. *et al.* Gate-Controlled Spin Injection at $LaAlO_3$ / $SrTiO_3$ Interfaces. *Physical Review Letters* **108,** 186802 (Apr. 2012).

93. Zhang, H. *et al.* Thermal Spin Injection and Inverse Edelstein Effect of the Two-Dimensional Electron Gas at EuO–$KTaO_3$ Interfaces. *Nano Letters* **19,** 1605–1612 (Mar. 2019).

94. Edelstein, V. Spin polarization of conduction electrons induced by electric current in two-dimensional asymmetric electron systems. *Solid State Communications* **73,** 233–235 (1990).

95. Sodemann, I. & Fu, L. Quantum Nonlinear Hall Effect Induced by Berry Curvature Dipole in Time-Reversal Invariant Materials. *Phys. Rev. Lett.* **115,** 216806 (21 Nov. 2015).

96. Ma, Q. *et al.* Observation of the nonlinear Hall effect under time-reversal-symmetric conditions. *Nature* **565,** 337–342 (Jan. 2019).

97. Xu, S.-Y. *et al.* Electrically switchable Berry curvature dipole in the monolayer topological insulator WTe2. *Nature Physics* **14,** 900–906 (Sept. 2018).

98. Zhang, Y., Van Den Brink, J., Felser, C. & Yan, B. Electrically tuneable nonlinear anomalous Hall effect in two-dimensional transition-metal dichalcogenides WTe_2 and $MoTe_2$. *2D Materials* **5,** 044001 (July 2018).

99. Pizzocchero, F. *et al.* The hot pick-up technique for batch assembly of van der Waals heterostructures. *Nature Communications* **7,** 11894 (June 2016).

100. Yu, Y.-J. *et al.* Tuning the Graphene Work Function by Electric Field Effect. *Nano Letters* **9,** 3430–3434 (Oct. 2009).

101. Britnell, L. *et al.* Field-Effect Tunneling Transistor Based on Vertical Graphene Heterostructures. *Science* **335,** 947–950 (Feb. 2012).

102. Georgiou, T. *et al.* Vertical field-effect transistor based on graphene–WS_2 heterostructures for flexible and transparent electronics. *Nature Nanotechnology* **8,** 100–103 (Feb. 2013).

103. Cao, Y. *et al.* Unconventional superconductivity in magic-angle graphene superlattices. *Nature* **556,** 43–50 (Apr. 2018).

104. Kang, K., Li, T., Sohn, E., Shan, J. & Mak, K. F. Nonlinear anomalous Hall effect in few-layer WTe_2. *Nature Materials* **18,** 324–328 (Apr. 2019).

105. Ye, X.-G. *et al.* Control over Berry Curvature Dipole with Electric Field in WTe_2. *Phys. Rev. Lett.* **130,** 016301 (1 Jan. 2023).

106. Duan, J. *et al.* Giant Second-Order Nonlinear Hall Effect in Twisted Bilayer Graphene. *Physical Review Letters* **129,** 186801 (Oct. 2022).

107. Ma, T. *et al.* Growth of bilayer $MoTe_2$ single crystals with strong non-linear Hall effect. *Nature Communications* **13,** 5465 (Sept. 2022).

108. Lao, B. *et al.* Anisotropic linear and nonlinear charge-spin conversion in topological semimetal $SrIrO_3$. *Physical Review B* **106,** L220409 (Dec. 2022).

109. Min, L. *et al.* Strong room-temperature bulk nonlinear Hall effect in a spin-valley locked Dirac material. *Nature Communications* **14,** 364 (Jan. 2023).

110. Esin, V. D., Avakyants, A. A., Timonina, A. V., Kolesnikov, N. N. & Deviatov, E. V. Second-Harmonic Response in Magnetic Nodal-Line Semimetal $Fe_3 GeTe_2$. *Chinese Physics Letters* **39,** 097303 (Aug. 2022).

111. Kiswandhi, A. & Osada, T. Observation of possible nonlinear anomalous Hall effect in organic two-dimensional Dirac fermion system. *Journal of Physics: Condensed Matter* **34,** 105602 (Mar. 2022).

112. Itahashi, Y. M. *et al.* Giant second harmonic transport under time-reversal symmetry in a trigonal superconductor. *Nature Communications* **13,** 1659 (Mar. 2022).

113. Dzsaber, S. *et al.* Giant spontaneous Hall effect in a nonmagnetic Weyl–Kondo semimetal. *Proceedings of the National Academy of Sciences* **118,** e2013386118 (Feb. 2021).

114. Schade, N. B., Schuster, D. I. & Nagel, S. R. A nonlinear, geometric Hall effect without magnetic field. *Proceedings of the National Academy of Sciences* **116,** 24475–24479 (Dec. 2019).

115. Ho, S.-C. *et al.* Hall effects in artificially corrugated bilayer graphene without breaking time-reversal symmetry. *Nature Electronics* **4,** 116–125 (Feb. 2021).

116. Webb, R. A., Washburn, S. & Umbach, C. P. Experimental study of nonlinear conductance in small metallic samples. *Physical Review B* **37,** 8455–8458 (May 1988).

117. Zhang, C.-P., Gao, X.-J., Xie, Y.-M., Po, H. C. & Law, K. T. Higher-order nonlinear anomalous Hall effects induced by Berry curvature multipoles. *Phys. Rev. B* **107,** 115142 (11 Mar. 2023).

118. Nakagawa, N., Hwang, H. Y. & Muller, D. A. Why some interfaces cannot be sharp. *Nature Materials* **5,** 204–209 (Mar. 2006).

119. Harrison, W. A., Kraut, E. A., Waldrop, J. R. & Grant, R. W. Polar heterojunction interfaces. *Phys. Rev. B* **18,** 4402–4410 (8 Oct. 1978).

120. Liu, Z. Q. *et al.* Origin of the Two-Dimensional Electron Gas at $LaAlO_3/SrTiO_3$ Interfaces: The Role of Oxygen Vacancies and Electronic Reconstruction. *Phys. Rev. X* **3,** 021010 (2 May 2013).

121. Rödel, T. C. *et al.* Universal Fabrication of 2D Electron Systems in Functional Oxides. *Advanced Materials* **28,** 1976–1980 (2016).

122. Tufte, O. N. & Chapman, P. W. Electron Mobility in Semiconducting Strontium Titanate. *Phys. Rev.* **155,** 796–802 (3 Mar. 1967).

123. Pavlenko, N., Kopp, T., Tsymbal, E. Y., Mannhart, J. & Sawatzky, G. A. Oxygen vacancies at titanate interfaces: Two-dimensional magnetism and orbital reconstruction. *Phys. Rev. B* **86,** 064431 (6 Aug. 2012).

124. Brinkman, A. *et al.* Magnetic effects at the interface between non-magnetic oxides. *Nature Materials* **6,** 493–496 (July 2007).

125. Al-Tawhid, A. H. *et al.* Oxygen Vacancy-Induced Anomalous Hall Effect in a Nominally Non-magnetic Oxide. *Journal of Electronic Materials* **51,** 7073–7077 (Dec. 2022).

126. Reyren, N. *et al.* Superconducting Interfaces Between Insulating Oxides. *Science* **317,** 1196–1199 (Aug. 2007).

127. Tinkham, M. *Introduction to Superconductivity* 2nd ed. ISBN: 0486435032 (Dover Publications, June 2004).

128. Chandrasekhar, P. V. *Lecture Notes from Phys 422-1, and Phys 422-2* Fall 2018 and Winter 2019.

129. in. *Collected Papers of L.D. Landau* (ed TER HAAR, D.) 217–225 (Pergamon, 1965). ISBN: 978-0-08-010586-4.

130. Aslamazov, L. & Larkin, A. I. The Influence of Fluctuation Pairing of Electrons on the Conductivity of Normal Metal. *Physics Letters* **26A,** 238–239 (Jan. 1968).

131. Maki, K. The Critical Fluctuation of the Order Parameter in Type-II Superconductors. *Progress of Theoretical Physics* **39,** 897–906 (Apr. 1968).

132. Thompson, R. S. Microwave, Flux Flow, and Fluctuation Resistance of Dirty Type-II Superconductors. *Phys. Rev. B* **1,** 327–333 (1 Jan. 1970).

133. Mehta, M. *Interplay between superconductivity and ferromagnetism at the LaAlO$_3$ / SrTiO$_3$ interface* PhD dissertation (Northwestern University, 2015).

134. Halperin, B. I. & Nelson, D. R. Resistive transition in superconducting films. *Journal of Low Temperature Physics* **36,** 599–616 (Sept. 1979).

135. Kosterlitz, J. M. & Thouless, D. J. Ordering, metastability and phase transitions in two-dimensional systems. *Journal of Physics C: Solid State Physics* **6,** 1181 (Apr. 1973).

136. Beasley, M. R., Mooij, J. E. & Orlando, T. P. Possibility of Vortex-Antivortex Pair Dissociation in Two-Dimensional Superconductors. *Phys. Rev. Lett.* **42,** 1165–1168 (17 Apr. 1979).

137. Ziman, J. M. *Principles of the Theory of Solids* 2nd ed. (Cambridge University Press, 1972).

138. Lee, P. A. & Ramakrishnan, T. V. Disordered electronic systems. *Rev. Mod. Phys.* **57,** 287–337 (2 Apr. 1985).

139. Bal, V. *Transport Measurements on (111) Oriented (La$_{0.3}$Sr$_{0.7}$)(Al$_{0.65}$Ta$_{0.35}$)O$_3$ / SrTiO$_3$ Heterostructures* PhD dissertation (Northwestern University, 2018).

140. Hikami, S., Larkin, A. I. & Nagaoka, Y. Spin-Orbit Interaction and Magnetoresistance in the Two Dimensional Random System. *Progress of Theoretical Physics* **63,** 707–710 (Feb. 1980).

141. Houghton, A., Senna, J. R. & Ying, S. C. Magnetoresistance and Hall effect of a disordered interacting two-dimensional electron gas. *Phys. Rev. B* **25,** 2196–2210 (4 Feb. 1982).

142. Ando, T., Fowler, A. B. & Stern, F. Electronic properties of two-dimensional systems. *Rev. Mod. Phys.* **54,** 437–672 (2 Apr. 1982).

143. Shoenberg, D. *Magnetic Oscillations in Metals* (Cambridge University Press, 1984).

144. McGuire, T. & Potter, R. Anisotropic magnetoresistance in ferromagnetic 3d alloys. *IEEE Transactions on Magnetics* **11,** 1018–1038 (1975).

145. Dikin, D. A. *et al.* Coexistence of Superconductivity and Ferromagnetism in Two Dimensions. *Phys. Rev. Lett.* **107,** 056802 (5 July 2011).

146. Luo, Y. *et al.* Hall effect in the extremely large magnetoresistance semimetal WTe2. *Applied Physics Letters* **107.** 182411 (Nov. 2015).

147. Wu, J., Bollinger, A. T., He, X. & Božović, I. Detecting Electronic Nematicity by the Angle-Resolved Transverse Resistivity Measurements. *Journal of Superconductivity and Novel Magnetism* **32,** 1623–1628 (June 2019).

148. Nagaosa, N., Sinova, J., Onoda, S., MacDonald, A. H. & Ong, N. P. Anomalous Hall effect. *Rev. Mod. Phys.* **82,** 1539–1592 (2 May 2010).

149. Brenevig, B. A. *Topological Insulators and Topological Superconductors* (ed Hughes, T. L.) (Princeton University Press, 2013).

150. Xiao, D., Chang, M.-C. & Niu, Q. Berry phase effects on electronic properties. *Rev. Mod. Phys.* **82,** 1959–2007 (3 July 2010).

151. Klitzing, K. v., Dorda, G. & Pepper, M. New Method for High-Accuracy Determination of the Fine-Structure Constant Based on Quantized Hall Resistance. *Phys. Rev. Lett.* **45,** 494–497 (6 Aug. 1980).

152. Laughlin, R. B. Quantized Hall conductivity in two dimensions. *Phys. Rev. B* **23,** 5632–5633 (10 May 1981).

153. Delahaye, J. & Grenet, T. Metallicity of the $SrTiO_3$ surface induced by room temperature evaporation of alumina. *Journal of Physics D: Applied Physics* **45,** 315301 (2012).

154. Davis, S. *Emergent Phenomena at the (111) LaAlO$_3$ / SrTiO$_3$ Interface* PhD dissertation (Northwestern University, 2017).

155. Tomar, R., Wadehra, N., Budhiraja, V., Prakash, B. & Chakraverty, S. Realization of single terminated surface of perovskite oxide single crystals and their band profile: (LSAT)*, $SrTiO_3$ and $KTaO_3$ case study. *Applied Surface Science* **427,** 861–866 (2018).

156. Bae, H.-j., Sigman, J., Norton, D. & Boatner, L. Surface treatment for forming unit-cell steps on the (001) KTaO3 substrate surface. *Applied Surface Science* **241,** 271–278 (2005).

157. Trepakov, V. *et al.* The negative thermo-optic effect in $KTaO_3$: an ellipsometry study. *Phase Transitions* **88,** 991–1000 (2015).

158. Jiang, Z. *Thermal Transport Near The Normal-Metal/Superconductor Interface In Mesoscopic Devices* PhD dissertation (Northwestern University, 2005).

159. Oh, J., Myoung, J., Bae, J. S. & Lim, S. Etch Behavior of ALD Al_2O_3 on HfSiO and HfSiON Stacks in Acidic and Basic Etchants. *Journal of The Electrochemical Society* **158,** D217 (Feb. 2011).

160. John, D. D. *Wet etching recipes* Nov. 2022. eprint: `https://wiki.nanotech.ucsb.edu/wiki/Wet_Etching_Recipes`.

161. Biscaras, J. *et al.* Limit of the electrostatic doping in two-dimensional electron gases of $LaXO_3(X = Al, Ti)/SrTiO_3$. *Scientific Reports* **4,** 6788 (May 2015).

162. Eom, J. *Electrical Properties of Mesoscopic Spin Glasses* PhD dissertation (Northwestern University, 1998).

163. Krantz, P. W. & Chandrasekhar, V. *Nonlocal Differential Resistance in AlO$_x$/KTaO$_3$ Heterostructures* 2022. arXiv: `2210.12146 [cond-mat.mes-hall]`.

164. Krantz, P., Tyner, A., Goswami, P. & Chandrasekhar, V. *Colossal Spontaneous Hall Effect and Emergent Magnetism in KTaO₃ Two-Dimensional Electron Gases* 2023. arXiv: `2209.10534 [cond-mat.mes-hall]`.

165. Lifshitz, I. M. Anomalies of the electron characteristics of a metal in the high pressure region. *JTEP* **11,** 1569–1576 (May 1960).

166. Ben Shalom, M., Ron, A., Palevski, A. & Dagan, Y. Shubnikov–De Haas Oscillations in $\mathrm{SrTiO_3/LaAlO_3}$ Interface. *Phys. Rev. Lett.* **105,** 206401 (20 Nov. 2010).

167. Singh, G. *et al.* Competition between electron pairing and phase coherence in superconducting interfaces. *Nature Communications* **9,** 407 (Jan. 2018).

168. Hall, H. E., Vinen, W. F. & Shoenberg, D. The rotation of liquid helium II II. The theory of mutual friction in uniformly rotating helium II. *Proceedings of the Royal Society of London. Series A. Mathematical and Physical Sciences* **238,** 215–234 (1956).

169. Mehta, M. *et al.* Evidence for charge–vortex duality at the LaAlO3/SrTiO3 interface. *Nature Communications* **3,** 955 (July 2012).

170. Wang, Z. D. & Ting, C. S. Anomalous Hall effect associated with pinning in high-κ superconductors. *Phys. Rev. Lett.* **67,** 3618–3621 (25 Dec. 1991).

171. Ferrell, R. A. Hall voltage sign reversal in thin superconducting films. *Phys. Rev. Lett.* **68,** 2524–2527 (16 Apr. 1992).

172. Geshkenbein, V. B. & Larkin, A. I. Comment on "Hall effect of vortices parallel to $\mathrm{CuO_2}$ layers and the origin of the negative Hall anomaly in $\mathrm{YBa_2Cu_3O_{7-\delta}}$". *Phys. Rev. Lett.* **73,** 609–609 (4 June 1994).

173. Zhao, S. Y. F. *et al.* Sign-Reversing Hall Effect in Atomically Thin High-Temperature $\mathrm{Bi_{2.1}Sr_{1.9}CaCu_{2.0}O_{8+\delta}}$ Superconductors. *Phys. Rev. Lett.* **122,** 247001 (24 June 2019).

174. Feigel'man, M. V., Geshkenbein, V. B., Larkin, A. & Vinokur, V. M. Sign change of the flux-flow Hall effect in HTSC. *JTEP* **62,** 811–817 (Nov. 1995).

175. Destraz, D., Ilin, K., Siegel, M., Schilling, A. & Chang, J. Superconducting fluctuations in a thin NbN film probed by the Hall effect. *Phys. Rev. B* **95,** 224501 (22 June 2017).

176. Agarwal, S. *et al.* Spin-valve-like magnetoresistance in a Ni-Mn-In thin film. *Phys. Rev. B* **97,** 214427 (21 June 2018).

177. Fowley, C., Chun, B. S. & Coey, J. M. D. Negative Magnetoresistance in Dual Spin Valve Structures With a Synthetic Antiferromagnetic Free Layer. *IEEE Transactions on Magnetics* **45,** 2403–2406 (2009).

178. Ryan, K. M. *et al.* Characterization of Nb films for superconducting qubits using phase boundary measurements. *Applied Physics Letters* **121.** 202601 (Nov. 2022).

179. Caviglia, A. D. *et al.* Tunable Rashba Spin-Orbit Interaction at Oxide Interfaces. *Phys. Rev. Lett.* **104,** 126803 (12 Mar. 2010).

LOW TEMPERATURE ELECTRICAL TRANSPORT BEHAVIOR OF ALO$_x$ / KTAO$_3$ BASED TWO DIMENSIONAL ELECTRON GASES

Approved by:

Venkat Chandrasekhar
Physics and Astronomy
Northwestern University

Venyak P. Dravid
Materials Science
Northwestern University

Pallab Goswami
Physics and Astronomy
Northwestern University

Date Approved: June 30, 2023

APPENDIX A

CRYSTAL DIRECTORY AND ORIENTATION

Below are summary tables of the six measured samples and the crystalline orientation. A sample is said to be described by the crystal direction of it principle axis, or alternatively the plane of the surface. A cubic crystal with principle axis along the [110] direction can also be described as terminated by the (110) plane, which is the normal nomenclature for this work. Such a crystal would have sets of perpendicular vectors on the surface, in the (110) plane. Those surface vectors describe the directions of the driving current of the the perpendicular Hall bars fabricated on the surface. If those surface vectors are aligned with the other axes of the crystal, they are most simply broken down into the [001] direction and [1$\bar{1}$0] directions for the long and short directions of the cut respectively. Similarly, all (001) crystals have [001] surface orientations, or more correctly, one of the $<$001$>$ group of surface orientations. For the case of the (111) the two oriented surface directions are [1$\bar{1}$0] and [1$\bar{1}$2]. [1$\bar{1}$2] is the direction aligned to the points of the Laue triangle, [1$\bar{1}$0] is perpendicular to that.

Table A.1 contains the crystal orientations for the normal metal samples, including relative

Table A.1: **Crystal orientation for the normal metal samples, as determined by Laue diffraction.** Sample name and crystal orientation are described, as are an estimate of the angle between the current and the in plane field. Also included are wiring pin-outs for ease of reference.

Sample	Orientation	$H_\parallel$ Angle (θ)	Current Contacts	Voltage Probes
(001)	[001]	0	(7,3g)	(1,2),(6,4)
(110)	[001]	180	(9,15g)	(11,12), (10,14)
(110) (1)	[1$\bar{1}$0]	180	(23,19g)	(17,18), (22,20)
(110) (2)	[1$\bar{1}$2]	-90	(31,26g)	(24,–), (28,27)

Table A.2: **Crystal orientation for the superconducting samples, as determined by Laue diffraction.** Sample name and crystal orientation are described, as are an estimate of the angle between the current and the in plane field. Also included are wiring pin-outs for ease of reference.

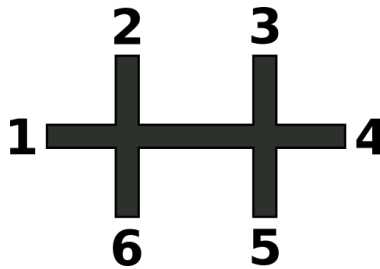| Sample	Orientation	$H_\parallel$ Angle (θ)	Current Contacts	Voltage Probes
(001)	[001]	0	(1,4g)	(2,3), (6,5)
(110)	[11$\sqrt{2}$]	90	(7,3g)	(8,12), (15,14)
(111) (1)	[1$\bar{1}$0]	0	(16,19g)	(17,18), (–,21)
(111) (2)	[1$\bar{1}$2]	-90	(22,26g)	(23,24), (28,27)

Figure A.1: **Standard Hall bar layout and lead labeling.** Standard Hall orientation used for each of the samples in the manuscript. 1 and 4 are current probes, while 2, 3, 5, and 6 are voltage probes. The pairs of (2, 3) and (5, 6) measure longitudinal resistances while pairs of (2, 6) and (3, 5) measure transverse resistances.

orientation to parallel-to-surface magnetic field. The (111) normal metal sample turned out to be (110), a mistake by the manufacturer in the wake of the pandemic. This was discovered by Laue well after the fact. Similarly, it was found that the (110) superconducting sample was aligned to the corners of the samples instead of the edges, so the effective crystal orientation is a mix of [001] and [1$\bar{1}$0], something close to [11$\sqrt{2}$]. Table A.2 contains the crystal orientations for the superconducting samples, including relative orientation to parallel-to-surface magnetic field. The wirebonding orientation are described in Fig. A.1, and was kept the same for all of the samples. The pin numbers of the wirebonding layouts for samples are also included in Tables A.1 and A.2 for the current and voltage leads as described by Fig. A.1.

APPENDIX B

ADDITIONAL MAGNETORESISTANCE SETS

Sets of perpendicular field magnetoresistance (MR) traces to ± 1.1 T were taken at several fixed temperatures to extract information about the carrier behavior. Both the longitudinal and transverse MR were measured as a function of applied back gate voltage, revealing dependences on the carrier concentration and other parameters. The longitudinal MR is shown in Fig. B.1 for the normal samples and Fig. B.2 for the s.c. samples as percent MR, $\%MR = \frac{R(H_\perp) - R(H_\perp = 0)}{R(H_\perp = 0)}$ for applied perpendicular magnetic field, $H_\perp$. All fields in this Appendix will drop the ($\perp$) subscript and simply be referred to as the applied magnetic field, H. Additionally, the presented longitudinal data were produced by following the drift correction procedure outlined in Chapter 4, with larger drifts and increased noise observed for lower values of applied back gate voltage, V_g.

The data show several prominent features including the low field dip sharpened for all sample with increasing V_g. This dip was first interpreted to be caused by weak anti-localization, but the scaling does not agree with this interpretation. Change in magnetoresistance due to weak localization is proportional to the sheet resistance divided by the resistance quantum, $\frac{\Delta R}{R} \propto \frac{R_{sq}}{\pi(h/e^2)}$. For low gate voltages and high $R_{sq.}$ this relation could produce the %MR seen in Fig. B.1, but the dips seen at low $R_{sq.}$ are many times too big to be solely from weak antilocalization. Thus, the feature will simply be referred to as the low field dip. In addition to this dip, the traces show a modulation of the shape of the higher field MR, indicating a tuning of spin-orbit interaction strength. Both the gate voltage tuning of the low field dip, and the tuning of the spin orbit interactions are expected in these samples, and agree with previous works.[13,56,139,179] Fig. B.1 (a) shows the data for the (001) sample measured at 5 K, which had the least tuning, with almost no change to the 0.50 % MR over

(a) (001) Normal Sample (5 K)

(b) (110) Normal Sample, [001] direction (5 K)

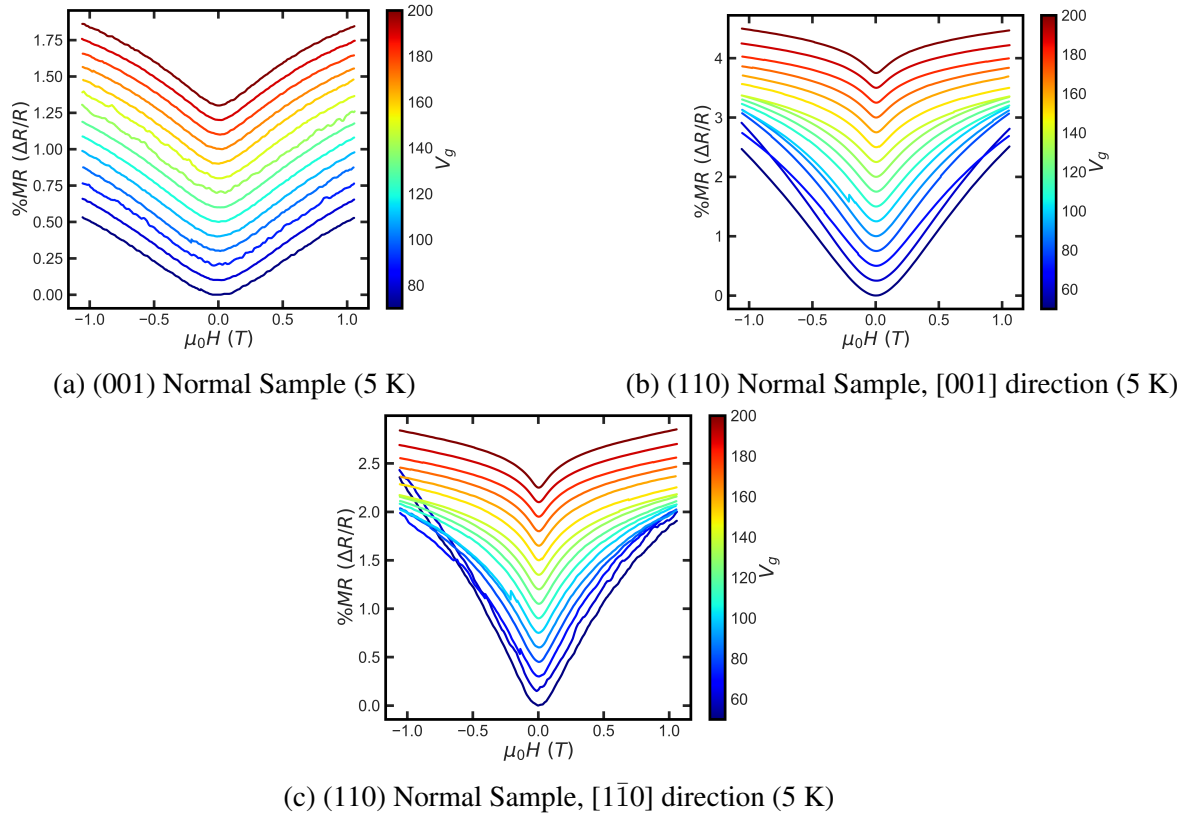(c) (110) Normal Sample, [1$\bar{1}$0] direction (5 K)

Figure B.1: **Gate voltage dependence of longitudinal magnetoresistance for normal samples.** (a) - (c) Magnetoresistance traces of the (001), (110), and (110) [1$\bar{1}$0] samples respectively. The curves have been incrementally shifted for clarity.

the full measurement range, and only a minimal sharpening of the low field dip with increased V_g. In contrast, the (110) samples shown in Fig. B.1 (b) and (c) boasted significantly larger changes in MR with maximal values of 2.5 % at V_g = 50 V reducing to $\approx$ 0.5 % at V_g = 50 V. Both the samples also showed spin-orbit tuning, evident in the crossing of traces as V_g is increased. Traces for both samples become more noisy at low V_g, stemming from large resistances and increased drift. Despite this, it appears that the sharpness of the low field dip is most prominent in the [1$\bar{1}$0] direction of the (110), but the edge of the dip is roughly the same field for each sample, indicating that the phase coherence length is similar for all samples.
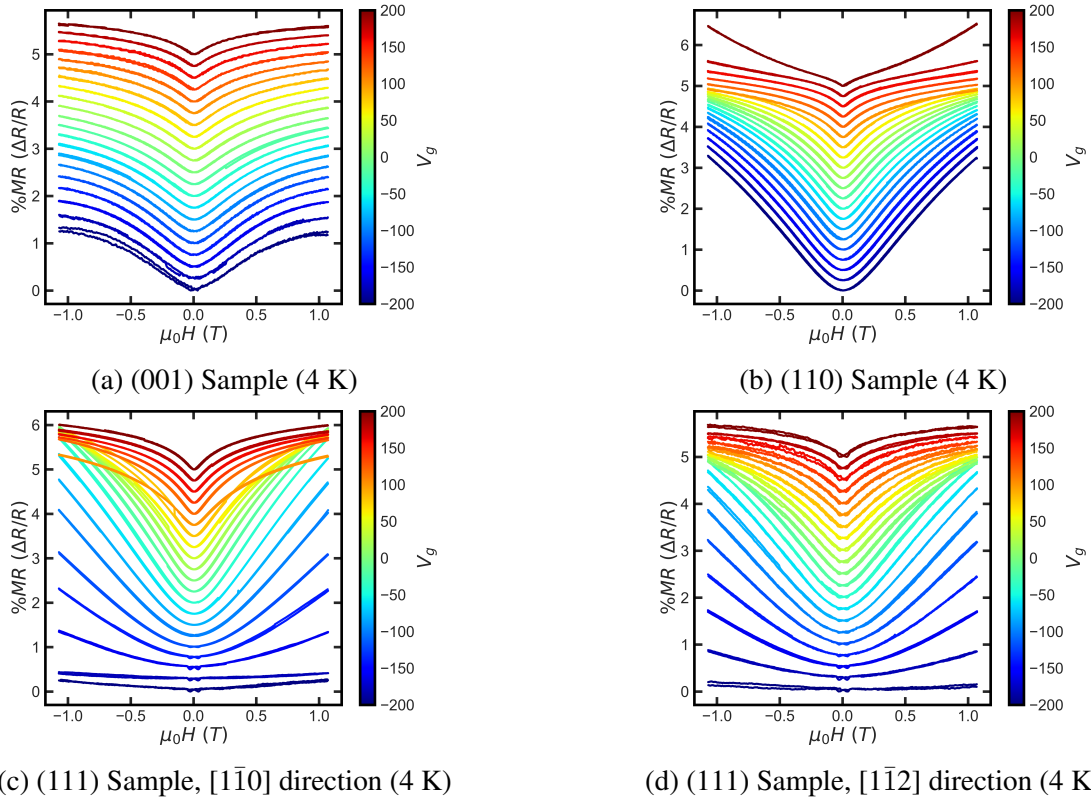
Figure B.2: **Gate voltage dependence of longitudinal magnetoresistance for superconducting samples.** (a) - (d) Magnetoresistance traces of the (001), (110), (111) [1$\bar{1}$0], and (111) [1$\bar{1}$2] samples respectively. The curves have been incrementally shifted for clarity. Tuning of spin orbit interactions are apparent for the (110) and (111) samples in the shape of the high field curves. The traces for the (111) Hall bars show the onset of hysteretic dips due to magnetic order, even at 4 K.

Comparatively, the longitudinal MR of the s.c. samples shown in Fig. B.2 have greater variation with gate voltage and crystal direction. The (001) sample in Fig. B.2 (a) was once again the least tunable, showing sharpening of the low field dip with increasing V_g, and a maximal change of only 1.25 % MR at V_g = -200 V. The shape of the higher field curves also showed only minimal change with V_g, agreeing with the expectation that the (001) has weaker spin-orbit character. In general, it may be interesting to measure these samples to a higher field, looking for negative MR or to allow for an analytical fit in manner of previous works.[56]

The (110) s.c. sample in Fig. B.2 (b) showed a more pronounced sharpening of the low field dip with increasing gate voltage, and an interesting dependence in the higher field spin-orbit interactions. The slopes of the traces at higher fields vary non-monotonically with gate voltage, with a maximal values at low V_g of nearly 3.3 % MR. The changes of the slope at higher field do not directly correspond to the changes in carrier concentration, discussed in Chapter 5, but seem to correlate to it loosely.

The two surface directions of the (111) sample are shown in Fig. B.2 (c – d), for the $[1\bar{1}0]$ direction in (c) and for the $[1\bar{1}2]$ direction in (d). The data show substantial, non-monotonic tuning of both the depth of the low field dip and the shape of the higher field curves. Both trends seems to reflect the changes in carrier concentration, as was suspected for the (110) sample. Both samples have maximum change in MR for V_g near 0 V, with 3.8 % and 2.8 % for the $[1\bar{1}0]$ and $[1\bar{1}2]$ directions respectively. The shape of the low field dip is also strongly dependent on V_g and is nearly extinguished for low values of V_g in contrast to the other samples. Both of the samples also show signs of hysteretic dips in resistance at around ± 60 mT, indicating the emergence of magnetic order in the samples. These dips appear only at low values of V_g for the $[1\bar{1}0]$ but across all values for the $[1\bar{1}2]$, which is somewhat puzzling. This emergent magnetism will be discussed in detail later, but this is the highest temperature at which the effect manifests, and this work is the first time such a signature has been observed in nominally non-magnetic samples.

Fig. B.3 show the Hall traces of the normal sample set taken at 5 K, measured simultaneously with the longitudinal data shown in Fig. B.1. The Hall are well behaved for the largest values of V_g and start to show emergent symmetric contributions at low values of V_g. The slope represents normal electron-like conduction, and fits to the data were used to calculate the carrier concentrations showed in Chapter 5.

(a) (001) Sample

(b) (110) Sample, [001] direction
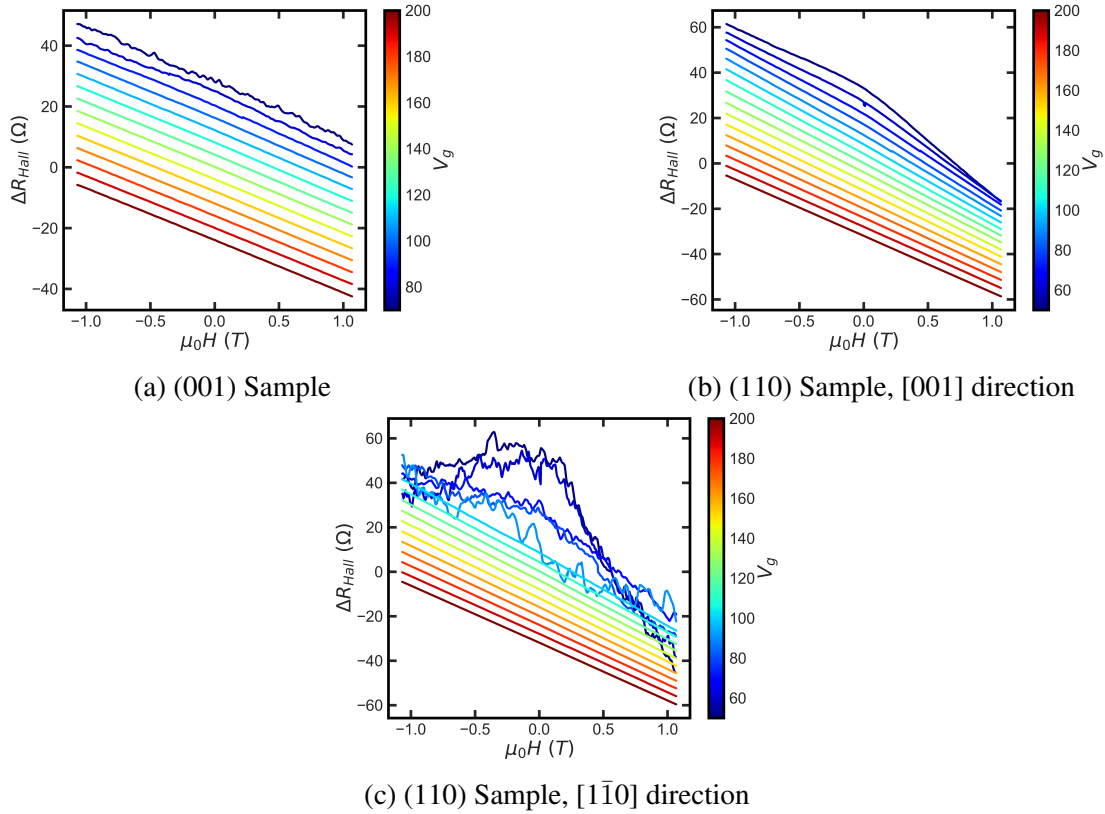
(c) (110) Sample, [1$\bar{1}$0] direction

Figure B.3: **Gate voltage dependence of transverse magnetoresistance for normal samples at 5 K.** (a) - (c) Transverse magnetoresistance traces of the (001) sample, the (110) sample, and the (110) sample, [1$\bar{1}$0] direction, respectively. The curves have been incrementally shifted for clarity. Increased noise and an emergent symmetric curvature arise for low values of V_g.

B.1   Magnetoresistance of the (001) Superconducting Sample

To complement the normal state traces of the previous section, we consider the longitudinal magnetoresistance (MR) of the (001) s.c. sample, which did not show a superconducting transition down to 25 mK. The longitudinal %MR and transverse MR measured at 30 mK are shown in Fig. B.4 (a) and (b), respectively. Both the longitudinal and transverse show hysteretic peaks from macroscopic magnetic order, in agreement with the results of the normal samples. The longitudinal MR shows tuning of the spin-orbit interactions evident in the change of high field MR, and a sharp

dip in resistance at low fields. The Hall signals agree with those measured at higher temperatures, indicating that the carrier concentrations did not change substantially over the temperature range, as expected. In all, the (001) did not show significant change from the previous set, but still serves as a foil to the change in behavior for the (110) and (111) samples.

(a) (001) Normal Sample (30 mK)

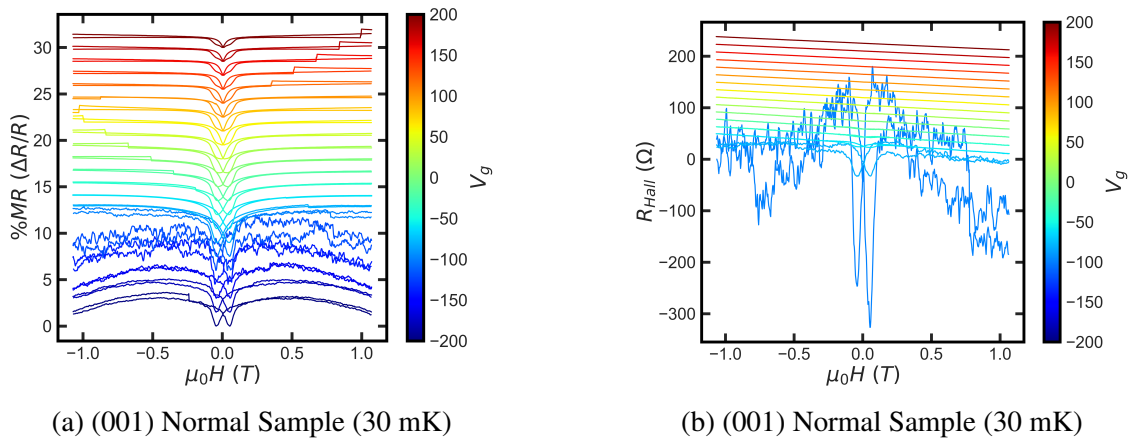(b) (001) Normal Sample (30 mK)

Figure B.4: **Magnetoresistance traces of the (001) superconducting sample measured at 30 mK.** (a) Longitudinal magnetoresistance reported as % MR, $(\Delta R/R)$, showing the expected tuning of spin orbit interactions in the high field limits, and a sharp dip due to weak antilocalization, equipped with hysteretic magnetic peaks. (b) Transverse magnetoresistance as a function of back gate voltage, uniformly shifted for clarity, showing hysteresis but otherwise weak dependencies.

VITA

Patrick W Krantz

Place of Birth: Lewes, Delaware
Year: November 18, 1989

Education

Northwestern University	Graduated 2023

Ph.D. Physics

University of Toledo	Graduated 2015

M.S. in Physics - Photovoltaics

The Ohio State University	Graduated 2013

B.S. Physics

Research Experience

Graduate Researcher|Physics	Sept 2017 - June 2023

Northwestern University, Evanston, IL — Chandrasekhar Group
•Measuring emergent phenomenon in complex oxide heterostructures.

Graduate Researcher|Physics - Photovoltaics	June 2013 - Jan 2015

University of Toledo, Toledo, OH — Heben Research Group
•Nanotube back contacts for transparent solar cells

Professional Experience

Hohman Plating and Manufacturing	Feb 2017 - Aug 2017

•Process Reliability Engineer for Vacuum Systems

First Solar, Inc	Feb 2015 - May 2016

•Developmental Engineering Technician

Selected Publications

Alexander, G.C.B., **Krantz, P.W.**, Jung, H.J., Davis, S.K., Xu, Y., Dravid, V.P., Chandrasekhar, V., and Kanatzidis, M.G.. 'Controllable nonclassical conductance switching in nanoscale phase-separated $(PbI_2)_{1-x}(BiI_3)_x$ layered crystals.' *Adv. Mat.*, 33(51):2103098, **2021**.

Krantz, P.W. and Chandrasekhar, V. 'Observation of Zero-field transverse resistance in AlO_x / SrTiO3 interface devices.' *Phys. Rev. Lett.*, 127:036801, **Jul 2021.**

Song, Z., McElvany, C., Phillips, A., Celik, I., **Krantz, P.**, Watthage, S., Liyanage, G., Apul, D., Heben, M. 'A technoeconomic analysis of perovskite solar module manufacturing with low-cost materials and techniques' *Energy Environ. Sci.* (**2017**), 10, 1297 – 1305.
DOI:10:1039/C7EE00757D